

# Design, Modelling, and Optimisation of Optical Systems for High-Temperature Concentrating Solar Applications

Lifeng Li



Australian  
National  
University

A thesis submitted for the degree of  
Doctor of Philosophy  
The Australian National University

April 2021

© Copyright by Lifeng Li 2021  
All Rights Reserved



---

## Supervisory Panel

---

**Chair of Supervisory Panel and Primary Supervisor:**

Professor Wojciech Lipiński

2015–2021

**Associate Supervisor:**

Associate Professor John Pye

2015–2021

**Associate Supervisor:**

Dr Roman Bader

2015–2017

**Associate Supervisor:**

Dr José Zapata

2018–2021



---

## Declaration

---

I certify that this thesis does not incorporate without acknowledgement any material previously submitted for a degree or diploma in any university, and that, to the best of my knowledge, it does not contain any material previously published or written by another person except where due reference is made in the text. The work in this thesis is my own, except for the contributions made by others as described in the Acknowledgements. This thesis is a compilation of six journal publications, all of which I am the first author. The details are given below.

Publication 1 is presented as Chapter 3 in this thesis.

- *Title:* Design of a Compound Parabolic Concentrator for a Multi-Source High-Flux Solar Simulator.
- *Authors:* Lifeng Li, Bo Wang, Johannes Pottas, and Wojciech Lipiński.
- *Current status:* published in *Solar Energy*, volume 183, pages 805–811, 2019.
- *Contributions:* Lifeng Li conceived the idea, performed the optical design and modelling, and wrote the original manuscript. Bo Wang conducted the thermal modelling of the cooling system of the compound parabolic concentrator (CPC). Johannes Pottas designed the CPC cooling channel layout and was in charge of the fabrication of the CPC. Wojciech Lipiński conceived the idea, contributed to the design and analyses, and supervised the project. All authors reviewed and edited the manuscript.
- Declaration signed by a senior author: *Wojciech Lipiński*

Publication 2 is presented as Chapter 4 in this thesis.

- *Title:* Reflective Optics for Redirecting Convergent Radiative Beams in Concentrating Solar Applications.
- *Authors:* Lifeng Li, Bo Wang, Roman Bader, José Zapata, and Wojciech Lipiński.
- *Current status:* published in *Solar Energy*, volume 191, pages 707–718, 2019.
- *Contributions:* Lifeng Li conceived the idea, performed the optical design, modelling and analysis, and wrote the original manuscript. Bo Wang supported the optical design, simulations, and analysis. Roman Bader conceived the idea, and contributed to the optical design and analysis. José Zapata contributed to the optical analysis. Wojciech Lipiński conceived the idea, contributed to the

optical design and analysis, and supervised the project. All authors reviewed and edited the manuscript.

- Declaration signed by a senior author: Wojciech Lipiński

Publication 3 is presented as Chapter 5 in this thesis.

- *Title:* Optics of Solar Central Receiver Systems: A Review.
- *Authors:* Lifeng Li, Joe Coventry, Roman Bader, John Pye, and Wojciech Lipiński.
- *Current status:* published in *Optics Express*, volume 24, issue 14, pages A985–A1007, 2016.
- *Contributions:* Lifeng Li conceived the idea, collected, reviewed, and summarised relevant literature, and wrote the original manuscript. Joe Coventry, Roman Bader, and John Pye supported the literature collection and analysis. Wojciech Lipiński conceived the idea, contributed to the literature collection and analysis, and supervised the project. All authors reviewed and edited the manuscript.

- Declaration signed by a senior author: Wojciech Lipiński


Publication 4 is presented as Chapter 6 in this thesis.

- *Title:* Temperature-Based Optical Design, Optimisation and Economics of Solar Polar-Field Central Receiver Systems with an Optional Compound Parabolic Concentrator.
- *Authors:* Lifeng Li, Bo Wang, John Pye, and Wojciech Lipiński.
- *Current status:* published in *Solar Energy*, volume 206, pages 1018–1032, 2020.
- *Contributions:* Lifeng Li conceived the idea, performed the optical design, modelling, optimisation, and economic analyses, and wrote the original manuscript. Bo Wang supported the optical design, simulations, and analyses. John Pye conceived the idea, and contributed to the optical design and analyses. Wojciech Lipiński conceived the idea, contributed to the optical design and analyses, and supervised the project. All authors reviewed and edited the manuscript.


- Declaration signed by a senior author: Wojciech Lipiński

Publication 5 is presented as Chapter 7 in this thesis.

- *Title:* Optical Analysis of a Multi-Aperture Solar Central Receiver System for High-Temperature Concentrating Solar Applications.

- *Authors:* Lifeng Li, Bo Wang, John Pye, Roman Bader, Wujun Wang, and Wojciech Lipiński.
- *Current status:* published in *Optics Express*, volume 28, issue 25, pages 37654–37668, 2020.
- *Contributions:* Lifeng Li conceived the idea, performed the optical design, modelling and analysis, and wrote the original manuscript. Bo Wang supported the optical design, simulations, and analysis. John Pye, Roman Bader, and Wujun Wang contributed to the optical design and analysis. Wojciech Lipiński conceived the idea, contributed to the optical design and analysis, and supervised the project. All authors reviewed and edited the manuscript.
- Declaration signed by a senior author: 

Publication 6 is presented as Chapter 8 in this thesis.

- *Title:* Optical Analysis of a Solar Thermochemical System with a Rotating Tower Reflector and a Receiver–Reactor Array.
- *Authors:* Lifeng Li, Song Yang, Bo Wang, John Pye, and Wojciech Lipiński.
- *Current status:* published in *Optics Express*, volume 28, pages 19429–19445, 2020.
- *Contributions:* Lifeng Li conceived the idea, performed the optical design, modelling, and analysis, and wrote the original manuscript. Song Yang and Bo Wang supported the optical design, simulations, and analysis. John Pye contributed to the optical analysis. Wojciech Lipiński conceived the idea, contributed to the optical design and analysis, and supervised the project. All authors reviewed and edited the manuscript.
- Declaration signed by a senior author: 

Four additional publications of which I am the joint author are:

1. B. Wang, L. Li, J. Pottas, R. Bader, V. Wheeler, P. Kreider, and W. Lipiński. Thermal model of a solar thermochemical reactor for metal oxide reduction. *Journal of Solar Energy Engineering*, 142(5):051002, 2019.
2. B. Wang, L. Li, F. Schäfer, J. Pottas, A. Kumar, V. Wheeler, and W. Lipiński, 2021. Thermal reduction of iron–manganese oxides particles in a high-temperature packed-bed solar thermochemical reactor. *Chemical Engineering Journal*, 410:128255, 2021.
3. W. Lipiński, E. Abbasi-Shavazi, J. Chen, J. Coventry, M. Hangi, S. Iyer, A. Kumar, L. Li, S. Li, J. Pye, J. F. Torres, B. Wang, Y. Wang, and V. Wheeler, 2020. Progress in heat transfer research for high-temperature solar thermal applications. *Applied Thermal Engineering*, 184:116137, 2020.

4. S. Yang, L. Li, B. Wang, S. Li, J. Wang, P. Lund, and W. Lipiński. Thermodynamic analyses of a novel solar thermochemical plant with a rotating tower reflector and a multi-receiver array. Submitted to *Frontiers in Energy Research*, under review, 2021.



Lifeng Li

7 April 2021

---

## Acknowledgements

---

Firstly, I would like to express my deepest gratitude to my primary supervisor Professor Wojciech Lipiński for his constant advice, encouragement, and support in every part of this work throughout my doctoral study. His professional and high-standard guidance introduced to me the beauty of research.

I am grateful to my co-supervisors Associate Professor John Pye, Dr Roman Bader, and Dr José Zapata for their strong support and patient guidance during the past five years. This work could not have been accomplished without their assistance.

I would like to also thank my colleagues and friends for all the specific discussions and assistance. Thank you for your presence and companionship and the joy you bring to my life.

The financial support from the Australian Renewable Energy Agency (grant no 2014/RND005) is gratefully acknowledged. The resources and services from the National Computational Infrastructure (NCI) supported by the Australian government are also gratefully acknowledged.

Finally, I would like to thank my parents for supporting my decisions all along. I would like to thank my daughter Hannah Wang for her sweet smile and kisses everyday, and especially my husband Bo Wang for his endless love and support.





---

## Abstract

---

Emerging high-temperature solar thermal and thermochemical systems aim to operate efficiently at temperatures above  $1000^{\circ}\text{C}$ , necessitating solar concentration ratios typically above 1000 suns. In research and development applications, the required high concentration ratios can be obtained by dedicated on-sun and indoor facilities of solar furnaces and high-flux solar simulators (HFSSs), respectively. For large-scale solar thermal and thermochemical plants, the requirement of high concentration ratios imposes great challenges on optical concentrators. Point-focusing optical concentrators, including parabolic dishes and heliostat fields in central receiver systems (CRSs), provide higher concentration ratios in the range of 500–10,000 suns than the concentration ratios of 2–100 suns provided by line-focusing optical concentrators such as parabolic troughs and linear Fresnel mirrors. Parabolic dish systems are capable of producing the required high concentration ratios above 1000 suns, however, their relatively small power output from each module limits the system economics. CRSs present higher power output but restricted concentration ratios up to 1000 suns to achieve reasonable optical efficiencies. Hence, optical concentrating systems that simultaneously provide high concentration ratios and high power output need to be explored.

In this work, design, modelling, and optimisation of primary and secondary solar concentrators are performed for the advancement and realisation of economically-feasible high-temperature concentrating solar technologies. This work focuses on two-stage solar optical concentrating systems designed for high-temperature applications. Two types of systems are investigated: (i) experimental-scale HFSS-based systems and (ii) commercial-scale CRSs. For maximising the design freedom, two-dimensional analytical ray-tracing and three-dimensional collision-based Monte-Carlo ray-tracing programs are developed in-house for simulating optical systems involved in this work.

For the HFSS-based experimental system, reflective optics in the shape of flat, ellipsoidal, hyperboloidal, and paraboloidal, and concentrating optics of the compound parabolic concentrator (CPC) are found to be capable of modifying the characteristics of the HFSS radiative output beam such as concentration ratio, ray distribution, and axis direction. The modification of the HFSS output beam characteristics enables the application of HFSSs to meet specific requirements of experimental testing of materials and device prototypes, and so on.

For commercial-scale CRSs, the optical, energetic, and economic performance of two types of system configurations are investigated and optimised, including a system with a single-aperture receiver and a polar field, and a system with a multi-aperture receiver and multiple sub-fields. For the study of polar-field CRSs, optical design and optimisation are performed for the receiver temperature ranging from

---

600 K to 1800 K to obtain optimal system energetic and economic performance, respectively. The working temperature thresholds at which the energetic and economic performance benefit from the addition of a CPC are identified as 900 K and 1200 K, respectively. In the study of multi-aperture CRSs, it is found that the increase of the number of apertures from one to four increases the maximum net receiver power from 116 MW to 332 MW. The use of more than four apertures results in a limited further gain of net receiver power but significantly decreased overall optical efficiency and solar-to-thermal efficiency. Furthermore, a novel solar beam-down system with a rotating tower-reflector and a receiver–reactor array is proposed and optically investigated, specifically for high-temperature solar thermochemical applications. This optical study predicts the required gain of the thermal-to-chemical efficiency from the receiver–reactor array by synchronising heat recuperation, reduction reaction, and oxidation reaction.

---

# Contents

---

<b>Supervisory panel</b>	<b>iii</b>
<b>Declaration</b>	<b>v</b>
<b>Acknowledgments</b>	<b>ix</b>
<b>Abstract</b>	<b>xi</b>
<b>1 Introduction</b>	<b>1</b>
1.1 Optical concentrators . . . . .	2
1.2 Context . . . . .	6
1.3 Objectives . . . . .	7
1.4 Overview . . . . .	8
<b>2 Background</b>	<b>9</b>
2.1 Radiative transfer . . . . .	9
2.2 Compound parabolic concentrators . . . . .	11
2.3 High-flux solar simulators . . . . .	13
2.4 Solar central receiver systems . . . . .	13
2.5 Methodology . . . . .	19
<b>3 Design of a compound parabolic concentrator for a multi-source high-flux solar simulator</b>	<b>25</b>
<b>4 Reflective optics for redirecting convergent radiative beams in concentrating solar applications</b>	<b>33</b>
<b>5 Optics of solar central receiver systems: A review</b>	<b>47</b>
<b>6 Temperature-based optical design, optimisation and economics of solar polar-field central receiver systems with an optional compound parabolic concentrator</b>	<b>71</b>
<b>7 Optical analysis of a multi-aperture solar central receiver system for high-temperature concentrating solar applications</b>	<b>87</b>
<b>8 Optical analysis of a solar thermochemical system with a rotating tower reflector and a receiver–reactor array</b>	<b>103</b>

---

<b>9 Summary and outlook</b>	<b>121</b>
9.1 Summary . . . . .	121
9.1.1 HFSS-based experimental systems . . . . .	121
9.1.2 Solar central receiver systems . . . . .	122
9.2 Outlook . . . . .	124
<b>Bibliography</b>	<b>126</b>

---

## Introduction

---

Solar energy plays a crucial role in the transformation of the world energy system to a more renewable and environmentally-friendly one due to its vast quantity, proven technology performance, and environmental safety. Solar energy technologies have the potential to eliminate the reliance of the global economy on fossil fuels [1]. Concentrating solar thermal systems are distinct by making use of the full solar spectrum available on the Earth, and by being compatible with a broad range of technical applications including those requiring continuous or dispatchable thermal energy input [2]. Solar irradiation onto the earth's surface exhibits dramatic variations in both time and geographical scales. The incompatibility of the intermittence of solar irradiation and the sensitivity of electricity demand necessitates energy storage. Concentrated solar technologies stand out among other sustainable technologies due to the inherent suitability for energy storage and capability of allowing for efficient conversion of thermal energy to energy in electrical or chemical form. Concentrating solar thermal technologies can be employed for power generation [3] and solar thermochemical processing [4–6].

Solar thermochemical processes include (i) H<sub>2</sub>O or CO<sub>2</sub> splitting via thermolysis and reduction–oxidation (redox) cycles of metal oxides, (ii) decarbonisation/upgrade of carbonaceous feedstocks via cracking, reforming, and gasification, and (iii) production of chemical commodities such as lime, ammonia, and metals via calcination and ablation [6]. Among them, the most-widely investigated is the solar thermochemical process based on the redox cycles of metal oxides, comprising two steps: (1) a solar-driven, high-temperature endothermic reduction step, and (2) a non-solar, low-temperature exothermic oxidation step [4, 6–9]. The reduction reaction of metal oxides typically requires a temperature ranging from 800 K to 1800 K [10], and is driven by the concentrated solar radiation. Energy storage, production of H<sub>2</sub> and/or CO, and CO<sub>2</sub> capture are accomplished during the oxidation step.

Thus, the advantages of high-temperature receivers/receiver–reactors include (i) enabling solar thermochemical processes and (ii) offering a high thermal-to-electric conversion efficiency for solar thermal power applications. However, high-temperature receivers/receiver–reactors also bring in high receiver emission losses that can only be mitigated by an increased concentration ratio<sup>1</sup> at the receiver aperture, imposing

---

<sup>1</sup>Definitions of metrics employed to characterise the performance of solar optical systems including concentration ratio, optical efficiency, receiver absorption and thermal efficiencies can be found in [11], [12], and Section 2.4.

great challenges on the design and manufacturing of optical concentrating systems [13]. Substantial costs of about 30–50% of the total plant costs are associated with optical concentrators. Optical approaches, particularly system-level design, have the great potential to assist in solving the challenges imposed by high-temperature thermal and thermochemical applications. Hence, optical concentrating systems are of paramount significance for the realisation of economically-feasible solar thermal or thermochemical technologies.

## 1.1 Optical concentrators

Optical concentrators applied in the field of solar energy can be classified as primary and secondary optics. Primary optics concentrate/reflect the quasi-collimated solar radiation into convergent radiative beams which can be further concentrated/redirected by secondary optics. Specifically, the optics of solar CRSs can be found in the literature review performed at the beginning of this doctoral work and prior to any optical design, as published in [11].

### Primary optics

Solar irradiation onto the earth's surface varies continuously, exhibiting variations at all time scales, from minutes to decades. The generally accepted annual mean value of the solar radiation impinging on the outer layer of the earth's atmosphere appears to be  $G_{\text{sol}} = 1366 \text{ W m}^{-2}$  [14]. If example radiative fluxes of 500, 1000, and  $1366 \text{ W m}^{-2}$ , respectively, are absorbed by a blackbody, the equilibrium temperatures of the blackbody are given by

$$\sigma T^4 = G_{\text{sol}} \quad (1.1)$$

and calculated to be 306, 364, and 394 K, where  $\sigma$  is the Stefan–Boltzmann constant equal to  $5.67 \times 10^{-8} \text{ W m}^{-2} \text{ K}^{-4}$ . These temperatures give low ideal thermodynamic conversion efficiencies of only 4.2%, 19.5%, and 25.6%, respectively, if being used for electric power generation with a cold sink of ambient temperature of 20°C. Hence, to overcome the inherent technical challenge of solar radiation as an energy source, namely that it is dilute, optical concentrators are used to obtain radiative fluxes ranging from a few  $\text{kW m}^{-2}$  to several  $\text{MW m}^{-2}$  [8, 11].

The direct sunlight arriving at the earth's surface is incoherent, quasi-collimated with a cone half-angle  $\theta_{\text{sun}}$  of 4.65 mrad as a result of the finite size of the sun, i.e. the sun shape [15–17], and the distance between the sun and the earth. The incident sun rays are redirected into a convergent beam by primary optics towards a common position that can be a surface, a line (line-focusing system), or a point (point-focusing system). Primary optics concentrating the quasi-collimated solar beams to convergent beams are typically in the shape of continuous or discrete paraboloidal surfaces. Typical primary optics encompass parabolic dishes [18], parabolic

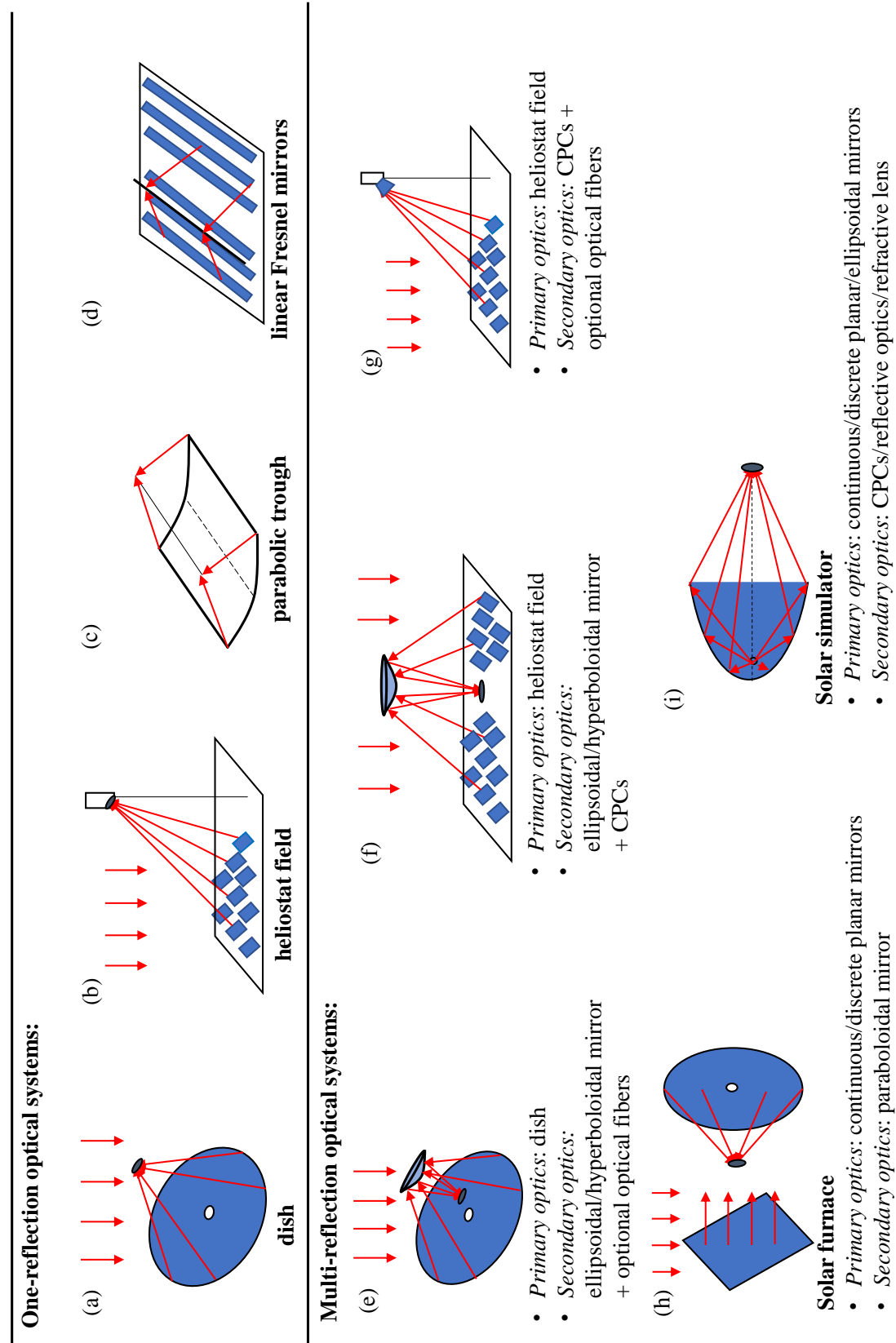


Figure 1.1: Optical configurations encountered in concentrating solar applications [8, 19].

troughs [20], heliostat fields [11], and linear Fresnel mirrors [21]. The corresponding concentrating solar power (CSP) systems with each optical concentrator differ in receiver configuration, concentration ratio, nominal receiver power, range of receiver working temperature along with others [3, 11, 22]. Typical solar concentrating systems are schematically depicted in Figure 1.1.

The theoretical maximum concentration ratios are given by the second law of thermodynamics and are limited by  $\theta_{\text{sun}}$ , namely the inverse of the sine of  $\theta_{\text{sun}}$  ( $C_{\text{max,line-focus}} = 215$ ) and the inverse of the square of the sine of  $\theta_{\text{sun}}$  ( $C_{\text{max,point-focus}} = 46,248$ ) for line-focusing and point-focusing solar concentrators, respectively [3]. Various design-specific geometrical constraints limit the achievable concentration to below this thermodynamic limit, such as slope error of optical surface and tracking error [23, 24]. Commonly used primary concentrators are reflective optics, since large-scale refractive lenses bear the drawbacks of large weight, high costs, and potential overheating due to the absorption of radiation.

Radiative beams encountered in concentrating solar applications feature quasi-collimated (natural solar irradiation) and line- and point-converging (concentrated radiation) geometries. Reflective optics adopted in solar applications for the purpose of redirecting or concentrating include planar, ellipsoidal, hyperboloidal, and paraboloidal mirrors. A planar reflector/concentrator redirects collimated or convergent radiative beams without changing the beam characteristics of rim angle and radiative distribution. Paraboloidal concentrators, such as parabolic dishes and parabolic troughs, enable the conversion between the collimated and convergent radiative beams. Linear Fresnel mirrors and heliostat fields can be represented as discretised parabolic troughs and dishes, respectively. Ellipsoidal and hyperboloidal reflectors/concentrators render the redirection of convergent radiative beams and the modification of beam rim angles and radiative distributions [25]. Aplanatic concentrators are designed for minimising spherical and comatic aberrations [26–28].

Heliostats are applied in CRSs that approximate elements of paraboloids of revolution with different focal lengths and with time-dependent orientation to follow the actual position of the sun in two dimensions, and focus solar radiation on a common focal area of a receiver (see Figure 1.1). The receiver can be positioned on top of a tower or at ground level, where the relevant CRSs are distinguished as ‘tower-receiver’ and ‘tower-reflector’ (beam-down) systems, respectively. CRSs have received considerable attention due to their potential of achieving higher receiver power and concentration ratios and consequently lower levelised costs of electricity. Advancement of heliostat fields towards efficient and cost-effective collection and focusing of sunlight are pivotal to the advancement of CRSs for electricity generation and chemical processing at large scales. Therefore, CRSs are considered in this work for the realisation of large-scale optical systems for the high-temperature concentrating thermal applications.



## Secondary optics

Receivers employed for high-temperature applications typically feature a cavity receiver, which is due to the large radiative emission loss from a large aperture area of an external receiver [11]. Absorption efficiency of cavity receivers can be further improved by applying secondary optical concentrators including a conical concentrator [29], a trumpet concentrator [30, 31], a tailored edge-ray concentrator (TERC) [32], a compound elliptic concentrator (CEC) [33, 34], a non-regular polygonal concentrator [35], and the most widely discussed compound parabolic concentrators (CPCs) [33, 36]. Kribus et al. investigated performance limits of CRSs with four types of secondary optical concentrators [37].

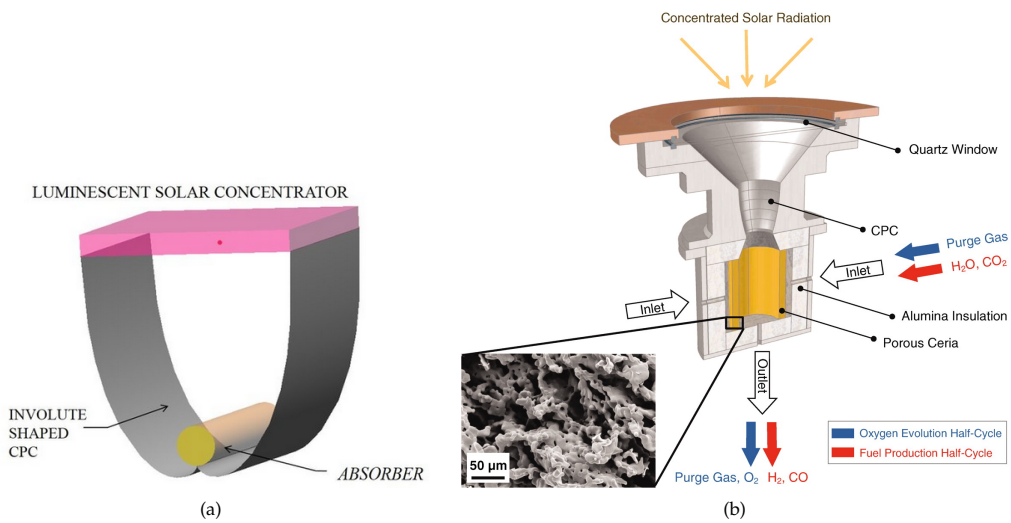


Figure 1.2: Examples of CPCs: (a) a 2D CPC working in tandem with a luminescent solar concentrator (reprinted from [38], with permission from ISES) and (b) a 3D CPC working in tandem with a solar thermochemical reactor for syngas production (reprinted from [39], with permission from AAAS).

It was demonstrated in the literature that the use of a CPC in an optical concentrating system brings in the benefits of increasing concentration ratios, allowing for utilisation of spillage radiation, and spreading the angular distribution of the transmitted radiation [33, 39–41]. The spreading of radiation allows for more uniform irradiation inside a receiver cavity, in particular for eliminating hot spots. Besides improving receiver absorption efficiency, the capture of spillage radiation helps protect the outer walls of receivers from overheating, thus lowering the requirements of using protective shields. Disadvantages of the use of secondary optics include additional optical losses due to surface absorption and backward reflection, difficulty to manufacture, and possibly required active cooling due to the operation under highly concentrated radiation and the radiative emission from the high-temperature solar receiver. Figure 1.2 shows examples of 2D and 3D CPCs in solar applications.

In this work, we discuss the application of a CPC in both the small-scale experimental system (Chapter 3) and the large-scale CRSs for the CPC's potential benefits in improving system optical, energetic, and economic performance (Chapters 6 and 7).

## High-flux solar simulators

To enable experimental studies of materials and device prototypes, high-flux radiation is provided by on-sun concentrators such as solar furnaces [42–48], solar towers [49–56], parabolic dishes [57], or indoor facilities of high-flux solar simulators (HFSSs) [8, 30, 58–79]. HFSSs provide a controlled, steady, and reproducible high-flux irradiation, independent of the availability of direct sunlight.

A 45 kW<sub>e</sub> multi-source HFSS has been constructed at the Australian National University (ANU) and used for experimental studies [66, 70, 80, 81]. The design and construction of the first-generation HFSSs are focused on the achievement of high radiative fluxes over a small target area. During the implementation of HFSSs for experimental testing, problems and limitations of the HFSS-based experimental setup are uncovered, such as that (1) multi-source HFSSs output radiation with high peak fluxes and angular flux non-uniformities due to the finite number of lamps, resulting in hot spots on target surfaces; and (2) the majority of HFSSs output radiative beams with a fixed axis, typically in a horizontal configuration. The horizontal-axis beam configuration limits the use of HFSSs for applications requiring beams of different axis directions, e.g. beam-up or beam-down reactors. Solutions of solving these problems are rarely discussed in the literature, except that Jin et al. used an optical integrator and a lens to obtain collimated light [76], and Song et al. used optical fiber bundles to achieve flexible radiative output [77]. Hence, in this work, secondary concentrating and reflective optics are investigated to tackle these problems and limitations, as in Chapters 3 and 4, respectively. Suggestions on the further design of the second-generation HFSSs are also put forward in this work.

## 1.2 Context

This doctoral work tackles tasks under the R&D project *High temperature solar thermal energy storage via manganese-oxide based redox cycling*, sponsored by the Australian Renewable Energy Agency (ARENA). The objective of the overall project is to develop novel high-temperature thermochemical energy storage technologies for dispatchable and efficient concentrating solar power generation via thermodynamic power cycles [4, 5, 8–10, 82, 83]. The proposed approach is based on the reduction and oxidation reactions of the manganese oxide (see Figure 1.3) [84–86]:

- solar-driven, endothermic reduction:  $\text{Mn}_2\text{O}_3 \rightarrow 2\text{MnO} + 1/2\text{O}_2$
- non-solar, exothermic oxidation:  $2\text{MnO} + 1/2\text{O}_2 \rightarrow \text{Mn}_2\text{O}_3$

The thermal reduction of  $\text{Mn}_2\text{O}_3$  to  $\text{MnO}$  theoretically requires temperatures above 1560°C [90]. The iron–manganese binary oxide systems have been recently suggested to improve the performance of pure iron and manganese oxides [91], and thus the iron–manganese oxide with a molar ratio of Fe/Mn 2:1 (Fe67) is considered as the thermochemical energy storage material in this work [85]. The required temperature for the reduction of Fe67 particles is reduced to 1200°C based on the thermodynamic and kinetic study of Fe67 particles [85].

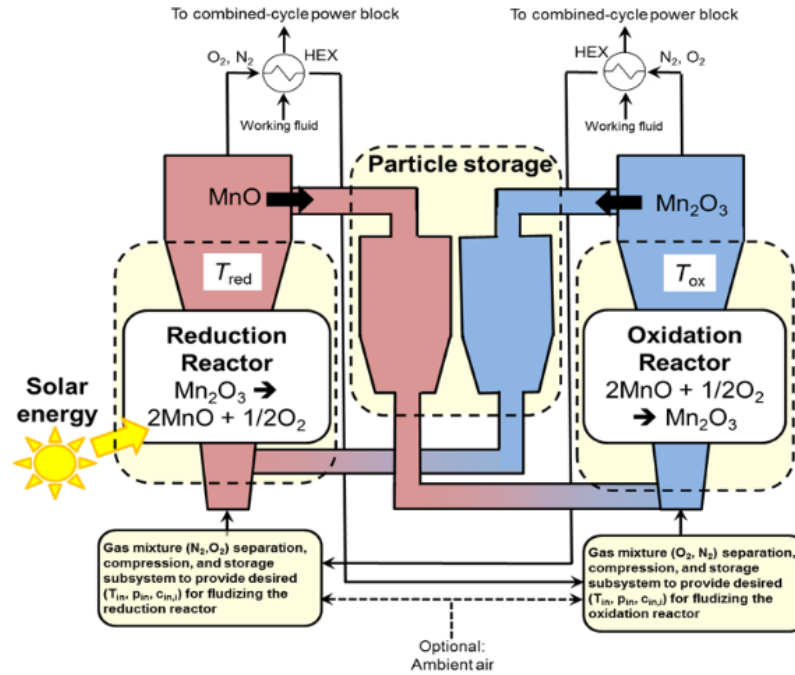


Figure 1.3: Solar thermochemical energy storage system based on manganese-oxide redox cycling proposed in 2014 [87]. Fe/Mn binary metal oxide of Fe/Mn molar ratio of 2:1 (Fe67) which was demonstrated to be able to improve the performance of pure Fe and Mn metal oxides is taken in this project [85, 86, 88, 89].

The project consists of four tasks: (1) active material development, (2) solar reactor development [88, 89], (3) optical field design, and (4) techno-economic analyses. In particular, this work undertakes the task (3) and provides inputs to tasks (2) and (4). Note that this work is unrestricted to the project tasks. Optical systems are studied for the generic high-temperature concentrating solar applications.

### 1.3 Objectives

Despite a large number of studies of optical solar concentrating systems, existing studies primarily focus on processes requiring temperatures up to 900 K. The challenges of high-temperature thermochemical processing up to 1800 K imposed on optical concentrating systems were rarely discussed in the literature, which is the focus of this work.

The optical design involved in this work is performed via numerical modelling. The Monte-Carlo ray-tracing (MCRT) technique, the most robust simulation technique for optical and radiative transfer modelling of a CRS, is applied in the development of programs for simulating the HFSSs, CRSs, and secondary optics [14, 92]. In particular, the tasks of this work comprise:

- (1) understanding the underlying physics of solar energy, geometrical optics, non-imaging optics, radiative transfer, and modelling methodology pertinent to HFSSs, CRSs, and secondary optics,

- (2) developing simulation programs for modelling CRSs with a CPC, allowing for predicting optical and energetic characteristics including optical efficiencies, radiative power, concentration ratios, and spatial and directional flux distributions of radiation on specified target surfaces,
- (3) providing support to the team working on material development, design and experiments of reactors and system-level techno-economic analyses, and
- (4) exploring the large-scale CRSs, particularly for high-temperature concentrating solar applications, and investigating their economic feasibility.

## 1.4 Overview

In this thesis, Chapter 2 presents the review of background information on solar CRSs, primary and secondary optics, HFSSs, and modelling methodology.

Chapters 3 and 4 describe the optical design and analyses of secondary optics for solving problems and limitations of the HFSS-based experimental system. The design and manufacturing of a 3D CPC to couple with HFSSs are described in Chapter 3. In Chapter 4, optical analysis of secondary, beam-redirecting optics for varying axis directions of beams from HFSSs is presented.

Chapters 5 to 7 present studies pertinent to commercial-scale CRSs. A review on the state of the art in optical design, modelling, and characterisation of CRSs is presented in Chapter 5. Chapter 6 contains an optical design, optimisation, and economic study of solar polar-field CRSs for receivers operating in the temperature range of 600–1800 K. The application of a 3D CPC is evaluated in terms of its benefits in improving system energetic and economic performance. In Chapter 7, the design of a multi-aperture receiver coupled to multiple sub-fields for increasing power output is explored. In Chapter 8, a novel solar beam-down system with a rotating tower reflector and a receiver–reactor array is proposed and optically investigated.

Finally, conclusions from the present work and suggestions for further work are discussed in Chapter 9.

---

## Background

---

This chapter introduces the fundamentals of radiative transfer and modelling methodology, and presents literature reviews of HFSSs, solar CRSs including the ‘tower-receiver’ and ‘tower-reflector’ optical systems, and the secondary optics of CPCs.

### 2.1 Radiative transfer

Macroscopic radiative transfer in solar concentrating systems is based on geometrical (ray) optics and classical radiative transfer equations (RTE) [14]. A model CRS used to elucidate the pertinent optics and radiative transfer concepts is depicted in Figure 2.1.

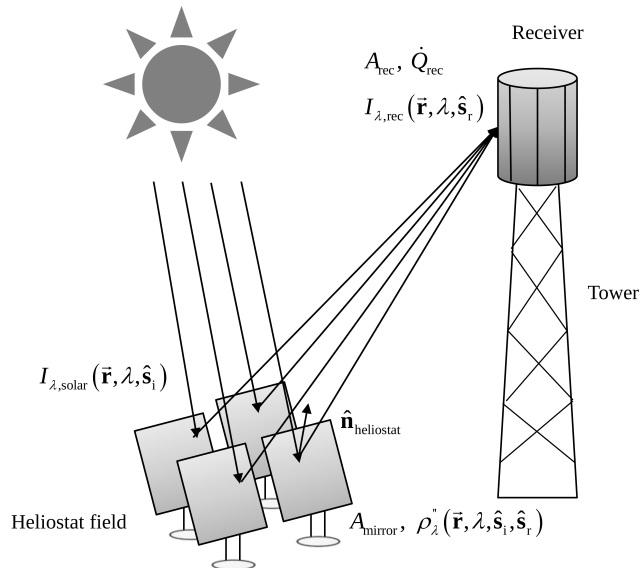


Figure 2.1: Simplified radiative transfer model of a solar CRS [11].

The spectral intensity and flux of solar radiation coming from direction  $\hat{s}$  and arriving on an arbitrary surface element  $dA$  with a normal  $\hat{n}$  and at position  $\hat{r}$  are

given by

$$I_{\lambda,\text{solar}}(\vec{\mathbf{r}}, \lambda, \hat{\mathbf{s}}, t) = \frac{dQ_{\text{solar}}(\vec{\mathbf{r}}, \lambda, \hat{\mathbf{s}}, t)}{|\hat{\mathbf{n}} \cdot \hat{\mathbf{s}}|dAd\lambda d\Omega dt} = \frac{d\dot{Q}_{\text{solar}}(\vec{\mathbf{r}}, \lambda, \hat{\mathbf{s}}, t)}{|\hat{\mathbf{n}} \cdot \hat{\mathbf{s}}|dAd\lambda d\Omega} \quad (2.1)$$

$$\dot{q}_{\lambda,\text{solar}}(\vec{\mathbf{r}}, \lambda, t) = \int_{\Omega=0}^{2\pi} I_{\lambda,\text{solar}}(\vec{\mathbf{r}}, \lambda, \hat{\mathbf{s}}, t)|\hat{\mathbf{n}} \cdot \hat{\mathbf{s}}|d\Omega \quad (2.2)$$

where  $dQ_{\text{solar}}(\vec{\mathbf{r}}, \lambda, \hat{\mathbf{s}}, t)$  and  $d\dot{Q}_{\text{solar}}(\vec{\mathbf{r}}, \lambda, \hat{\mathbf{s}}, t)$  are, respectively, the solar radiative energy and radiative power intercepted by  $dA$  within the wavelength interval  $d\lambda$  around the wavelength  $\lambda$ , and  $d\Omega$  is an infinitesimal solid angle (an infinitesimal area on a unit sphere), i.e.  $d\Omega = \sin\theta d\theta d\psi$  [14]. Detailed spectral optical models of solar concentrators typically use the air mass 1.5 spectral distribution (AM 1.5) as the reference spectrum, further modified according to local atmospheric conditions [93, 94]. Simplified spectral optical models typically employ the spectral distribution of a blackbody at an effective temperature of the sun of approximately 5780 K [14]. The directional distribution of the incident solar irradiation results from the sun–earth geometry, with the solid and half-cone angles of the solar disk equal to  $6.79 \times 10^{-5}$  sr and 4.65 mrad (0.27°), respectively, and the effect of the sunshape, i.e. solar radiation distribution observed from the earth within the solar disk and the circumsolar aureole. The ratio of the amount of energy contained in the circumsolar aureole to the total amount of direct energy coming from the sun is defined as the circumsolar ratio. It is an important parameter that directly influences the flux distribution and solar image size at the focal plane. Examples of sunshape models employed in optical analyses of CRSs are the pillbox, Kuiper, Biggs and Vittitoe [15], Rabl and Bendt [16], and Buie [17] distributions. Buie sunshape model greatly approximates the actual measured solar radiation distribution with affordable computational effort and thus is adopted in this work.

Solar radiation incident on a reflector surface element  $dA$  with a local normal  $\hat{\mathbf{n}}$  of a solar concentrator is partially reflected into a direction  $\hat{\mathbf{s}}_r$ . In geometrical optics, the most fundamental property describing the reflection process under the local thermodynamic equilibrium condition is the spectral bi-directional reflection function  $\rho''_{\lambda}(\vec{\mathbf{r}}, \lambda, \hat{\mathbf{s}}_i, \hat{\mathbf{s}}_r)$ , defined as [95, 96]

$$\rho''_{\lambda}(\vec{\mathbf{r}}, \lambda, \hat{\mathbf{s}}_i, \hat{\mathbf{s}}_r) = \frac{dI_{\lambda}(\vec{\mathbf{r}}, \lambda, \hat{\mathbf{s}}_i, \hat{\mathbf{s}}_r)}{I_{\lambda}(\vec{\mathbf{r}}, \lambda, \hat{\mathbf{s}}_i)|\hat{\mathbf{n}} \cdot \hat{\mathbf{s}}_i|d\Omega_i} \quad (2.3)$$

In the limiting cases of optically smooth and diffuse surfaces,

$$\rho''_{\lambda}(\vec{\mathbf{r}}, \lambda, \hat{\mathbf{s}}_i, \hat{\mathbf{s}}_r) = \begin{cases} \infty, & \text{for } \theta_r = \theta_i, \psi_r = \psi_i + \pi \\ 0, & \text{for all other } \hat{\mathbf{s}}_r \end{cases} \quad \text{optically smooth} \quad (2.4)$$

$$\rho''_{\lambda}(\vec{\mathbf{r}}, \lambda) = \rho'_{\lambda}(\vec{\mathbf{r}}, \lambda)/\pi \quad \text{diffuse} \quad (2.5)$$

where the unit direction vector  $\hat{\mathbf{s}}$  is expressed in terms of the polar angle  $\theta$  (measured from the surface normal  $\hat{\mathbf{n}}$ ) and the azimuth angle  $\psi$  (measured between an arbitrary

axis on the surface and the projection of  $\hat{\mathbf{s}}$  on that surface). The reflecting surfaces of involved optical concentrators in this work are assumed to be optically smooth (specular) and their reflectance is wavelength- and direction-independent.

Minimum spectral attenuation and angular spread of the reflected intensity  $I_\lambda(\vec{\mathbf{r}}, \lambda, \hat{\mathbf{s}}_r)$  are the desired reflection characteristics of a reflecting surface to maximise the total radiative power intercepted by the receiver aperture of an area  $A_{\text{rec}}$ ,

$$\dot{Q}_{\text{rec}}(\vec{\mathbf{r}}) = \int_{\lambda=0}^{\infty} \int_{A_{\text{rec}}} \int_{\Omega=0}^{2\pi} I_{\lambda,\text{rec}}(\vec{\mathbf{r}}, \lambda, \hat{\mathbf{s}}) |\hat{\mathbf{n}} \cdot \hat{\mathbf{s}}| d\Omega dA d\lambda. \quad (2.6)$$

Note that the optical concentrator of a CRS may consist of more than one reflector between the reference location of the incident solar radiation and the receiver.

The atmospheric transfer of radiation, and thus the spatial variation of radiative intensity between the reference location of incidence, reflectors, and a receiver are modelled using the quasi-steady form of the RTE,

$$\frac{dI_\lambda(\vec{\mathbf{r}}, \lambda, \hat{\mathbf{s}})}{ds} + \beta_\lambda I_\lambda(\vec{\mathbf{r}}, \lambda, \hat{\mathbf{s}}) = \kappa_\lambda I_{\lambda,b}(\vec{\mathbf{r}}, \lambda) + \frac{\sigma_{s,\lambda}}{4\pi} \int_{\Omega_i=0}^{4\pi} I_\lambda(\vec{\mathbf{r}}, \lambda, \hat{\mathbf{s}}_i) \Phi_\lambda(\vec{\mathbf{r}}, \lambda, \hat{\mathbf{s}}_i, \hat{\mathbf{s}}) d\Omega_i \quad (2.7)$$

where  $\kappa_\lambda$  and  $\sigma_{s,\lambda}$  are the spectral absorption and scattering coefficients, respectively,  $\beta_\lambda = \kappa_\lambda + \sigma_{s,\lambda}$ ,  $\lambda$  is the extinction coefficient, and  $\Phi_\lambda(\vec{\mathbf{r}}, \lambda, \hat{\mathbf{s}}_i, \hat{\mathbf{s}})$  is the scattering phase function of radiation from the direction  $\hat{\mathbf{s}}_i$  into  $\hat{\mathbf{s}}$ . Atmospheric radiative properties are determined by employing models that account for the actual composition of the gas, liquid, and solid phases [97, 98]. The quasi-steady form of RTE is employed as justified by the small characteristic radiation propagation times at length-scales associated with the overall dimensions of solar thermal systems.

## 2.2 Compound parabolic concentrators

CPC was first proposed by Hinterberg and Winston in mid-1960s as an efficient way to collect Čerenkov radiation [99], and thereafter applied to solar energy systems [100–107]. The basic geometry of a 2D CPC is composed of two parabolic sections with foci at the end points of the exit aperture (Figure 2.2). The reflecting surface of a 3D CPC is formed by rotating the cross-section of a 2D CPC about the CPC axis.

An annular CPC (ACPC) was proposed by Lipiński and Steinfeld for the utilisation of low-grade spillage radiation outside the hot spot [108]. Except from conventional axis-symmetric secondary optical concentrators, secondary optical concentrators with non-regular cross-sections were proposed and evaluated in tandem with heliostat fields with a wider range of possible contours [35, 104].

The geometry of a 3D CPC is determined by the acceptance angle  $\theta_{\text{CPC}}$  and the entry aperture radius  $r_{\text{in}}$ . The radius of the exit aperture  $r_{\text{out}}$  and the full (untruncated) length  $L_{\text{CPC}}$  can be calculated as functions of  $\theta_{\text{CPC}}$  and  $r_{\text{in}}$ ,

$$r_{\text{out}} = r_{\text{in}} \sin \theta_{\text{CPC}}, \quad (2.8)$$

$$L_{\text{CPC}} = \frac{r_{\text{in}} + r_{\text{out}}}{\tan\theta_{\text{CPC}}} = r_{\text{in}} \frac{1 + \sin\theta_{\text{CPC}}}{\tan\theta_{\text{CPC}}}. \quad (2.9)$$

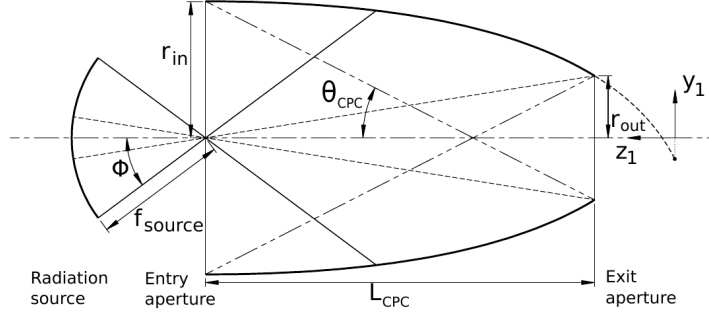


Figure 2.2: Cross-section of a three-dimensional compound parabolic concentrator (CPC) [109].

The interception efficiency  $\eta_{\text{int,CPC}}$  is defined as the ratio of the radiative power entering the CPC entry aperture to the total radiative power from a source incident on the CPC entry aperture plane. Optical losses in a CPC result from surface absorption and backward reflection [33]. The transmission efficiency  $\eta_{\text{opt,CPC}}$  of a CPC is defined as the ratio of transmitted radiative power to that entering a CPC. A CPC increases the theoretical concentration ratio by a factor of  $1/\sin\theta_{\text{CPC}}$  or  $1/\sin^2\theta_{\text{CPC}}$  for a 2D or 3D CPC, respectively. Thus, the concentration ratio of a practical 3D CPC is

$$C_{\text{CPC}} = \frac{\eta_{\text{opt,CPC}}}{\sin^2\theta_{\text{CPC}}}. \quad (2.10)$$

The overall concentration ratio  $C_{\text{out}}$  taken at the exit aperture of the CPC is then,

$$C_{\text{out}} = C_{\text{in}}C_{\text{CPC}}. \quad (2.11)$$

$C_{\text{in}}$  is the concentration ratio at the CPC entry aperture and is defined as:

$$C_{\text{in}} = \frac{\dot{Q}_{\text{in}}}{\pi r_{\text{in}}^2 G_0}, \quad (2.12)$$

where  $\dot{Q}_{\text{in}}$  is the radiative power entering the CPC entry aperture and  $G_0$  is the reference unconcentrated solar radiation used for the definition of flux (energetic) solar concentration ratio, typically taken as  $1000 \text{ W m}^{-2}$  [11].

The ideal CPC is difficult and expensive to manufacture due to the relatively complex shape and the difficulty of polishing the reflective surface enclosed in a cavity. Hence, a large variety of modified CPCs have been developed for purposes such as easier manufacturing, more convenient packing, and larger acceptance angles [104, 110–112].



### 2.3 High-flux solar simulators

HFSSs have been widely designed and used for experimental uses in the applications of solar thermal, thermochemical, photoelectrochemical, and photovoltaic. A summary of existing HFSSs facilities was given by Bader et al. [113] and Gallo et al. [114]. Typically, HFSSs consist of a number of identical radiation modules. In each module, the light source of a xenon, argon, or metal halide arc lamp is used and is positioned at the focus of an elliptical specular reflector, either a point-focusing truncated ellipsoid of revolution or a line-focusing truncated elliptical trough. The reflectors are oriented to have a common secondary focus where a high radiative flux is achieved. The emission spectrum of a xenon arc lamp resembles that of blackbody radiation at 6000 K and hence approximates the terrestrial solar spectrum.

HFSSs differ in the type, number, power, size, and emission characteristics of the light source, the geometry and quality of the reflectors, as well as the relative alignment of the light source and reflector. The radiative power output of the existing HFSSs ranges approximately from 1 to 280 kW with the average radiative flux on the specified focal plane ranging approximately from 0.25 to 10 MW m<sup>-2</sup>[113]. The HFSS constructed at the ANU consisting of 18 radiation modules is shown in Figure 2.3 as an example.



Figure 2.3: Photograph of the multi-source high-flux solar simulator (HFSS) at the Australian National University (ANU) [66].

### 2.4 Solar central receiver systems

A basic concentrating collector system consists of a solar concentrator and a solar receiver. The concentrated solar radiation is absorbed by a receiver where the solar energy is converted into thermal energy, driving thermal or thermochemical processes. The receiver performance is characterised by the receiver absorption efficiency, de-

defined as the ratio of radiative power absorbed by the receiver to the concentrated radiative power intercepted by the receiver aperture. The solar receiver design is inherently coupled to the optical concentrator design. Cavity and volumetric receivers exhibit higher apparent absorptance than external receivers, and are suitable for high-temperature solar applications [19, 115]. Solar CRSs are introduced and discussed in this section.

Solar CRSs can be classified as ‘tower-receiver’ and ‘tower-reflector’ (beam-down) systems according to the position of the module of the receiver and the optional secondary optical concentrator such as a CPC in the optical system. In a ‘tower-receiver’ system, heliostats reflect radiation directly towards the receiver on a central tower (see Figure 2.4). In a ‘tower-reflector’ system, heliostats reflect radiation towards a secondary reflector positioned on the top of a tower, which in turn reflects radiation towards the receiver located at ground level [101–103, 116–119] (see Figure 2.5).

Solar CRSs are designed by matching thermal requirements of thermal or thermochemical processes such as temperature, power level, transient variations, to thermal characteristics of a receiver. Receiver selection/design is inherently coupled to the selection/design of an optical concentrator. A broad variety of receiver designs specific to solar CRSs have been conceptualised, designed, and demonstrated as summarised in [120–124]. Romero et al. [125], Garcia et al. [126], Ávila-Marín [121], Behar et al. [127], Reddy et al. [128], Ho and Iverson [122], Coventry et al. [123] and Ho [124] conducted review studies of central receiver systems, components, projects, and technologies. Plant-level CRSs are included in review studies of global CSP plants by Pavlović et al. [129] and Zhang et al. [130].

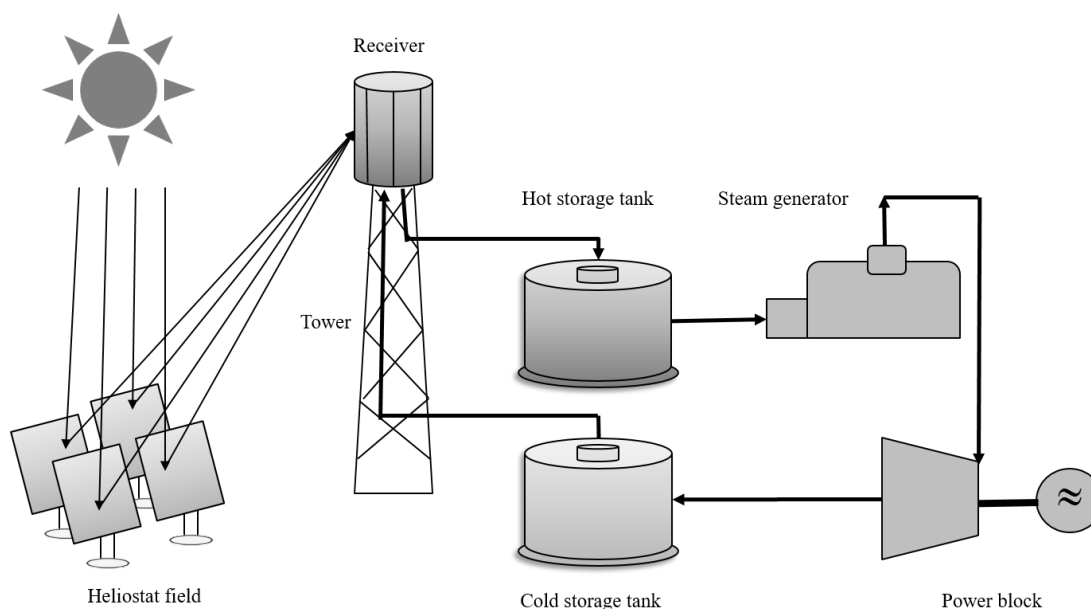


Figure 2.4: Model solar ‘tower-receiver’ system comprising a heliostat field, a receiver on top of a tower, a thermal storage system, and a power block [11]. The optional CPC is not included in this figure.

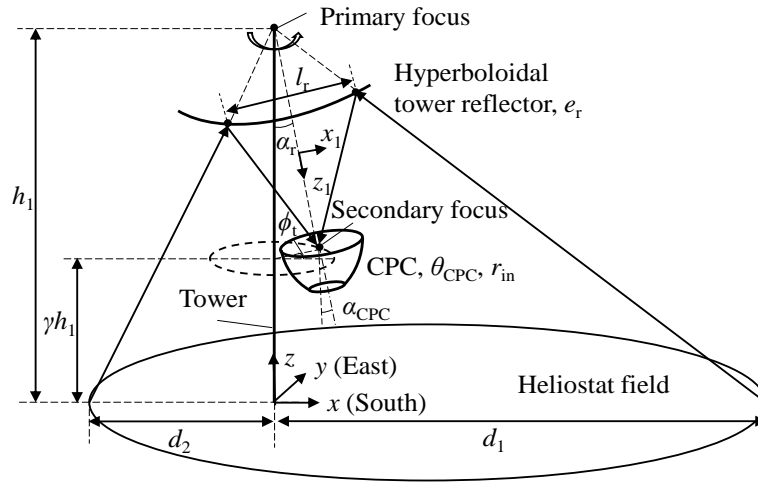


Figure 2.5: Model solar 'tower-reflector' optical system comprising a heliostat field, a hyperboloidal tower reflector, a tower, and a ground-level receiver coupled with a CPC [131].

This work focuses on the optics of heliostats and heliostat fields as motivated by a need to understand the potential to adapt and improve state-of-the-art designs to meet the needs of emerging applications of CRS technologies.

### 'Tower-receiver' systems

In this section, heliostats, heliostat fields, and solar receivers will be introduced sequentially. An individual heliostat is composed of a reflector (one or more mirror facets), a supporting structure including foundations, and an actuation system. Heliostats can be classified in various ways. For example, by the material of the reflector surface, heliostats are classified as glass, metal, and membrane types. The size and specular reflectance of mirror facets, the alignment of mirror facets, the alignment of the tracking system, and the structural rigidity (particularly under operational wind loads) must be optimised for the best optical performance of an individual heliostat. Review studies of the state of the art in heliostat design and cost reduction are given by Coventry and Pye [132], Pfahl [133], and Dowling et al. [134].

Based on the heliostat field boundary, polar and surround fields are distinguished. In a surround field, the east and west heliostats can collect solar radiation at a lower solar azimuth angle. For a given power level, the height of the central tower with a surround field is smaller as compared to that for a polar field, thus reducing thermal losses from the tower and piping, the amount of construction materials, and consequently the cost. Additionally, the distance between the most remote heliostats of a surround field and the receiver is smaller compared to that for a polar field, reducing optical losses from atmospheric attenuation within the system. However, a larger aperture area is required for the receiver coupled to a surround field. Alternatively, the heliostats in a polar field configuration (north/south field configuration for plants located in the northern/southern hemisphere, respectively) are all arranged

at one side of the tower and operate with lower cosine losses. The polar field approach may generally be used when a cavity receiver is needed for high-temperature applications as discussed in this work. There are four traditional types of heliostat layout patterns: (a) radial cornfield, (b) radially-staggered field, (c) N–S cornfield, and (d) N–S staggered field [135]. The radially-staggered pattern is used in a majority of developments due to its proven superior performance over the other patterns from the above list. Recently, the biomimetic and Campo layout patterns based on the radially-staggered pattern are developed by Noone et al. and Collado and Gualar, respectively [136, 137]. They were found to render higher optical efficiency and ground coverage than the radially-staggered pattern. Other layout patterns were reported in the literature including layouts generated by graphical method [138], DELSOL code [139], HFLD code [140], and so on. Comparative studies of different field layouts were included in the literature [141, 142].

Solar receivers can be classified as external receivers and cavity receivers, which are coupled to surround and polar heliostat fields, respectively. Due to the large surface area required for heat transfer, at high temperatures, external receivers exhibit high radiative and convective losses, limiting their applications for high-temperature processes. For a cavity receiver, high-flux irradiation enters the receiver cavity through an open or windowed aperture, and is absorbed at internal surfaces or/and in a volume of a radiatively participating medium inside the cavity. Cavity receivers are preferred for high-temperature applications due to their high absorption efficiency.

### **‘Tower-reflector’ systems**

The solar ‘tower-reflector’ optical system makes use of the Cassegrain optical configuration [143]. The optics of the ‘tower-reflector’ system have been studied in the literature [101–103, 116–119, 144]. ‘Tower-reflector’ systems have been successfully constructed and tested including demonstration-level systems [55, 56, 145] and a 50 MW<sub>e</sub> commercial system [146]. The ‘tower-reflector’ optical system comprises three main components: a heliostat field, a tower reflector (TR) placed on the top of a tower, and a receiver on the ground (see Figure 2.5). The tower reflector approximates a hyperboloidal reflector if being placed below the heliostat field focal point, or an ellipsoidal reflector if being placed above the heliostat field focal point. The receiver is typically coupled to secondary optical concentrators such as CPCs for increasing the concentration ratio at the expense of active cooling and additional optical losses [102, 109].

For the ‘tower-receiver’ system, a secondary reflector on top of a tower limits the shape and size of the heliostat field to its view angle. In particular, if higher concentration ratios are required, the view angle has to be smaller, resulting in a smaller size of the field. The beam-down optical concept has the advantage of facilitating the use of surround heliostat fields and the view angle of the ground-level secondary reflector is linked to the tower reflector instead of the heliostat field. It also offers great advantages for high-temperature solar thermochemical applications. The redirected convergent beam at ground level enables simpler and cheaper installation and oper-

ation of the high-temperature receiver and auxiliary equipment. Besides, the beam-down optical concept enables novel designs of the solar receiver [39, 65, 145, 147–154]. However, disadvantages of the beam-down system include the decreased optical efficiency due to non-ideal reflectance of the additional tower reflector and CPC, the increased beam spread, the large size of the tower reflector, and the requirement to rigidly mount the tower reflector near the primary focus.

### Performance metrics

The basic optical performance metrics of a CRS are optical efficiencies, radiative power, and concentration ratio. The overall optical efficiency of a CRS is defined as the ratio of the radiative energy intercepted by the receiver with an aperture area  $A_{\text{rec}}$  to the maximum possible energy that can be intercepted by the total concentrator (heliostat field) area for a given time period. The overall optical efficiency accounts for cosine, shading, blocking, spillage, heliostat surface absorption, and atmospheric attenuation losses [11, 155]:

$$\eta_{\text{optical}} = \frac{\int_{\Delta t} \dot{Q}_{\text{rec}} dt}{GA_{\text{hel}}N_{\text{hel}}\Delta t} = \eta_{\text{cosine}}\eta_{\text{shading}}\eta_{\text{blocking}}\eta_{\text{spillage}}\eta_{\text{absorption}}\eta_{\text{attenuation}} \quad (2.13)$$

where  $\dot{Q}_{\text{rec}}$  is the concentrated radiative power intercepted at the receiver aperture,  $W$ ,  $G$  is the real-time direct normal irradiance (DNI) reaching the ground,  $W\ m^{-2}$ ,  $A_{\text{hel}}$  is the surface area of each heliostat,  $m^2$ ,  $\Delta t$  is the accounted time period, and  $N_{\text{hel}}$  is the total number of installed heliostats. A representative schematic showing each of these optical losses is given in Figure 2.6.

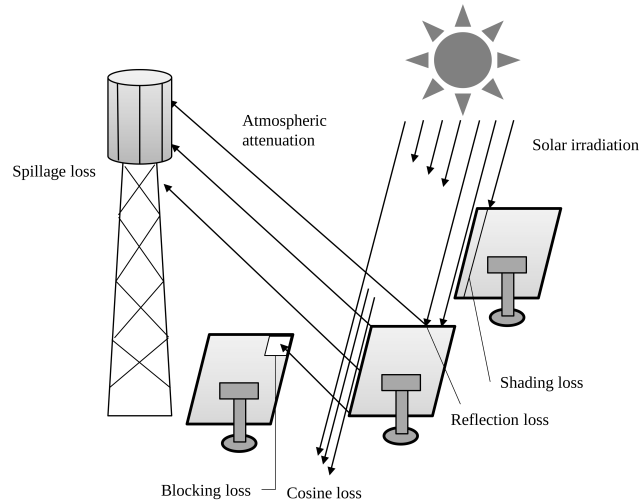


Figure 2.6: Optical losses in a solar ‘tower-receiver’ system that are pertinent to the definition of the optical efficiency [11].

The upper overall theoretical efficiency limit of a CRS, a vector for coupled receiver and heliostat field optimisation, is the product of the overall optical efficiency

$\eta_{\text{optical}}$  and the ideal thermodynamic conversion efficiency  $\eta_{\text{ideal}}$ . The ideal thermodynamic conversion efficiency is defined as the ratio of the work rate produced by a Carnot engine operating between a hot reservoir at the receiver cavity temperature  $T_{\text{rec}}$  and a cold reservoir at ambient temperature  $T_{\text{amb}}$  assumed as 293 K, to the concentrated radiative power intercepted at the receiver aperture. Assuming the receiver is an isothermal, perfectly-insulated blackbody with no conductive and convective heat losses, the instantaneous receiver absorption efficiency  $\eta_{\text{rec}}$  is calculated as

$$\eta_{\text{rec}} = 1 - \frac{\varepsilon\sigma T_{\text{rec}}^4}{G_0 C_{\text{rec}}} \quad (2.14)$$

where  $\varepsilon$  is the receiver cavity apparent emissivity assumed to be unity,  $T_{\text{rec}}$  is the receiver cavity temperature, and  $C_{\text{rec}}$  is the concentration ratio at the receiver aperture. Hence, the ideal thermodynamic conversion efficiency  $\eta_{\text{ideal}}$  is calculated as the product of the blackbody receiver absorption efficiency and Carnot efficiency

$$\eta_{\text{ideal}} = \eta_{\text{rec}}\eta_{\text{Carnot}} = \left(1 - \frac{\sigma T_{\text{rec}}^4}{G_0 C_{\text{rec}}}\right) \left(1 - \frac{T_{\text{amb}}}{T_{\text{rec}}}\right). \quad (2.15)$$

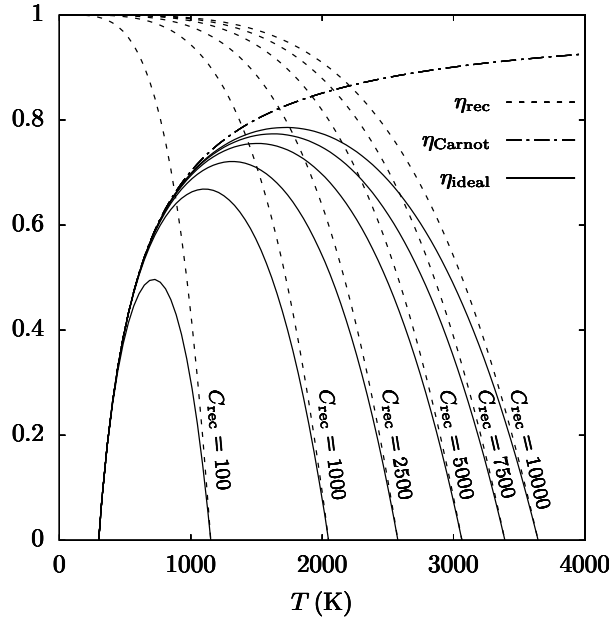


Figure 2.7: Blackbody receiver absorption efficiency  $\eta_{\text{rec}}$ , Carnot efficiency  $\eta_{\text{Carnot}}$  and ideal thermal-to-electricity conversion efficiency  $\eta_{\text{ideal}}$  as a function of the receiver cavity temperature  $T_{\text{rec}}$  for selected values of concentration ratio at the receiver aperture  $C_{\text{rec}}$  [11].

Figure 2.7 depicts the blackbody receiver absorption efficiency, Carnot efficiency, and ideal thermodynamic conversion efficiency as a function of the receiver cavity temperature for selected values of the concentration ratio at the receiver aperture in the range of 100 to 10,000. According to Figure 2.7, a higher concentration ratio leads to an increased ideal thermodynamic conversion efficiency, imposing challenges on

the optical system to provide high concentration ratios to the receiver with satisfactory optical efficiency.

## 2.5 Methodology

Modelling tools for solar CRSs can be found in review studies by Garcia et al. [126], Ho [156], and Bode and Gauché [157]. The tools differ in methods for radiative flux computations, types of optical losses accounted for, types of optical and radiative output characteristics, availability of user-defined field layout and receiver configurations, size limits of heliostat field and/or CRSs, annual performance and optimisation capabilities, and computational cost and efficiency. Despite a large number of available optical modelling tools, we develop in-house simulation programs for all involved optical modelling in this doctoral work, for the following two reasons: (1) None of the existing modelling tools fulfills all the design requirements involved in this work such as simulations of CPCs, ‘tower-reflector’ systems, and secondary reflectors of new geometries. A program that renders the greatest degree of design freedom is desired; (2) The in-house development of simulation programs necessitates a solid understanding of the underlying physics of solar concentrating systems. Hence, we develop optical simulation programs guided by the MCRT technique [14, 158].

### Monte-Carlo ray-tracing technique

The MCRT technique is implemented throughout this work for the evaluation of the optical and energetic characteristics of investigated systems including the HFSS-based experimental system, commercial-scale CRSs, and beam-down (‘tower-reflector’) optical systems. The MCRT technique is the most robust simulation technique for optical and radiative transfer modelling of solar CRSs [14, 92, 159]. As statistical methods, they can incorporate spatial, angular, spectral, and temporal variations of radiative intensity, arbitrary spectral, and directional properties of opaque and transmitting surfaces as well as participating media. The MCRT methods come in multiple variants, from simple methods such as the basic collision-based method to advanced methods implementing various strategies towards increased computational efficiency and accuracy such as the energy partitioning and pathlength methods.

Methods are developed to accelerate the computation. Ray paths are tracked from the point of emission to the (last) target surface along the ray path. Rays carrying the same amount of radiative power are generated uniformly from assumed planes perpendicular to the normal of heliostats. Thus the computational efficiency is increased by avoiding simulating rays hitting the ground. Moreover, the number of generated rays for each heliostat is proportional to the cosine efficiency of the heliostat.

The details of modelling CRSs are presented in the following text.

### Sun position

The sun's position relative to an observer on the ground,  $\hat{\mathbf{r}}_{\text{sol}}$ , is described by two angles: the solar altitude  $\alpha_{\text{sol}}$  and azimuth angle  $\gamma_{\text{sol}}$  [22]:

$$\hat{\mathbf{r}}_{\text{sol}} = -\cos\alpha_{\text{sol}}\cos\gamma_{\text{sol}}\hat{\mathbf{i}} + \cos\alpha_{\text{sol}}\sin\gamma_{\text{sol}}\hat{\mathbf{j}} - \sin\alpha_{\text{sol}}\hat{\mathbf{k}} \quad (2.16)$$

The solar altitude and azimuth angle of the sun  $\{\alpha_{\text{sol}}, \gamma_{\text{sol}}\}$  are functions of solar declination  $\delta_{\text{sol}}$ , hour angle  $\omega_{\text{sol}}$ , and latitude  $\phi_{\text{sol}}$ .

$$\alpha_{\text{sol}} = \sin^{-1}(\cos\phi_{\text{sol}}\cos\delta_{\text{sol}}\cos\omega_{\text{sol}} + \sin\phi_{\text{sol}}\sin\delta_{\text{sol}}) \quad (2.17)$$

$$\gamma_{\text{sol}} = \text{sgn}(\omega_{\text{sol}}) \left| \cos^{-1} \left( \frac{\sin\alpha_{\text{sol}}\sin\phi_{\text{sol}} - \sin\delta_{\text{sol}}}{\cos\alpha_{\text{sol}}\cos\phi_{\text{sol}}} \right) \right| \quad (2.18)$$

$\delta_{\text{sol}}$  and  $\omega_{\text{sol}}$  are functions of day number  $n_{\text{day}}$ , the specified hour  $p_{\text{hour}}$ , and minute  $p_{\text{minute}}$ , for simulations, respectively [22].

$$B = (n_{\text{day}} - 1) \frac{360}{365} \quad (2.19)$$

$$\delta_{\text{sol}} = (180/\pi)(0.006918 - 0.399912\cos B + 0.070257\sin B - 0.006758\cos 2B + 0.000907\sin 2B - 0.002697\cos 3B + 0.00148\sin 3B) \quad (2.20)$$

$$\omega_{\text{sol}} = (\pi/180) \times 15 \times (p_{\text{hour}} + p_{\text{minute}}/60 - 12) \quad (2.21)$$

Alternatively, the solar declination angle  $\delta_{\text{sol}}$  can be obtained from ecliptic longitude  $\lambda_{\text{sol}}$  [160].

$$\delta_{\text{sol}} = 23.44^\circ \sin\lambda_{\text{sol}} \quad (2.22)$$

Equations (2.19) and (2.20) are employed in this work.

### Clear-sky irradiance

The model of Ineichen [161] is employed to describe the clear-sky irradiance in a generic manner, independent of local weather conditions. It reads

$$G = G_{\text{sol},0} \exp(-\tau / \sin^{p_{\text{DNI}}}\alpha_{\text{sol}}) \quad (2.23)$$

where  $G_{\text{sol},0}$  is extra-terrestrial irradiance,  $\text{W m}^{-2}$ ,  $\tau$  is total atmospheric optical depth, and  $p_{\text{DNI}}$  is a fitting parameter obtained from radiative transport model calculations at two different solar elevation angles. In a general case, the following values of parameters are recommended for direction irradiance calculation and used in this work:  $G_{\text{sol},0} = 1617 \text{ W m}^{-2}$ ,  $\tau = 0.606$ ,  $p_{\text{DNI}} = 0.491$  [161]. The solar irradiance predicted by this model can be applied to any specific plant location.



### Atmospheric attenuation

Atmospheric attenuation accounts for radiation losses that occur through the atmosphere when rays travel in the atmosphere. The atmospheric attenuation efficiency  $\eta_{\text{attenuation}}$  is calculated as a function of the distance rays travel  $d_{\text{slant}}$  [162]:

$$\eta_{\text{attenuation}} = \begin{cases} 0.99321 - 0.0001176d_{\text{slant}} + 1.97 \times 10^{-8}d_{\text{slant}}^2 & d_{\text{slant}} \leq 1000 \text{ m} \\ \exp(-0.0001106d_{\text{slant}}) & d_{\text{slant}} > 1000 \text{ m} \end{cases} \quad (2.24)$$

These losses are approximated assuming a visibility distance of about 40 km.

### Optical surface imperfections

The ideal surface normal vector on a reflective optical surface,  $\hat{\mathbf{n}}_{\text{ideal}}$ , is obtained by

$$\hat{\mathbf{n}}_{\text{ideal}} = \frac{\left[ \frac{\partial \mathbf{E}}{\partial x_1}, \frac{\partial \mathbf{E}}{\partial y_1}, \frac{\partial \mathbf{E}}{\partial z_1} \right]}{\sqrt{\left( \frac{\partial \mathbf{E}}{\partial x_1} \right)^2 + \left( \frac{\partial \mathbf{E}}{\partial y_1} \right)^2 + \left( \frac{\partial \mathbf{E}}{\partial z_1} \right)^2}} \quad (2.25)$$

where  $\mathbf{E}$  is the surface equation of the optical reflector expressed in its local coordinates system.

Azimuth–elevation tracking with zero tracking error is assumed. The imperfections of optical reflective surfaces were numerically modelled using different approaches [163]. In all models, it is assumed that the length scale of the surface error is much larger than the wavelength of the reflected radiation, and that surface errors are uniformly distributed over the reflector surface. In this work, the surface error is simulated by modifying the analytically calculated surface normal vector. The modification is described with the azimuthal angle  $\phi_{\text{err}}$  assumed to be uniformly distributed between 0 and  $2\pi$ , and the polar angle  $\theta_{\text{err}}$  assumed to have a Rayleigh probability density function with mode  $\sigma_{\text{err}}$  [66].

$$\theta_{\text{err}} = \sin^{-1} \sqrt{-2\sigma_{\text{err}}^2 \log(1 - R_\theta)} \quad (2.26)$$

$$\phi_{\text{err}} = 2\pi R_\phi \quad (2.27)$$

$R_\theta$  and  $R_\phi$  are numerically generated random numbers between 0 and 1. The mode of the Rayleigh distribution is assumed for each optical reflector ranging between 1 and 3 mrad. The corresponding coordinates of the modified heliostat normal vector  $\hat{\mathbf{n}}_{\text{err}}$  are

$$\hat{\mathbf{n}}_{\text{err}} = \sin\theta_{\text{err}}\cos\phi_{\text{err}}\hat{\mathbf{i}} + \sin\theta_{\text{err}}\sin\phi_{\text{err}}\hat{\mathbf{j}} + \cos\theta_{\text{err}}\hat{\mathbf{k}} \quad (2.28)$$

where  $\hat{\mathbf{i}}$ ,  $\hat{\mathbf{j}}$ , and  $\hat{\mathbf{k}}$  are the unit vectors along the local coordinates axes created with  $\hat{\mathbf{k}}$  equal to the ideal normal vector  $\hat{\mathbf{n}}_{\text{ideal}}$ . Hence, specular reflection on a surface with

local unit surface normal vector  $\hat{\mathbf{n}}_{\text{err}}$  is described by the law of reflection

$$\hat{\mathbf{s}}_r = \hat{\mathbf{s}}_i - 2(\hat{\mathbf{s}}_i \cdot \hat{\mathbf{n}}_{\text{err}})\hat{\mathbf{n}}_{\text{err}} \quad (2.29)$$

### Annual simulations

The sun position can be also described in terms of ecliptic longitude  $\lambda_{\text{sol}}$  and hour angle  $\omega_{\text{sol}}$  [160] so that sun positions are mapped on a rectangular domain discretised by using a 2D grid with equidistant steps [164]. The annual heliostat field performance is evaluated using the method as in [164] and by employing bicubic spline interpolation [165] of results for discrete sun positions. Grigoriev et al. (2016) proved that by applying the spring–autumn, east–west, and day–night symmetry, sufficiently good accuracy was obtained with only 32 sampling points for a year, as shown in Fig. 2.8. The instantaneous performance of all the 32 sampling points is obtained from the MCRT simulation. For obtaining the annual efficiencies, bicubic spline interpolation is used [165]. The interpolation error is calculated and found with a maximum value of 6% at sun position near winter sunrise and below 1% for other sun positions. Hence, this interpolation method provides sufficient accuracy for this work.

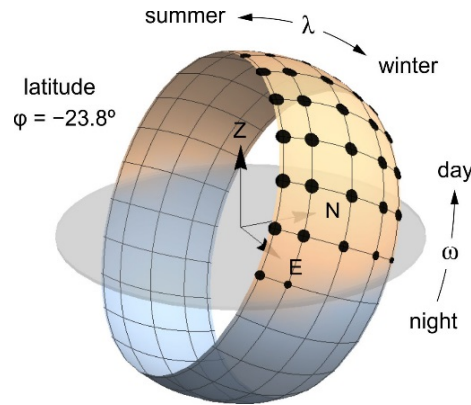


Figure 2.8: The sun path of the latitude of Alice Springs, Australia. The 32 simulated independent points on the sampling grid are marked by dots (reprinted from [164], with permission from AIP Publishing).

### Verification of in-house developed programs

The in-house developed MCRT program for modelling the 3D CPC is verified by computing the transmission-angle curve of a CPC with an acceptance angle  $\theta_{\text{CPC}}$  of  $16^\circ$ , and comparing the results with those taken from Winston et al. (2005) [33]. Excellent agreement was found as seen in Figure 2.9. The MCRT code for modelling CRSs is verified by simulating the instantaneous performance of the PS10 heliostat field. Figure 2.10 shows the predicted radiative flux distributions on a receiver aperture using selected ray-tracing tools including Tonatiuh [84], SOLSTICE [166], Tracer

[167], and the in-house developed program used in this work [24]. Excellent agreement has been found. More details of the verification work can be found in [12, 109].

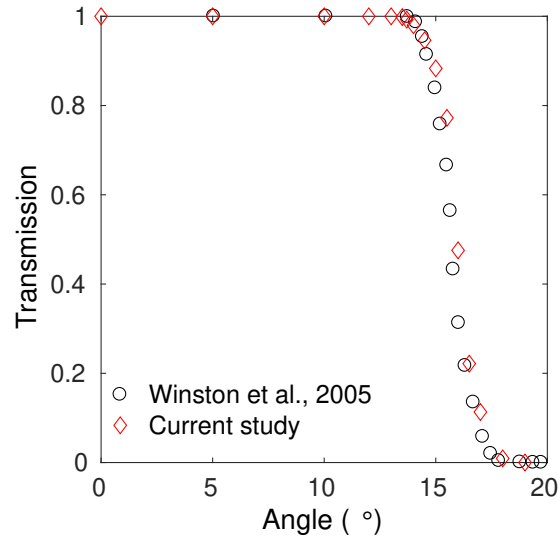


Figure 2.9: Transmission-angle curve of a CPC with the acceptance angle of  $\theta_{\text{CPC}} = 16^\circ$  [109].

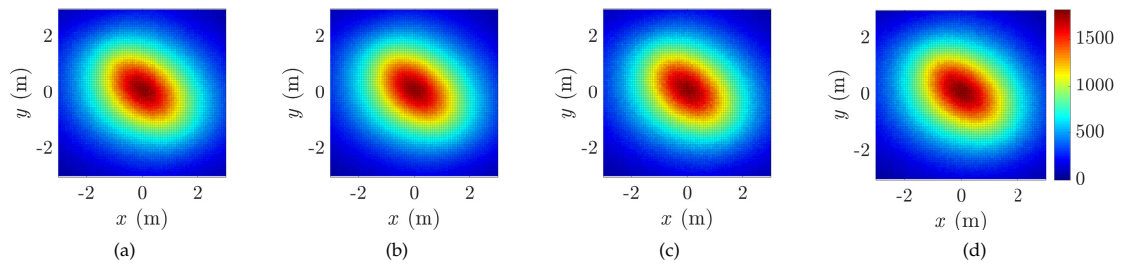


Figure 2.10: Radiative flux (in the unit of  $\text{W m}^{-2}$ ) on a target plane calculated by using the ray-tracing tool of (a) Tonatiuh [168], (b) SOLSTICE [166], (c) Tracer [167] and (d) the in-house developed program implemented in present work [12, 24].

The performance of the overall CRS is maximised through rigorous design of optical components and receivers by iterative optimisation of their geometry, number, orientation, position, and materials.



---

## Design of a compound parabolic concentrator for a multi-source high-flux solar simulator

---

This chapter presents an optical study of designing a CPC for use in the ANU HFSS [109]<sup>1</sup>. The multi-source HFSSs output radiation with angular non-uniformities due to the finite number of radiation modules, which results in hot spots on the reactor cavity surface. A solar reduction reactor was designed with a tilted aperture for mimicking the solar receiver in a central receiver system, i.e. the reactor intercepts only irradiation emitted from the lower lamps of the HFSSs. This configuration leads to potentially reduced concentration ratios. Hence, a CPC with the capability of increasing radiative flux uniformity and concentration ratio is designed and manufactured for assisting in the experimental testing of a solar reduction reactor driven by the simulated high-flux radiation from the ANU HFSS.

The geometrical parameters of the 3D CPC, including the acceptance angle and the entry aperture radius, are determined by optical simulations guided by the MCRT technique. The CPC requires active cooling due to the operation under high-flux irradiation through the CPC entry aperture and the exposure to thermal radiation from the reactor cavity. A cooling system is designed using engineering heat transfer correlations to achieve the goal of keeping the CPC surface temperature and the cooling water pressure drop below 40°C and 450 kPa, respectively.

Experimental testing and thermal modelling of the solar reduction reactor with the designed CPC are reported in [88, 89]. Transient 3D heat and mass transfer modelling of the high-temperature packed-bed solar thermochemical reactor is performed. The model couples reaction kinetics and fluid flow to conductive, convective, and radiative heat transfer. The reactor achieves a peak temperature of 1350 K. The numerically predicted temperature profiles and oxygen generation rates are in good agreement with the experimental data. An energy rate balance analysis shows the instantaneous peak solar-to-chemical energy efficiency reaches 9.3% [89].

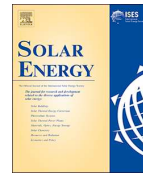
---

<sup>1</sup>In this study, the unit of concentration ratio was mistakenly written as  $\text{kW m}^{-2}$  in Fig. 7(c), whereas concentration ratio should be dimensionless. Alternatively, the unit of one sun should be used.



Contents lists available at ScienceDirect

Solar Energy

journal homepage: [www.elsevier.com/locate/solener](http://www.elsevier.com/locate/solener)

## Design of a compound parabolic concentrator for a multi-source high-flux solar simulator



Lifeng Li, Bo Wang, Johannes Pottas, Wojciech Lipiński\*

Research School of Electrical, Energy and Materials Engineering, The Australian National University, Canberra, ACT 2601, Australia

### ARTICLE INFO

#### Keywords:

Compound parabolic concentrator  
Nonimaging optics  
High-flux solar simulator  
Concentrating solar power

### ABSTRACT

A three-dimensional compound parabolic concentrator (CPC) is designed for high-temperature solar thermochemical applications driven by radiation from a multi-source high-flux solar simulator. The basic geometrical parameters of the CPC including the acceptance angle and the entry aperture radius are determined using optical simulations. A cooling system for overheating protection is designed using engineering heat transfer correlations. A prototype CPC is manufactured using additive manufacturing and single point diamond turning techniques. The optical simulations show that the CPC increases the concentration ratio by a factor of 4.1 at an optical efficiency of 85.4%, reduces spillage loss from 78.9% to 32.1%, and reduces the flux non-uniformity on the target surface.

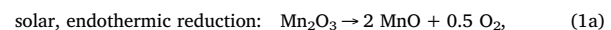
### 1. Introduction

Concentrating solar technologies (CST) typically make use of point- or line-focusing imaging concentrating systems to obtain high radiative fluxes. However, flux concentration ratios obtained using imaging optics fall short of the thermodynamic limit of maximum attainable concentration ratio due to off-axis aberration and coma effects causing image blurring and broadening. Furthermore, emerging high-temperature solar thermal and thermochemical systems aim to operate efficiently at temperatures above 1000 °C, requiring concentration ratios typically above 1000 suns and utilization of spillage radiation (Ho and Iverson 2014; Bader and Lipiński, 2017; Sandoval et al., 2018). Increased optical requirements lead to high cost of primary concentrators (Li et al., 2016; Levêque et al., 2017). In small-scale research and development applications, the required high concentration ratios can be obtained using dedicated facilities such as solar furnaces or high-flux solar simulators (HFSSs) (Haueter et al., 1999; Petrasch et al., 2006; Krueger et al., 2011; Bader et al., 2015; Ekman et al., 2015; Gill et al., 2015; Levêque et al., 2016; Wieghardt et al., 2016; Wang et al., 2017). Fig. 1 shows an example high-flux solar simulator consisting of 18 radiation sources. Multi-source high-flux solar simulators output radiation with angular non-uniformities due to the finite number of intense radiative sources, which results in hot spots on receiver surfaces (Bader et al., 2015).

Since optical imaging is not required in concentrating solar energy systems, nonimaging secondary concentrators can be employed to

increase the concentration ratio without substantially increasing the cost of a primary concentrator. The compound parabolic concentrator (CPC) was first proposed by Hinterberg and Winston in mid 1960s as an efficient way to collect Čerenkov radiation (Hinterberger and Winston, 1966), and thereafter applied to solar energy systems (Gleckman et al., 1989; Yogev et al., 1998; Cooper et al., 2013; Madala and Boehm, 2017). The basic geometry of a two-dimensional (2D) CPC is composed of two parabolic sections with foci at the end points of the exit aperture (Fig. 2). The reflecting surface of a three-dimensional (3D) CPC is formed by rotating the cross-section of a 2D CPC about the CPC axis. The use of a CPC ideally increases the concentration ratio by a factor of  $1/\sin\theta_1$  and  $1/\sin^2\theta_1$  for a 2D and a 3D CPC, respectively, where  $\theta_1$  is the acceptance angle. This allows for utilization of spillage radiation directly around the hot spot, and spreads the angular distribution of the transmitted radiation (Winston et al., 2005).

In this study, we design a 3D CPC for high-temperature solar thermochemical applications driven by radiation from a multi-source high-flux solar simulator. Fig. 3 shows the laboratory setup with selected lamps of the HFSS providing conical radiation, a CPC and a model solar thermochemical reactor with a tilted aperture. The configuration of solar reduction reactor with a tilted aperture is selected to mimic the large-scale solar central receiver (SCR) system with a cavity receiver–reactor irradiated from a heliostat field. Specifically, the selected model reactor realizes the first step (1a) of a two-step manganese oxide based redox cycle given by



\* Corresponding author.

E-mail address: [wojciech.lipinski@anu.edu.au](mailto:wojciech.lipinski@anu.edu.au) (W. Lipiński).<https://doi.org/10.1016/j.solener.2019.03.017>

Received 17 December 2018; Received in revised form 4 March 2019; Accepted 5 March 2019

0038-092X/ © 2019 International Solar Energy Society. Published by Elsevier Ltd. All rights reserved.

**Nomenclature**

$A$	area, m <sup>2</sup>
$C$	concentration ratio, kW m <sup>-2</sup>
$c_p$	specific heat at constant pressure, J kg <sup>-1</sup> K <sup>-1</sup>
$d$	diameter, m
$f$	focal length, m
$f_D$	Darcy friction factor
$g$	acceleration of gravity, m s <sup>-2</sup>
$G$	direct normal solar irradiance, W m <sup>-2</sup>
$h$	heat transfer coefficient, W m <sup>-2</sup> K <sup>-1</sup>
$H$	irradiation, W m <sup>-2</sup>
$k$	thermal conductivity, W m <sup>-1</sup> K <sup>-1</sup>
$L$	length, m
$\dot{m}$	mass flow rate, kg s <sup>-1</sup>
$n$	number
$\hat{n}$	surface normal vector
Nu	Nusselt number
Pr	Prandtl number
$\Delta P$	pressure drop, Pa
$q$	power or heat rate, W
$r$	radius, m
Re	Reynolds number
$T$	temperature, K
$u$	average velocity, m s <sup>-1</sup>

**Greek**

$\alpha$	absorptivity
$\beta$	bent angle, °
$\delta$	thickness, m
$\varepsilon$	roughness, mm

$\eta$	efficiency
$\theta_i$	acceptance angle, °
$\xi$	bend loss coefficient
$\Phi$	rim angle, °
$\rho$	density, kg m <sup>-3</sup>
$\rho_{CPC}$	CPC surface reflectivity
$\mu$	dynamic viscosity, Pa s
$\sigma$	Stefan–Boltzmann constant, W m <sup>-2</sup> K <sup>-4</sup>

**Subscripts**

b	bent
c	cooling channel
f	final
in	inlet
out	outlet
opt	optical
rad	radiation
rec	receiver
s	straight
t	total
th	thermal
w	water

**Abbreviations**

CPC	compound parabolic concentrator
CSP	concentrating solar power
CST	concentrating solar technologies
HFSS	high-flux solar simulator
MCRT	Monte Carlo ray-tracing
SCR	solar central receiver

non-solar, exothermic oxidation:  $2 \text{MnO} + 0.5 \text{O}_2 \rightarrow \text{Mn}_2\text{O}_3$ . (1b)

Assuming the reactor is a perfectly-insulated and isothermal blackbody receiver, thermal efficiency of the reactor can be calculated as (Fletcher and Moen, 1977),

$$\eta_{\text{th}} = 1 - \frac{\sigma T_{\text{rec}}^4}{GC_{\text{rec}}}, \quad (2)$$

where  $\sigma$  is the Stefan–Boltzmann constant,  $\sigma = 5.67 \times 10^{-8} \text{W m}^{-2} \text{K}^{-4}$ ,  $T_{\text{rec}}$  is the receiver cavity temperature,  $G$  is the direct normal irradiance equal to  $1000 \text{W m}^{-2}$ , and  $C_{\text{rec}}$  is the concentration ratio at the receiver aperture. For operation of the reduction reactor at  $1800 \text{K}$  and  $80\%$  thermal efficiency, a concentration ratio of at least  $3000 \text{suns}$  is required.

**2. Methodology****2.1. Optical design**

Optical design based on geometric optics is applied to determine the geometrical parameters of the 3D CPC including the acceptance angle  $\theta_i$  and the entry aperture radius  $r_{\text{in}}$ . The radius of the exit aperture  $r_{\text{out}}$  and the full (untruncated) length  $L_{\text{CPC}}$  can be calculated as functions of  $\theta_i$  and  $r_{\text{in}}$  (Winston et al., 2005),

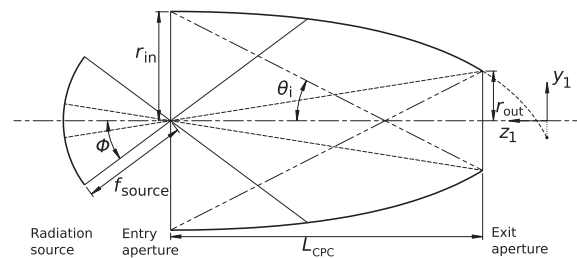


Fig. 2. Cross-section of a compound parabolic concentrator (CPC).

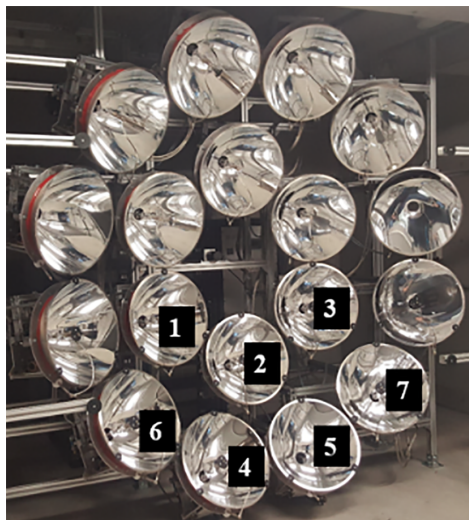


Fig. 1. Photograph of a multi-source high-flux solar simulator (HFSS) at the Australian National University (Bader et al., 2015). Included is the lamp numbering notation for the analyses presented in this study.

L. Li, et al.

Solar Energy 183 (2019) 805–811

$$r_{\text{out}} = r_{\text{in}} \sin \theta_i, \quad (3)$$

$$L_{\text{CPC}} = \frac{r_{\text{in}} + r_{\text{out}}}{\tan \theta_i} = r_{\text{in}} \frac{1 + \sin \theta_i}{\tan \theta_i}. \quad (4)$$

The interception efficiency  $\eta_{\text{int}}$  is defined as the ratio of the radiative power entering the CPC entry aperture to the total radiative power from a source incident on the CPC entry aperture plane. Optical losses in a CPC result from surface absorption and backward reflection (Winston et al., 2005). The optical efficiency of a CPC  $\eta_{\text{opt}}$  is defined as the ratio of transmitted radiative power to that entering a CPC. Thus, the concentration ratio of a CPC is

$$C_{\text{CPC}} = \frac{\eta_{\text{opt}}}{\sin^2 \theta_i}. \quad (5)$$

The overall concentration ratio  $C_f$  taken at the exit aperture of the CPC is then,

$$C_f = C_0 C_{\text{CPC}}. \quad (6)$$

$C_0$  is the concentration ratio at the CPC entry aperture and is defined as:

$$C_0 = \frac{q_{\text{in}}}{\pi r_{\text{in}}^2 G}, \quad (7)$$

where  $q_{\text{in}}$  is the radiative power entering the CPC entry aperture.

The optical design is guided by Monte Carlo ray-tracing (MCRT) simulations, which allows for convenient evaluation of the CPC optical performance metrics, including interception efficiency  $\eta_{\text{int}}$ , CPC optical efficiency  $\eta_{\text{opt}}$ , actual concentration ratio  $C_f$  and radiative power  $q_{\text{rec}}$  at CPC exit aperture, as functions of the design parameters, including CPC acceptance angle  $\theta_i$  and CPC entry aperture radius  $r_{\text{in}}$ . The MCRT methodology for simulating CPCs was previously described in (Lipiński and Steinfeld, 2006), and is applied in the present study. Two types of irradiation on the CPC entry aperture are considered in this study: (i) a conical beam of convergent rays launched uniformly from a spherical cap surface, and (ii) a multi-cone beam from a multi-source high-flux solar simulator. Irradiation (i) is studied to elucidate basic geometrical beam characteristics as a reference case. Irradiation (ii) is studied to obtain the actual beam characteristics of practical relevance to high-flux solar simulation systems.

## 2.2. Thermal design

The CPC requires active cooling due to operation under high-flux irradiation at the entry aperture and exposure to thermal radiation from the reactor cavity through the exit aperture. The CPC surface temperature and cooling water pressure drop are required to be below 40 °C and 450 kPa, respectively.

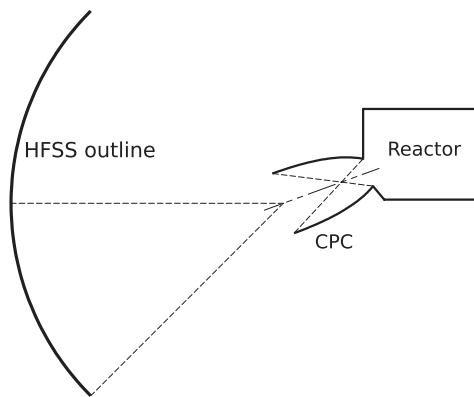


Fig. 3. Laboratory setup with a HFSS, a CPC, and a reactor with a tilted aperture.

In the following analysis, we assume steady state, no volumetric heat sources/sinks, all but the internal, irradiated CPC surface adiabatic, and one-dimensional conduction in the CPC wall. By applying the energy conservation, the enthalpy gain rate of the cooling water equals to the absorbed heat rate at the CPC reflective surface,

$$q = \dot{m} c_p (T_{\text{out}} - T_{\text{in}}) = \int_{A_{\text{CPC}}} \alpha H \, dA, \quad \dot{m} = \rho u \pi r_c^2, \quad (8)$$

where  $q$  is the heat rate absorbed at the CPC surface,  $\dot{m}$  is the mass flow rate of cooling water,  $c_p$  is the specific heat of water,  $T_{\text{in}}$  and  $T_{\text{out}}$  are the inlet and outlet temperature of cooling water, respectively,  $\alpha$  is the absorptivity of the CPC surface, which is assumed to be direction-independent,  $H$  is the total-hemispherical irradiation,  $A_{\text{CPC}}$  is the area of the CPC internal reflective surface,  $\rho$  is density of water,  $u$  is the average velocity of cooling water, and  $r_c$  is the radius of the cooling channel. MCRT method is used to calculate the net heat rate absorbed by CPC reflective surface as well as the peak radiative flux.

The heat rate through the CPC wall to the cooling water is calculated as

$$q = h A_c (T_c - T_w) = k_{\text{CPC}} A_c \frac{T_{\text{CPC}} - T_c}{\delta_c}, \quad h = \frac{k_w \text{Nu}_d}{d_c} \quad (9)$$

where  $h$  the heat transfer coefficient,  $A_c$  and  $\delta_c$  is the cooling channel surface area and wall thickness,  $k_{\text{CPC}}$  and  $k_w$  is the thermal conductivity of the CPC material and the cooling water, respectively, and  $T_c$ ,  $T_w$ , and  $T_{\text{CPC}}$  are the temperatures of cooling channel surface, cooling water, and CPC irradiated surface, respectively. Nusselt number is calculated from the Gnielinski correlation (valid for  $3000 < \text{Re}_d < 500,000$ ,  $0.5 < \text{Pr} < 2000$ ) for turbulent flow in tubes,

$$\text{Nu}_d = \frac{(f_D/8)(\text{Re}_d - 1000)\text{Pr}}{1 + 12.7(f_D/8)^{1/2}(\text{Pr}^{2/3} - 1)}, \quad \text{Pr} = \frac{c_p \mu}{k_w}. \quad (10)$$

Consequently, the temperature of the irradiated CPC surface is

$$T_{\text{CPC}} = T_w + \frac{q}{A_c} \left( \frac{1}{h} + \frac{\delta_c}{k_{\text{CPC}}} \right). \quad (11)$$

The pressure drop of water in the CPC cooling channel arises from two contributions: pressure drop in the straight channels (Darcy–Weisbach equation) and pressure drop in the bends,

$$\Delta P_t = \Delta P_s + n_b \Delta P_b = \rho f_D \frac{L}{d_c} \frac{u^2}{2g} + n_b \left( \frac{1}{2} f_D \rho u^2 \frac{\pi r_b}{d_c} \frac{\beta}{180} + \frac{1}{2} \xi \rho u^2 \right), \quad (12)$$

where  $\Delta P_t$ ,  $\Delta P_s$  and  $\Delta P_b$  are the total pressure drop and pressure drop for straight channel and bends,  $f_D$  is the Darcy friction factor,  $L$  is the channel length,  $d_c$  is the channel diameter,  $u$  is the average velocity of cooling water,  $g$  is the acceleration of gravity,  $n_b$  is the number of bends,  $r_b$  is the bend radius,  $\beta$  is the bending angle in degree, and  $\xi$  is bend loss coefficient taken from Idelchik (Idelchik, 1986).

## 3. Results and discussion

### 3.1. Optical design

The MCRT code is verified by computing the transmission-angle curve of a CPC with an acceptance angle  $\theta_i = 16^\circ$ , and comparing the results with those taken from Winston et al. (2005). Excellent agreement is found as seen in Fig. 4.

The performance of a 3D CPC irradiated by a conical beam (i) launched uniformly from a spherical cap surface with a rim angle of  $17.5^\circ$  is investigated first. Fig. 5 shows paths of rays co-planar with a 3D CPC axial cross-section plane for the CPC acceptance angle of (a)  $10^\circ$ , (b)  $25^\circ$ , and (c)  $40^\circ$ , respectively. In each case, the exit aperture size is set equal to 0.016 m. The center point of the CPC entry aperture is collocated with the focal point of the irradiation beam. Due to the symmetry, only rays emitted from half of the radiation source and incident on half of the CPC are shown in Fig. 5. Fig. 6 shows the 2D



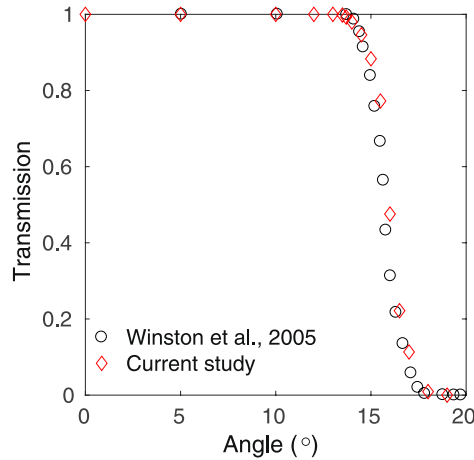


Fig. 4. Transmission-angle curve of a CPC with the acceptance angle of  $\theta_i = 16^\circ$ .

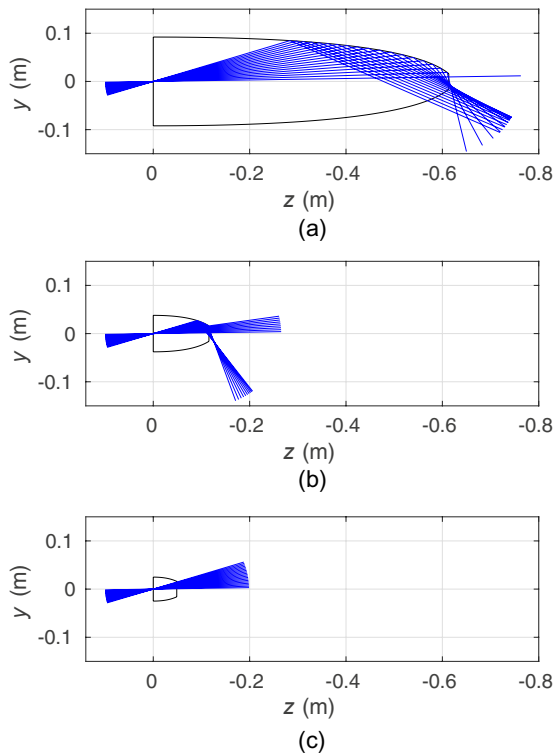


Fig. 5. Paths of rays co-planar with a 3D CPC axial cross-section plane for the CPC acceptance angle of (a)  $10^\circ$ , (b)  $25^\circ$ , and (c)  $40^\circ$ , respectively, and a conical irradiation beam from a spherical cap surface of  $17.5^\circ$  rim angle.

projections of radiative flux distributions on a hemispherical target of radius 0.1 m. Based on the results shown in Figs. 5 and 6, we conclude that: (i) a finite fraction of incident rays pass through the CPC without interacting with the surface of the CPC, while the remaining fraction is reflected by the CPC surface; (ii) the ratio of the number of reflected rays to the number of all incident rays increases with decreasing  $\theta_i$ , indicating that a smaller  $\theta_i$  benefits redistributing the incident radiation; and (iii) for  $\theta_i$  exceeding a threshold value, no rays are reflected by

the surface of the CPC.

Next, the two geometrical parameters, the acceptance angle  $\theta_i$  and the entry aperture radius  $r_{in}$ , of a 3D CPC are to be determined for the HFSS-based laboratory setup. The CPC surface reflectivity and slope error are assumed to be 0.88 and 0.5 mrad, respectively. The position of the CPC relative to the HFSS is fixed, with the center point of the CPC entry aperture coincident with the HFSS focal point, and the center point (geometrical average of coordinates of central arc points) of lamps #1, #3, #4, #5 (see Fig. 1) on the CPC axis. Five HFSS lamps are used for providing the radiation, including three lamps from the inner row and two lamps from the outer row (lamps #1–#5 in Fig. 1).

Optical simulations were performed for the acceptance angle  $\theta_i$  varying from  $20^\circ$  to  $32^\circ$  in  $2^\circ$  increments, and the entry aperture radius  $r_{in}$  varying from 0.02 m to 0.05 m in 0.005 m increments. Fig. 7 shows the simulation results of intercept efficiency  $\eta_{int}$ , CPC optical efficiency  $\eta_{opt}$ , concentration ratio  $C_f$ , and radiative power  $q_{rec}$  for each combination of  $\theta_i$  and  $r_{in}$ . As seen in Fig. 6a,  $\eta_{int}$  is dependent on  $r_{in}$  only. A smaller CPC entry aperture leads to larger spillage loss. Fig. 7b shows that  $\eta_{opt}$  is mainly affected by  $\theta_i$ . For fixed sources, the backward reflection becomes less pronounced for increasing  $\theta_i$ . As observed in Fig. 7c and 7d, increasing  $r_{in}$  or  $\theta_i$  leads to increasing radiative power  $q_{rec}$  at the expense of a decreased concentration ratio  $C_f$ . With increasing  $\theta_i$ ,  $\eta_{opt}$  will increase but the theoretical concentration ratio ( $=1/\sin^2\theta_i$ ) provided from an ideal 3D CPC without optical losses will decrease. Hence, a peak  $C_f$  is observed in Fig. 7c for each fixed  $r_{in}$ .

To obtain higher concentration ratio, smaller  $\theta_i$  and smaller  $r_{in}$  are desired. However,  $\eta_{opt}$  and  $q_{rec}$  decrease with smaller  $\theta_i$ , and  $\eta_{int}$  and  $q_{rec}$  decrease with smaller  $r_{in}$ . Therefore, the case of  $\theta_i = 27^\circ$  and  $r_{in} = 0.035$  m is eventually selected for the laboratory setup, as it provides the maximum  $\eta_{int}$ ,  $\eta_{opt}$  and  $q_{rec}$  among all of the cases that satisfy the minimum concentration ratio requirement of 3000 suns.

Projections of radiative flux distribution on a hemispherical target of radius 0.1 m placed at the CPC exit is presented in Fig. 8a for the case when lamps #1–#5 are used. The peak flux observed at the center of the target results predominantly from irradiation by lamp #2 for which the majority of radiation is transmitted through the CPC without interacting with the CPC reflecting surface. The peak flux is largely reduced as observed by comparing to the distribution obtained without any CPC applied (Fig. 8b), and consequently the flux uniformity is significantly improved. Quantitative results of  $r_{rec}$ ,  $\eta_{int}$ ,  $\eta_{opt}$ ,  $C_f$  and  $q_{rec}$  with the designed CPC, for turning on different numbers of the HFSS lamps, are shown in Table 1. For comparison, results of  $r_{rec}$ ,  $\eta_{int}$ ,  $C_f$  and  $q_{rec}$  for cases without CPCs, when turning on different numbers of HFSS lamps, are included in Table 1. Two cases of different selected receiver aperture radius  $r_{rec}$  are simulated. In case #1, receiver aperture radius  $r_{rec}$  is designed to meet the required concentration ratio of 3000 suns. In case #2, receiver aperture radius  $r_{rec}$  is fixed to be equal to the entry aperture radius  $r_{in}$  of the designed CPC. It is found that the application of CPCs greatly increases the interception efficiency and obtained power into the target receiver with the concentration ratio requirement of minimum 3000 suns satisfied.

### 3.2. Thermal design

The parameters of the final cooling system are listed in Table 2. From the thermal simulation, the CPC surface temperature and the pressure drop of the water in the cooling channel were found to be  $38^\circ\text{C}$  and 130 kPa, respectively, meeting the design requirements.

### 3.3. Final specification and manufacturing

The final design of the CPC including the cooling channel layout is shown in Fig. 9. The cooling water system is a one-inlet and one-outlet serpentine return channel, arranged in the concentrator wall with non-uniform spacing. This arrangement allows for effective capture of excessive heat at the highest-flux region in the lower part of the

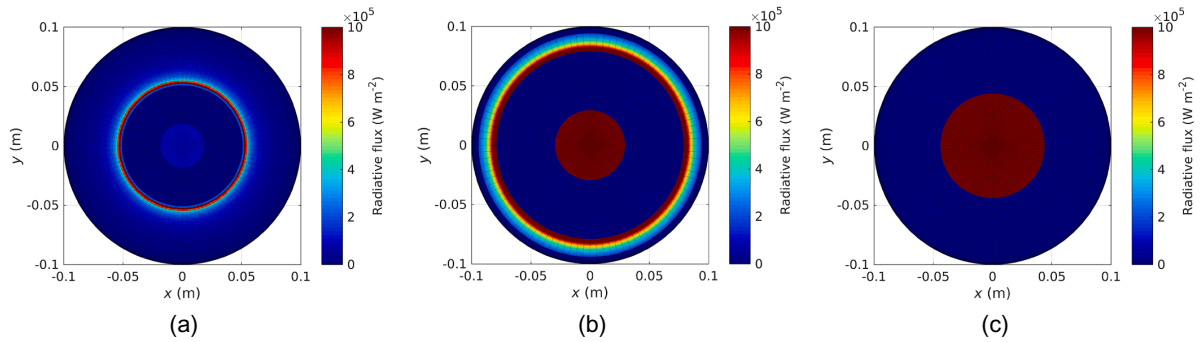


Fig. 6. 2D projections of radiative flux distribution on a hemispherical target with a 0.1 m radius located directly behind the CPC exit aperture for the CPC acceptance angle of (a) 10°, (b) 25°, and (c) 40°, respectively, and a conical irradiation beam from a spherical cap surface of 17.5° rim angle.

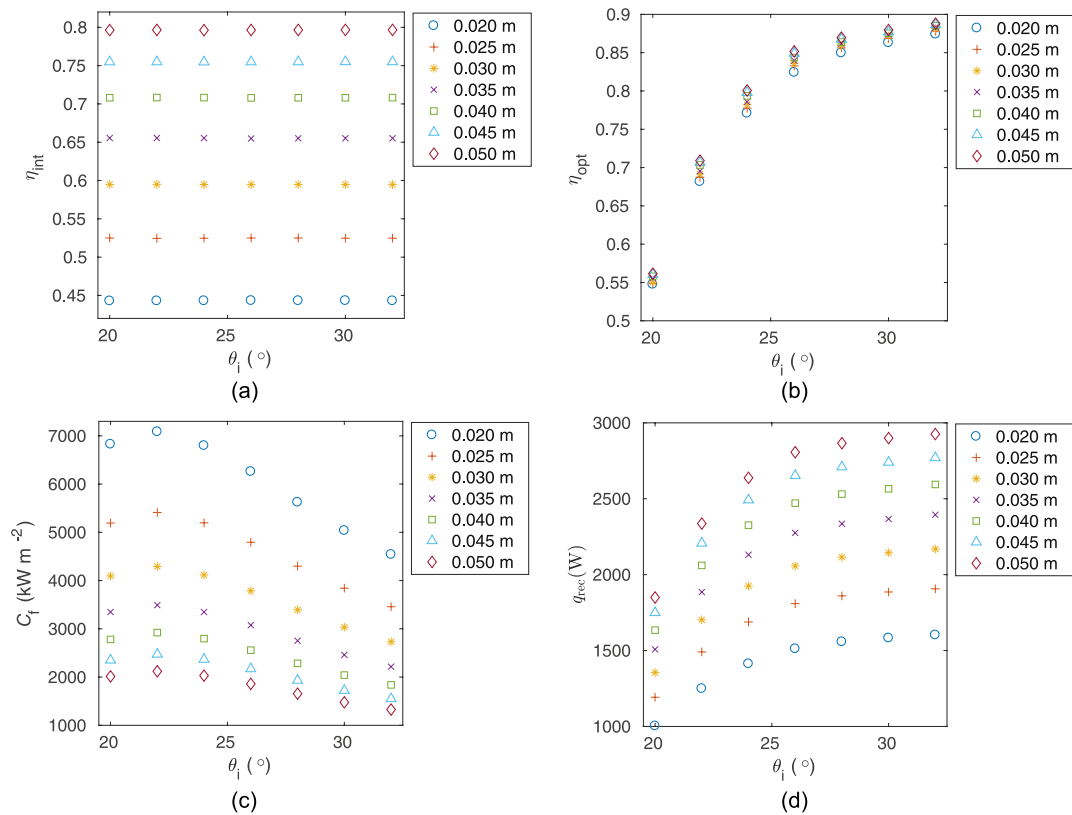


Fig. 7. Simulation results of CPC performance metrics including (a) interception efficiency  $\eta_{int}$ , (b) CPC optical efficiency  $\eta_{opt}$ , obtained (c) concentration ratio  $C_r$  and (d) radiative power  $q_{rec}$  as functions of the CPC acceptance angles  $\theta_i$  and the CPC entry aperture radius  $r_{in}$ , when lamp #1–#5 are turned on.

concentrator, predicted numerically. The CPC wall thickness was minimized to reduce the exposure of the surface area to radiation from the cavity, and to reduce the displaced volume of reactor insulation.

In addition to the CPC component, a concentric water-cooled radiation shield was developed. A vertical cross-section of the CPC and radiation shield as integrated with the solar reactor, are shown in Fig. 10.

The CPC was 3D printed in aluminum alloy using direct metal laser sintering. The surface features were machined using a conventional CNC lathe with tungsten carbide and monocrystalline diamond tools for the non-reflective and reflective surfaces, respectively. The alloy was selected for its high thermal conductivity and high specular reflectance

when diamond-turned. The final CPC and radiation shield are shown installed in the reactor housing in Fig. 11.

#### 4. Summary and conclusions

A 3D compound parabolic concentrator (CPC) has been designed for a laboratory-scale high-temperature solar reduction reactor irradiated by a multi-source high-flux solar simulator. The CPC geometrical parameters including acceptance angle and entry aperture radius were determined through an optical design guided by optical Monte Carlo ray-tracing simulations. Thermal management strategy of the CPC was developed using simple analytical relations based on the Gnielinski

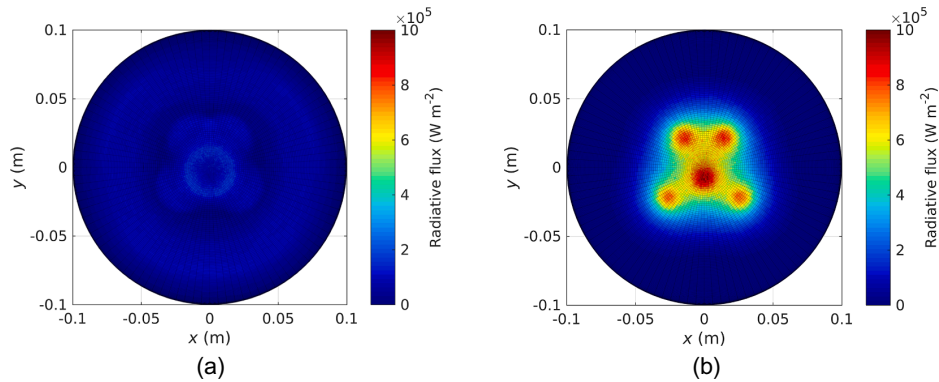


Fig. 8. 2D projection of radiative flux distribution on a hemispherical target with radius of 0.1 m (a) at the CPC exit aperture, with CPC of  $\theta_i = 27^\circ$  and  $r_{in} = 0.035$  m, and (b) without any CPC applied. Lamps #1–#5 are in use.

Table 1

Receiver aperture radius  $r_{rec}$ , interception efficiency  $\eta_{int}$ , CPC optical efficiency  $\eta_{CPC}$ , concentration ratio  $C_f$ , and power  $q_{rec}$  for different combinations of HFSS lamps in use with and without a CPC.

With/without CPCs	HFSS lamps in use	$r_{rec}$ (m)	$\eta_{int}$	$\eta_{opt}$	$C_f$ (suns)	$q_{rec}$ (kW)
With CPC	#1, #2, #3, #4, #5	0.016	67.9%	85.4%	3001	2.38
	#1, #2, #3, #4, #5, #6	0.016	66.3%	78.5%	3211	2.55
	#1, #2, #3, #4, #5, #6, #7	0.016	66.0%	73.6%	3503	2.78
Without CPC (Case #1)	#1, #2, #3, #4, #5	0.009	21.1%	–	3000	0.85
	#1, #2, #3, #4, #5, #6	0.011	27.1%	–	3000	1.32
	#1, #2, #3, #4, #5, #6, #7	0.012	31.8%	–	3000	1.80
Without CPC (Case #2)	#1, #2, #3, #4, #5	0.035	67.9%	–	725	2.79
	#1, #2, #3, #4, #5, #6	0.035	66.3%	–	844	3.25
	#1, #2, #3, #4, #5, #6, #7	0.035	66.0%	–	982	3.78

Table 2

Parameters used in the thermal model.

Parameters	Symbol	Value	Unit
<i>Pre-calculated</i>			
Incident radiative power from HFSS absorbed by CPC	$q_{CPC}$	491.57	W
Emitted power from cavity absorbed by CPC	$q_{cav}$	391.56	W
<i>Thermophysical property</i>			
Thermal conductivity of CPC wall	$k_{CPC}$	205	$W\ m^{-1}\ K^{-1}$
CPC reflective surface reflectance	$\rho_{CPC}$	0.88	–
Specific heat of water	$c_p$	4200	$J\ kg^{-1}\ K^{-1}$
Density of water	$\rho$	1000	$kg\ m^{-3}$
Dynamic viscosity of water	$\mu$	0.001	Pa s
Thermal conductivity of water	$k_w$	0.58	$W\ m^{-1}\ K^{-1}$
<i>Geometry</i>			
Cooling channel diameter	$d_c$	0.003	m
Cooling channel length	$L_c$	3.21	m
Amount of 90° bend	$n_{b90}$	18	–
Amount of 180° bend	$n_{b180}$	8	–
Bend center radius	$r_b$	0.00225	m
Cooling channel roughness	$\epsilon_c$	0.03	mm
Thickness of conduction layer from CPC surface to cooling channel		0.00135	m
<i>Operation</i>			
Inlet water temperature	$T_{in}$	20	°C
Outlet water temperature	$T_{out}$	30	°C

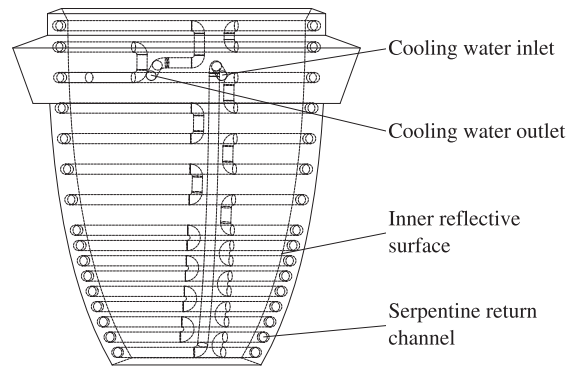


Fig. 9. CPC cooling channel layout.

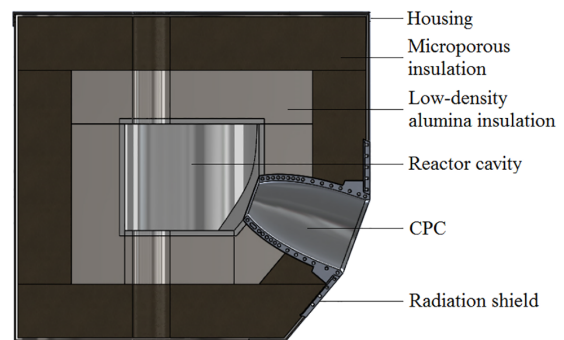


Fig. 10. Vertical cross-section view of the reactor with the CPC integrated.

correlation and the Darcy–Weisbach equation for heat transfer of turbulent flow and pressure drop of cooling water, respectively.

The optical simulations demonstrated that the proposed CPC design can significantly reduce flux non-uniformity and radiative peak flux on target surfaces as compared to the case without any CPCs applied. The CPC increases the concentration ratio by a factor of 4.1 at an optical

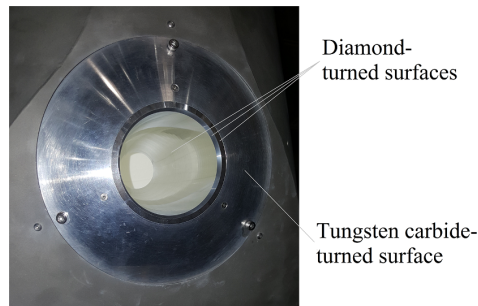


Fig. 11. CPC and radiation shield installed in the reactor.

efficiency of 85.4%, and reduces the spillage loss from 78.9% to 32.1%. Moreover, the CPC increases the degree of flexibility for utilization of different combinations of lamps of a multi-source high-flux solar simulator.

#### Acknowledgements

The financial support from the Australian Renewable Energy Agency (grant no 2014/RND005) is gratefully acknowledged. The authors thank Dr Joe Coventry, Dr John Pye, Dr José Zapata, and Dr Keith Lovegrove for discussions of the solar reactor design.

#### References

- Bader, R., Haussener, S., Lipiński, W., 2015. Optical design of multisource high-flux solar simulators. *ASME J. Sol. Energy Eng.* 137, 021012.
- Bader, R., Lipiński, W., 2017. Solar thermal processing. In: Blanco, M., Ramirez, Santigosa L. (Eds.), *Advances in concentrating solar thermal research and technology*. Woodhead Publishing, pp. 403–447.
- Cooper, T., Dähler, F., Ambrosetti, G., Pedretti, A., Steinfeld, A., 2013. Performance of compound parabolic concentrators with polygonal apertures. *Sol. Energy* 95, 308–318.
- Ekman, B.M., Brooks, G., Akbar, Rhamdhani M., 2015. Development of high flux solar simulators for solar thermal research. *Sol. Energy Mater. Sol. Cells* 141, 436–446.
- Fletcher, E.A., Moen, R.L., 1977. Hydrogen and oxygen from water. *Science* 197 (4308), 1050–1056.
- Gill, R., Bush, E., Haueter, P., Loutzenhiser, P., 2015. Characterization of a 6 kW high-flux solar simulator with an array of xenon arc lamps capable of concentrations of nearly 5000 suns. *Rev. Sci. Instrum.* 86, 125107.
- Gleckman, P., O'Gallagher, J., Winston, R., 1989. Concentration of sunlight to solar-surface levels using non-imaging optics. *Nature* 339, 198–220.
- Haueter, P., Seitz, T., Steinfeld, A., 1999. A new high-flux solar furnace for high-temperature thermochemical research. *ASME J. Sol. Energy Eng.* 121 (1), 77–80.
- Hinterberger, H., Winston, R., 1966. Efficient light coupler for threshold Čerenkov counters. *Rev. Sci. Instrum.* 37, 1094–1095.
- Ho, C.K., Iverson, B.D., 2014. Review of high-temperature central receiver designs for concentrating solar power. *Renew. Sust. Energy Rev.* 29, 835–846.
- Idelchik, I.E., 1986. *Handbook of hydraulic resistance*. Hemisphere Publishing Corp.
- Krueger, K.R., Davidson, J.H., Lipiński, W., 2011. Design of a new 45 kW high-flux solar simulator for high-temperature solar thermal and thermochemical research. *ASME J. Sol. Energy Eng.* 133 (1), 11013.
- Levêque, G., Bader, R., Lipiński, W., Haussener, S., 2016. Experimental and numerical characterization of a new 45 kW<sub>e</sub> multisource high-flux solar simulator. *Opt. Express* 24 (22), A1360–A1373.
- Levêque, G., Bader, R., Lipiński, W., Haussener, S., 2017. High-flux optical systems for solar thermochemistry. *Sol. Energy* 156, 133–148.
- Lipiński, W., Steinfeld, A., 2006. Annular compound parabolic concentrator. *ASME J. Sol. Energy Eng.* 128, 121–124.
- Li, L., Coventry, J., Bader, R., Pye, J., Lipiński, W., 2016. Optics of solar central receiver systems: A review. *Opt. Express* 24 (14), A985–A1007.
- Madala, S., Boehm, R.F., 2017. A review of nonimaging solar concentrators for stationary and passive tracking applications. *Renew. Sust. Energy Rev.* 71, 309–322.
- Petrusch, J., Coray, P., Meier, A., Brack, M., Häberling, P., Wüillemin, D., Steinfeld, A., 2006. A novel 50 kW 11000 suns high-flux solar simulator based on an array of Xenon arc lamps. *ASME J. Sol. Energy Eng.* 129 (4), 405–411.
- Sandoval, A.B., Bader, R., Jafarian, M., Fedunik-Hofman, L., Sun, Y., Hinkley, J., Miller, S., Lipiński, W., 2018. Techno-economic assessment of solid-gas thermochemical energy storage systems for solar thermal power applications. *Energy* 149, 473–484.
- Wang, W., Aichmayer, L., Garrido, J., Laumert, B., 2017. Development of a Fresnel lens based high-flux solar simulator. *Sol. Energy* 144, 436–444.
- Wieghardt, K., Funken, K.-H., Dibowski, G., Hoffschmidt, B., Laaber, D., Hilger, P., Eßer, K.-P., 2016. Synlight-the world's largest artificial sun. *AIP Conference proceedings* 1734, 030038.
- Winston, R., Miñano, J.C., Benítez, P., 2005. *Nonimaging optics*. Elsevier.
- Yogev, A., Kribus, A., Epstein, M., Kogan, A., 1998. Solar “tower reflector” systems: A new approach for high-temperature solar plants. *Int. J. Hydrogen Energy* 23 (4), 239–245.

---

## Reflective optics for redirecting convergent radiative beams in concentrating solar applications

---

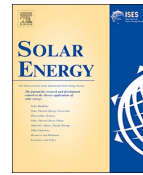
This chapter presents an optical study of redirecting optics for use in the ANU HFSS [25]. Reflective optics are investigated for realising the redirection of convergent radiative beams. This study originates from solving the limitation of the HFSS-based experimental system that the majority of HFSSs output radiative beams with a fixed axis direction, typically horizontal, which limits the use of HFSSs for applications requiring beams of various axis directions. Convergent radiative beams are common in large-scale concentrating solar systems, such as the concentrated beams by parabolic dishes and heliostat fields. Beam-redirecting reflectors were used in parabolic dish systems for purposes such as realisation of upward-facing receivers [169], realisation of moving focal point [170], and improvement of optical performance [171–173]. In CRSs, the redirection enables more convenient and cheaper installation, and operation of the high-temperature solar receivers and the instrumentation connections at ground level. However, selected optical characteristics, including redirected-beam rim angle and relative position between sources and reflected images, were not exhaustively covered in the literature.

Hence, the flat, ellipsoidal, hyperboloidal, and paraboloidal reflectors are optically explored in this study for realising the redirection of convergent radiative beams. 2D analytical ray-tracing simulations are conducted for an ideal optical system without optical imperfections. System optical performance is evaluated in terms of output beam optical characteristics of rim angle, ray distribution, and relative position to the input beam. MCRT simulations are performed for a practical optical system with realistic solar simulators as the radiation source and the four beam-redirecting reflectors. The optical and radiative characteristics of resulting radiative power, spatial and directional flux distribution, optical efficiencies on specified flat and hemispherical targets, and clearance between simulator, reflector, and target are predicted.



Contents lists available at ScienceDirect

Solar Energy

journal homepage: [www.elsevier.com/locate/solener](http://www.elsevier.com/locate/solener)

## Reflective optics for redirecting convergent radiative beams in concentrating solar applications

Lifeng Li<sup>a</sup>, Bo Wang<sup>a</sup>, Roman Bader<sup>b</sup>, José Zapata<sup>c</sup>, Wojciech Lipiński<sup>a,\*</sup><sup>a</sup> Research School of Electrical, Energy and Materials Engineering, The Australian National University, Canberra, ACT 2601, Australia<sup>b</sup> Weiskopf Partner GmbH, Switzerland<sup>c</sup> ITP Renewables, Australia

## ARTICLE INFO

## Keywords:

Reflective optics  
High-flux solar simulator  
Concentrating solar technology  
Beam redirection

## ABSTRACT

We investigate optical characteristics of flat, ellipsoidal, hyperboloidal, and paraboloidal reflectors for redirecting convergent radiative beams common in concentrating solar applications. Optical simulations are performed with selected types of radiative sources including a generic uniformly-emitting spherical cap and a specific realization of a multi-source high-flux solar simulator. Two-dimensional ray-tracing simulations are conducted for an ideal optical system without optical imperfections consisting of a spherical cap source, a beam-redirecting reflector, and a target tailored to capture all radiation. System optical performance is evaluated in terms of output beam optical characteristics of rim angle, ray distribution and relative position to the input beam. Three-dimensional Monte-Carlo ray-tracing simulations are performed for a practical optical system with a realistic solar simulator as radiation source and the four beam-redirecting reflectors. We predict optical characteristics of resulting radiative power, spatial and directional flux distribution, optical efficiencies on specified flat and hemispherical targets, and clearance between simulator, reflector and target. From the model system with a solar simulator and exemplary parameters, it is concluded that the investigated four types of reflectors enable redirection of the horizontal-axis beam from the solar simulator to non-horizontal axis targets. The flat reflector enables the highest system optical efficiency of 97% at the expense of the smallest clearance between the source, the reflector and the reflected image. Curved reflectors render a larger degree of freedom to design the characteristics of the output beam. Thus, curved reflectors are suitable for applications that require large clearance between system components and/or high radiative flux output on cavity surface, but at the expense of lower system optical efficiency.

### 1. Introduction

Redirection of solar radiative beams is typically realized in concentrating solar thermal (CST) technologies, in which solar beams from primary concentrators such as solar dishes, heliostats, linear Fresnel reflectors, or parabolic troughs are used to irradiate receivers encountered in a multitude of configurations. In particular, solar reactors for thermochemical processing are designed in configurations and with aperture orientations that rely on directionally diverse concentrated solar irradiation conditions (Bader and Lipiński, 2017; Levêque et al., 2017; Wang et al., 2018; Carrillo et al., 2019). In a solar central receiver system (CRS), redirecting the focused beam on the central tower enables more convenient and cheaper installation and operation of the high-temperature receiver–reactor and the instrumentation connections at ground level (Li et al., 2016). This can be achieved by employing flat,

ellipsoidal or hyperboloidal beam-redirecting reflectors (Yogev et al., 1998; Segal and Epstein, 1999; Segal and Epstein, 2000). Beam-redirecting reflector is also used in solar dish systems for purposes such as realization of upward-facing receivers (Feuermann and Gordon, 1999), realization of moving focal point (Dähler et al., 2018), and optical performance improvement (Zhang et al., 2014; Wang et al., 2017; Yang et al., 2018). Previous studies mainly focused on evaluating performance of beam-directing reflectors in terms of radiative power and concentration ratio metrics for prescribed targets. However, selected optical characteristics including redirected-beam rim angle and relative position between sources and reflected images are not exhaustively covered in literature.

In laboratory-scale experiments, concentrated solar radiation can be emulated with artificial light sources such as the high-flux solar simulators (HFSSs) (Kuhn and Hunt, 1991; Hirsch et al., 2003; Petrasch

\* Corresponding author.

E-mail address: [wojciech.lipinski@anu.edu.au](mailto:wojciech.lipinski@anu.edu.au) (W. Lipiński).<https://doi.org/10.1016/j.solener.2019.08.077>Received 15 June 2019; Received in revised form 27 August 2019; Accepted 30 August 2019  
0038-092X/ © 2019 International Solar Energy Society. Published by Elsevier Ltd. All rights reserved.

Nomenclature			
$a$	ellipse or hyperbola semi-major axis, m	$e$	ellipsoidal
$b$	ellipse or hyperbola semi-minor axis, m	$f$	flat
$c$	linear eccentricity, m	$h$	hyperboloidal
$e$	eccentricity	inc	incident
$d$	distance, m	$m$	reflector
$f$	focal length, m	$p$	paraboloidal
$p$	semi-focal chord, m	spill	spillage
$L$	length, m	sys	system
		$t$	target
Greek		Abbreviations	
$\alpha$	reflector tilt angle, °	CPC	compound parabolic concentrator
$\beta$	axis rotation angle, °	CRS	central receiver system
$\phi$	rim angle, °	CST	concentrating solar thermal
		HFSS	high-flux solar simulator
		MCRT	Monte Carlo ray tracing
		2D	two-dimensional
		3D	three-dimensional
Subscripts			
abs	absorption		
cap	capture		

et al., 2007; Codd et al., 2010; Krueger et al., 2011; Krueger et al., 2013; Sarwar et al., 2014; Bader et al., 2015; Boubault et al., 2015; Dong et al., 2015; Ekman et al., 2015; Gill et al., 2015; Levêque et al., 2016; Wieghardt et al., 2016; Xu et al., 2016; Levêque et al., 2017; Wang et al., 2017; Jin et al., 2019). These devices are designed to enable experimental studies of materials and device prototypes under weather-independent, controlled high-flux irradiation conditions. A typical geometry of an HFSS radiative output is configured with a horizontal beam axis, which limits the use of HFSSs for applications requiring non-horizontal axis beams. Non-horizontal axis HFSS beams can be in

principle obtained by (i) designing a solar simulator with a tunable tilt angle, (ii) working with only selected, non-horizontal axis radiative sources of a multi-source HFSS, and (iii) using secondary, beam-redirecting optics. Approach (i) presents inherent technical challenges including precise tilt control of an overall HFSS structure and possible out-of-specification operation of arc lamps. Approach (ii) limits power level and direction of radiative output, and possibly requires non-imaging optics such as a compound parabolic concentrator (CPC) for meeting the concentration ratio requirement (Li et al., 2019). Approach (iii) of using secondary, beam-redirecting optics in HFSSs is not

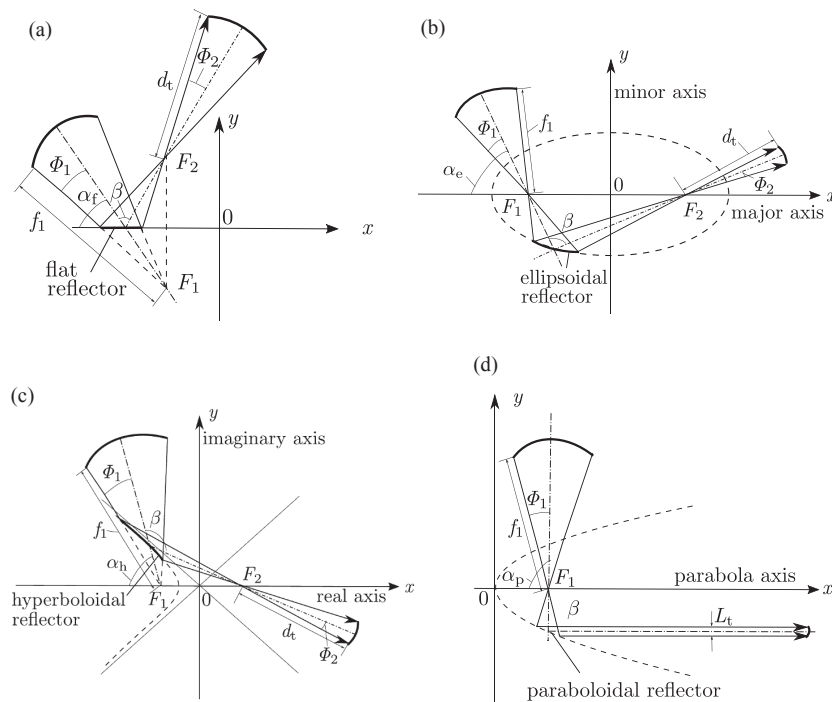


Fig. 1. Optical configurations of a generic uniformly-emitting spherical cap source coupled with (a) flat, (b) ellipsoidal, (c) hyperboloidal, and (d) paraboloidal reflectors.



**Table 1**  
Shape equations and design parameters for the investigated types of reflectors. The equations are written in co-ordinates shown in Fig. 1.

Reflector	Line/curve equation	3D surface equation	Geometrical parameters
Flat	$y = 0$ (5)	$y = 0$	$d_f$
Ellipsoidal	$\frac{x^2}{a_e^2} + \frac{y^2}{b_e^2} = 1$ (6)	$\frac{x^2}{a_e^2} + \frac{y^2}{b_e^2} + \frac{z^2}{b_e^2} = 1$ (7)	$c_e, e_e$
Hyperboloidal	$\frac{x^2}{a_h^2} - \frac{y^2}{b_h^2} = 1$ (8)	$\frac{x^2}{a_h^2} + \frac{y^2}{b_h^2} - \frac{z^2}{b_h^2} = -1$ (9)	$c_h, e_h$
Paraboloidal	$y^2 = 2p_p x$ (10)	$2p_p x = y^2 + z^2$ (11)	$p_p$

**Table 2**  
Baseline parameter set for parametric studies of model system I.

Reflector	Input beam rim angle $\phi_1$	Reflector tilt angle $\alpha$	Reflector geometrical parameters
Flat	30°	$\alpha_f = 50^\circ$	$d_f = 1$ m
Ellipsoidal	30°	$\alpha_e = 90^\circ$	$c_e = 1.6$ m, $e_e = 0.8$
Hyperboloidal	30°	$\alpha_h = 90^\circ$	$c_h = 3$ m, $e_h = 1.5$
Paraboloidal	30°	$\alpha_p = 50^\circ$	$p_p = 1$ m

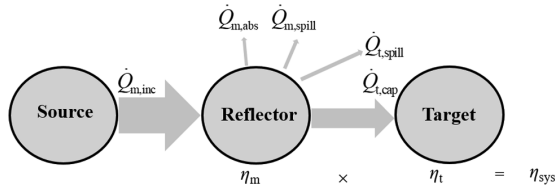


**Fig. 2.** Power flow including defined optical efficiencies in an optical system with a radiative source, a beam-redirecting reflector, and a target.

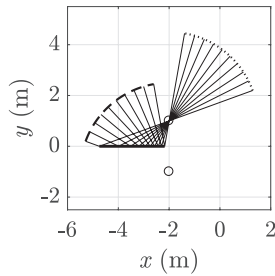


**Fig. 3.** Example of ray paths for an optical system with a spherical cap source and a flat reflector, generated for the baseline parameter set. Solid thickened line: reflector; dashed line: source; dotted line: target.

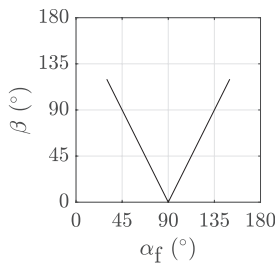


**Fig. 4.** Axis rotation angle  $\beta$  as a function of the reflector tilt angle  $\alpha_f$  for an example input beam with rim angle  $\phi_1 = 30^\circ$ .

discussed in literature except the study by Jin et al. (2019) involving a diffraction lens system for collimating high-flux solar simulator output.

In this study, we investigate the application of beam-redirecting reflectors for convergent beams in solar systems. Two types of radiation sources are investigated including a generic uniformly-emitting spherical cap source, where rays are uniformly launched and directed towards the sphere center and a specific realization of a multi-source high-flux solar simulator. Four types of reflectors are investigated: flat, ellipsoidal, hyperboloidal and paraboloidal. First, we perform two-dimensional (2D) ray-tracing simulations to parametrically study the effects of input beam rim angle, beam-redirecting reflector geometrical parameters and relative position between the source and the reflector, for the optical system with the uniformly-emitting spherical cap source. Optical performance is evaluated in terms of output beam rim angle, ray distribution, and relative position to input beam. Second, three-dimensional (3D) Monte-Carlo ray-tracing (MCRT) simulations are conducted for investigating the practical application of the four types of reflectors for a multi-source high-flux solar simulator (HFSS) constructed at the Australian National University (ANU) (Bader et al., 2015). Evaluated system optical characteristics include radiative power, spatial and directional flux distribution, system optical efficiency (throughput) and rendered clearances between the source, the reflector and the reflected image.

## 2. Optical model

### 2.1. Model system I: Uniformly-emitting spherical cap source

The ideal optical system consisting of the uniformly-emitting spherical cap source, the beam-redirecting reflector and the target tailored to capture all the radiation contains no optical imperfection. The uniformly-emitting spherical cap source is a simplified model for convergent beams in concentrating solar applications such as the concentrated radiation from a solar simulator, a solar dish, or a heliostat field. For the geometrical symmetry, two-dimensional ray tracing is sufficient to qualitatively assess the optical performance of the beam-redirecting reflector and the overall system.

Fig. 1 depicts the optical system configurations involving the four types of reflectors and shows the system geometrical parameters. The input beam is characterized by the rim angle  $\phi_1$  and focal length  $f_1$ . The output beam is characterized by the rim angle  $\phi_2$  for a convergent output beam (Fig. 1a–c), and a beam width  $L_t$  for a collimated output beam (Fig. 1d). For the system with a convergent output beam, the distance between the output beam focal point and the hemispherical target is  $d_t$  (Fig. 1a–c). The ellipsoidal, hyperboloidal, and paraboloidal reflectors are generated from revolving the elliptic, hyperbolic and parabolic curves around their major, real and central axes, respectively. One element of a two-sheeted hyperboloid of revolution is used as the beam-redirecting reflector. Table 1 summarizes two-dimensional curve equations, three-dimensional surface equations and geometrical parameters for the investigated reflectors. For ellipsoidal and hyperboloidal reflectors, major and minor axis lengths,  $2a$  and  $2b$ , respectively, can be calculated as functions of the geometrical design parameters of eccentricity  $e$  and linear eccentricity  $c$ .

$$a_e = c_e/e_e, \quad (0 < e_e < 1) \tag{1}$$

$$b_e = c_e \sqrt{1/e_e^2 - 1} \tag{2}$$

$$a_h = c_h/e_h, \quad (e_h > 1) \tag{3}$$

$$b_h = c_h \sqrt{1 - 1/e_h^2} \tag{4}$$

Ellipsoidal and hyperboloidal reflectors reflect all incoming light rays directed at one of the reflector's two foci towards its other focus. Hence, with flat, ellipsoidal and hyperboloidal reflectors, the output beam remains focused without any decrease in its concentration ratio.



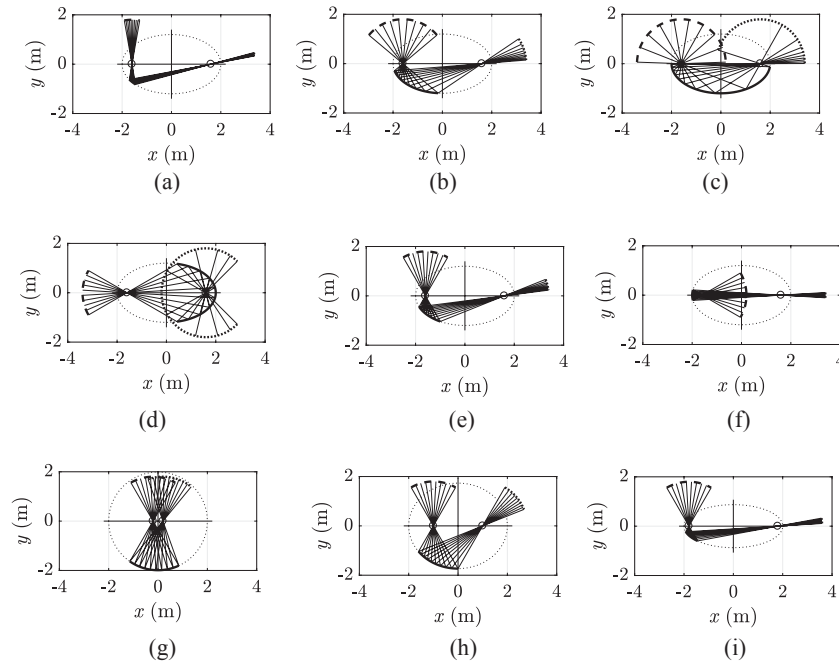


Fig. 5. Change of ray paths with (a–c): input beam rim angle  $\Phi_1$  of (a)  $10^\circ$ , (b)  $50^\circ$ , (c)  $88^\circ$ ; (d–f): ellipsoid tilt angle  $\alpha_e$  of (d)  $0^\circ$ , (e)  $90^\circ$ , (f)  $180^\circ$ ; (g–i): ellipsoid eccentricity  $e_e$  of (g) 0.1, (h) 0.5, (i) 0.8, for the baseline parameter set of Table 2.

In contrast, the paraboloidal reflector reflects the incoming focused radiation by collimating it parallel to the paraboloid axis. According to the edge-ray principle, only truncated ellipsoidal, hyperboloidal or paraboloidal surfaces are needed to provide the beam-redirecting reflector function.

The optical performance of the optical system with the generic source of a spherical cap is measured by the output beam rim angle  $\Phi_2$ , ray distribution, angle between input and output axes,  $\beta$ , (referred to as axis rotation angle in the following text for brevity), and the distance between focal points of input and output beams for cases of using flat, ellipsoidal and hyperboloidal reflectors. The free parameters are:

- input beam rim angle  $\Phi_1$ ;
- angle between input beam axis and reflector axis,  $\alpha$ , (referred to as reflector tilt angle in the following text for brevity);
- *flat reflector*: distance from input beam focal point to flat reflector surface,  $d_f$   
*ellipsoidal reflector*: eccentricity  $e_e$  and linear eccentricity  $c_e$   
*hyperboloidal reflector*: eccentricity  $e_h$  and linear eccentricity  $c_h$   
*paraboloidal reflector*: semi-focal chord  $p_p$

Final clearance between the input and output beams is determined from rim angles of input and output beams, axis rotation angle and the relative position of output beam focal point to input beam focal point. Rays are traced while varying design parameters for each beam-redirecting reflector. This allows for calculating output beam rim angle  $\Phi_2$  and axis rotation angle  $\beta$  as functions of the design parameters. In the parametric studies, one parameter is varied at a time while other parameters are taken on the baseline values listed in Table 2.

### 2.1.1. Flat reflector

The investigated free parameters of an optical system involving the flat reflector include the input beam rim angle  $\Phi_1$ , the distance between input beam focal point and flat reflector surface  $d_f$ , and the flat reflector tilt angle  $\alpha_f$ . The latter two parameters are analytically determined to be

in the range of  $(0, f_1 \sin(\alpha_f - \Phi_1))$  and  $(\Phi_1, 180^\circ - \Phi_1)$ , respectively, which allows the flat reflector to capture all rays of the input beam and eliminates the intersection of the flat reflector with the source. Axis rotation angle,  $\beta$ , is calculated to be equal to  $180^\circ - 2\alpha_f$  (for  $0 \leq \alpha_f \leq 90^\circ$ ) and  $2\alpha_f - 180^\circ$  (for  $90^\circ \leq \alpha_f \leq 180^\circ$ ). The distance between focal points of input and output beams is equal to  $2d_f$ . When the flat reflector tilt angle is in the range of  $[90^\circ - \Phi_1, 90^\circ + \Phi_1]$ , the output beam overlaps with the input beam, which would bring additional shading loss for most concentrating solar applications where the receiver/reactor aperture center is placed at the output beam focal point.

### 2.1.2. Ellipsoidal reflector

Mathematical solutions of radiative intensity after reflection by curved reflectors for a point-focusing radiation source can be found in Olikier et al., 1993. Unlike flat or spherical surfaces that have constant curvatures throughout the entire surface, the three investigated curved reflectors have different curvatures at different locations on their surfaces. The defined parameter of reflector tilt angle determines which part of the surface is to be used as the reflector. The input beam rim angle determines the surface size needed to provide the reflector function. In general, the output beam rim angle is positively proportional to the input beam rim angle. A smaller output beam rim angle is acquired from using a part of the reflector surface with a larger curvature.

The investigated free parameters of an optical system involving the ellipsoidal reflector include input beam rim angle  $\Phi_1$ , ellipsoid tilt angle  $\alpha_e$ , and ellipsoid eccentricity  $e_e$ . Input and output beams overlap if ellipsoidal reflector tilt angle is in the range of  $[180^\circ - \Phi_1, 180^\circ + \Phi_1]$ . The distance between focal points of input and output beams is equal to  $2a_e e_e$ . Hence, the required distance between focal points of input and output beams can be satisfied from choosing the ellipsoid major axis length  $2a_e$ , which is discovered to have no impact on the output beam characteristics of rim angle, ray distribution and axis rotation angle.

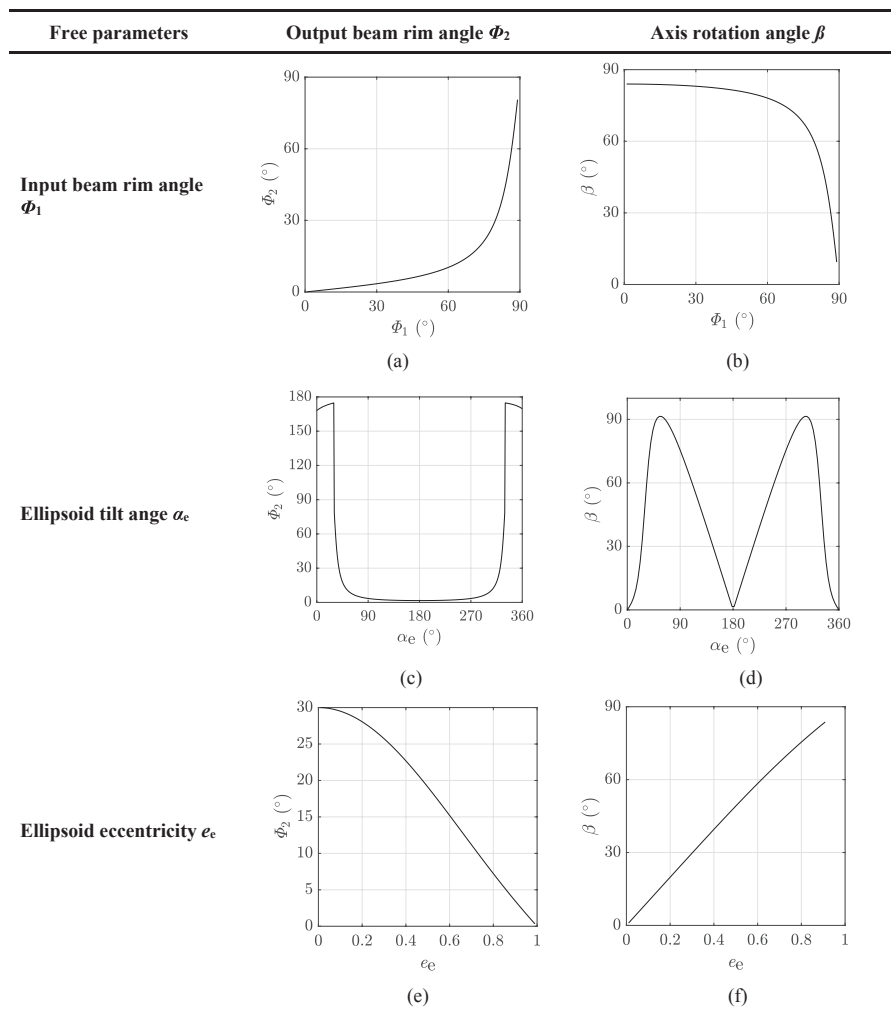


Fig. 6. Effects of input beam rim angle  $\Phi_1$ , ellipsoid tilt angle  $\alpha_e$ , and ellipsoid eccentricity  $e_e$ , on output beam rim angle  $\Phi_2$  and axis rotation angle  $\beta$ , for the baseline parameter set of Table 2.

2.1.3. Hyperboloidal reflector

The investigated free parameters of an optical system involving the hyperboloidal reflector include the input beam rim angle  $\Phi_1$ , the hyperboloid tilt angle  $\alpha_h$ , and the hyperboloid eccentricity  $e_h$ . Comparable to the ellipsoidal reflector case, input and output beams overlap if the hyperboloid tilt angle is in the range of  $[180^\circ - \Phi_1, 180^\circ + \Phi_1]$ . The distance between the focal points of input and output beams is equal to  $2a_h e_h$ . The required clearance between the two focal points can be met by choosing reflector major axis length  $2a_h$  that does not affect the output beam rim angle, ray distribution or axis rotation angle.

Since the hyperboloidal surface is not closed, the incident input beam may be separated by the hyperboloidal reflector and rays will be incident on both sides of the hyperboloidal surface. The rays that are incident on the backside of the hyperboloidal reflector surface will miss the second focus and therefore contribute to optical losses.

2.1.4. Paraboloidal reflector

The investigated free parameters of an optical system involving the paraboloidal reflector include the input beam rim angle  $\Phi_1$ , paraboloid tilt angle  $\alpha_p$ , and paraboloid semi-focal chord  $p_p$ .

For the focused output beams reflected from flat, ellipsoidal, and

hyperboloidal reflectors, radiative intensity on a hemispherical target surface decreases dramatically with an increasing distance to the output beam focal point. The size of the reflected image increases with the optical length that the rays have traveled. In contrast, for the collimated beam reflected from a paraboloidal reflector, radiative intensity on the target surface does not depend on the distance to the reflector, if atmospheric attenuation is neglected. It allows for placing the target device at different relative positions to the reflector without decreasing the radiative flux.

2.2. Model system II: High-flux solar simulator as radiation source

For the optical system with the ANU HFSS as the radiation source, optical imperfections are included in the analysis. Beam-redirecting reflectors are investigated for accomplishing the task of redirecting the horizontal-axis beam from the simulator ( $\Phi_1 = 45^\circ, f_1 = 1.933 \text{ m}$ ) onto non-horizontal axis targets. Three-dimensional Monte-Carlo ray-tracing simulations are performed to obtain both qualitative and quantitative optical performances. We follow the MCRT methodology previously used to study optical performance of compound parabolic concentrators and outlined in Lipiński and Steinfeld (2006) and Li et al., 2019. Beam-

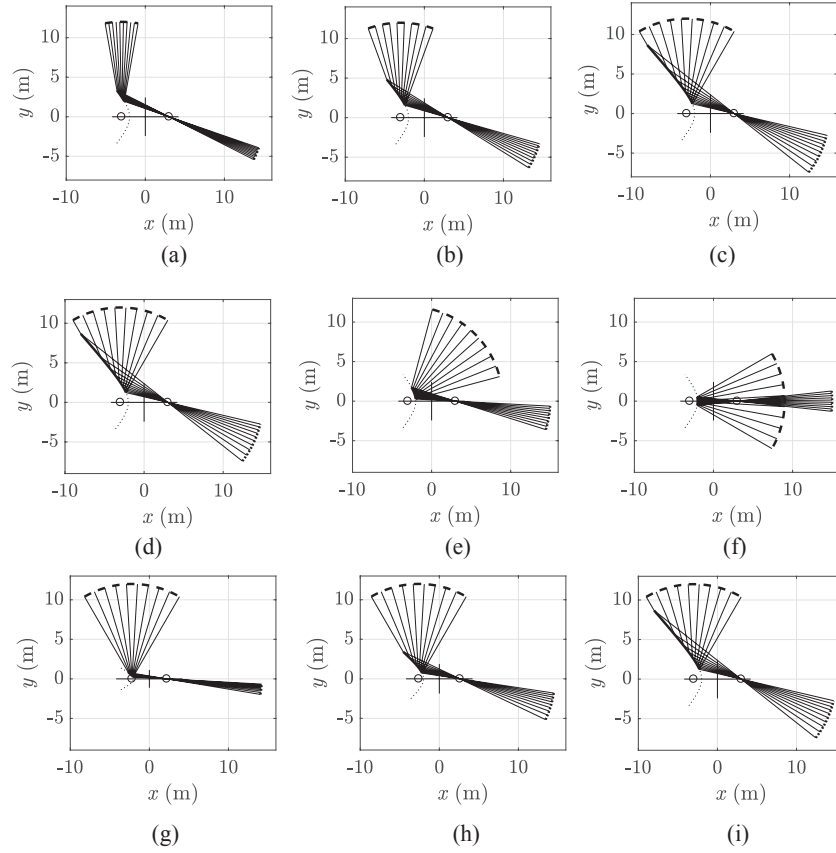


Fig. 7. Change of ray paths with (a–c): input beam rim angle  $\phi_1$  of (a)  $10^\circ$ , (b)  $20^\circ$ , (c)  $30^\circ$ ; (d–f): hyperboloid tilt angle  $\alpha_h$  of (d)  $90^\circ$ , (e)  $135^\circ$ , (f)  $180^\circ$ ; (g–i): hyperboloid eccentricity  $e_h$  of (g) 1.1, (h) 1.3, (i) 1.5, for the baseline parameter set of Table 2.

redirecting reflector surfaces are modeled using an assumed reflectance of unity and Gaussian surface normal error distribution with an assumed standard deviation of 0.85 mrad. Output radiative distributions are predicted on a flat target that is horizontally placed and passes through the output beam focal point and a hemispherical target with its center at the output beam focal point, respectively.

Optical losses occur in the optical system with optical imperfections. Fig. 2 depicts the optical system power flow as well as defined optical efficiencies including reflector optical efficiency  $\eta_m$ , target optical efficiency  $\eta_t$ , and system optical efficiency  $\eta_{sys}$ . Reflector optical efficiency accounts for optical losses of the radiative power absorbed by the reflector surface  $\dot{Q}_{m,abs}$  and the spilled radiative power that is not captured by the reflector  $\dot{Q}_{m,spill}$ . Target optical efficiency accounts for the spilled radiative power outside the target  $\dot{Q}_{t,spill}$ .  $\dot{Q}_{t,cap}$  represents the total radiative power captured by the target.

$$\dot{Q}_{m,inc} = \dot{Q}_{m,abs} + \dot{Q}_{m,spill} + \dot{Q}_{t,cap} + \dot{Q}_{t,spill} \quad (12)$$

$$\eta_m = 1 - \frac{\dot{Q}_{m,abs} + \dot{Q}_{m,spill}}{\dot{Q}_{m,inc}} \quad (13)$$

$$\eta_t = \frac{\dot{Q}_{t,cap}}{\dot{Q}_{t,cap} + \dot{Q}_{t,spill}} \quad (14)$$

$$\eta_{sys} = \eta_m \eta_t \quad (15)$$

### 3. Results and discussions

#### 3.1. Model system I: Uniformly-emitting spherical cap source

In this section, we explore the effects of input beam rim angle  $\phi_1$ , reflector tilt angle  $\alpha$ , and reflector geometrical parameters on the output beam characteristics of the rim angle  $\phi_2$ , ray distribution, the axis rotation angle  $\beta$ , and the distance between focal points of the input and output beams.

##### 3.1.1. Flat reflector

Fig. 3 shows the ray paths in the optical system involving a flat reflector with the baseline parameters listed in Table 2. The reflection on the flat reflector does not change the beam characteristics of the rim angle and ray distribution. However, the clearance between the input and output beams is small and it decreases with a larger input beam rim angle or a larger reflector tilt angle  $\alpha_r$  (for  $0 \leq \alpha_r \leq 90^\circ$ ), as can be seen in Fig. 4. The axis rotation angles  $\beta$  are equal for the systems with flat reflector tilt angles of  $\alpha_r$  and  $180^\circ - \alpha_r$  due to system geometrical symmetry. Output beam characteristics of rim angle, ray distribution and axis rotation angle are independent of input beam focal length.

##### 3.1.2. Ellipsoidal reflector

Fig. 5 and Fig. 6 show that the reflection on an ellipsoidal reflector leads to output beams with nonuniformly-distributed rays. Input beams with larger rim angles lead to larger output beam rim angles and smaller axis rotation angles. Fig. 5(d–f) and Fig. 6(c,d) depict effects of

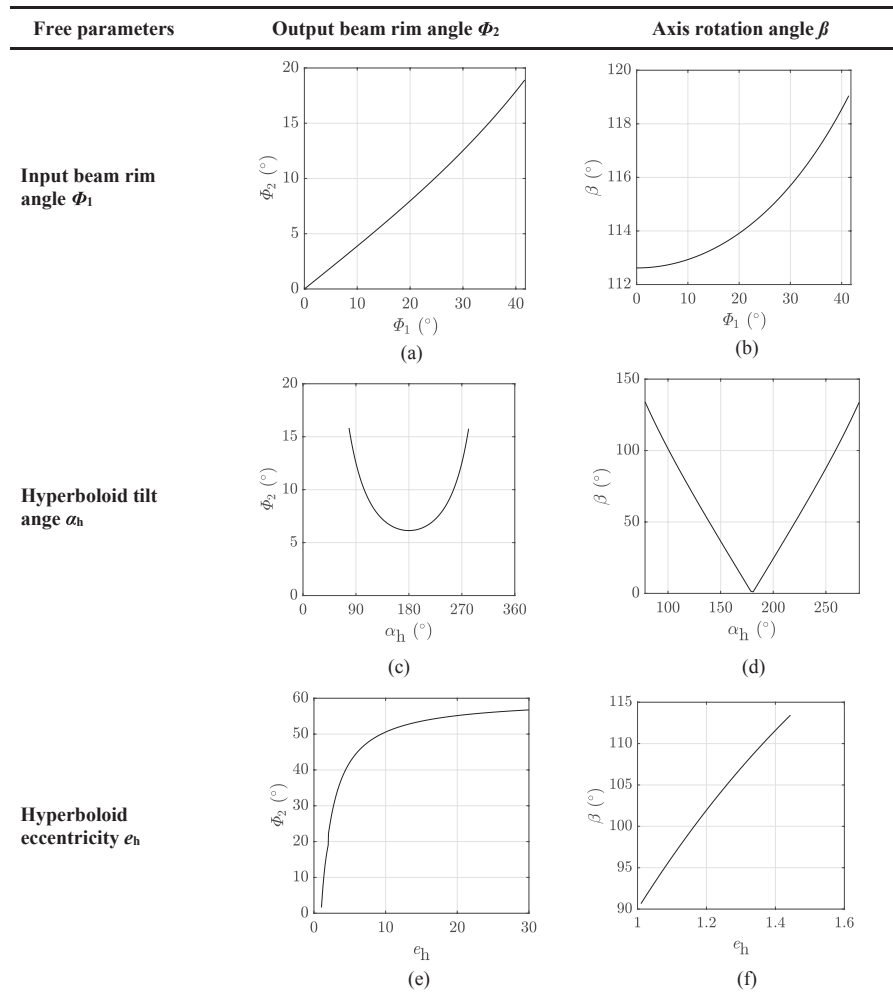


Fig. 8. Effects of input beam rim angle  $\Phi_1$ , hyperboloid tilt angle  $\alpha_h$ , and hyperboloid eccentricity  $e_h$ , on output beam rim angle  $\Phi_2$  and axis rotation angle  $\beta$ , for the baseline parameter set of Table 2.

the ellipsoid tilt angle. Same results are observed for optical systems with ellipsoids of tilt angles  $180^\circ - \alpha_e$  and  $\alpha_e$  due to geometrical symmetry of the system. A minimum output beam rim angle is observed when ellipsoid tilt angle is equal to  $180^\circ$  (Fig. 5f) since the part of the ellipsoidal surface near the vertex on the major axis with largest curvatures is used. A typical solar beam down system where the ellipsoidal reflector is coaxial with the reflected beam from a heliostat field has the same optical configuration as Fig. 5(f). Output beams have an increasing rim angle as the ellipsoid tilt angle moves away from  $180^\circ$  and the output beam rim angle peaks for reflector tilt angle  $\alpha_r$  equal to  $30^\circ$  ( $= \Phi_1$ ) or  $330^\circ$  ( $= 360^\circ - \Phi_1$ ) (Fig. 6c). Output beams with rim angles larger than  $90^\circ$  are not suitable for most concentrating solar applications. Larger ellipsoid eccentricities lead to output beams with smaller rim angles due to the increase of surface curvature with larger eccentricity.

Ellipsoidal reflectors are common in high-flux solar simulators (Krueger et al., 2011; Bader et al., 2015; Levêque et al., 2017). Assuming the radiation arc lamp to be a point source, the considered system becomes equivalent to that shown in Fig. 5(d) with an input beam rim angle of  $180^\circ$ .

### 3.1.3. Hyperboloidal reflector

Based on Fig. 7 and Fig. 8, it is found that, comparable to the ellipsoidal reflector, reflection on a hyperboloidal surface leads to output beams with nonuniformly-distributed rays. Output beam rim angles and axis rotation angles increase with larger input beam rim angles. Hyperboloidal surface curvatures decrease as eccentricity increases, which results in larger output beam rim angles. For a defined source, output beams with smaller rim angles can be obtained by selecting smaller hyperboloid eccentricities and placing the hyperboloidal reflector with a tilt angle close to  $180^\circ$ . For  $\alpha_h = 180^\circ$ , the hyperboloidal surface near the vertex with the largest curvature is used as the reflector. A typical solar beam down system with a hyperboloidal reflector is equivalent to the optical configuration in Fig. 7(f). A larger axis rotation angle for larger system component clearance can be achieved via selecting hyperboloids with a smaller tilt angle or a larger eccentricity. Compared to the ellipsoidal reflector, the hyperboloidal reflector renders a larger range of axis rotation angles, where output beams can be located at either side of the hyperbola real axis as input beam, i.e.  $\beta_h > 90^\circ$  is possible.

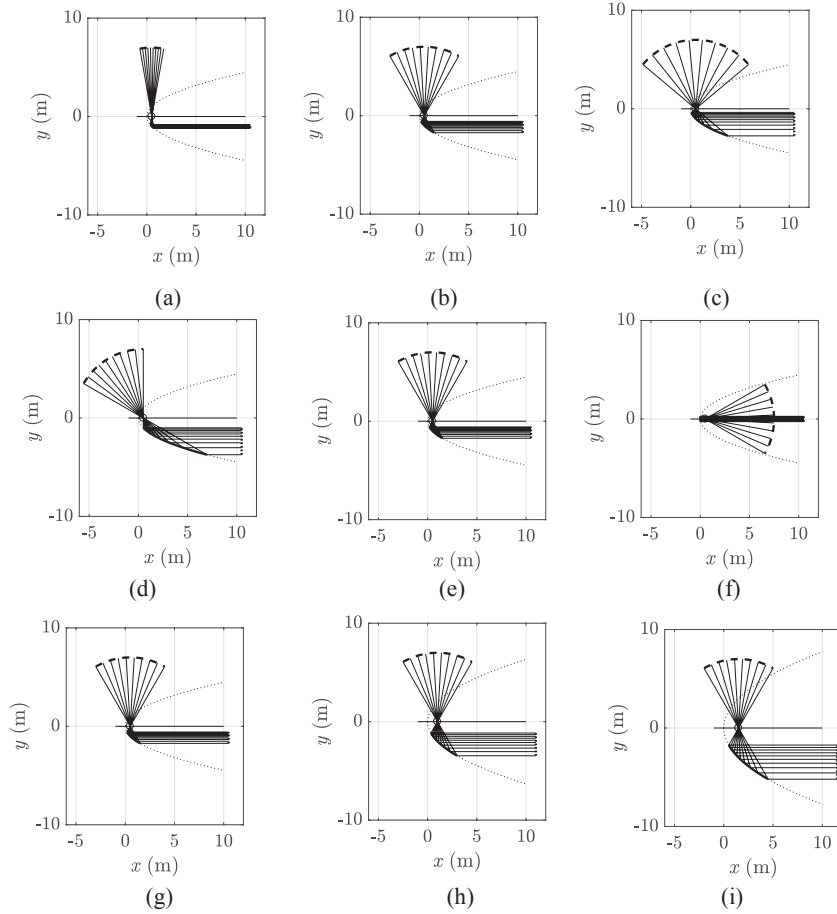


Fig. 9. Change of ray paths with (a–c): input beam rim angle  $\Phi_1$  of (a)  $10^\circ$ , (b)  $30^\circ$ , (c)  $50^\circ$ ; (d–f): paraboloid tilt angle  $\alpha_p$  of (d)  $60^\circ$ , (e)  $90^\circ$ , (f)  $180^\circ$ ; (g–i): paraboloid semi-focal chord  $p_p$  of (g) 1, (h) 2, (i) 3, for the baseline parameter set of Table 2.

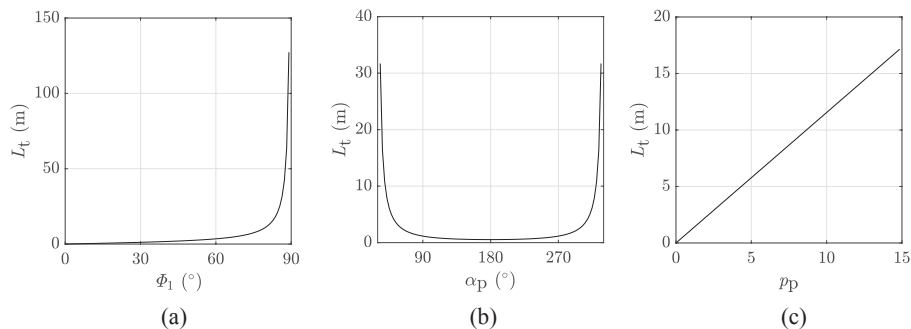


Fig. 10. Effects of input beam rim angle  $\Phi_1$ , paraboloid tilt angle  $\alpha_p$ , and paraboloid semi-focal chord  $p_p$ , on output beam width  $L_t$ , for the baseline parameter set of Table 2.

3.1.4. Paraboloidal reflector

According to Fig. 9 and Fig. 10, the output beam width increases with paraboloid semi-focal chord. A minimum output beam width is observed for a paraboloid tilt angle of  $180^\circ$  when the part of the paraboloidal surface near the vertex with the largest curvatures is used as the reflector, e.g. in a solar dish system (Fig. 9f). A desired beam width can be achieved by designing the paraboloid tilt angle and semi-focal chord as shown in Fig. 10(b, c). The collimated output beam

results in a larger spot on the target aperture and a higher spillage loss than focused output beams.

High radiative flux can be achieved by using a part of the curved reflector surface with the largest curvature for a better concentrating effect, however, at the expense of a severely reduced clearance between the input and output beams (Fig. 5f, Fig. 7f, Fig. 9f).

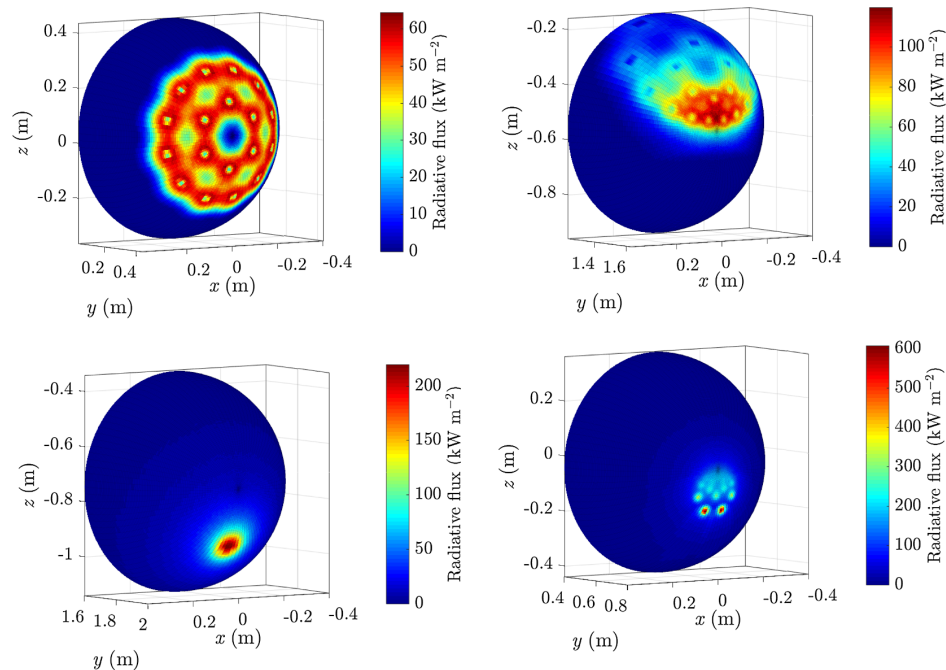


Fig. 11. Radiative flux distribution on a hemispherical target in the optical systems involving (a) a flat reflector (horizontal displacement,  $d_f$ , of 0.035 m from  $F_1$ ), (b) an ellipsoidal reflector ( $e_e = 0.6$ ,  $\alpha_e = 65^\circ$ ,  $c_e = 0.33$  m), (c) a hyperboloidal reflector ( $e_h = 1.05$ ,  $\alpha_h = 65^\circ$ ,  $c_h = 0.44$  m), and (d) a paraboloidal reflector ( $p_p = 0.1$  m), working in tandem with the ANU high-flux solar simulator.

### 3.2. Model system II: High-flux solar simulator as radiation source

To illustrate a practical application of the findings presented in Section 3.1, the discussed four types of the beam-redirecting reflector are investigated in an optical system with a solar simulator as a radiation source. Different from the model system I, which includes no optical imperfections, optical errors of the solar simulator primary reflectors and redirecting reflectors are included in the model system II. Besides, the radiation arc lamps have a finite size and are not an ideal point radiation source. As a result, a fraction of the emitted radiation from the solar simulator lamps misses the focal point  $F_1$  of the input beam. For curved reflectors, the distance between the focal point  $F_1$  of the input beam and the reflector vertex closest to  $F_1$  is too small, resulting in a large number of rays missing the truncated reflector surface. Therefore, the distance between one focus and the closest reflector vertex, calculated as  $a_e - c_e (= c_e(1/e_e - 1))$ ,  $c_h - a_h (= c_h(1 - 1/e_h))$ , and  $p_p/2$  for ellipsoidal, hyperboloidal, and paraboloidal reflectors, respectively, influences the reflector optical efficiency for any actual radiation sources with optical imperfections. When the linear eccentricity  $c$  is fixed, reflector optical efficiency increases with a decreasing eccentricity of an ellipsoidal reflector, increases with an increasing eccentricity of a hyperboloidal reflector, and increases with an increasing semi-focal chord length of a paraboloidal reflector.

The tilt angles of the reflectors relative to the central axis of the input beam from the solar simulator are taken as following: the flat reflector is tilted at an angle  $\alpha_f = 45^\circ$ , giving an output beam with a vertical axis; the ellipsoid and hyperboloid reflectors are tilted at an angle  $\alpha_e = \alpha_h = 65^\circ$ ; the paraboloidal reflector has a vertical axis ( $\alpha_p = 90^\circ$ ), giving an output beam with a vertical axis. Fig. 11 shows the MCRT results of radiative flux distributions on a hemispherical target with exemplary, non-optimized parameter values. Fig. 12 shows the path of rays in an optical system with an input beam of a same rim angle  $45^\circ$  as the solar simulator and a smaller focal length of 0.5 m that does not affect ray directionality. It is concluded that:

- (1) For the flat reflector, with a reflector tilt angle  $\alpha_f = 45^\circ$ , the output beam will have a vertical axis, i.e. the axis rotation angle is  $\beta = 90^\circ$ . The other design parameter, the distance between the input beam focal point and the flat reflector,  $d_f$ , determines the clearance between system components. The distance between the reflected image and the reflector increases as the flat reflector is placed closer to the solar simulator, i.e.  $d_f$  increases. However, the output beam focal point  $F_2$  gets closer to the upper edge of the input beam as  $d_f$  increases. For a receiver placed with its aperture center at the output beam focal point  $F_2$ , a fraction of rays emitted from the upper part of the solar simulator are more likely to be blocked by the receiver external surface, and the fraction of blocked rays increases with increasing  $d_f$ . Besides, a fraction of rays emitted from the bottom part of the solar simulator may miss the flat reflector (Fig. 12a) and the fraction of lost rays increases with increasing  $d_f$ .
- (2) The reflection on ellipsoidal and hyperboloidal reflectors changes the ray distribution substantially. Higher peak fluxes are observed on the hemispherical target for the curved reflectors than for the flat reflector. For both ellipsoidal and hyperboloidal reflectors, a higher reflector optical efficiency can be obtained by choosing a larger linear eccentricity  $c$ , also resulting in a larger distance between the focal points of the input and output beams. However, the increasing linear eccentricity increases the size of the reflected image, resulting in a decreased target optical efficiency. Hence, an optimal linear eccentricity can be identified that offers the maximum system optical efficiency. The reflector optical efficiency is also influenced by the eccentricity  $e$  of the ellipsoid and hyperboloid. A smaller ellipsoid eccentricity gives a higher reflector optical efficiency, but leads to a decreased clearance between system components, as indicated in Fig. 6(f). For a hyperboloidal reflector, both the reflector optical efficiency and the clearance between system components increase with a larger eccentricity as indicated in Fig. 8(f). However, the ratio of rays that intersect the backside of the hyperboloidal surface increases with a larger eccentricity.

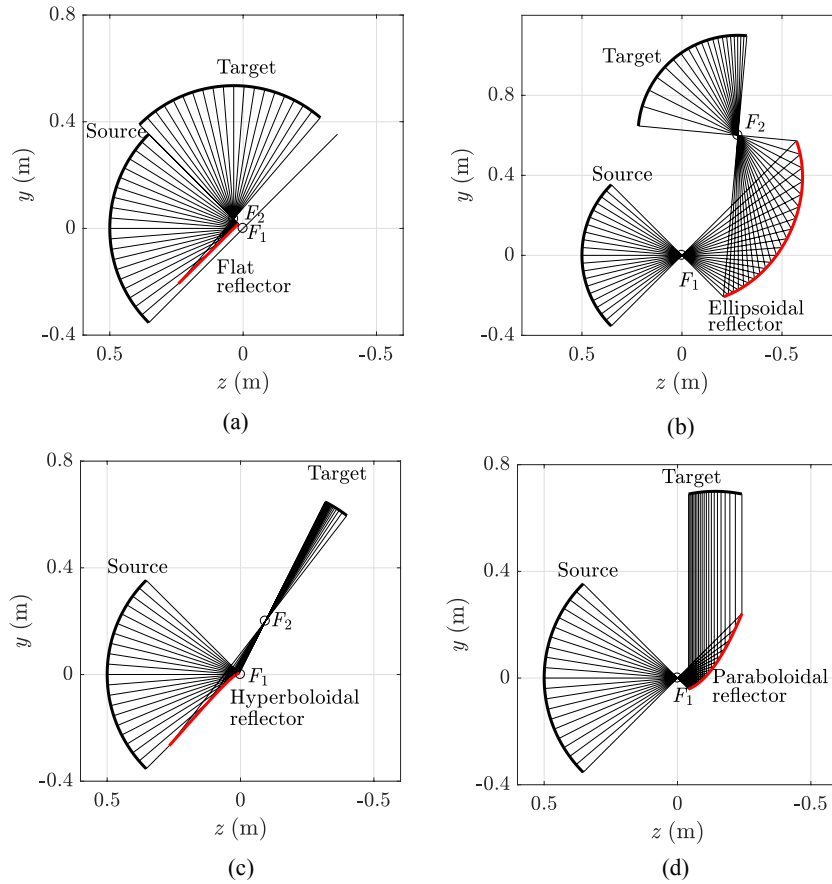


Fig. 12. Paths of rays for the optical system consisting of an input beam of rim angle  $45^\circ$  and focal length 0.5 m emitted from a spherical cap, a hemispherical target of radius 0.5 m, and (a) a flat reflector ( $d_r = 0.035$  m), (b) an ellipsoidal reflector ( $e_e = 0.6$ ,  $\alpha_e = 65^\circ$ ,  $c_e = 0.33$  m), (c) a hyperboloidal reflector ( $e_h = 1.04$ ,  $\alpha_h = 65^\circ$ ,  $c_h = 0.11$  m), and (d) a paraboloidal reflector ( $p_p = 0.1$  m).

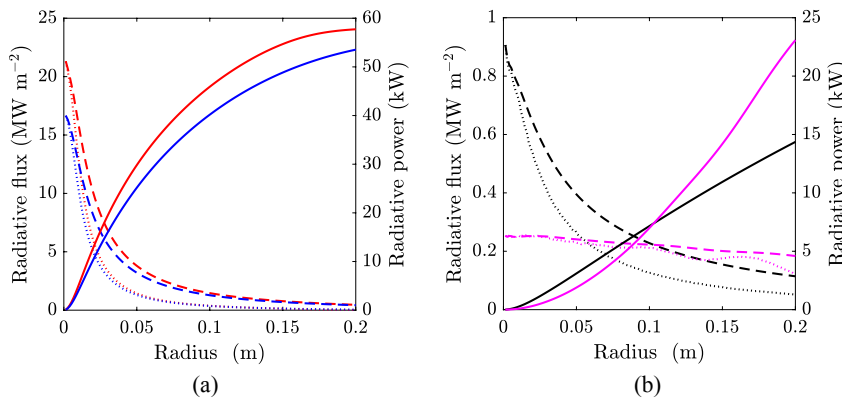


Fig. 13. Local radiative flux (dotted curves), mean radiative flux (dashed curves), and cumulative radiative power (solid curves) as functions of the radial coordinate measured from the center of the target plane, for the flat (red), ellipsoidal (blue), hyperboloidal (black) and paraboloidal (magenta) reflectors. (For interpretation of the references to colour in this figure legend, the reader is referred to the web version of this article.)

Table 3  
Total captured radiative power, peak flux and system optical efficiency for the four types of reflectors.

Optical characteristics	Unit	Flat reflector	Ellipsoidal reflector	Hyperboloidal reflector	Paraboloidal reflector
Captured power	kW	14.43	13.39	3.59	7.87
Peak flux	$\text{MW m}^{-2}$	21.31	16.66	9.07	0.45
System optical efficiency	-	0.97	0.9	0.24	0.53



**Table 4**  
Summary of beam-redirecting reflector features.

Reflector	Features
Flat	<ul style="list-style-type: none"> <li>o Output beam is convergent;</li> <li>o Input beam rim angle and ray distribution are retained;</li> <li>+ System optical efficiency is the highest among all;</li> <li>– Clearance between system components is small.</li> </ul>
Ellipsoidal	<ul style="list-style-type: none"> <li>o Output beam is convergent;</li> <li>o Characteristic of beam ray distribution is changed after the reflection;</li> <li>+ Required clearance between system components can be satisfied;</li> <li>+ A larger range of selections of output beam rim angle are enabled;</li> <li>– Additional optical loss may result from rays missing the reflector.</li> </ul>
Hyperboloidal	<ul style="list-style-type: none"> <li>o Output beam is convergent;</li> <li>o Characteristic of beam ray distribution is changed after the reflection;</li> <li>+ Required clearance between system components can be satisfied;</li> <li>+ The range of possible axis rotation angle is larger than the ellipsoidal reflector;</li> <li>– Additional optical loss may result from rays missing the reflector.</li> </ul>
Paraboloidal	<ul style="list-style-type: none"> <li>o Output beam is collimated;</li> <li>+ Required clearance between system components can be satisfied;</li> <li>– Additional optical loss may result from rays missing the reflector.</li> </ul>

Hence, an optimal hyperboloid eccentricity can be identified that offers the maximum reflector optical efficiency.

- (3) The highest peak flux on the hemispherical target surface is observed in the optical system involving a paraboloidal reflector, an effect which can be predicted based on the discussion of Section 2.1.4. A larger semi-focal chord results in reduced target optical efficiency due to increased reflected image size and increased reflector efficiency as stated in Section 2.2. Hence, an optimal value of paraboloid semi-focal chord can be identified that gives the maximum system optical efficiency.

The radial distribution of the radiative flux and the cumulative power on the flat target of radius 0.1 m are reported in Fig. 13 and Table 3, for the four types of beam-redirecting reflectors. For the systems with the flat, ellipsoidal, and hyperboloidal reflectors, the flat target plane is positioned horizontally with its center at the focal point of the output beam. For the system with the paraboloidal reflector, the flat target plane is positioned horizontally with a vertical distance of 0.4 m to the HFSS focal point. For the paraboloidal reflector, the resulting radiative flux on the target plane is relatively low and more uniformly distributed. The simulated total emitted radiative power from the solar simulator is 14.9 kW. The highest radiative peak flux, captured power and system optical efficiency are obtained with the flat reflector, followed by the ellipsoidal, paraboloidal, and hyperboloidal reflectors. System optical efficiency is lower for the systems with the curved reflectors instead of the flat reflector. With optimization, an ellipsoidal reflector can allow for a system optical efficiency close to that of the flat reflector. System optical efficiency for using the hyperboloidal reflector can be improved by designing the output beam focal point  $F_2$  placed at the side closer to the solar simulator (i.e.  $\alpha_h > 90^\circ$ ). However, it potentially reduces distances between the system components. Table 4 summarizes concluded features of these four types of reflectors.

#### 4. Summary and conclusions

Optical characteristics of beam-redirecting optical systems involving flat, ellipsoidal, hyperboloidal and paraboloidal reflectors have been investigated for concentrating solar systems with convergent radiative beams. Two selected types of radiation sources have been discussed: a generic uniformly-emitting spherical cap source and a high-flux solar simulator. Two-dimensional ray-tracing simulations have been performed for an ideal optical system without optical imperfection that consists of the generic spherical cap source, the investigated reflectors and the target tailored to capture all the radiation. Three-dimensional Monte-Carlo ray-tracing simulations have been performed

for a realistic multi-source high-flux solar simulator working in tandem with the four types of beam-redirecting reflectors. Evaluated characteristics include radiative power, spatial and directional flux distribution, system optical efficiency (throughput) and resulting distances between the source, the reflector and the reflected image.

The four types of the investigated beam-redirecting reflectors redirect a horizontal-axis beam from a solar simulator onto non-horizontal axis targets. The flat reflector retains the characteristics of the rim angle and ray distribution of the input beam and enables the highest system optical efficiency at the expense of the smallest clearance between the source, the reflector and the reflected image. Distances between the system components increase with a decreasing rim angle of the input beam. The investigated curved reflectors render a larger degree of freedom to design the characteristics of the output beam. Thus, the curved reflectors are suitable for applications that require large clearance between system components and/or high peak flux on a cavity surface, but at the expense of lower optical efficiency of the system.

#### Acknowledgements

The financial support from the Australian Renewable Energy Agency (grant no 2014/RND005) is gratefully acknowledged. The authors thank Mr Greg Burgess for the initial discussions of the beam-redirecting optical systems.

#### References

- Bader, R., Haussener, S., Lipiński, W., 2015. Optical design of multisource high-flux solar simulators. *J. Sol. Energy Eng.* 137 (2), 021012.
- Bader, R., Lipiński, W., 2017. Solar thermal processing. In: Blanco, M., Ramirez, Santigosa L. (Eds.), *Advances in Concentrating Solar Thermal Research and Technology*. Woodhead Publishing, pp. 403–447.
- Boubault, A., Yellowhair, J., Ho, C.K., 2015. Design and characterization of a 7.2 kW solar simulator. *Proc. ASME 2015 9th Int. Conf. Energy Sustainability*. ES2015-49472.
- Carrillo, A.J., González-Aguilar, J., Romero, M., Coronado, J.M., 2019. Solar energy on demand: a review on high temperature thermochemical heat storage systems and materials. *Chem. Rev.* 119, 4777–4816.
- Codd, D.S., Carlson, A., Rees, J., Slocum, A.H., 2010. A low cost high flux solar simulator. *Sol. Energy* 84, 2202–2212.
- Dähler, F., Wild, M., Schäppi, R., Haueter, P., Cooper, T., Good, P., Larrea, C., Schmitz, M., Furler, P., Steinfeld, A., 2018. Optical design and experimental characterization of a solar concentrating dish system for fuel production via thermochemical redox cycles. *Sol. Energy* 170, 568–575.
- Dong, X., Sun, Z., Nathan, G.J., Ashman, P.J., Gu, D., 2015. Time-resolved spectra of solar simulators employing metal halide and xenon arc lamps. *Sol. Energy* 115, 613–620.
- Ekman, B.M., Brooks, G., Akbar Rhamdhani, M., 2015. Development of high flux solar simulators for solar thermal research. *Sol. Energy Mater. Sol. Cells* 141, 436–446.
- Feuermann, D., Gordon, J.M., 1999. Solar fiber-optic mini-dishes: a new approach to the efficient collection of sunlight. *Sol. Energy* 65, 159–170.
- Gill, R., Bush, E., Haueter, P., Loutzenhiser, P., 2015. Characterization of a 6 kW high-flux



- solar simulator with an array of xenon arc lamps capable of concentrations of nearly 5000 suns. *Rev. Sci. Instrum.* 86, 125107.
- Hirsch, D., Zedtwitz, P.V., Osinga, T., Kinamore, J., Steinfeld, A., 2003. A new 75 kW high-flux solar simulator for high-temperature thermal and thermochemical research. *J. Sol. Energy Eng.* 125 (1), 117.
- Jin, J., Hao, Y., Jin, H., 2019. A universal solar simulator for focused and quasi-collimated beams. *Appl. Energy* 235, 1266–1276.
- Krueger, K.R., Davidson, J.H., Lipiński, W., 2011. Design of a new 45 kW<sub>e</sub> high-flux solar simulator for high-temperature solar thermal and thermochemical research. *J. Sol. Energy Eng.* 133 (1), 011013.
- Krueger, K.R., Lipiński, W., Davidson, J.H., 2013. Operational performance of the University of Minnesota 45 kW<sub>e</sub> high-flux solar simulator. *J. Sol. Energy Eng.* 135, 044501.
- Kuhn, P., Hunt, A., 1991. A new solar simulator to study high temperature solid-state reactions with highly concentrated radiation. *Sol. Energy Mater.* 24, 742–750.
- Levêque, G., Bader, R., Lipiński, W., Haussener, S., 2016. Experimental and numerical characterization of a new 45 kW<sub>e</sub> multisource high-flux solar simulator. *Opt. Express* 24 (22), A1360–A1373.
- Levêque, G., Bader, R., Lipiński, W., Haussener, S., 2017. High-flux optical systems for solar thermochemistry. *Sol. Energy* 156, 133–148.
- Li, L., Coventry, J., Bader, R., Pye, J., Lipiński, W., 2016. Optics of solar central receiver systems: a review. *Opt. Express* 24 (14), A985–A1007.
- Li, L., Wang, B., Pottas, J., Lipiński, W., 2019. Design of a compound parabolic concentrator for a multi-source high-flux solar simulator. *Sol. Energy* 183, 805–811.
- Lipiński, W., Steinfeld, A., 2006. Annular compound parabolic concentrator. *ASME J. Sol. Energy Eng.* 128, 121–124.
- Oliker, V., Newman, E., Prussner, L., 1993. Formula for computing illumination intensity in a mirror optical system. *J. Opt. Soc. Am.* 10 (9), 1895–1901.
- Petrasch, J., Coray, P., Meier, A., Brack, M., Häberling, P., Wüillemin, D., Steinfeld, A., 2007. A Novel 50 kW 11,000 suns high-flux solar simulator based on an array of xenon arc lamps. *J. Sol. Energy Eng.* 129 (4), 405–411.
- Sarwar, J., Georgakis, G., LaChance, R., Ozalp, N., 2014. Description and characterization of an adjustable flux solar simulator for solar thermal, thermochemical and photovoltaic applications. *Sol. Energy* 100, 179–194.
- Segal, A., Epstein, M., 1999. Comparative performances of “tower-top” and “tower-reflector” central solar receivers. *Sol. Energy* 65 (4), 207–226.
- Segal, A., Epstein, M., 2000. The optics of the solar tower reflector. *Sol. Energy* 69, 229–241.
- Wang, B., Wheeler, V.M., Pottas, J., Kreider, P.B., Lipiński, W., 2018. Thermal modelling of a solar thermochemical reactor for metal oxide reduction. In: *Proceedings of the 16th International Heat Transfer Conference*, pp. 7443–7449.
- Wang, J., Yang, S., Jiang, C., Yan, Q., Lund, P.D., 2017a. A novel 2-stage dish concentrator with improved optical performance for concentrating solar power plants. *Renew. Energy* 108, 92–97.
- Wang, W., Aichmayer, L., Garrido, J., Laumert, B., 2017b. Development of a Fresnel lens based high-flux solar simulator. *Sol. Energy* 144, 436–444.
- Wiegardt, K., Funken, K.-H., Dibowski, G., Hoffschmidt, B., Laaber, D., Hilger, P., Eßer, K.-P., 2016. Synlight—the world’s largest artificial sun. *AIP Conf. Proc.* 1734, 030038.
- Xu, J., Tang, C., Cheng, Y., Li, Z., Cao, H., Yu, X., Li, Y., Wang, Y., 2016. Design, construction, and characterization of an adjustable 70 kW high-flux solar simulator. *J. Sol. Energy Eng.* 138 (4), 041010.
- Yang, S., Wang, J., Lund, P.D., Jiang, C., Liu, D., 2018. Assessing the impact of optical errors in a novel 2-stage dish concentrator using Monte-Carlo ray-tracing simulation. *Renew. Energy* 123, 603–615.
- Yogev, A., Kribus, A., Epstein, M., Kogan, A., 1998. Solar “tower-reflector” systems: A new approach for high-temperature solar plants. *Int. J. Hydrogen Energy* 23 (4), 239–245.
- Zhang, Y., Xiao, G., Luo, Z., Ni, M., Yang, T., Xu, W., 2014. Comparison of different types of secondary reflectors for solar application. *Optik* 125, 1106–1112.



---

## Optics of solar central receiver systems: A review

---

Solar CRSs coupled with secondary concentrators are capable of simultaneously providing high concentration ratios and high power levels, and thus are considered for the high-temperature concentrating solar applications. This chapter presents a comprehensive review of optics of solar CRSs. It precedes the optical design studies presented in the next chapters. The following aspects are reviewed: (1) system configurations, (2) theoretical background including radiative transfer and performance metrics, (3) system classification, (4) optics of heliostats including heliostat classification, astigmatism, canting and focusing, tracking, and wind load, (5) optics of heliostat fields including field classification, layout generation, and optimisation, (6) optical modelling methodology and tools, and (7) on-sun demonstration-level and commercial-scale CRSs.

## Optics of solar central receiver systems: a review

Lifeng Li, Joe Coventry, Roman Bader, John Pye, and Wojciech Lipiński\*

Research School of Engineering, The Australian National University, Canberra, ACT 2601, Australia

\*wojciech.lipinski@anu.edu.au

**Abstract:** This article reviews the state of the art in optical design, modeling and characterization of solar central receiver systems.

©2016 Optical Society of America

**OCIS codes:** (350.6050) Solar energy; (350.5610) Radiation; (220.1770) Concentrators; (230.4040) Mirrors; (350.4600) Optical engineering.

### References and links

1. V. A. Baum, R. R. Aparasi, and B. A. Garf, "High-power solar installations," *Sol. Energy* **1**(1), 6–12 (1957).
2. G. Francia, "Pilot plants of solar steam generating stations," *Sol. Energy* **12**(1), 51–64 (1968).
3. P. K. Falcone, "A handbook for solar central receiver design," Technical Report, SAND86–8009 (Sandia National Laboratories, 1986).
4. M. Romero, R. Buck, and J. E. Pacheco, "An update on solar central receiver systems, projects, and technologies," *J. Sol. Energy Eng.* **124**(2), 98–108 (2002).
5. O. Behar, A. Khellaf, and K. Mohammadi, "A review of studies on central receiver solar thermal power plants," *Renew. Sustain. Energy Rev.* **23**, 12–39 (2013).
6. T. M. Pavlović, I. S. Radonjić, D. D. Milosavljević, and L. S. Pantić, "A review of concentrating solar power plants in the world and their potential use in Serbia," *Renew. Sustain. Energy Rev.* **16**(6), 3891–3902 (2012).
7. H. L. Zhang, J. Baeyens, J. Degève, and G. Cacères, "Concentrated solar power plants: Review and design methodology," *Renew. Sustain. Energy Rev.* **22**, 466–481 (2013).
8. R. Buck, "Heliostat field layout using non-restricted optimization," in *Proceedings of the 18th SolarPACES Int. Symposium on Concentrating Solar Power and Chemical Energy Marrakech, Morocco, 2012*, pp. 11–24.
9. A. Steinfeld and R. Palumbo, "Solar thermochemical process technology," in *Encyclopedia of Physical Science and Technology*, Vol. 15 (Academic Press, 2001), pp. 237–256.
10. G. Flamant, A. Ferriere, D. Laplace, and C. Monty, "Solar processing of materials: Opportunities and new frontiers," *Sol. Energy* **66**(2), 117–132 (1999).
11. K. Lovegrove and W. Stein, eds., *Concentrating Solar Power Technology: Principles, Developments and Applications* (Elsevier, 2012).
12. M. F. Modest, *Radiative Heat Transfer* (Academic Press, 2013), 3rd edition.
13. C. A. Gueymard, D. Myers, and K. Emery, "Proposed reference irradiance spectra for solar energy systems testing," *Sol. Energy* **73**(6), 443–467 (2002).
14. C. A. Gueymard, "The sun's total and spectral irradiance for solar energy applications and solar radiation models," *Sol. Energy* **76**(4), 423–453 (2004).
15. G. P. Kuiper, editor, *The Photosphere, The Sun, The Solar System I* (University of Chicago Press, 1953).
16. C. N. Vittitoe and F. Biggs, "Six-gaussian representation of the angular-brightness distribution for solar radiation," *Sol. Energy* **27**(6), 469–490 (1981).
17. A. Rabl and P. Bendt, "Effect of circumsolar radiation on performance of focusing collectors," *J. Sol. Energy Eng.* **104**(3), 237–250 (1982).
18. D. Buie, A. Monger, and C. Dey, "Sunshape distributions for terrestrial solar simulations," *Sol. Energy* **74**(2), 113–122 (2003).
19. F. E. Nicodemus, "Directional reflectance and emissivity of an opaque surface," *Appl. Opt.* **4**(7), 767–775 (1965).
20. K. E. Torrance and E. M. Sparrow, "Theory for off-specular reflection from roughened surfaces," *J. Opt. Soc. Am.* **57**(9), 1105–1114 (1967).
21. R. M. Goody and Y. L. Yung, *Atmospheric Radiation* (Oxford University Press, 1989), 2nd edition.
22. V. V. Rozanov, A. V. Rozanov, A. A. Kokhanovsky, and J. P. Burrows, "Radiative transfer through terrestrial atmosphere and ocean: Software package SCIATRAN," *J. Quant. Spectrosc. Ra.* **133**, 13–71 (2014).
23. K. Lovegrove and J. Pye, "Fundamental principles of concentrating solar power (CSP) systems," in *Concentrating Solar Power Technology: Principles, Developments and Applications*, K. Lovegrove and W. Stein, eds. (Elsevier, 2012).
24. L. L. Vant-Hull, "Concentrator optics," in *Solar Thermal Power Plants: Fundamentals, Technology, Systems, Economics*, C.-J. Winter, R. L. Sizmann, L. L. Vant-Hull, eds. (Springer-Verlag, 1991).
25. J. A. Duffie and W. A. Beckman, *Solar Engineering of Thermal Processes* (Wiley, 1980).
26. F. Rinaldi, M. Binotti, A. Giostri, and G. Manzolini, "Comparison of linear and point focus collectors in solar power plants," *Energy Procedia* **49**, 1491–1500 (2014).

27. A. Rabl, "Comparison of solar concentrators," *Sol. Energy* **18**(2), 93–111 (1976).
28. S. A. Kalogirou, "Solar thermal collectors and applications," *Prog. Energy. Combust* **30**(3), 231–295 (2004).
29. E. A. Fletcher and R. L. Moen, "Hydrogen- and oxygen from water," *Science* **197**(4308), 1050–1056 (1977).
30. M. S. Mehos, "Part 3: Status report Task I: Solar thermal electric systems," in IEA SolarPACES IA Annual Report 2006 (German Aerospace Center DLR, 2007).
31. M. Schmitz, P. Schwarzbözl, R. Buck, and R. Pitz-Paál, "Assessment of the potential improvement due to multiple apertures in central receiver systems with secondary concentrators," *Sol. Energy* **80**(1), 111–120 (2006).
32. A. Segal and M. Epstein, "Comparative performances of 'tower-top' and 'tower-reflector' central solar receivers," *Sol. Energy* **65**(4), 207–226 (1999).
33. P. Schramek and D. R. Mills, "Multi-tower solar array," *Sol. Energy* **75**(3), 249–260 (2003).
34. A. Yogev, A. Kribus, M. Epstein, and A. Kogan, "Solar tower reflector systems: a new approach for high-temperature solar plants," *Int. J. Hydrogen Energy* **23**(4), 239–245 (1998).
35. R. N. Wilson, *Reflecting Telescope Optics I*, 2<sup>nd</sup> edition (Springer, 2004).
36. L. L. Vant-Hull, "Issues with beam-down concepts," *Energy Procedia* **49**, 257–264 (2014).
37. A. L. Ávila-Marín, "Volumetric receivers in solar thermal power plants with central receiver system technology: A review," *Sol. Energy* **85**(5), 891–910 (2011).
38. C. K. Ho and B. D. Iverson, "Review of high-temperature central receiver designs for concentrating solar power," *Renew. Sustain. Energy Rev.* **29**, 835–846 (2014).
39. C. S. P. World, [www.cspworld.org/cspworldmap](http://www.cspworld.org/cspworldmap). Last retrieved on 21 January 2016.
40. NREL, "Concentrating Solar Power projects," [www.nrel.gov/csp/solarpaces/](http://www.nrel.gov/csp/solarpaces/). Last retrieved on 21 January 2016.
41. A. Segal and M. Epstein, "Modeling of solar receiver for cracking of liquid petroleum gas," *J. Sol. Energy Eng.* **119**(1), 48–51 (1997).
42. W. T. Welford and R. Winston, *High Collection Nonimaging Optics* (Academic Press, 1989).
43. A. Kribus, V. Krupkin, A. Yogev, and W. Spirkel, "Performance limits of heliostat fields," *J. Sol. Energy Eng.* **120**(4), 240–246 (1998).
44. W. Lipiński and A. Steinfeld, "Annular compound parabolic concentrator," *J. Sol. Energy Eng.* **128**(1), 121–124 (2006).
45. A. Kribus, M. Huleihil, A. Timinger, and R. Ben-Mair, "Performance of a rectangular secondary concentrator with an asymmetric heliostat field," *Sol. Energy* **69**(2), 139–151 (2000).
46. S. Schell, "Design and evaluation of eSolar's heliostat fields," *Sol. Energy* **85**(4), 614–619 (2011).
47. G. Weinrebe, M. Schmitz-Goeb, and W. Schiel, "On the performance of the ASM 150 stressed membrane heliostat," in Proceedings of the ASME Int. Solar Energy Conference, San Antonio, USA, 1996.
48. W. Bender, "Final technical progress report: Development of low-cost suspension heliostat," Technical Report, NREL/SR-5200–57611 National Renewable Energy Laboratory (Colorado, USA 2013).
49. Schlaich Bergermann und Partner, <http://www.sbp.de/en/themes/stellio-heliostat-the-state-of-the-art-concentrating-solar-power-csp/>. Last retrieved on April 23, 2016.
50. J. Coventry, M. Arjomandi, J. Barry, M. Blanco, G. Burgess, J. Campbell, P. Connor, M. Emes, P. Fairman, D. Farrant, F. Ghanadi, V. Grigoriev, C. Hall, P. Koltun, D. Lewis, S. Martin, G. Nathan, J. Pye, A. Qiu, W. Stuart, Y. Tang, F. Venn, and J. Yu, "Development of the ASTRI heliostat," in Proceedings of the 21st SolarPACES Int. Symposium on Concentrating Solar Power and Chemical Energy, Cape Town, South Africa, 2015.
51. L. L. Vant-Hull, "Central tower concentrating solar power (CSP) systems," in *Concentrating Solar Power Technology: Principles, Developments and Applications*, K. Lovegrove and W. Stein, eds. (Woodhead Publishing Limited, 2012).
52. K. R. Bhargava, F. Gross, and P. Schramek, "Life cycle cost optimized heliostat size for power towers," *Energy Procedia* **49**, 40–49 (2014).
53. J. Coventry and J. Pye, "Heliostat cost reduction—where to now?" *Energy Procedia* **49**, 60–70 (2014).
54. A. Pfahl, "Survey of heliostat concepts for cost reduction," *J. Sol. Energy Eng.* **136**(1), 014501 (2013).
55. F. Biggs and C. N. Vittitoe, "HELIOS: A computational model for solar concentrators," Technical Report, SAND77–1185C (Sandia National Laboratories, 1977).
56. E. A. Igel and R. L. Hughes, "Optical analysis of solar facility heliostats," *Sol. Energy* **22**(3), 283–295 (1979).
57. Y. T. Chen, K. K. Chong, T. P. Bligh, L. C. Chen, J. Yunus, K. S. Kannan, B. H. Lim, C. S. Lim, M. A. Alias, N. Bdi, O. Aliman, S. Salehan, S. A. H. Sheikh Abdul Rezan, C. M. Tam, and K. K. Tan, "Non-imaging, focusing heliostat," *Sol. Energy* **71**(3), 155–164 (2001).
58. Y. T. Chen, C. S. Lim, T. H. Ho, B. H. Lim, and Y. N. Wang, "Off-axis aberration correction surface in solar energy application," *Sol. Energy* **80**(3), 268–271 (2006).
59. K. K. Chong, "Optimization of nonimaging focusing heliostat in dynamic correction of astigmatism for a wide range of incident angles," *Opt. Lett.* **35**(10), 1614–1616 (2010).
60. K. K. Chong, "Optical analysis for simplified astigmatic correction of non-imaging focusing heliostat," *Sol. Energy* **84**(8), 1356–1365 (2010).
61. A. Grobler and P. Gauché, "A review of aiming strategies for central receivers," in Proceedings of the second Southern African Solar Energy Conference, Port Elizabeth, South Africa, 2014.
62. A. Salomé, F. Chhel, G. Flamant, A. Ferrière, and F. Thiery, "Control of the flux distribution on a solar tower receiver using an optimized aiming point strategy: Application to THEMIS solar tower," *Sol. Energy* **94**, 352–366 (2013).

63. R. Buck and E. Teufel, "Comparison and optimization of heliostat canting methods," *J. Sol. Energy Eng.* **131**(1), 011001 (2009).
64. S. A. Jones, "A comparison of on-axis and off-axis heliostat alignment strategies," Technical Report, SAND96-0566C (Sandia National Laboratories, 1996).
65. J. Yellowhair and C. K. Ho, "Heliostat canting and focusing methods: an overview and comparison," in *Proceedings of ASME 2010 4th Int. Conference on Energy Sustainability*, Phoenix, Arizona, USA, 2010, pp. 609–615.
66. L. Ren, X. Wei, Z. Lu, W. Yu, W. Xu, and Z. Shen, "A review of available methods for the alignment of mirror facets of solar concentrator in solar thermal power system," *Renew. Sustain. Energy Rev.* **32**, 76–83 (2014).
67. J. Yellowhair, K. Chavez, and E. Sproul, "Canting of heliostat facets using a target in reflection," Technical Report, SAND2010-5413C (Sandia National Laboratories, 2008).
68. A. Segal and M. Epstein, "Method for canting tower reflector facets," in *Proceedings of the 14th SolarPACES Int. Symposium on Concentrating Solar Power and Chemical Energy*, Las Vegas, USA 2008.
69. D. G. Brown and K. W. Stone, "High accuracy/low cost tracking system for solar concentrators using a neural network," in *Proceedings of the 28th Intersociety Energy Conversion Engineering Conference*, Atlanta, USA, 1993.
70. C. Y. Lee, P. C. Chou, C. M. Chiang, and C. F. Lin, "Sun tracking systems: a review," *Sensors (Basel)* **9**(5), 3875–3890 (2009).
71. H. Mousazadeh, A. Keyhani, A. Javadi, H. Mobli, K. Abrinia, and A. Sharifi, "A review of principle and sun-tracking methods for maximizing solar systems output," *Renew. Sustain. Energy Rev.* **13**(8), 1800–1818 (2009).
72. H. Ries and M. Schubnell, "The optics of a two stage solar furnace," *Sol. Energy Mater.* **21**(2–3), 213–217 (1990).
73. R. Zaibel, E. Dagan, J. Karni, and H. Ries, "An astigmatic corrected target aligned heliostat for high concentration," *Sol. Energy Mater. Sol. Cells* **37**(2), 191–202 (1995).
74. Y. Chen, A. Kribus, B. Lim, C. Lim, K. Chong, J. Karni, R. Buck, A. Pfahl, and T. Blich, "Comparison of two sun tracking methods in the application of a heliostat field," *J. Sol. Energy Eng.* **126**(1), 638–644 (2004).
75. K.-K. Chong and M. H. Tan, "Comparison study of two different sun-tracking methods in optical efficiency of heliostat field," *Int. J. Photoenergy* **2012**, 908364 (2012).
76. S. Khalsa, C. K. Ho, and C. Andraka, "An automated method to correct heliostat tracking errors," in *Proceedings of the 17th SolarPACES Int. Symposium on Concentrating Solar Power and Chemical Energy*, Granada, Spain, 2011.
77. E. Smith and C. K. Ho, "Field demonstration of an automated heliostat tracking correction method," *Energy Procedia* **49**, 2201–2210 (2014).
78. R. Flesch, B. Belhomme, N. Ahlbrink, and R. Pitz-Paal, "Automatic determination of heliostat orientation using an auxiliary mirror," in *Proceedings of the 18th SolarPACES Int. Symposium on Concentrating Solar Power and Chemical Energy*, Marrakech, Morocco, 2012.
79. H. Sun, B. Gong, and Q. Yao, "A review of wind loads on heliostats and trough collectors," *Renew. Sustain. Energy Rev.* **32**, 206–221 (2014).
80. C. C. Zang, J. M. Christian, J. K. Yuan, J. Sment, A. C. Moya, C. K. Ho, and Z. F. Wang, "Numerical simulation of wind loads and wind induced dynamic response of heliostats," *Energy Procedia* **49**, 1582–1591 (2014).
81. J. W. Strachan and R. M. Houser, "Testing and evaluation of large-area heliostats for solar thermal applications," Technical Report, SAND92-1381 (Sandia National Laboratories, 1993).
82. F. Lipps and L. Vant-Hull, "A cellwise method for the optimization of large central receiver systems," *Sol. Energy* **20**(6), 505–516 (1978).
83. C. J. Noone, M. Torrilhon, and A. Mitsos, "Heliostat field optimization: A new computationally efficient model and biomimetic layout," *Sol. Energy* **86**(2), 792–803 (2012).
84. F. Siala and M. Elayeb, "Mathematical formulation of a graphical method for a no-blocking heliostat field layout," *Renew. Energy* **23**(1), 77–92 (2001).
85. M. Sánchez and M. Romero, "Methodology for generation of heliostat field layout in central receiver systems based on yearly normalized energy surfaces," *Sol. Energy* **80**(7), 861–874 (2006).
86. F. J. Collado, "Preliminary design of surrounding heliostat fields," *Renew. Energy* **34**(5), 1359–1363 (2009).
87. F. J. Collado and J. Guallar, "Campo: Generation of regular heliostat fields," *Renew. Energy* **46**, 49–59 (2012).
88. X. Wei, Z. Lu, Z. Wang, W. Yu, H. Zhang, and Z. Yao, "A new method for the design of the heliostat field layout for solar tower power plant," *Renew. Energy* **35**(9), 1970–1975 (2010).
89. R. Pitz-Paal, N. B. Botero, and A. Steinfeld, "Heliostat field layout optimization for high-temperature solar thermochemical processing," *Sol. Energy* **85**(2), 334–343 (2011).
90. S. M. Besarati and D. Y. Goswami, "A computationally efficient method for the design of the heliostat field for solar power tower plant," *Renew. Energy* **69**, 226–232 (2014).
91. X. Wei, Z. Lu, Z. Lin, H. Zhang, and Z. Ni, "Optimization procedure for design of heliostat field layout of a 1 MWe solar tower thermal power plant," *Proc. SPIE* **6841**, 684119 (2007).
92. L. Pisani, M. Cogoni, B. D'Aguzzo, and E. Leonardi, "Optimization of heliostat fields for solar tower systems," in *Proceedings of the 18th SolarPACES Int. Symposium on Concentrating Solar Power and Chemical Energy*, Perpignan, Morocco, 2012.
93. M. T. Dunham, R. Kasetty, A. Mathur, and W. Lipiński, "Optical analysis of a heliostat array with linked tracking," *J. Sol. Energy Eng.* **135**(3), 034501 (2013).

94. M. Atif and F. A. Al-Sulaiman, "Optimization of heliostat field layout in solar central receiver systems on annual basis using differential evolution algorithm," *Energy Convers. Manage.* **95**, 1–9 (2015).
95. A. Mutuberría, J. Pascual, M. Guisado, and F. Mallor, "Comparison of heliostat field layout design methodologies and impact on power plant efficiency," presented in the 20th SolarPACES Int. Symposium on Concentrating Solar Power and Chemical Energy, Beijing, China, 2014.
96. C.-A. Asselineau, J. Zapata, and J. Pye, "Integration of Monte-Carlo ray tracing with a stochastic optimisation method: application to the design of solar receiver geometry," *Opt. Express* **23**(11), A437–A443 (2015).
97. J. R. Howell, "The Monte Carlo method in radiative heat transfer," *J. Heat Transfer* **120**(3), 547–560 (1998).
98. J. T. Farmer and J. R. Howell, "Comparison of Monte Carlo strategies for radiative transfer in participating media," *Adv. Heat Transf.* **31**, 333–429 (1998).
99. T. A. Dellin and M. J. Fish, "User's manual for DELSOL: A computer code for calculating the optical performance, field layout and optimal system design for solar central receiver plants," Technical Report, SAND79–8215 (Sandia National Laboratories, 1979).
100. B. L. Kistler, "A user's manual for DELSOL3: a computer code for calculating the optical performance and optimal system design for solar thermal central receiver plants," Technical Report, SAND86–8018 (Sandia National Laboratories, 1986).
101. P. Schwarzbözl, R. Pitz-Paal, and M. Schmitz, "Visual HFLCAL—A software tool for layout and optimisation of heliostat fields," in Proceedings of the 15th SolarPACES Int. Symposium on Concentrating Solar Power and Chemical Energy, Berlin, Germany, 2009.
102. P. L. Leary and J. D. Hankins, "Users guide for MIRVAL: a computer code for comparing designs of heliostat-receiver optics for central receiver solar power plants," Technical Report, SAND77–8280 (Sandia National Laboratories, 1977).
103. T. Wendelin, "SolTRACE: a new optical modeling tool for concentrating solar optics," in Proceedings of the ISEC 2003: International Solar Energy Conference, New York, USA, 2003, pp. 253–260.
104. P. García, A. Ferriere, and J. J. Bezan, "Codes for solar flux calculation dedicated to central receiver system applications: A comparative review," *Sol. Energy* **82**(3), 189–197 (2008).
105. C. K. Ho, "Software and codes for analysis of concentrating solar power technologies," Technical Report, SAND2008–8053 (Sandia National Laboratories, 2008).
106. J. Bode and P. Gauché, "Review of optical software for use in concentrating solar power systems," in Proceedings of South African Solar Energy Conference, Stellenbosch, South Africa, 2012.
107. J. Yellowhair, J. D. Ortega, J. M. Christian, and C. K. Ho, "Solar optical codes evaluation for modeling and analyzing complex solar receiver geometries," *Proc. SPIE* **9191**, 91910M (2014).
108. P. A. C. E. S. Solar, <http://solarpaces.org/library>. Last retrieved on 21 January 2016.
109. Wikipedia, "List of solar thermal power stations," [https://en.wikipedia.org/wiki/List\\_of\\_solar\\_thermal\\_power\\_stations](https://en.wikipedia.org/wiki/List_of_solar_thermal_power_stations). Last retrieved on 21 January 2016.
110. F. Sun, Z. Wang, M. Guo, Q. Yu, and F. Bai, "Optical performance of a heliostat in the DAHAN solar power plant," *Energy Procedia* **49**, 239–248 (2014).
111. H.-J. Lee, J.-K. Kim, S.-N. Lee, H.-K. Yoon, Y.-H. Kang, and M.-H. Park, "Calculation of optical efficiency for the first central-receiver solar concentrator system in Korea," *Energy Procedia* **69**, 126–131 (2015).
112. C. A. Arancibia-Bulnes, M. I. Peña-Cruz, D. Marroquín-García, R. E. Cabanillas, C. A. Pérez-Rábago, D. Riveros-Rosas, J. F. Hinojosa, and C. A. Estrada, "Heliostat testing at a new facility in Sonora, Mexico," in Proceedings of the 17th SolarPACES Int. Symposium on Concentrating Solar Power and Chemical Energy, Granada, Spain, 2011.
113. F. García-Martín, M. Berenguel, A. Valverde, and E. Camacho, "Heuristic knowledge-based heliostat field control for the optimization of the temperature distribution in a volumetric receiver," *Sol. Energy* **66**(5), 355–369 (1999).
114. M. M. Okhtar, S. A. Meyers, P. R. Armstrong, and M. Chiesa, "Performance of a 100 kW<sub>th</sub> concentrated solar beam down optical experiment," *J. Sol. Energy Eng.* **136**(4), 041007 (2014).
115. A. Mutuberría, A. Monreal, A. Albert, and M. Blanco, "Results of the empirical validation of Tonatiuh at Mini-Pegase CNRS-PROMES facility," in Proceedings of the 17th SolarPACES Int. Symposium on Concentrating Solar Power and Chemical Energy, Granada, Spain, 2011.
116. S. Kubisch, M. Randt, R. Buck, A. Pfahl, and S. Unterschutz, "Wireless heliostat and control system for large self-powered heliostat fields," in Proceedings of the 17th SolarPACES Int. Symposium on Concentrating Solar Power and Chemical Energy, Granada, Spain, 2011.
117. G. García, A. Egea, and M. Romero, "Performance evaluation of the first solar tower operating with autonomous heliostats: PCHA project," in Proceedings of the 12th SolarPACES Int. Symposium on Concentrating Solar Power and Chemical Energy, Oaxaca, Mexico, 2004.
118. E. Leonardi and B. D'Aguanno, "CRS4-2: A numerical code for the calculation of the solar power collected in a central receiver system," *Energy* **36**(8), 4828–4837 (2011).
119. M. Blanco and D. Alarcon, "EnerTracer: A new computer tool for energy analysis of concentrating systems," in Proceedings of the 10th SolarPACES Int. Symposium on Concentrating Solar Power and Chemical Energy, Sydney, Australia, 2000.
120. R. Monterreal, "A new computer code for solar concentrating optics simulation," *Le Journal de Physique IV* **9**, Pr3–77–Pr3–82 (1999).

121. S. Koikari and K. Yoshida, "Development and preliminary evaluation of CUDA code for concentrating solar power system of tower reflector type," in Proceedings of the 18th SolarPACES Int. Symposium on Concentrating Solar Power and Chemical Energy, Marrakech, Morocco, 2012.
122. F. Ramos and L. Crespo, "A new powerful tool for heliostat field layout and receiver geometry optimization: NSPOC," in Proceedings of the 15th SolarPACES Int. Symposium on Concentrating Solar Power and Chemical Energy, Berlin, Germany, 2009.
123. R. Branke and A. Heimsath, "Raytrace3D power tower—A novel optical model for central receiver systems," in Proceedings of the 16th SolarPACES Int. Symposium on Concentrating Solar Power and Chemical Energy, Perpignan, France, 2010, pp. 21–24.
124. S. Relloso and M. Domingo, "Solar projects analysis using SENSOL," in Proceedings of the 13th SolarPACES Int. Symposium on Concentrating Solar Power and Chemical Energy, Seville, Spain, 2006.
125. C. Gertig, A. Delgado, C. Hidalgo, and R. Ron, "SoFiA—A novel simulation tool for central receiver systems," Energy Procedia **49**, 1361–1370 (2014).
126. J. P. Roccia, B. Piau, C. Coustet, C. Caliot, E. Guillot, G. Flamant, and J. Delatorre, "SOLFAST, a ray-tracing Monte-Carlo software for solar concentrating facilities," J. Phys. Conf. Ser. **369**, 012029 (2012).
127. R. Buck, *Solar Power Raytracing Tool SPRAY User Manual* (German Aerospace Center (DLR), 2011).
128. B. Belhomme, R. Pitz-Paal, P. Schwarzbözl, and S. Ulmer, "A new fast ray tracing tool for high-precision simulation of heliostat fields," J. Sol. Energy Eng. **131**(3), 031002 (2009).
129. I. Michel, A. Peter, N. Claus, and V. Ngoc, "TieSOL—A GPU-based suite of software for central receiver solar power plants," in Proceedings of the 17th SolarPACES Int. Symposium on Concentrating Solar Power and Chemical Energy, Granada, Spain, 2011.
130. Y. Meller, "Tracer—a Pythonic ray-tracing package with solar energy focus," <https://github.com/yosefm/tracer> 2013. Last retrieved on 23 April 2016.
131. M. J. Blanco, "Tonatiuh: An object oriented, distributed computing, Monte-Carlo ray tracer for the design and simulation of solar concentrating systems," [http://www1.eere.energy.gov/solar/review\\_meeting/pdfs/p\\_34\\_blanco\\_univ\\_tx\\_brownsville.pdf](http://www1.eere.energy.gov/solar/review_meeting/pdfs/p_34_blanco_univ_tx_brownsville.pdf). Last retrieved on 23 January 2016.
132. J. Petrasch, "A free and open source Monte Carlo ray tracing program for concentrating solar energy research," in Proceedings of the ASME 2010 4th Int. Conference on Energy Sustainability, Phoenix, USA 2010.
133. S. Zunft, M. Hänel, M. Krüger, V. Dreißigacker, F. Göhring, and E. Wahl, "Jülich solar power tower—Experimental evaluation of the storage subsystem and performance calculation," J. Sol. Energy Eng. **133**(3), 031019 (2011).
134. W. Grasse, H. P. Hertlein, C.-J. Winter, and G. W. Braun, "Thermal solar power plants experience," in *Solar Thermal Power Plants: Fundamentals, Technology, Systems, Economics*, C.-J. Winter, R. L. Sizmann, L. L. Vant-Hull, eds. (Springer-Verlag, 1991).

## 1. Introduction

Solar central receiver (SCR) systems are considered to be a promising technology for solar radiation collection and conversion into high-temperature thermal energy for electricity production and chemical processing. The pioneering experimental study of an SCR system was reported in 1957 by the Soviet researchers Baum et al. [1]. An optical system consisting of 1,293 mirrors was investigated to produce steam at 400°C. Another early use of an SCR system for steam generation was reported in 1968 by Francia [2], followed by numerous studies around the world. In an SCR system, individual mirrors, called heliostats, approximate elements of paraboloids of revolution with different focal lengths and with time-dependent orientation to follow the actual position of the sun in two-dimensions, and focus solar radiation on a common focal area of a receiver positioned on a central tower. Radiation absorbed by the receiver is converted into high-temperature thermal energy and transferred further to a heat transfer medium or used directly in chemical reactions. The heat transfer medium carries thermal energy to other sub-systems such as power blocks or chemical reactors, with a possible intermediate heat storage sub-system that allows for matching solar and demand transients. Figure 1 shows the basic components of an SCR system for power generation. The SCR system technology has attracted much attention due to its inherent suitability for energy storage, and the potential to achieve low overall levelized cost of energy through a combination of high optical and thermal performance, and high working temperature (up to 1000°C in state-of-the-art designs) that allows for efficient conversion of thermal energy to electrical or chemical form. Romero et al. [4] and Behar et al. [5] provided broad review studies on SCR systems, projects, and technologies. Full-scale SCR systems are included in the review study of global concentrating solar power (CSP) plants by Pavlovic et al. [6] and Zhang et al. [7].



High capital cost of SCR systems still limits its commercial deployment. Improvements in optical and mechanical performance of the optical sub-system are crucial for capital cost reduction as the heliostat field typically represents 30–50% of the capital cost of the system and the required size of the heliostat field for a given nominal power level of a solar plant is reduced with an increased optical efficiency [8]. Similarly, increasing thermal performance of the receiver decreases the required size of the heliostat field and the associated capital cost.

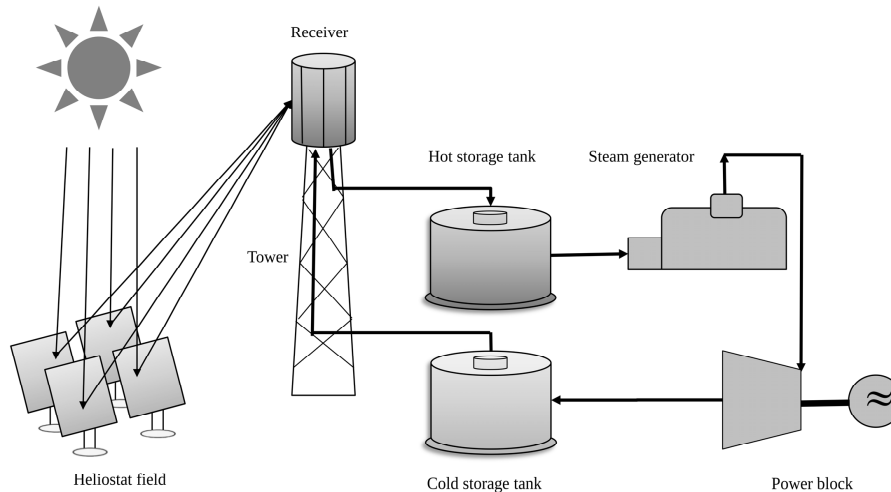


Fig. 1. Schematic of a SCR system consisting of a heliostat field, a central tower receiver, thermal energy storage system, and a power block [3].

The present article reviews pertinent studies related to optical modeling, design, optimization and demonstration of SCR systems. It focuses on optics of heliostats and heliostat fields as motivated by a need to understand the potential to adapt and improve state-of-the-art designs to meet the needs of emerging applications of the SCR technology [9,10]. Advancement of heliostat fields towards efficient and cost-effective collection and focusing of sunlight is pivotal to the advancement of SCR systems for electricity generation and chemical processing at large scale. A review of receiver optics and heat transfer is beyond the scope of this study. For a broader study in the field of concentrating solar power technologies, the reader is referred to [11].

## 2. Theoretical background

### 2.1 Radiative transfer

Macroscopic radiative transfer models of solar concentrating systems use the laws of geometrical (ray) optics and the classical radiative transfer theory based on the radiative transfer equation (RTE) [12]. A model SCR system used to elucidate the pertinent optics and radiative transfer concepts is depicted in Fig. 2.

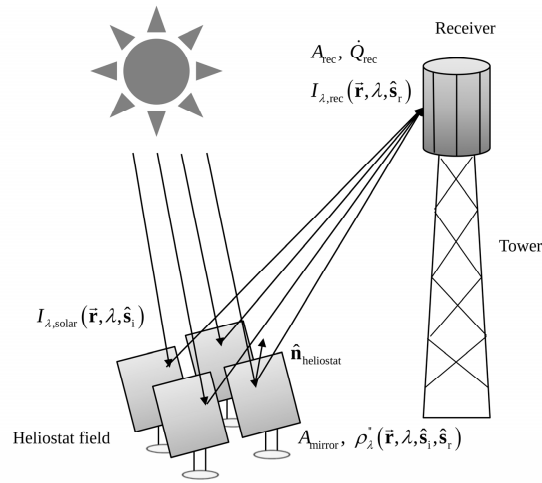


Fig. 2. Simplified radiative transfer model of an SCR system.

The spectral intensity and flux of solar radiation incident from direction  $\hat{\mathbf{s}}$  on an arbitrary surface element  $dA$  with a normal  $\hat{\mathbf{n}}$  and at position  $\vec{\mathbf{r}}$  are given by

$$I_{\lambda,\text{solar}}(\vec{\mathbf{r}}, \lambda, \hat{\mathbf{s}}, t) = \frac{dQ_{\text{solar}}(\vec{\mathbf{r}}, \lambda, \hat{\mathbf{s}}, t)}{|\hat{\mathbf{n}} \cdot \hat{\mathbf{s}}| dA d\lambda d\Omega dt} = \frac{d\dot{Q}_{\text{solar}}(\vec{\mathbf{r}}, \lambda, \hat{\mathbf{s}}, t)}{|\hat{\mathbf{n}} \cdot \hat{\mathbf{s}}| dA d\lambda d\Omega} \quad (1)$$

$$\dot{q}_{\lambda,\text{solar}}(\vec{\mathbf{r}}, \lambda, t) = \int_{\Omega=0}^{2\pi} I_{\lambda,\text{solar}}(\vec{\mathbf{r}}, \lambda, \hat{\mathbf{s}}, t) |\hat{\mathbf{n}} \cdot \hat{\mathbf{s}}| d\Omega \quad (2)$$

where  $dQ_{\text{solar}}(\vec{\mathbf{r}}, \lambda, \hat{\mathbf{s}}, t)$  and  $d\dot{Q}_{\text{solar}}(\vec{\mathbf{r}}, \lambda, \hat{\mathbf{s}}, t)$  are, respectively, the solar radiative energy and radiative power intercepted by  $dA$  within the wavelength interval  $d\lambda$  around the wavelength  $\lambda$ . In this work, the radiative transfer nomenclature is adopted from [12] unless stated otherwise. In the following text, the time notation  $t$  of radiative properties and transfer quantities is omitted for brevity. Detailed spectral optical models of solar concentrators typically use the air mass 1.5 spectral distribution (AM 1.5) as the reference spectrum, further modified according to local atmospheric conditions [13,14]. Simplified spectral optical models typically employ the spectral distribution of a blackbody at an effective temperature of the sun of approximately 5780 K [12]. The directional distribution of the incident solar irradiation results from the sun–earth geometry, with the solid and half-cone angles of the solar disk equal to  $6.79 \times 10^{-5}$  sr and 4.65 mrad (0.27°), respectively, and the effect of a sunshape, i.e. solar radiation distribution observed from the earth within the solar disk and the circumsolar aureole. The ratio of the amount of energy contained in the circumsolar aureole to the total amount of direct energy arriving from the sun is defined as the circumsolar ratio (CSR). It is an important parameter that directly influences the flux distribution and solar image size at the focal plane. Examples of sunshape models used in optical analyses of SCR systems are the pillbox, Kuiper [15], Biggs and Vittitoe [16], Rabl and Bendt [17], and Buie [18] distributions.

Solar radiation incident on a reflector surface element  $dA$  with a local normal  $\hat{\mathbf{n}}$  of a solar concentrator is partially reflected into a direction  $\hat{\mathbf{s}}_r$ . In geometrical optics, the most fundamental property describing the reflection process under the local thermodynamic equilibrium condition is the spectral bi-directional reflection function  $\rho_{\lambda}^*(\vec{\mathbf{r}}, \lambda, \hat{\mathbf{s}}_i, \hat{\mathbf{s}}_r)$ , defined as [19,20]

$$\rho_{\lambda}^* (\bar{\mathbf{r}}, \lambda, \hat{\mathbf{s}}_i, \hat{\mathbf{s}}_r) = \frac{dI_{\lambda} (\bar{\mathbf{r}}, \lambda, \hat{\mathbf{s}}_i, \hat{\mathbf{s}}_r)}{I_{\lambda} (\bar{\mathbf{r}}, \lambda, \hat{\mathbf{s}}_i) |\hat{\mathbf{n}} \cdot \hat{\mathbf{s}}_i| d\Omega_i} \quad (3)$$

In the limiting cases of optically smooth and diffuse surfaces,

$$\rho_{\lambda}^* (\bar{\mathbf{r}}, \lambda, \hat{\mathbf{s}}_i, \hat{\mathbf{s}}_r) = \begin{cases} \infty, & \text{for } \theta_r = \theta_i, \psi_r = \psi_i + \pi \\ 0, & \text{for all other } \hat{\mathbf{s}}_r \end{cases} \quad \text{optically smooth} \quad (4a)$$

$$\rho_{\lambda}^* (\bar{\mathbf{r}}, \lambda) = \rho_{\lambda}^{\text{diff}} (\bar{\mathbf{r}}, \lambda) / \pi \quad \text{diffuse} \quad (4b)$$

where the unit direction vector  $\hat{\mathbf{s}}$  is expressed in terms of the polar angle  $\theta$  (measured from the surface normal  $\hat{\mathbf{n}}$ ) and the azimuth angle  $\psi$  (measured between an arbitrary axis on the surface and the projection of  $\hat{\mathbf{s}}$  on that surface). Minimum spectral attenuation and angular spread of the reflected intensity  $I_{\lambda} (\bar{\mathbf{r}}, \lambda, \hat{\mathbf{s}}_i)$  are the desired reflection characteristics of a reflecting surface to maximize the total radiative power intercepted by the receiver aperture of an area  $A_{\text{rec}}$ ,

$$\dot{Q}_{\text{rec}} (\bar{\mathbf{r}}) = \int_{\lambda=0}^{\infty} \int_{A_{\text{rec}}} \int_{\Omega=0}^{2\pi} I_{\lambda, \text{rec}} (\bar{\mathbf{r}}, \lambda, \hat{\mathbf{s}}) |\hat{\mathbf{n}} \cdot \hat{\mathbf{s}}| d\Omega dA d\lambda \quad (5)$$

Note that the optical concentrator of an SCR system may consist of more than one reflector between the reference location of the incident solar radiation and the receiver.

The atmospheric transfer of radiation, and thus the spatial variation of radiative intensity between the reference location of incidence, reflectors and a receiver is modeled using the quasi-steady form of the radiative transfer equation,

$$\frac{dI_{\lambda} (\bar{\mathbf{r}}, \lambda, \hat{\mathbf{s}})}{ds} + \beta_{\lambda} I_{\lambda} (\bar{\mathbf{r}}, \lambda, \hat{\mathbf{s}}) = \kappa_{\lambda} I_{\lambda, \text{b}} (\bar{\mathbf{r}}, \lambda) + \frac{\sigma_{s, \lambda}}{4\pi} \int_{\Omega_i=0}^{4\pi} I_{\lambda} (\bar{\mathbf{r}}, \lambda, \hat{\mathbf{s}}_i) \Phi_{\lambda} (\bar{\mathbf{r}}, \lambda, \hat{\mathbf{s}}_i, \hat{\mathbf{s}}) d\Omega_i \quad (6)$$

where  $\kappa_{\lambda}$  and  $\sigma_{s, \lambda}$  are the spectral absorption and scattering coefficients, respectively,  $\beta_{\lambda} = \kappa_{\lambda} + \sigma_{s, \lambda}$  is the extinction coefficient, and  $\Phi_{\lambda} (\bar{\mathbf{r}}, \lambda, \hat{\mathbf{s}}_i, \hat{\mathbf{s}})$  is the scattering phase function of radiation from the direction  $\hat{\mathbf{s}}_i$  into  $\hat{\mathbf{s}}$ . The radiative properties are determined by employing atmospheric models that account for the actual composition of the gas, liquid and solid phases [21,22]. The quasi-steady form of RTE is employed as justified by the small characteristic radiation propagation times at length-scales associated with the overall dimensions of solar thermal systems.

## 2.2 Performance metrics

The performance metrics of concentrating solar thermal systems can be categorized as optical and thermodynamic. The basic optical performance metrics are the optical efficiency and the solar concentration ratio. The basic thermodynamic performance metrics are the absorption efficiency, the ideal thermodynamic conversion efficiency, and the receiver thermal efficiency.

### 2.2.1 Optical efficiency

The overall optical efficiency is defined as the ratio of the radiative energy intercepted by the receiver with an aperture area  $A_{\text{rec}}$  to the maximum possible energy that can be intercepted by the total concentrator (heliostat field) area for a given time period. The maximum possible radiative power that can be collected by the heliostat field is calculated as radiative power collected when solar rays are incident normally on an area equal to the total installed mirror area  $A_{\text{mirror}}$  of the heliostat field [23]. It should be noted that this efficiency is not based on the

land area covered by the entire field, nor the heliostat field aperture area which takes into account the cosine effect (see below) and the open or opaque spaces among mirrors [24].

$$\eta_{\text{optical}} = \frac{\int \dot{Q}_{\text{rec}} dt}{GA_{\text{mirror}} \Delta t} \quad (7)$$

where  $G$  is the direct normal irradiance (DNI). The nomenclature for the irradiance  $G$  is adopted from [25]. For simulation or reference purposes,  $G$  is often taken equal to  $1 \text{ kW m}^{-2}$  [25]. Hence, optical efficiency is a measure of how well the mirror surface performs in transferring radiation to the receiver, compared with an absolute upper bound based on the DNI and the total mirror area. This representation is useful, as heliostat field costs scale essentially linearly with total mirror area.

The overall optical efficiency accounts for cosine, shading, blocking, spillage, reflection, and atmospheric attenuation losses:

$$\eta_{\text{optical}} = \eta_{\text{cosine}} \eta_{\text{shading}} \eta_{\text{reflection}} \eta_{\text{blocking}} \eta_{\text{spillage}} \eta_{\text{atmosphere}} \quad (8)$$

The cosine effect refers to the fact that the amount of radiative power intercepted by the heliostat is proportional to the cosine of the angle between the heliostat surface normal and the direction of incident solar rays. The shading loss occurs when part of a heliostat surface is in shadow of a preceding heliostat, the tower or the receiver. The reflection loss results from the less-than-unity reflectivity of the heliostat surface. Some of the solar rays reflected from heliostats may hit the back surface of another heliostat instead of reaching the receiver, resulting in the blocking loss. The spillage loss occurs when solar rays reflected from the heliostat field miss the target. Spillage results from small receiver aperture size, heliostat surface error and heliostat misalignment. Atmospheric scattering and absorption result in the atmospheric attenuation loss, which increases with the distance between the heliostat and the receiver aperture and the water vapor or aerosol content in the atmosphere. A representative schematic showing each of these optical losses is shown in Fig. 3. A representative value for the annual overall optical efficiency of the PS10 solar power plant is approximately 67.5%, which is broken down as 84.4%, 96.6%, 88.0%, 99.1%, 99.4%, and 95.5% for cosine, shading, reflection, blocking, spillage, and atmospheric attenuation efficiencies [26]. This optical assessment was performed with winDELSOL (see Section 5.3).

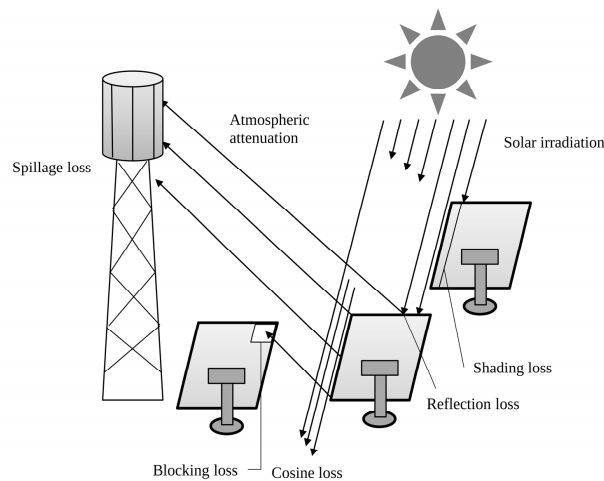


Fig. 3. Optical losses in an SCR system that are pertinent to the definition of the optical efficiency [3].

### 2.2.2 Concentration ratio

The commonly used definition of concentration ratio is the area (geometric) concentration ratio. It is defined as the ratio of the concentrator aperture area  $A_{\text{conc}}$  to the receiver aperture area  $A_{\text{rec}}$  [25],

$$C_a = \frac{A_{\text{conc}}}{A_{\text{rec}}} \quad (9)$$

The instantaneous, area-average flux (energetic) concentration ratio is defined as the ratio of the area-average radiative flux incident at the receiver aperture to that on the concentrator aperture, which is normally referred to as the direct normal irradiance  $G$ ,

$$C_f = \frac{\dot{Q}_{\text{rec}}}{A_{\text{rec}} G} \quad (10)$$

Due to the dramatic variation of the radiative flux over the receiver aperture, the local flux (energetic) concentration ratio can be defined as the ratio of the local radiative flux at any point of the receiver aperture to that on the concentrator aperture.

The time- and area-average flux concentration ratio over a time period  $\Delta t$  is obtained as:

$$\bar{C}_f = \frac{\int \dot{Q}_{\text{rec}} dt}{G A_{\text{rec}} \Delta t} \quad (11)$$

Higher temperatures at the receiver can be attained from higher concentration ratios that imply less radiation loss from a smaller receiver. However, there is a fundamental thermodynamic limit of achievable concentration. The ideal or maximum concentration ratio that a two-dimensional (linear concentrators) and three-dimensional (point-focus concentrators) concentrating system can achieve are

$$C_{a,\text{ideal},2D} = \frac{1}{\sin \theta_c}, \quad (12)$$

$$C_{a,\text{ideal},3D} = \frac{1}{\sin^2 \theta_c}, \quad (13)$$

where  $\theta_c$  is the acceptance half angle that is half of the angular range over which radiation is accepted without moving all or part of the receivers. The ideal concentration ratio cannot be infinitely large due to the actual angular size of the sun (half-cone angle 4.65mrad) giving the thermodynamic limit concentration for point-focus concentrators 46,250 and for linear concentrators 215 [23,25,27]. A multitude of practical issues further limit the concentration ratios of engineered systems. The solar flux concentration ratio typically varies between 30 and 100 for trough systems, 1000–10,000 for dish systems, and 500–5,000 for tower systems [9]. The concentration can be increased with the help of secondary concentrators (see Section 3). For SCR systems with two-axis tracking, the typical range of area concentration ratio and indicative temperature are 100–1500 and 150–2000°C, respectively [28].

### 2.2.3 Absorption, ideal thermodynamic conversion, and receiver thermal efficiencies

The absorption efficiency of a solar receiver is defined as the ratio of radiative power absorbed by a perfectly insulated and isothermal receiver at temperature  $T_H$  to the concentrated radiative power intercepted by the receiver aperture,

$$\eta_{\text{absorption}} = \alpha - \frac{\varepsilon \sigma T_H^4}{GC} \quad (14)$$

where  $\sigma$  is the Stefan–Boltzmann constant equal to  $5.67 \times 10^{-8} \text{ W m}^{-2} \text{ K}^{-4}$ ;  $\alpha$ ,  $\varepsilon$  and  $C$  are the total apparent absorptivity and emissivity at the receiver aperture, and the area-average flux concentration ratio, respectively. The receiver thermal efficiency is a generalization of the absorption efficiency definition (Eq. (14)) introduced above. The receiver thermal efficiency accounts for losses due to forced and natural convection, conduction through receiver walls, and thermal re-radiation through the aperture. It is defined as the ratio of the net heat rate gained in the receiver to the concentrated radiative power intercepted at the receiver aperture.

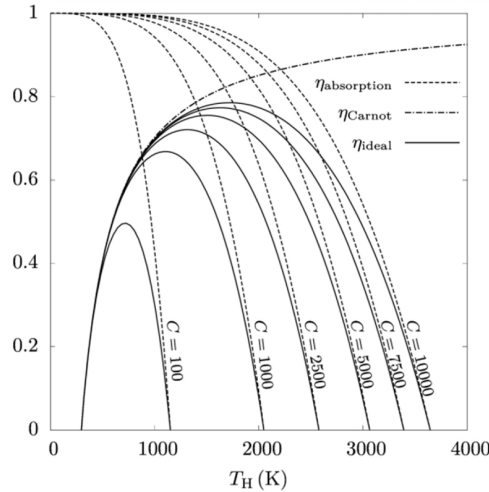


Fig. 4. Blackbody absorption, Carnot and ideal thermodynamic conversion efficiencies as functions of the receiver temperature for selected values of the solar concentration ratio [29].

$$\eta_{\text{thermal}} = \frac{\dot{Q}_{\text{net}}}{A_{\text{rec}} GC} \quad (15)$$

The ideal thermodynamic conversion efficiency is defined as the ratio of work rate produced by a Carnot engine operating between a perfectly insulated and isothermal blackbody receiver and a cold reservoir at  $T_H$  and  $T_L$ , respectively, to the concentrated radiative power intercepted at the receiver aperture. It provides the upper theoretical limit of conversion of concentrated solar radiation into work, and is equal to the product of the blackbody-receiver absorption and Carnot efficiencies,

$$\eta_{\text{ideal}} = \eta_{\text{absorption,bb}} \eta_{\text{Carnot}} = \left(1 - \frac{\sigma T_H^4}{GC}\right) \left(1 - \frac{T_L}{T_H}\right) \quad (16)$$

Figure 4 shows the blackbody absorption, Carnot, and ideal thermodynamic system efficiencies as functions of receiver temperature for selected values of the concentration ratio  $C$  in the range 100–10,000.

The upper overall theoretical efficiency limit of an SCR system is the product of the optical efficiency and the ideal thermodynamic conversion efficiency. It is a vector for coupled receiver and heliostat field optimization. The optical performance is maximized through rigorous design of individual heliostats, heliostat fields, and receivers by iterative optimization of their geometry, orientation, position and materials.

### 3. Classification of solar central receiver systems

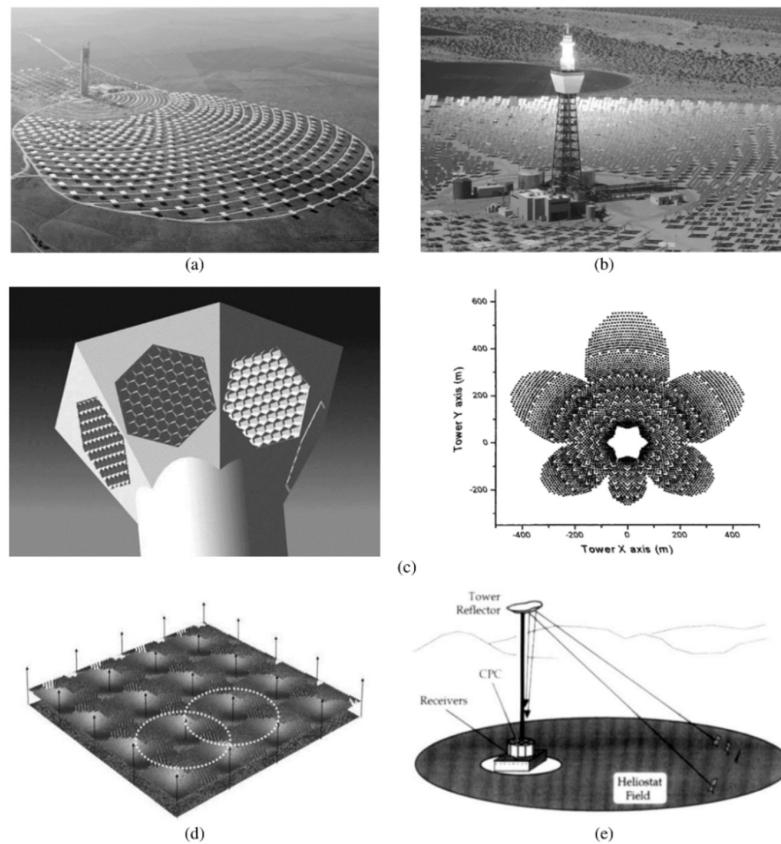


Fig. 5. Examples of SCR system configurations: (a) a single tower receiver with a single asymmetric aperture and a polar heliostat field (reprinted from [30], Copyright (2007), with permission from SolarPACES) b) a single tower receiver with a circumferential aperture and a surround field (reprinted from [4], Copyright (2002), with permission from the American Society of Mechanical Engineers) c) a single tower receiver with multiple apertures and multiple polar fields located concentrically around the receiver (left: reprinted from [31], Copyright (2006), with permission from Elsevier; right: reprinted from [32], Copyright (1999), with permission from Elsevier) d) multiple tower receivers immersed in a surround field constructed as a superposition of multiple fields (reprinted from [33], Copyright (2003), with permission from Elsevier), and (e) tower-reflector system (reprinted from [34], Copyright (1998), with permission from Elsevier).

Solar central receiver systems can be classified according to the geometrical configuration of secondary concentrator at the aperture of a receiver such as a compound parabolic concentrator (CPC). In the basic classification, tower-receiver and tower-reflector (beam-down) systems are distinguished. In a tower-receiver system, heliostats reflect radiation directly towards the receiver on a central tower. Figures 5(a)–5(d) shows the basic configurations of tower-receiver systems: (a) a single receiver with a single asymmetrically-located aperture and a polar heliostat field b) a single receiver with a circumferential aperture and a surround field c) a single receiver with multiple apertures/partitions and multiple polar fields located concentrically around the receiver, and (d) multiple receivers of any type located within a surround field constructed as a superposition of multiple fields or field segments. A multi-aperture cavity receiver system with each aperture equipped with a separate secondary concentrator and matched to a separate heliostat field was developed by

Schmitz et al. and is shown in Fig. 5(c) left [31]. A “butterfly” field with six concentrators to match the multi-aperture receiver design was developed by Segal and Epstein and is shown in Fig. 5(c) right [32]. A multi-tower system (Fig. 5(d)) was developed by Schramek and Mills for the purpose of maximizing the ground area usage [33].

A tower-reflector system (Fig. 5(e)) makes use of the Cassegrain optical configuration [35]. Heliostats reflect radiation towards a secondary reflector located on a tower, which in turn reflects radiation towards the receiver located on the ground level. The tower reflector approximates a hyperboloidal reflector if placed below the heliostat field focal point, or an ellipsoidal reflector if placed above the heliostat field focal point. A CPC is coupled with the receiver for increasing the concentration ratio at the expense of active cooling and additional optical losses [32]. Despite allowing for ground-level location of the receiver and related equipment as in the existing demonstration systems, no large-scale beam-down system has been built yet. Disadvantages of beam-down SCR systems include the decreased optical efficiency due to non-ideal mirror reflectivity, the increased beam spread, the large size of the secondary mirror, and the requirement to rigidly mount the secondary mirror near the primary focus [36].

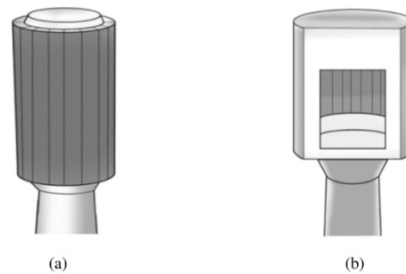


Fig. 6. Basic receiver types: (a) external receiver and (b) cavity receiver. Reprinted from [38], Copyright (2014), with permission from Elsevier.

Solar central receiver systems are designed by matching thermal requirements of thermal or thermochemical processes such as temperature, power level, transient variations, to thermal characteristics of a receiver. Receiver selection/design is inherently coupled to the selection/design of an optical concentrator. A broad variety of receiver designs specific to SCR systems have been conceptualized, designed and demonstrated as summarized by Ávila-Marín [37] and Ho and Iverson [38]. In this study, we omit a detailed discussion of receiver optics, and thus limit the classification to the basic receiver types, an external receiver and a cavity receiver, as schematically shown in Fig. 6. For an external receiver (Fig. 6(a)), radiation absorption, radiative and convective heat losses to the surrounding, and heat transfer to a working fluid or chemical reaction occur at the same surface. Due to the large surface area required for heat transfer, at high temperatures external receivers exhibit high radiative and convective losses. Radiative losses can be minimized by employing high-temperature selective coatings. Thus, the current use of external receivers is limited to applications with operating temperatures below approximately 1000 K. An external receiver can have a circumferential aperture to match a surround field as shown in Fig. 5(b), enabling very wide acceptance angles. Practical advantages are that it is conceptually simple, has light supporting structures, allows simpler maintenance, and reduces atmospheric attenuation losses by reducing the mean distance to heliostats.

For a cavity receiver (Fig. 6(b)), high-flux irradiation enters the receiver cavity through an open or windowed aperture, and is absorbed at internal surfaces or/and in a volume of a radiatively participating medium inside the cavity. Numerous cavity configurations and radiative absorption scenarios have been proposed, from direct irradiation of active heat transfer media or chemical reactions to indirect heating by heat transfer through absorbing



solid elements of the cavity, from stationary designs to designs with moving internal parts and variable aperture sizes. Cavity receivers are preferred for high-temperature applications due to their high absorption efficiency. Because of the high-flux requirement, cavity receivers are best matched with polar (segment) heliostat fields of high optical efficiency. Multi-cavity receiver designs requiring moderate-flux concentration, such as at the Khi Solar One power plant [39,40] may have a hybrid polar-surround type heliostat layout (similar to Fig. 5(c) *right*).

Radiative performance of cavity receivers in SCR systems can be further improved by applying secondary concentrators such as CPCs as in an example study by Segal and Epstein [41]. The use of a CPC increases the concentration ratio (ideally by a factor  $1/\sin^2\theta$ , where  $\theta$  is the half-acceptance angle of a CPC), allows for utilization of spillage radiation directly around the hot spot, and spreads the angular distribution of the exiting radiation [42]. The latter allows for more uniform irradiation inside a receiver cavity, in particular for eliminating hot spots. Kribus et al. investigated performance limits of tower systems with four secondary concentrator options [43]: tower-top CPC, tailored edge-ray concentrator (TERC) approximated by a cone, and a Cassegrain system with ground-level CPC or compound elliptic concentrator (CEC). An annular compound parabolic concentrator (ACPC) was proposed by Lipiński and Steinfeld for utilization of low-grade spillage radiation outside the hot spot [44]. Except from conventional axi-symmetric secondary concentrators, secondary concentrators with non-regular cross sections were proposed and evaluated in tandem with heliostat fields with wider range of possible contours [45]. Beside improving overall optical system performance, the capture of spillage radiation helps protect outer walls of receivers from overheating, thus lowering the requirements for using protective shields and active cooling.

#### 4. Optics of heliostats

An individual heliostat is composed of a reflector (one or more mirror facets), a supporting structure including foundations, and an actuation system. The specular reflectivity of the mirror facets, the alignment of the mirror facets, the alignment of the tracking system, and the structural rigidity (particularly under operational wind loads) must be optimized for best optical performance of an individual heliostat.

##### 4.1 Classification

Heliostats can be classified in various ways, for example, by reflector type or by tracking arrangement. An extensive evaluation and classification of heliostat designs according to mirror type was conducted at Sandia National Laboratories in the 1980s [3]: glass-metal heliostats (Figs. 7(a) and 7(c)) utilize multiple individually curved glass mirror facets, supported by a rigid steel structure; stressed-membrane heliostats are based on two membranes (one reflective) with curvature provided by active control of the pressure between the membranes (Fig. 7(b)). Most recent heliostat designs include the Stello heliostat developed by SBP Sonne [49], the proposed ASTRI sandwich-panel heliostat [50], and the suspension heliostat such as that proposed by Solaflect [48].

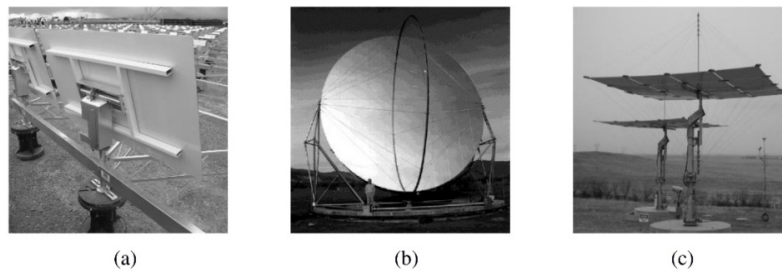


Fig. 7. Heliostat design examples: (a) flat glass–metal heliostat (1.14 m<sup>2</sup> eSolar heliostat) (reprinted from [46], Copyright (2011), with permission from Elsevier) b) stressed–membrane heliostat (150 m<sup>2</sup> metal membrane heliostat, PSA) (reprinted from [47], Copyright (1996), with permission from Schlaich Bergermann und Partner (SBP)), and (c) focusing glass–metal heliostat (16 m<sup>2</sup> Solaflect’s suspension heliostat) (reprinted from [48], Copyright (2013), with permission from Solaflect Energy).

A heliostat with a flat mirror produces a degraded focal spot at the receiver aperture, especially for large mirrors [51]. Thus, focusing (curved) heliostats have been developed that display optical performance nearly independent of their size. However, it is noted that astigmatic aberration (see Section 4.2.1) becomes worse for larger heliostats, which imposes optical constraints on large heliostats. The question of optimal heliostat size is debated by many authors [52,53] and is both an optical and cost related trade-off. The reflecting surface is divided into pre-aligned flat or curved and canted mirror facets. For any type of heliostats, decreasing their size is beneficial for ensuring a high optical quality of the reflecting surface, and minimizing shading and blocking losses in the field. A review of the state of the art in heliostat design and cost reduction is given by Coventry and Pye [53] and Pfahl [54].

#### 4.2 Optical studies

The relevant optical losses associated with individual heliostats are due to imperfect reflection (reflectivity value less than unity, angular spread), cosine effect, and spillage. The reflectivity of the mirror depends on the surface material and its manufacturing precision. The non-normal orientation of a heliostat with respect to the directions of solar irradiation and towards the receiver results in the cosine loss. The spillage loss results from radiation incident at an area outside the prescribed receiver aperture. In seeking to achieve higher-temperature SCR systems, higher concentration ratios are required without increasing optical losses. This imposes challenging constraints on SCR system components.

##### 4.2.1 Astigmatism

A key factor limiting the concentration ratio for a focusing collector system is the astigmatism effect, or off-axis aberration, from non-normal incidence. For tangential and sagittal rays, the focal lengths are shorter or longer than the nominal focal length, respectively, which results in degradation of the focal spot [55,56]. The astigmatism effect increases with increased slant range and increased cosine value of the angle between the heliostat surface normal and the incident rays [56]. The method used to correct the astigmatism effect in telescopes adapted to heliostats requires  $2m \times n$  motors for a heliostat composed of  $m \times n$  facets, which is impractical. A non-imaging focusing heliostat which manoeuvres the facets in a group manner so that the required number of motors can be reduced to  $m + n - 2$  or even 2 has been studied by Chen et al. [57,58] and Chong [59,60].

##### 4.2.2 Aiming

The concentrated flux distribution at the receiver aperture requires controlling according to receiver geometry, lifetime and the specific requirements of thermal or thermal-chemical processes. Therefore, dynamic adjustment of flux distribution at the receiver aperture, i.e.

aiming strategy, is indispensable for the optical sub-system design and optimization. A review study of aiming strategies for central receivers was performed by Grobler and Gauché [61]. Salomé et al. presented an open-loop approach to control the flux density distribution by selecting the best aiming point for each heliostat [62].

#### 4.2.3 Canting and focusing

Mirrors or their individual facets of focusing heliostats are canted to focus solar irradiation on the receiver aperture. The canting concepts mainly include typical on- and off-axis canting, and newly proposed stretched-parabolic and target-aligned canting. Buck and Teufel presented a study to compare and optimize the canting methods [63]. In on-axis canting, heliostat elements are aligned while the sun and target vectors are perpendicular to the heliostat plane. In off-axis canting, the alignment is performed when the sun vector is oblique to the heliostat plane. Jones assessed the two approaches and concluded that on-axis canting consistently results in high optical performance while off-axis canting can lead to superior upper theoretical limit in optical performance with the actual performance strongly dependent on day and seasonal time [64]. Review studies of canting and focusing methods are published by Yellowhair and Ho [65] and Ren et al. [66]. Optical and mechanical canting methods were summarized, including the gauge blocks, inclinometers, photogrammetry, fringe reflection, imaging with theoretical image overlays, laser beam projections, camera look-back, and target reflection. New heliostat facet canting method was investigated for example by Yellowhair et al. by using a target in reflection [67]. Segal and Epstein investigated canting and focusing of facets of the hyperboloidal tower reflector at the Weizmann Institute of Science (WIS) by grouping facets to reduce the canting time [68].

#### 4.2.4 Tracking

Tracking systems control movement of heliostats to align them according to the actual position of the sun. Accurate heliostat tracking is crucial to minimize the cosine loss and spillage loss on the receiver aperture. The tracking accuracy is characterized by the value of a tracking error. A good tracking system has a tracking error as low as 0.2 mrad ( $0.01^\circ$ ) as developed by Brown and Stone [69]. Based on the signal operation mode, closed-loop or open-loop tracking systems are distinguished, with the commercial systems opting for the latter with periodic closed-loop ‘alignment correction’ applied. Sun tracking systems were reviewed by Lee et al. [70] and Mousazadeh et al. [71]. The principle of spinning-elevation tracking or target-aligned tracking method was first discussed by Ries and Schubnell [72] and Zaibel et al. [73]. Performance of the two tracking methods, the azimuth-elevation method and the spinning-elevation method was compared by Chen et al. [74] and Chong and Tan [75]. The spinning-elevation method was found to offer a smaller image spread, as well as spatially and temporally more uniform radiative flux distributions, which in turn results in reduced spillage loss. An automated open-loop eight-dimensional tracking error characterization and correction method was presented by Khalsa et al. [76]. The method was demonstrated to lead to highly-reduced heliostat elevation and azimuth pointing errors using the National Solar Thermal Test Facilities (NSTTF) at Sandia National Laboratories [77]. In the study by Flesch et al., an auxiliary mirror attached to every heliostat in a field was used to create a small reflection image on a target, which in turn was used to automatically adjust the heliostat orientation [78].

#### 4.2.5 Wind load

Wind loads generate mirror instabilities degrading the optical quality of the image on the receiver aperture. Most studies have focused on mechanical analyses of wind load on heliostats [79,80], a subject beyond the scope of the present review. Addressing the issue of wind loads effects on optical performance of heliostats is crucial for optical performance improvement and cost reduction of heliostats [53]. Strachan and Houser experimentally

investigated wind load effects on optical performance of Advanced Thermal Systems (ATS) and Solar Power Engineering Company (SPECO) heliostats [81].

### 5. Optics of heliostat fields

The optical design and optimization of a heliostat field are the culminating tasks in a SCR system designed for high optical efficiency. The optical losses associated with a heliostat field are due to shading, blocking and atmospheric attenuation. A general design process for a heliostat field with prescribed heliostat and receiver types is to (i) determine the basic system configuration, i.e. the heliostat field type, the relative position of the heliostat field and the receiver (ii) generate and optimize the heliostat field layout by specifying the heliostat locations through a tradeoff between performance and cost via a simplified optical analysis, and (iii) iteratively obtain a high-fidelity heliostat field layout and accurate optical performance predictions through detailed optical/radiative transfer models of the system coupled to thermal and thermochemical models of receivers and receiver-reactors, respectively, and incorporating annual performance and overall techno-economic analyses of the system.

#### 5.1 Classification

Based on the heliostat field layout boundary, polar fields and surround fields are distinguished as shown in Figs. 5(a) and 5(b), respectively. A surround heliostat field allows for circumferential irradiation of a central receiver, while a polar field results in highly-asymmetric irradiation. In a surround field, the east and west heliostats can collect solar radiation at lower values of the solar azimuth angle. For a given power level, the height of the central tower with a surround field is smaller as compared to that for a polar field, thus reducing thermal losses from the tower and piping, the amount of construction materials, and consequently the cost. Additionally, the distance between the most remote heliostats of a surround field and the receiver is smaller as compared to that for a polar field, reducing optical losses from atmospheric attenuation within the system. Alternatively, the heliostats in a polar field configuration (north or south field configuration for plants located in the norther or southern hemisphere, respectively) are all arranged on one side of the tower and operate with lower cosine losses. The polar field approach may generally be used when a cavity receiver is needed for high-temperature applications as discussed in Section 3.

#### 5.2 Layout generation and optimization

Numerous studies on generation and refinement of heliostat layouts have been reported in literature. Basically, there are four categories of heliostat patterns: (a) radial cornfield b) radially-staggered field c) N-S cornfield, and (d) N-S staggered field [82]. The radially-staggered pattern is used in a majority of developments due to its proven superior performance over the other patterns from the above list. However, the biomimetic pattern developed by Noone et al. was found to have optical efficiency and ground coverage even higher than the radially-staggered pattern [83].

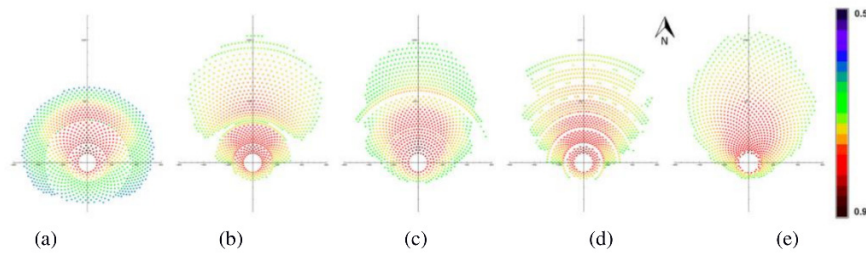


Fig. 8. Heliostat field layouts developed with different approaches: (a) dense radial staggered method b) Campo code c) graphical method d) DELSOL code and (e) biomimetic pattern. The color bar shows the annual optical efficiency values. Reprinted from [95], Copyright (2014), with permission from SolarPACES.

With the basic heliostat pattern selected, a field layout is generated and optimized. Examples of studies on generating heliostat field layouts include the cellwise method [82], the graphical method [84], the Yearly Normalized Energy Surface data based method [85], the method based on direct determination of heliostats position in the field as proposed by Collado [86], the Campo code [87], and the Heliostat Field Layout Design code [88].

More studies have been reported on heliostat field layout optimization. The optimization methods differ in fidelity (e.g. types of optical losses considered, weather conditions, and sunshape models), optimization criteria, and computation time. Pitz-Paal et al. published a study on heliostat field layout optimization for maximum annual solar-to-chemical energy conversion efficiency [89]. A computationally efficient method for designing and optimizing heliostat field layout was developed by Besarati and Goswami based on a new proposed method for calculating shading and blocking losses [90]. Further pertinent studies were published by Wei et al. [91], Pisani et al. [92], Buck [8], Dunham et al. [93], and Atif and Al-Sulaiman [94]. A comparative study of heliostat field layout characteristics designed and optimized with selected methods including dense radially-staggered layout, graphical method, Campo code, DELSOL software, and biomimetic pattern (see Fig. 8) was conducted by Mutuberia et al. [95]. The number of heliostats, annual optical efficiency and annual energy collected were used as the comparative criteria. It was found that for the three design power levels of 100, 120, and 150 MW<sub>th</sub>, the layout generated with the dense radially-staggered method had the lowest optical efficiency of 71.1%, 68.9%, 61.0%, respectively, while among the other four methods, the highest optical efficiencies were achieved by the biomimetic pattern, 75.2%, 74.2%, 72.9%. The layout generated by the Campo code showed performance close to that of the biomimetic pattern in terms of the annual optical efficiency [95].

### 5.3 Optical modeling

Detailed optical models are used to obtain accurate predictions of spatial and temporal radiative flux distributions at the receiver aperture. The cone optics, hermite polynomial expansion/convolution and Monte Carlo ray-tracing (MCRT)/statistical methods are used in optical simulations.

Monte Carlo ray-tracing methods are the most robust simulation techniques for optical and radiative transfer modeling of SCR systems [96]. As statistical methods, they can incorporate spatial, angular, spectral and temporal variations of radiative intensity, arbitrary spectral and directional properties of opaque and transmitting surfaces as well as participating media [12,97,98]. Monte Carlo ray-tracing methods come in multiple variants, from simple methods such as the basic collision-based method to advanced methods implementing various strategies towards increased computational efficiency and accuracy such as the energy partitioning and pathlength methods.

Hermite polynomial expansion/convolution method was used for flux calculation in codes such as DELSOL/winDELSOL [99,100], HFLCAL [101], and UHC/RCELL [82]. Monte-

Carlo ray-tracing was used for developing codes such as MIRVAL [102] and SolTRACE [103]. HELIOS, an early model developed in late 1970s and based on cone optics, was used to predict a concentrated solar flux distribution on an arbitrary target grid obtained from a heliostat field [55]. Modeling tools for SCR systems can be found in review studies by Garcia et al. [104], Ho [105], and Bode and Gauché [106]. Yellowhair et al. compared DELSOL, HELIOS, SolTrace, Tonatiuh for modeling complex receiver geometries [107].

In the present study, selected modeling tools for SCR systems are summarized in Table 1. The tools differ in methods for radiative flux computations, types of optical losses accounted for, types of optical and radiative output characteristics, availability of user-defined field layout and receiver configurations, size limits of heliostat field and/or SCR systems, annual performance and optimization capabilities, and computational cost and efficiency.

#### 5.4 On-sun optical characterization and demonstration

This section reviews SCR systems at the research, demonstration and commercial scales. Listings of SCR research, demonstration and commercial systems are also available as Internet resources including crowdsourcing and include the most recent global developments (e.g [39,40,108,109]). A selection of systems designed for research and development purposes are listed in Table 2. Exemplary systems are shown in Fig. 9. Demonstration studies of tracking strategies were conducted by Smith and Ho at NSTTF [77], and by Flesch et al. at the Jülich Solar Tower of the German Aerospace Center (DLR) [78]. Examples of studies on investigating optical performance evaluated primarily through measurements of temperature and flux distribution at receiver or reactor apertures can be found in [110–114]. Other optical studies on heliostats include experimental analysis of heliostat surface deformation due to gravity in the Themis solar tower facility in France [115], wireless heliostat control system for self-powered heliostat fields in Jülich Solar Tower [116], on- and off-axis canting methods investigation in DAHAN tower plant [110], and the experimental study of the first fully autonomous heliostat field carried out with the Small Solar Power Systems (SSPS-CRS) facility in Spain [117].

Table 3 gives an overview of selected commercial SCR systems that are in operation or under development/construction [108]. These SCR systems are generally used to provide heat to steam turbine power cycles operating at up to 565°C. Consequently, these systems typically use external receivers, which are suitable at this temperature level. There is a larger number of demonstration SCR systems designed to achieve higher temperatures for the research purpose on optics, materials, thermochemistry, and/or thermophysics. At higher temperature levels, cavity receivers and/or secondary concentrators are required to reduce the re-radiation losses from the receiver.

The size of commercial SCR systems varies greatly. Currently, the largest reported SCR system, used in the Ivanpah Solar Power Facility generating up to 377 MW<sub>e</sub> of electric power, has a solar field aperture area of 2.6 km<sup>2</sup>. Commercial SCR systems use a range of heliostat types with heliostat aperture areas ranging from ~1 m<sup>2</sup> (eSolar heliostat) to 140 m<sup>2</sup> (Abengoa Solar heliostat).

Table 1. Tools for solar central receiver system modeling

Tool	Year	Full name	Developed by	Programming language <sup>1</sup>	Flux calculation methods	Applications <sup>2</sup>	References
CAMPO	2011	-	Zaragoza University	MATLAB	-	CRS	[87]
CRS4-2	2011	CRS4 Research Software for Central Receiver Solar System Simulations	Center for Advanced Studies, Parco Scientifico e Tecnologico, Italy	Fortran	-	CRS, BD	[118]
DELSOL	1979	-	Sandia National Laboratories (SANDIA)	FORTTRAN77	Hermite polynomial expansion/convolution	CRS	[99]
windELSOL	1986	-	SANDIA	FORTTRAN77	Hermite polynomial expansion/convolution	CRS	[100]
EnerTracer	2000	-	Plataforma Solar de Almeria (PSA)	C++	MCRT	Light reflecting system	[119]
Fiat_Lux	1997	-	PSA	MATLAB	MCRT	CRS	[120]
HELIOS	1981	-	SANDIA	FORTTRAN extended - version 4	Cone optics	CRS, PT, DS	[55]
HELICAL	1986	HelioStar Field Layout Calculations	DLR	-	Convolution	CRS	[101]
HFLD	2010	HelioStar Field Layout Design	Chinese Academy of Sciences (CAS)	MATLAB	MCRT	CRS	[88]
Koikari & Yoshida	2012	-	Institute of Applied Energy, Tokyo	CUDA, GPU by NVIDIA	MCRT	Tower reflector system	[121]
MIRVAL	1978	-	SANDIA	Fortran	MCRT	CRS	[102]
MIT code /Biomimetic	2012	-	Massachusetts Institute of Technology (MIT)	Fortran	Convolution	CRS	[83]
MUEEN	2000	-	Center for Solar Energy studies, Tripoli, Libya	C++	Graphical	CRS	[84]
NSPOC	2009	New Solar Plant Optimization Code	-	Fortran	-	CRS	[122]
Raytrace3D-PowerTower	2010	-	Fraunhofer Institute for Solar Energy Systems (ISE)	-	MCRT	CRS	[123]
SCT	2006	Solar Concentration Toolbox	Centro de Investigaciones Energéticas Medioambientales y Tecnológicas (CIEMAT) lab	MATLAB	MCRT	CRS	[85]
SENSOL	2005	-	SENER	Fortran	-	CRS, PT, PV, BD	[124]
SoFIA	2015	Solar Field Assessment	-	-	MCRT	CRS	[125]
SOLFAST	2012	SOLar Facilities Simulation Tools	HPC-SA and PROMES-CNRS lab	-	MCRT	CRS, PT, DS	[126]
SoTRACE	2003	-	National Renewable Energy Laboratory (NREL)	C++	MCRT	Solar power optical systems	[103]
SPRAY	-	-	DLR	Fortran90	MCRT	CRS, PT, BD, Linear-Fresnel	[127]
STRAL	2009	Solar Tower Ray-tracing Laboratory	DLR	C++, assembler	MCRT	CRS	[128]
TieSOL	2011	-	Tietronix Software Inc.	C, C++, C#, OpenGL	MCRT	CRS	[129]
Tracer	2009	-	Tel Aviv University, Australian National University (ANU)	Python	MCRT	Optical systems	[130]
Tonatiuh	2009	-	National Renewable Energy Centre (CENER), Spain	C++	MCRT	Solar concentrating systems	[131]
UHC-RCELL	1974	University of Houston Code	University of Houston	FORTTRAN77, C++	Hermite polynomial expansion/convolution	CRS	[82]
VEGAS	2010	-	ETH Zurich	Fortran90	MCRT	Reflector geometries	[132]

<sup>1</sup> Fortran (without any version specification) is written for codes without version specification by the vendor.

<sup>2</sup> BD: solar beam-down system; PT: solar parabolic-trough system; DS: solar dish system; PV: photovoltaics

Table 2. Demonstration solar central receiver systems [39,40]

Country	Developed by	SCR systems	Turbine power/ Thermal power	Tower height (m)	Heliostats number	Solar field maximum aperture area (m <sup>2</sup> )	Storage	Heat transfer medium	Location	Start year
Australia	CSIRO	CSIRO solar tower	-	30	450	800	-	Water/Steam	Newcastle, New South Wales	2006
	Solastor	Cooma tower	-	-	-	-	-	-	Cooma, New South Wales	2007
Australia	Graphite Energy	Lake Cargelligo	3 MW <sub>e</sub>	-	620	6,080	Yes	Water/Steam	Lake Cargelligo, New South Wales	2011
	Vast Solar	Jemalong Solar Thermal Station	1.1 MW <sub>e</sub>	25 (5x)	3500	15,000	Yes	Sodium	Jemalong, New South Wales	2016
China	CAS	DAHAN tower plant	1 MW <sub>e</sub>	120	100	10,000	Yes	Water/Steam	Yanqing, Beijing	2012
Cyprus	Cyprus Institute	Pentakomo solar field	-	-	50	-	-	-	Cyprus	-
France	CNRS-PRGMES	Themis solar tower	2 MW <sub>e</sub>	104	201	11,800	Yes	Molten salts	Tangassonne	1983
Germany	DJR	Jülich solar tower	1.5 MW <sub>e</sub>	60	2153	17,650	Yes	Air	Jülich	2008
Germany	-	Algeria CSP tower pilot plant	7 MW <sub>e</sub>	-	-	-	-	Air	Boughzoul, Medea	2013
Greece	ACME	MINOS CSP tower	50 MW <sub>e</sub>	-	-	-	-	Water/Steam	Crete	-
India	ACME	Acme solar thermal tower	2.5 MW <sub>e</sub>	46	14,280	16,222	No	Water/Steam	Bikaner, Rajasthan	2011
India	AORA	AORA Solar Tulip Tower	0.1 MW <sub>e</sub> +0.17 MW <sub>e</sub>	-	-	-	Yes	-	Samar	2009
Israel	BrightSource	Solar Energy Center (SEDC)	6 MW <sub>t</sub>	60	1,600	-	-	-	Rotem	2008
Italy	WIS	WIS solar tower	-	54	64	-	-	-	Rehovot	1988
Italy	-	EURELIOS	1 MW <sub>e</sub>	55	182	-	Yes	Water/Steam	Adriano	1981
Mexico	-	Heliostat test facility	-	32	16	-	-	-	Scnora	2010
Saudi Arabia	Solar Tower Technologies (STT)	-	-	-	66	528	-	-	Riyadh	2015
South Korea	Daesung Energy	Daegu Solar Power Tower	0.2 MW <sub>e</sub>	50	450	1,800	-	Air	Daegu	2011
Spain	Abengoa Solar	Eureka	2 MW <sub>e</sub>	50	35	4,200	-	Water/Steam	Sanlúcar la Mayor, Sevilla	-
	-	CTAER variable geometry solar test facility	8 MW <sub>t</sub>	-	13	1,560	-	-	Tabernas, Almeria	2012
	-	Solugas	4.6 MW <sub>e</sub>	-	-	-	No	Air	Sanlúcar la Mayor, Sevilla	2013
Spain	AORA	AORA Solar Tulip Tower	0.1 MW <sub>e</sub>	-	-	-	-	-	Tabernas, Almeria	2012
	Almeria	Almeria	7 MW <sub>t</sub>	80	300	82,500	Yes	-	Tabernas, Almeria	1983
Spain	PSA	SSPS-CRS	2.7 MW <sub>t</sub>	43	111	-	-	Air	Tabernas, Almeria	1981
Turkey	Greenway CSP	Greenway CSP Mersin Solar Tower Plant	5 MW <sub>t</sub>	60	510	-	Yes	Water/Steam	Mersin	2012
UAE	Cosmo Oil, Masdar, Tokyo Institute of Technology	Solar Beam Down Plant	0.1 MW <sub>t</sub>	16	33	280.5	-	-	Masdar City	2010
USA	eSolar	Sierra Sun Tower	5 MW <sub>e</sub>	55	24,360	27,670	No	Water/Steam	Lancaster, California	2009
	-	Solar One	10 MW <sub>e</sub>	-	1,818	72,650	-	Water	Daggett, California	1982-1986
	-	Solar Two	10 MW <sub>e</sub>	-	1,926	82,750	-	Molten Salt	Daggett, California	1995-2009
USA	SANDIA	NSTTF	6 MW <sub>t</sub>	61	218	2,800	-	-	Albuquerque, New Mexico	-



Table 3. Commercial solar central receiver systems [39,40]

Country	Developed by	SCR systems	Turbine power (MW)	Tower height (m)	Heliostats number	Solar field maximum aperture area (m <sup>2</sup> )	Storage	Heat transfer medium	Location	Start or planned start year	Status
Australia	Aalborg CSP	Sundrop CSP Project	1.5	127	23,000	51,500	No	Water/Steam	Port Augusta	2016	Under construction
Chile	Abengoa Solar	Atacama-1	110	243	10,600	1,484,000	Yes	Molten Salt	Calama	2018	Under construction
	Solar Reserve	Copiapó	260	-	-	-	Yes	-	Copiapó	2019	Under development
	BrightSource Energy, Shanghai Electric Group	Qinghai Deilingha Solar Thermal Generation Project	270	-	-	-	Yes	Molten Salt	Qinghai	2017	Under development
China	Qinghai CSP Electric Power Group	Golmud	200	-	-	-	Yes	Molten Salt	Qinghai	2018	Under construction
	Supcon Solar	Deilingha Supcon Tower Plant	50	80	217,440	434,880	Yes	-	Qinghai	-	Under construction
Israel	Megaim Solar Power Ltd	Ashalim Plot B	121	250	50,600	1,052,480	No	Water/Steam	Ashalim	2017	Under construction
Morocco	ACWA	NOOR III	150	-	-	-	Yes	-	Ouarzazate	2017	Under construction
South Africa	Abengoa Solar	Khi Solar One	50	205	4,120	576,800	Yes	Water/Steam	Uppington	2016	Operational
	ACWA, Solar Reserve	Redstone Solar Thermal Power Plant	100	-	-	-	Yes	Molten Salt	Postmasburg	2018	Under development
Spain	Abengoa Solar	PS10 Solar Power Plant	11	115	624	75,000	Yes	Water/Steam	Seville	2007	Operational
	Abengoa Solar	PS20 Solar Power Plant	20	165	1,255	150,000	Yes	Water/Steam	Seville	2009	Operational
	Torresol Energy	Gemasolar	20	140	2,650	304,750	Yes	Molten salts	Seville	2011	Operational
USA	BrightSource Energy, Google, NRG Energy	Ivanpah Solar Power Facility	377	137	175,000	2,600,000	No	Water/Steam	San Bernardino County, California	2014	Operational
	eSolar	Sierra SunTower	5	55	24,360	27,670	No	Water/Steam	Lancaster, California	2009	Operational
	Solar Reserve	Crescent Dunes Solar Energy Project	110	160	10,347	1,197,148	Yes	Molten salts	Nye County, Nevada	2015	Operational

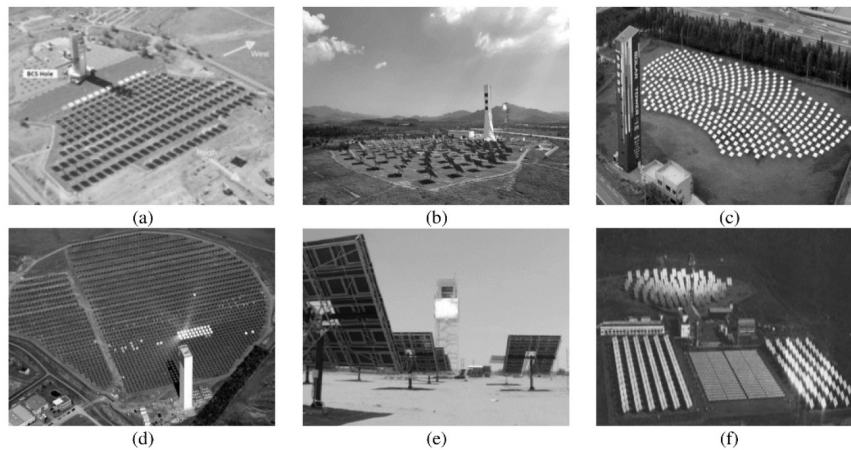


Fig. 9. Selected SCR demonstration systems: (a) NSTTF, USA (reprinted from [77], Copyright (1999), with permission from Elsevier) b) DAHAN tower plant, China (reprinted from [110], Copyright (2014), with permission from solar thermal group of Chinese Academy of Sciences) c) Daegu Solar Power Tower, South Korea (reprinted from [111], Copyright (2015), with permission from Elsevier) d) Jülich Solar Tower, Germany (reprinted from [133], Copyright (2011), with permission from the American Society of Mechanical Engineers) e) Heliostat Test Field, Sonora, Mexico (reprinted from [112], Copyright (2011), with permission from SolarPACES) f) SSPS-CRS facility, Spain (reprinted from [134], Copyright (1991), with permission from Springer).

## 6. Summary and conclusions

In this study, we have reviewed basic concepts associated with optics of solar central receiver systems. Typical system configurations were discussed along with the main components, heliostat, heliostat field, secondary concentrator, and receiver. A review of research studies on optical design, optimization and characterization of heliostats and heliostat fields was conducted. A large variety of optical analysis tools have been developed, and applied to design and optimization of demonstration and commercial facilities. A relatively small number of published studies report experimental results of on-sun optical characterization of central receiver systems. Modeling the optical performance of central receiver systems is an efficient and accurate approach for the design and optimization without incurring substantial costs associated with construction of early-stage prototype systems. The large number of available tools allows optical engineers to reduce the development time. However, the specific configurations of individual designs typically necessitate extension or development of new, advanced tools that allow for increased simulation accuracy and flexibility, in particular for problems coupling optics, thermophysics and thermochemistry in plant sub-systems. Optical design and optimization of SCR systems is the key to reduce their capital cost.

## Acknowledgments

Financial support by the Australian Renewable Energy Agency (ARENA), grant *Solar R&D 2014/RND005*, is gratefully acknowledged. We thank Dr Keith Lovegrove of IT Power Australia Pty Ltd for numerous discussions related to solar central receiver system design, performance and economics.

---

## Temperature-based optical design, optimisation and economics of solar polar-field central receiver systems with an optional compound parabolic concentrator

---

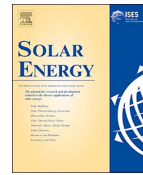
This chapter presents an optical and economic study of CRSs consisting of a polar heliostat field, a single-aperture receiver coupled to an optional CPC, and a tower [12]. The polar-field CRS outputs a relatively lower radiative power compared to surround-field CRSs. Optical and cost characteristics of heliostat fields are key parameters conditioning the overall efficiency and cost, and consequently industry-scale deployment of CRSs for power generation and chemical processing [132–134, 174, 175]. The cost model used in this study is derived from cost models in the System Advisory Model (SAM) of version 2011 [176], except that the cost model of cavity receivers is derived from SAM of the previous version 2007 [177]. The cost of cavity receivers in SAM 2007 is based on the complex and expensive tubular molten salt receivers. However, the recent developments in solar receivers promise a significant cost reduction [3].

Despite a large number of studies performed on the design and optimisation of CRSs [136, 178], temperature-based optimisation of CRSs for achieving optimal energetic and economic performance is absent in the literature. Moreover, the use of CPCs in CRSs was included in prior pertinent studies of high-temperature applications [179, 180]. However, the justification of the addition of a CPC in CRSs concerning the receiver temperature was rarely discussed in the literature. Hence, the effects of receiver temperature and the addition of a CPC on the energetic and economic performance of solar CRSs with a polar heliostat field are investigated in this study. Optical configurations of the polar-field CRSs with an optional CPC are optimised for their maximum annual solar-to-thermal and solar-to-exergy efficiencies, and the lowest levelised cost of exergy, respectively. Receivers in a wide range of temperatures varying from 600 K to 1800 K are investigated. The working temperature thresholds above which the energetic and economic performance benefit from the addition of a CPC are identified.



Contents lists available at ScienceDirect

Solar Energy

journal homepage: [www.elsevier.com/locate/solener](http://www.elsevier.com/locate/solener)

## Temperature-based optical design, optimization and economics of solar polar-field central receiver systems with an optional compound parabolic concentrator



Lifeng Li, Bo Wang, John Pye\*, Wojciech Lipiński\*

Research School of Electrical, Energy and Materials Engineering, The Australian National University, Canberra, ACT 2601, Australia

## ARTICLE INFO

## Keywords:

Concentrating solar technology  
Non-imaging optics  
Heliostat field  
Levelized cost of exergy

## ABSTRACT

Energetic and economic characteristics are studied for solar central receiver systems consisting of a polar heliostat field, a tower, a single-aperture cavity receiver, and an optional compound parabolic concentrator (CPC). System characterization and optimization are performed with a numerical model combining an in-house developed Monte-Carlo ray-tracing optical model, a simplified receiver heat transfer model, and a cost model based on the System Advisor Model (SAM). Based on the model, the effects of receiver temperature on the optical configuration of cost-optimal systems are elucidated, along with the benefits of using a CPC for improved energetic and economic performance. Under the assumptions made in this study, it is found that the overall minimum levelized cost of exergy is obtained by a non-CPC system with a receiver operated at approximately 900 K. A CPC benefits both the energetic and economic performance of systems only at elevated temperatures. The working temperature thresholds at which the energetic and economic performance benefit from the addition of a CPC are identified as 900 K and 1200 K, respectively. The general formulation of the model and broad range of values of the investigated parameters provide a universal predictive capability for studying techno-economic performance of concentrating solar thermal systems.

## 1. Introduction

Optical and cost characteristics of heliostat fields are key parameters conditioning the overall efficiency and cost, and consequently industry-scale deployment of solar central receiver systems (CRSs) for power generation and chemical processing (Kolb et al., 2011; Buck, 2012; Hinkley et al., 2013; Coventry and Pye, 2014; Pfahl, 2014; Bader and Lipiński, 2017; Dowling et al., 2017). High-temperature receivers are pursued for a potentially higher system-level efficiency from an increase of the power-cycle efficiency (Mehos et al., 2017). CRSs with receivers operated at temperatures above 1000 K require concentration ratios exceeding 1000 suns to mitigate receiver emission losses, imposing great challenges to the design of a heliostat field (Bader and Lipiński, 2017; Bayon et al., 2018; Behar et al., 2013; Carrillo et al., 2019; Dunham et al., 2013; Hischer et al., 2012; Ho and Iverson, 2014; Levêque et al., 2017; Li et al., 2016; Wang et al., 2020).

One possible avenue for meeting the high concentration ratio demand is the application of secondary optical concentrators such as compound parabolic concentrators (CPCs) (Winston et al., 2005; Chaves, 2017). A CPC increases the theoretical maximum concentration

ratio by a factor of  $1/\sin\theta_{\text{CPC}}$  or  $1/\sin^2\theta_{\text{CPC}}$  for a two-dimensional (2D) or three-dimensional (3D) CPC, respectively, where  $\theta_{\text{CPC}}$  is the CPC acceptance angle. The application of a CPC implies additional optical losses due to CPC backward reflection and surface absorption, as well as additional costs due to CPC manufacturing and maintenance (Cooper et al., 2013a,b; Li et al., 2019). The use of CPCs in CRSs has been investigated in prior pertinent studies. Pitz-Paal et al. (2011) optimized design parameters of the optical system consisting of a heliostat field, a CPC, and a receiver to maximize annual solar-to-chemical energy conversion efficiency for two exemplary solar fuel production processes at temperatures of 2000 K and 1400 K. Schmitz et al. (2006) compared the concentration cost and optical efficiency of CRSs with a CPC at different power levels, for single-aperture and multi-aperture receivers. A CPC was applied in the high-temperature solar beam-down system for increasing the concentration ratio as discussed by Yogeve et al. (1998). Segal and Epstein (2003) studied optimal working temperatures of solar beam-down systems with heliostat fields of selected densities for maximizing the plant-level efficiency. However, temperature-dependent optimization studies of CRSs for maximized energetic and economic performance are absent in the literature, as well as the justification of

\* Corresponding authors.

E-mail addresses: [john.pye@anu.edu.au](mailto:john.pye@anu.edu.au) (J. Pye), [wojciech.lipinski@anu.edu.au](mailto:wojciech.lipinski@anu.edu.au) (W. Lipiński).<https://doi.org/10.1016/j.solener.2020.05.088>

Received 10 November 2019; Received in revised form 20 May 2020; Accepted 26 May 2020

0038-092X/ © 2020 International Solar Energy Society. Published by Elsevier Ltd. All rights reserved.



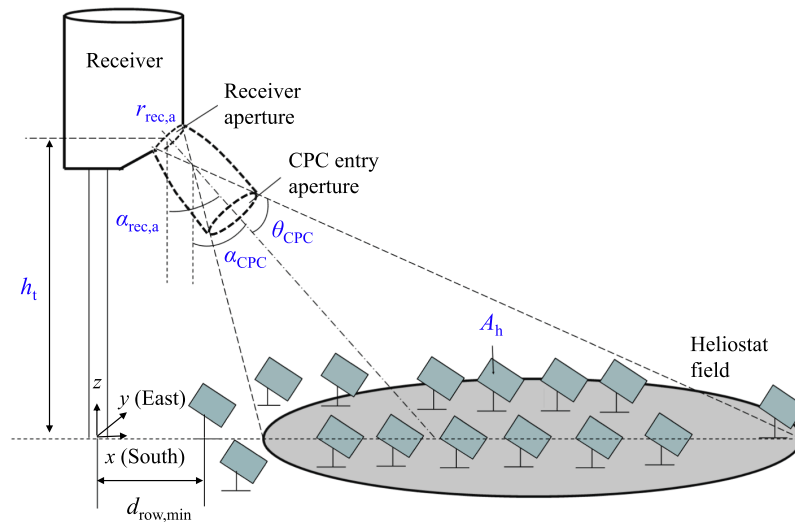


Fig. 1. A model solar central receiver system with a heliostat field, a tower, a cavity receiver, and an optional CPC.

parameters are studied, including tower height  $h_t$ , heliostat surface area  $A_h$ , receiver aperture radius  $r_{rec,a}$ , CPC acceptance angle  $\theta_{CPC}$ , CPC axis tilt angle  $\alpha_{CPC}$ , and efficiency trimming threshold  $\eta_{tr}$ .

The determination process of the heliostat field boundary for a system with a CPC is shown conceptually in Fig. 2. A surround heliostat field is firstly generated with a selected heliostat field layout pattern. Secondly, we calculate the conic section created by intersecting the CPC acceptance cone with the horizontal plane containing heliostat centers. The heliostats located outside the conic section are removed since rays reflected by these heliostats are rejected by the CPC due to backward reflection (Winston et al., 2005). The heliostat field is further trimmed by removing heliostats with the overall instantaneous (at autumn equinox noon) optical efficiency  $\eta_h$  lower than an efficiency trimming threshold  $\eta_{tr}$ .

The conic section can be an ellipse, a parabola, or a hyperbola depending on the relative position of the horizontal plane and the CPC acceptance cone. The shape and size of the intersected conic section are determined by the tower height  $h_t$ , the CPC acceptance angle  $\theta_{CPC}$ , and the CPC axis tilt angle  $\alpha_{CPC}$ , as schematically presented in Figs. 3 and 4. The range of  $\alpha_{CPC}$  is set as  $[0, \pi/2]$ , i.e., ranging from CPC facing vertically down ( $\alpha_{CPC} = 0$ ) to CPC facing horizontally towards the south/north in south/north hemispheres ( $\alpha_{CPC} = \pi/2$ ). We include configurations with a part of the CPC acceptance cone facing towards the sky (i.e., when  $\alpha_{CPC} + \theta_{CPC} > \pi/2$ , see Fig. 3) since their potential for better performance needs to be explored. Based on Fig. 4, in general, the size of the conic section increases with an increasing  $h_t$ ,  $\theta_{CPC}$ , or

$\alpha_{CPC}$ . The shape of the conic section changes from an ellipse to a parabola or a hyperbola with the increase of  $h_t$ ,  $\theta_{CPC}$ , or  $\alpha_{CPC}$ .

### 2.2. Assumptions

The model plant location is Alice Springs, Australia (-23.8°N, 133.9°E). The plant is located on flat land. Buie sun shape model with a circumsolar ratio of 0.02 is used (Buie et al., 2003). All heliostats have the same geometrical and optical properties, and all heliostat centers are located with the same vertical height to the ground. Heliostat is single-facet, point-focusing, and square. The reflectance of the heliostat and CPC surfaces are assumed to be specular, wavelength- and direction-independent, and equal to 0.9 and 0.95, respectively. Gaussian surface normal error distributions with assumed standard deviations of 1.5 mrad and 0.5 mrad are applied for the heliostat and CPC surfaces, respectively. The aiming point of all heliostats is at the center of the target aperture. Azimuth-elevation tracking with zero tracking error is assumed. Shading and blocking losses due to the tower, CPC, and receiver are neglected. We use the Campo field layout pattern as described by Collado and Guallar (2012) and discussed by Mutuberría et al. (2015). We assume the parameters defining the Campo layout pattern, including the total number of zones,  $n_{zone} = 3$ , the distance from the closest and furthest heliostats to the tower,  $d_{row,min} = 60$  m and  $d_{row,max} = 1500$  m, and reference blocking factor  $f_{b,ref} = 0.75$ . The selected total zone number of 3 is commonly found in the literature using the Campo layout pattern (Collado and Guallar,

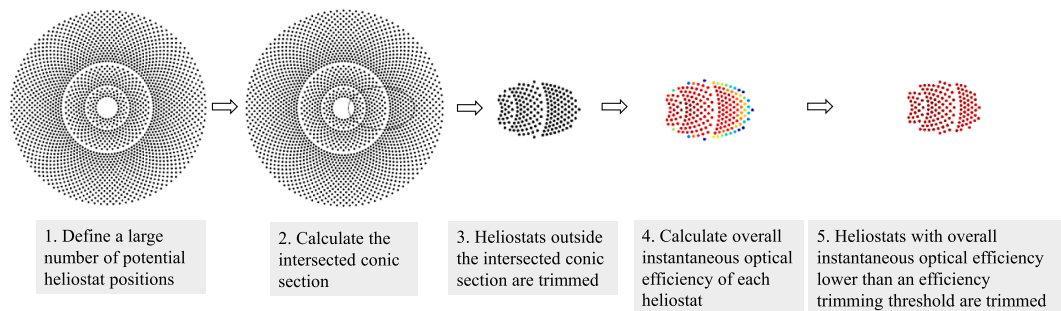


Fig. 2. Determination procedure of a heliostat field boundary, taking an elliptic conic section as an example (adapted from Pfahl et al., 2017).

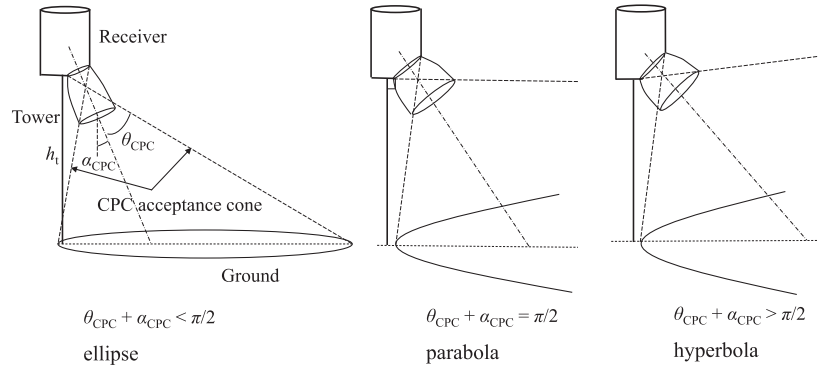


Fig. 3. Conic sections obtained by intersecting a CPC acceptance cone with a horizontal plane, for three specific combinations of tower height  $h_t$ , CPC acceptance angle  $\theta_{CPC}$ , and CPC axis tilt angle  $\alpha_{CPC}$ , resulting in elliptical (left), parabolic (center), and hyperbolic (right) section layouts, respectively.

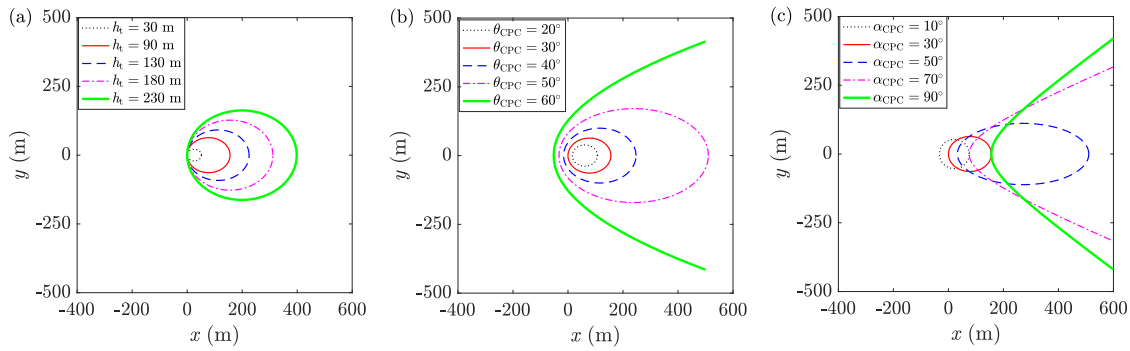


Fig. 4. Effects of (a) tower height  $h_t$ , (b) CPC acceptance angle  $\theta_{CPC}$ , and (c) CPC axis tilt angle  $\alpha_{CPC}$ , on the shape and size of conic sections, for a selected system of  $h_t = 90$  m,  $\theta_{CPC} = 30^\circ$ , and  $\alpha_{CPC} = 30^\circ$ .

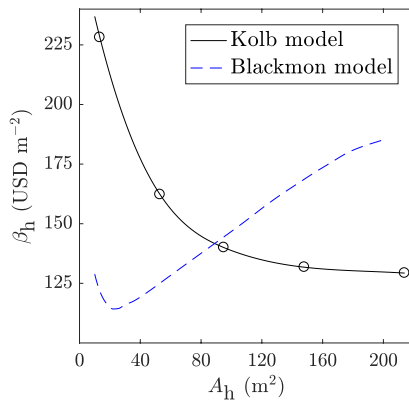


Fig. 5. Cost of heliostat per unit surface area  $\beta_h$  as a function of heliostat surface area  $A_h$  obtained using two models: the Kolb model (black curve) (Kolb et al., 2007; Blair et al., 2018) and the Blackmon model (blue curve) (Blackmon, 2012). For the Kolb model, cubic spline interpolation is used for obtaining costs of heliostats with  $A_h \leq 220$  m<sup>2</sup>.

2012; Collado and Guallar, 2013). The reference blocking factor is a parameter to control the radial spacing along the field of expanded layouts (Collado and Guallar, 2012). Note that the reference blocking factor is a different quantity as the blocking efficiency. Field density, the ratio of the total heliostat area and the land area covered by all heliostats, is determined by setting the distance between the centers of two adjacent heliostats equal to the heliostat diagonal length multiplied

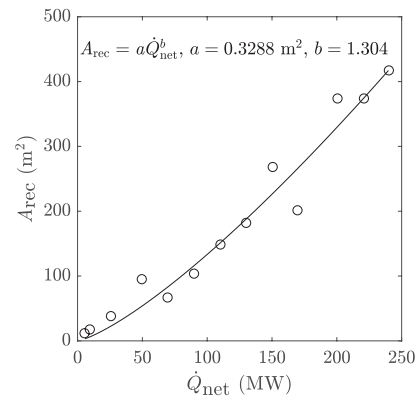


Fig. 6. Receiver area  $A_{rec}$  as a function of net receiver power  $\dot{Q}_{net}$  (in MW) optimized using SAM (Version 2014.1.14).

by an assumed factor of 1.1.

The cost of the CRS optical components are based on the System Advisory Model (SAM) (Blair et al., 2018). The cost of land  $C_{land}$  is assumed to be  $\beta_{land} A_{land}$ , where  $\beta_{land} = 2.5$  USD m<sup>-2</sup>. The land area  $A_{land}$  is calculated as the area of a rectangle that has one edge length equal to the distance between the two furthestmost heliostats along the global x-axis and the other edge length equal to the distance between the two furthestmost heliostats along the global y-axis. The cost of heliostat per unit area,  $\beta_h$ , depends on the heliostat size  $A_h$ . Different models have been discussed in the literature for estimating  $\beta_h$ . As shown in Fig. 5,



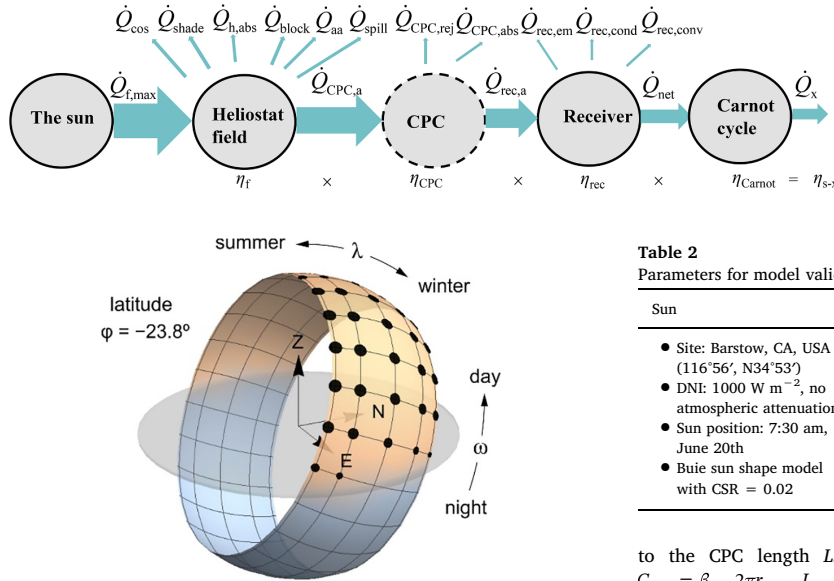


Fig. 7. Power flow, losses and efficiencies in a solar central receiver system.

Fig. 8. The sun path of the latitude of Alice Springs, Australia. The 32 simulated independent points on the sampling grid are marked by dots (Grigoriev et al., 2016) (Reproduced with permission from AIP Publishing).

five data points of  $\beta_h$  as a function of  $A_h$  are taken from Kolb et al. (2007).  $\beta_h$  is further reduced by 20% to match a relatively lower average  $\beta_h$  of 140 USD  $m^{-2}$  in SAM of version 2017.9.5 (Blair et al., 2018). The cubic spline interpolation method is applied for obtaining  $\beta_h$  of heliostats with  $A_h \leq 220 m^2$ .  $\beta_h$  of heliostats with  $A_h > 220 m^2$  are assumed to be the same as  $\beta_h$  of the 220  $m^2$  heliostat. For comparison, Fig. 5 includes another heliostat cost model by Blackmon (2012) that distributed heliostat costs into three categories and stated that the minimum  $\beta_h$  occurs for heliostats with  $A_h$  in the range of 30–50  $m^2$ . In this study, we employ the model by Kolb et al. (2007) where the relatively large heliostat is more cost-effective, which agrees well with heliostat sizes found in commercial CRSs. The total heliostat cost  $C_{h,tot}$  is equal to  $\beta_h n_h A_h$ . Tower cost  $C_t$  is assumed to be a function of tower height  $h_t$  as  $\beta_t \exp(0.0113h_t)$ , where  $\beta_t = 3,000,000$  USD. The cost of a cavity receiver  $C_{rec}$  is calculated as  $C_{rec} = C_{rec,ref} (A_{rec}/1571)^{0.7}$ , where  $C_{rec,ref}$  is the receiver reference cost and equal to 103,000,000 USD. We assume that the receiver area  $A_{rec}$  depends on the net receiver power  $\dot{Q}_{net}$ , and the dependency is obtained by optimizing CRSs with SAM of version 2014.1.14 (the cost of cavity receiver has been removed from SAM of versions  $> 2014.1.14$ ). The data are fitted with the power function  $A_{rec} = 0.3288 \dot{Q}_{net}^{1.304}$  and are shown in Fig. 6. The effect of receiver temperature on the receiver cost is neglected. Manufacturing of a 3D CPC has not been demonstrated yet for the scales considered in this study. Hence, we assume the cost  $C_{CPC}$  of a 3D CPC depends on the CPC reflective surface area with a factor of  $\beta_{CPC}$ . The CPC reflective surface area is proportional to the area of a cylindrical surface that has a radius equal to the CPC entry aperture radius  $r_{CPC,in}$  and a height equal

Table 1  
Parameters simulated in the optimization of systems without and with a CPC.

Parameters	Unit	Systems without a CPC	Systems with a CPC
Tower height $h_t$	m	30, 50, 90, 130, 170, 210, 250	30, 50, 90, 130, 170, 210, 250
Heliostat surface area $A_h$	$m^2$	40, 70, 100, 130, 160, 190, 220, 250	40, 70, 100, 130, 160, 190
Parameter determining target aperture radius, $f_a$	–	0.4, 0.75, 0.93, 0.97, 0.99	0.6, 0.7, 0.8, 0.9, 0.95
Efficiency trimming threshold $\eta_{tr}$	–	0.2, 0.3, 0.4, 0.5, 0.6, 0.7	0.2, 0.3, 0.4, 0.5, 0.6
Target aperture tilt angle $\alpha_{rec,a}$ or $\alpha_{CPC}$	$^\circ$	20, 30, 40, 50, 60, 70, 80	10, 30, 50, 70, 90
CPC acceptance angle $\theta_{CPC}$	$^\circ$	–	25, 30, 35, 40, 45, 50, 55, 60

Table 2  
Parameters for model validation (Wang et al., 2020b).

Sun	Heliostat field	Target
<ul style="list-style-type: none"> <li>Site: Barstow, CA, USA (116°56', N34°53')</li> <li>DNI: 1000 <math>W m^{-2}</math>, no atmospheric attenuation</li> <li>Sun position: 7:30 am, June 20th</li> <li>Buie sun shape model with CSR = 0.02</li> </ul>	<ul style="list-style-type: none"> <li>522 heliostats</li> <li>10 m <math>\times</math> 10 m, single-facet</li> <li>Normal slope error: 2 mrad</li> <li>Reflectance: 0.95</li> <li>Ideal focal length</li> </ul>	<ul style="list-style-type: none"> <li>62 m tower</li> <li>Aiming point: (0,0,62)</li> <li>Receiver aperture: 6 m <math>\times</math> 8 m</li> <li>Absorptance: 0.9</li> </ul>

to the CPC length  $L_{CPC}$ . Hence, the CPC cost is calculated as  $C_{CPC} = \beta_{CPC} 2\pi r_{CPC,in} L_{CPC}$ , where  $\beta_{CPC}$  is assumed as 3,000 USD  $m^{-2}$  ( $> 10$  times the cost per unit area of the most expensive heliostat currently available on the market) (Coventry and Pye, 2014). The sensitivity study on the assumed CPC cost is presented in Section 4.4

### 2.3. Performance metrics

Fig. 7 shows the power flow, losses, and efficiencies of a CRS. The basic optical performance metrics of a CRS include the instantaneous (at autumn equinox noon) and annual efficiencies of a heliostat field, a CPC, and a receiver, and the instantaneous (at autumn equinox noon) radiative power and concentration ratio obtained at the receiver aperture. Energy ratio  $\rho_{loss}$  is introduced to evaluate the system optical and radiative losses  $\dot{Q}_{loss}$  (used in Section 4.3),

$$\rho_{loss} = \frac{\dot{Q}_{loss}}{\dot{Q}_{t,max}} = \frac{\dot{Q}_{loss}}{\dot{q}_{sol} n_h A_h}, \quad (3)$$

where  $\dot{Q}_{t,max}$  is the maximum total radiative power collected when sun rays incident normally on an area equal to the total area of installed heliostats  $A_{h,tot} = n_h A_h$  ( $n_h$  is the total number of installed heliostats) and  $\dot{q}_{sol}$  is the real-time clear sky irradiance,  $W m^{-2}$ . The clear-sky irradiance is modeled as (Ineichen, 2008),

$$\dot{q}_{sol} = G_0 \exp(-\tau/\sin^{f_{DNI}} \alpha_{sol}) \quad (4)$$

where  $G_0$  is extra-terrestrial irradiance,  $W m^{-2}$ ,  $\tau$  is total atmospheric optical depth,  $\alpha_{sol}$  is the solar elevation angle, and  $f_{DNI}$  is a fitting parameter obtained from radiative transport model calculations at two different  $\alpha_{sol}$ . We take the following values of parameters recommended for a general calculation of direct irradiance:  $G_0 = 1618 W m^{-2}$ ,  $\tau = 0.606$ ,  $f_{DNI} = 0.491$  (Ineichen, 2008).

The performance metrics used in this study are elucidated next.



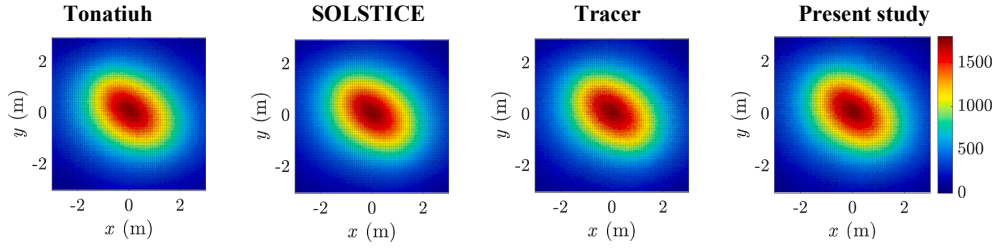


Fig. 9. Radiative flux distributions (in the unit of  $\text{W m}^{-2}$ ) on a target plane calculated by using selected ray-tracing tools.

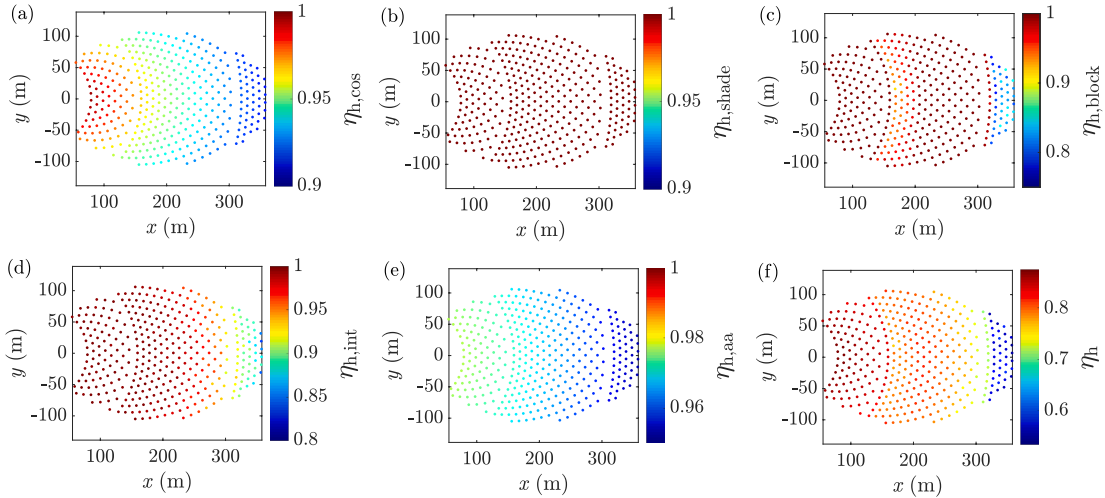


Fig. 10. Instantaneous (at autumn equinox noon) optical efficiencies of each heliostat: (a) cosine efficiency  $\eta_{h,\cos}$ , (b) shading efficiency  $\eta_{h,\text{shade}}$ , (c) blocking efficiency  $\eta_{h,\text{block}}$ , (d) interception efficiency  $\eta_{h,\text{int}}$ , (e) atmospheric attenuation  $\eta_{h,\text{aa}}$ , and (f) overall optical efficiency  $\eta_h$ , for a baseline system of  $h_t = 120$  m,  $A_h = 50$  m<sup>2</sup>,  $r_{\text{rec},a} = 3$  m, and  $\alpha_{\text{rec},a} = 60^\circ$ .

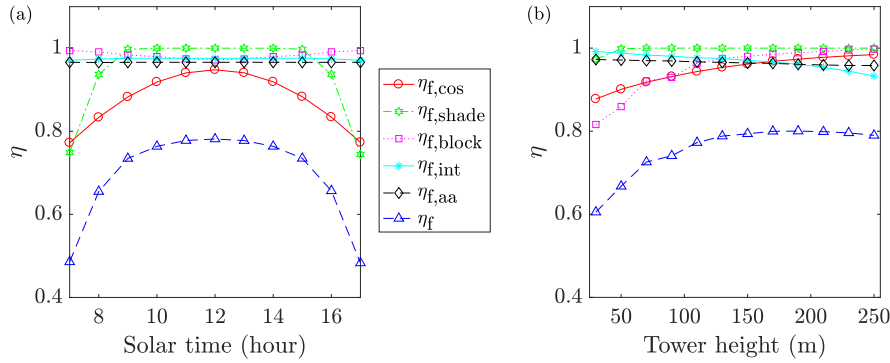


Fig. 11. Effects of (a) solar time and (b) tower height on the instantaneous (at autumn equinox noon) field-average optical efficiencies for the same baseline system as in Fig. 10.

(1) **Overall instantaneous optical efficiency of single heliostat or heliostat field**,  $\eta_h$  or  $\eta_f$ , is defined as the ratio of the radiative power,  $\dot{Q}_{h,a}$  or  $\dot{Q}_{f,a}$ , intercepted by target aperture and  $\dot{Q}_{h,\text{max}}$  ( $\dot{Q}_{h,\text{max}} = \dot{q}_{\text{sol}} A_h$ ) or  $\dot{Q}_{f,\text{max}}$ , respectively. Target aperture refers to the receiver aperture or the CPC entry aperture, for a system without or with a CPC, respectively. The overall optical efficiencies of a single heliostat and a heliostat field account for cosine, shading, absorption, blocking, atmospheric attenuation, and spillage losses (Li et al., 2016).

$$\eta_h \equiv \frac{\dot{Q}_{h,a}}{\dot{Q}_{h,\text{max}}} = \eta_{h,\cos} \eta_{h,\text{shade}} \eta_{h,\text{abs}} \eta_{h,\text{block}} \eta_{h,\text{aa}} \eta_{h,\text{int}} \quad (5a)$$

$$\eta_f \equiv \frac{\dot{Q}_{f,a}}{\dot{Q}_{f,\text{max}}} = \eta_{f,\cos} \eta_{f,\text{shade}} \eta_{f,\text{abs}} \eta_{f,\text{block}} \eta_{f,\text{aa}} \eta_{f,\text{int}} \quad (5b)$$

(2) **Instantaneous CPC transmission efficiency**,  $\eta_{\text{CPC}}$ , is defined as the ratio of the transmitted radiative power to the radiative power entering the CPC entry aperture. CPC optical losses include the absorbed radiation  $\dot{Q}_{\text{CPC,abs}}$  by CPC reflective surface and the

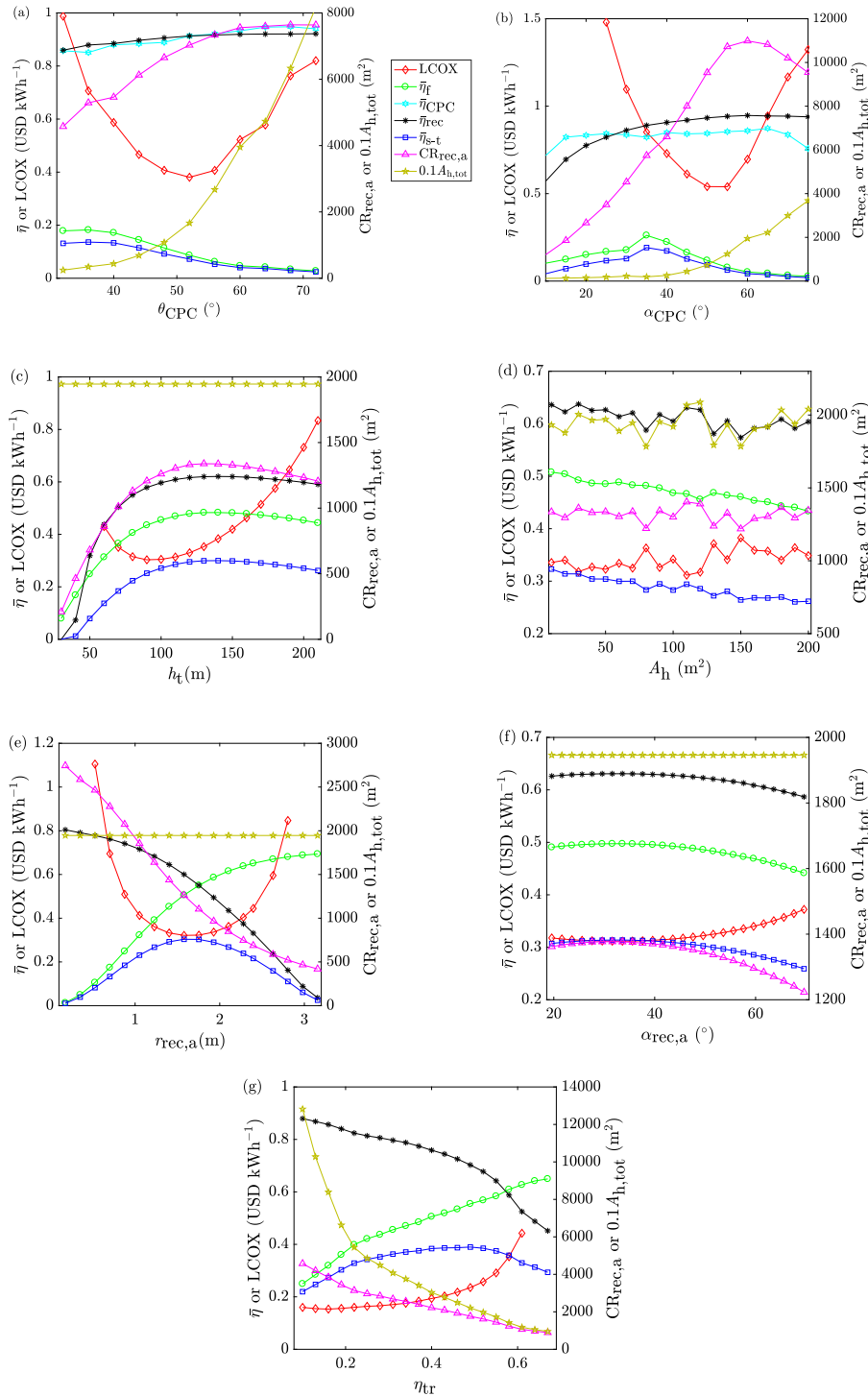


**Fig. 12.** Effects of design parameters including (a) CPC acceptance angle  $\theta_{CPC}$ , (b) CPC axis tilt angle  $\alpha_{CPC}$ , (c) tower height  $h_t$ , (d) heliostat surface area  $A_h$ , (e) receiver aperture radius  $r_{rec,a}$ , (f) receiver tilt angle  $\alpha_{rec,a}$ , and (g) trimming efficiency threshold  $\eta_{tr}$ , on LCOX and performance metrics including overall annual field optical efficiency  $\bar{\eta}_f$ , annual receiver absorption efficiency  $\bar{\eta}_{rec}$ , annual solar-to-thermal efficiency  $\bar{\eta}_{s-t}$ , total area  $A_{h,tot}$  of installed heliostats, annual CPC transmission efficiency  $\bar{\eta}_{CPC}$ , and concentration ratio  $CR_{rec,a}$  at receiver aperture. (a,b) are for a baseline system with a CPC:  $h_t = 90$  m,  $A_h = 100$  m<sup>2</sup>,  $r_{rec,a} = 0.6$  m,  $\eta_{tr} = 0$ ,  $\theta_{CPC} = 30^\circ$ ,  $\alpha_{CPC} = 30^\circ$ . (c-g) are for a baseline system without a CPC:  $h_t = 120$  m,  $A_h = 70$  m<sup>2</sup>,  $r_{rec,a} = 1.5$  m,  $\alpha_{rec,a} = 30^\circ$ . These results are obtained for assuming receiver temperature  $T_{rec}$  of 1600 K.

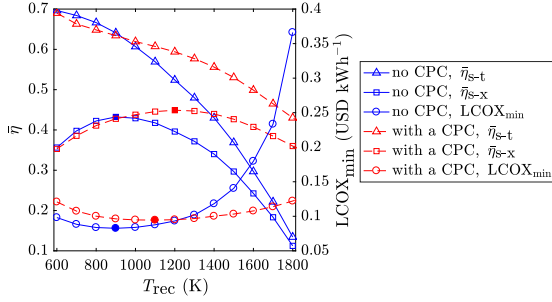


Fig. 13. Maximum annual solar-to-thermal efficiency  $\bar{\eta}_{s-t}$ , maximum annual solar-to-exergy efficiency  $\bar{\eta}_{s-x}$ , and  $LCOX_{\min}$  predicted for systems without and with a CPC as a function of receiver temperature  $T_{rec}$ .

rejected radiation  $\dot{Q}_{CPC,ref}$  due to backward reflection.

$$\eta_{CPC} \equiv \frac{\dot{Q}_{rec,a}}{\dot{Q}_{CPC,a}} = 1 - \frac{\dot{Q}_{CPC,abs} + \dot{Q}_{CPC,ref}}{\dot{Q}_{CPC,a}} \quad (6)$$

(3) **Instantaneous receiver absorption efficiency,  $\eta_{rec}$** , is defined and calculated as:

$$\eta_{rec} \equiv \frac{\dot{Q}_{net}}{\dot{Q}_{rec,a}} = 1 - \frac{\dot{Q}_{rec,em} + \dot{Q}_{rec,cond} + \dot{Q}_{rec,conv}}{\dot{Q}_{rec,a}} \quad (7)$$

where  $\dot{Q}_{net}$  is the net radiative power absorbed by the receiver at autumn equinox noon and  $\dot{Q}_{rec,a}$  is the total radiative power intercepted by the receiver aperture. Assumptions are made that the receiver is a perfectly-insulated blackbody with no reflective, conductive, or convective heat losses, i.e.  $\dot{Q}_{rec,cond} = \dot{Q}_{rec,conv} = 0$ , and the receiver is isothermal and operating at a nominal temperature  $T_{rec}$ . Under the assumption, the upper performance limit of the receiver can be calculated and used for characterizing the receiver performance without detailed knowledge of the receiver design (Fletcher and Moen, 1977; Pitz-Paal et al., 2011),

$$\eta_{rec} = 1 - \frac{\sigma T_{rec}^4}{G_1 CR_{rec,a}} \quad (8)$$

where  $\sigma$  is the Stefan–Boltzmann constant,  $5.6704 \times 10^{-8} \text{ W m}^{-2} \text{ K}^{-4}$ , and  $CR_{rec,a}$  is the flux concentration ratio over the receiver aperture area, defined as the ratio of the mean incident solar flux and the reference flux of  $G_1 = 1000 \text{ W m}^{-2}$ .

(4) **Instantaneous solar-to-thermal efficiency,  $\eta_{s-t}$**  is defined and

calculated as

$$\eta_{s-t} \equiv \frac{\dot{Q}_{net}}{\dot{Q}_{f,max}} = \eta_f \eta_{CPC} \eta_{rec} \quad (9)$$

$\eta_{s-t}$  measures the performance of the overall optical system comprising a heliostat field, a CPC, and a receiver.

(5) **Instantaneous solar-to-exergy efficiency,  $\eta_{s-x}$**  is defined as the ratio of the system exergy output  $\dot{Q}_x$  and  $\dot{Q}_{f,max}$ .  $\dot{Q}_x$  is equal to the net receiver power multiplied by the Carnot efficiency.

$$\dot{Q}_x = \dot{Q}_{net} \eta_{Carnot} = \dot{Q}_{net} \left(1 - \frac{T_L}{T_H}\right) \quad (10a)$$

$$\eta_{s-x} \equiv \frac{\dot{Q}_x}{\dot{Q}_{f,max}} = \eta_{s-t} \eta_{Carnot} = \eta_f \eta_{CPC} \eta_{rec} \eta_{Carnot} \quad (10b)$$

where  $T_H$  and  $T_L$  are the upper and lower operating temperatures of the (equivalent) Carnot heat engine, respectively (Romero and Steinfeld, 2012). In this study,  $T_L$  is taken as the ambient temperature assumed as 293 K and  $T_H = T_{rec} - \Delta T$ . The temperature drop  $\Delta T$  is associated with heat transport from the solar receiver to the hot reservoir of the (equivalent) Carnot heat engine.  $\eta_{s-x}$  measures the upper limit of solar-to-electricity efficiency for a solar power plant, as well as the maximum solar-to-fuel efficiency for an ideal cyclic process for a solar thermo-chemical plant.

The annual energetic performance is evaluated using the annual efficiency defined as:

$$\bar{\eta} = \frac{\sum_{\text{year}} \int_{\text{sunrise}}^{\text{sunset}} \dot{Q}_{\text{output}} dt}{\sum_{\text{year}} \int_{\text{sunrise}}^{\text{sunset}} \dot{Q}_{\text{input}} dt} \quad (11)$$

where  $\dot{Q}_{\text{output}}$  and  $\dot{Q}_{\text{input}}$  represent the output and input radiative power, respectively. The annual efficiencies used in this study are calculated using analogous expressions to Eq. (11), including overall annual field optical efficiency  $\bar{\eta}_f$ , annual CPC transmission efficiency  $\bar{\eta}_{CPC}$ , annual receiver absorption efficiency  $\bar{\eta}_{rec}$ , annual solar-to-thermal efficiency  $\bar{\eta}_{s-t}$ , and annual solar-to-exergy efficiency  $\bar{\eta}_{s-x}$ .

The economics of the solar central receiver optical system is characterized by the levelized cost of exergy (LCOX) defined as:

$$LCOX = \frac{CRF C_{\text{capital}}}{Q_x} \quad (12a)$$

$$CRF = \frac{i(1+i)^{n_{\text{year}}}}{(1+i)^{n_{\text{year}}} - 1} \quad (12b)$$

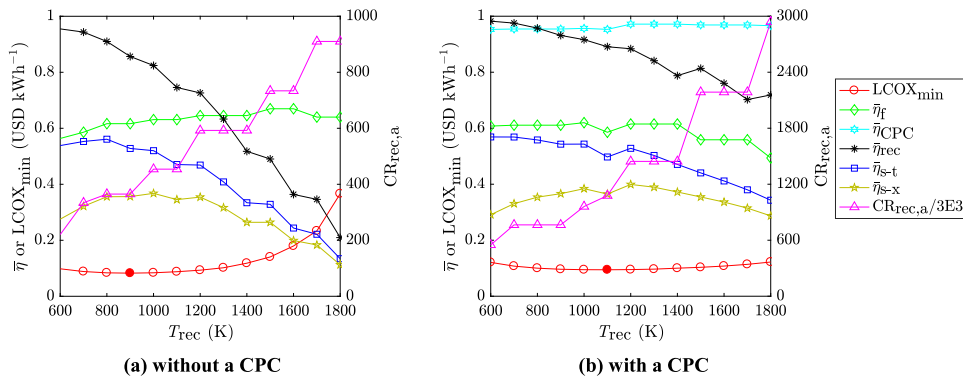


Fig. 14.  $LCOX_{\min}$  and performance metrics including overall annual field optical efficiency  $\bar{\eta}_f$ , annual receiver absorption efficiency  $\bar{\eta}_{rec}$ , annual solar-to-thermal efficiency  $\bar{\eta}_{s-t}$ , annual solar-to-exergy efficiency  $\bar{\eta}_{s-x}$ , annual CPC transmission efficiency  $\bar{\eta}_{CPC}$ , and concentration ratio  $CR_{rec,a}$  at the receiver aperture, for cost-optimal systems (a) without and (b) with a CPC as a function of receiver temperature  $T_{rec}$ .

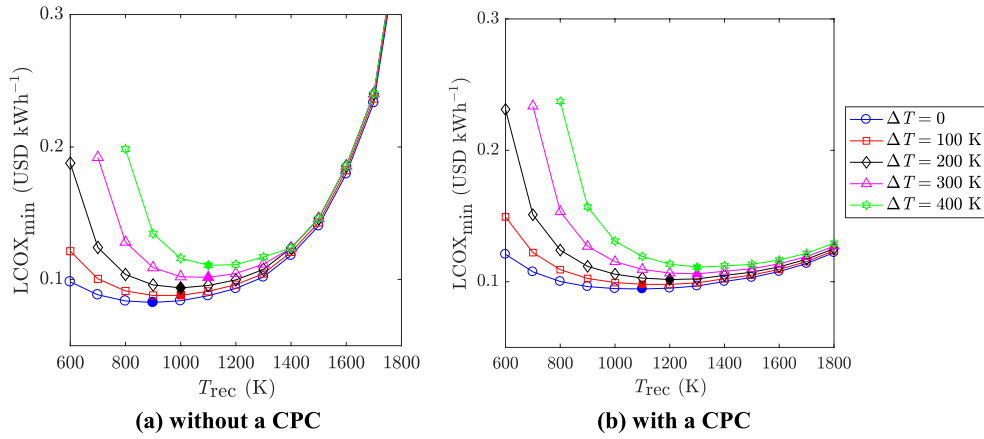


Fig. 15.  $LCOX_{min}$  of cost-optimal systems (a) without and (b) with a CPC, as a function of temperature drop  $\Delta T$  between the receiver and the hot reservoir of a Carnot heat engine.

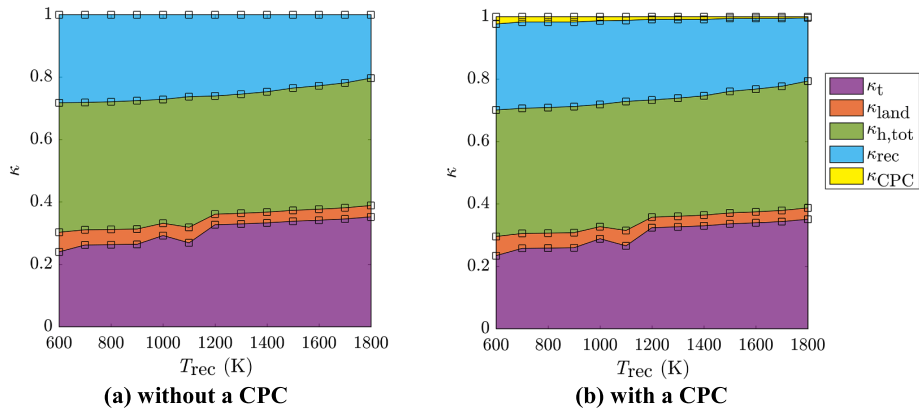


Fig. 16. Component cost fractions  $\kappa$  for cost-optimal systems (a) without and (b) with a CPC, as a function of receiver temperature  $T_{rec}$ .

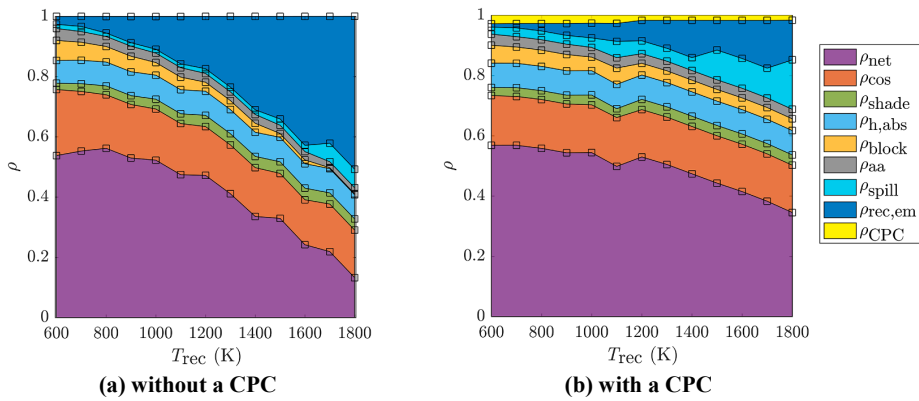


Fig. 17. Energy ratios  $\rho$  in the cost-optimal systems (a) without and (b) with a CPC, as a function of receiver temperature  $T_{rec}$ .

$$Q_x = \left(1 - \frac{T_L}{T_H}\right) \sum_{year} \int_{sunrise}^{sunset} \dot{Q}_{net} dt \quad (12c)$$

where CRF is the capital recovery factor,  $i$  is the real interest rate assumed as 5% per annum in this study,  $n_{year}$  is the number of annuities received assumed as 20 years, and  $C_{capital}$  is the total installation cost of land, heliostat, tower, receiver, and optional CPC:

$$\begin{aligned} C_{capital} &= C_{land} + C_{h,tot} + C_t + C_{rec} + C_{CPC} \\ &= \beta_{land} A_{land} + \beta_h n_h A_h + \beta_t \exp(0.0113 h_t) + 103,000,000 \\ &\quad (0.3288 \dot{Q}_{net}^{1.304} / 1571)^{0.7} + \beta_{CPC} 2\pi r_{CPC,in} L_{CPC} \end{aligned} \quad (13)$$

Operation and maintenance costs are not considered. For comparison, the fraction of each component cost  $\kappa$ , defined as the ratio of the

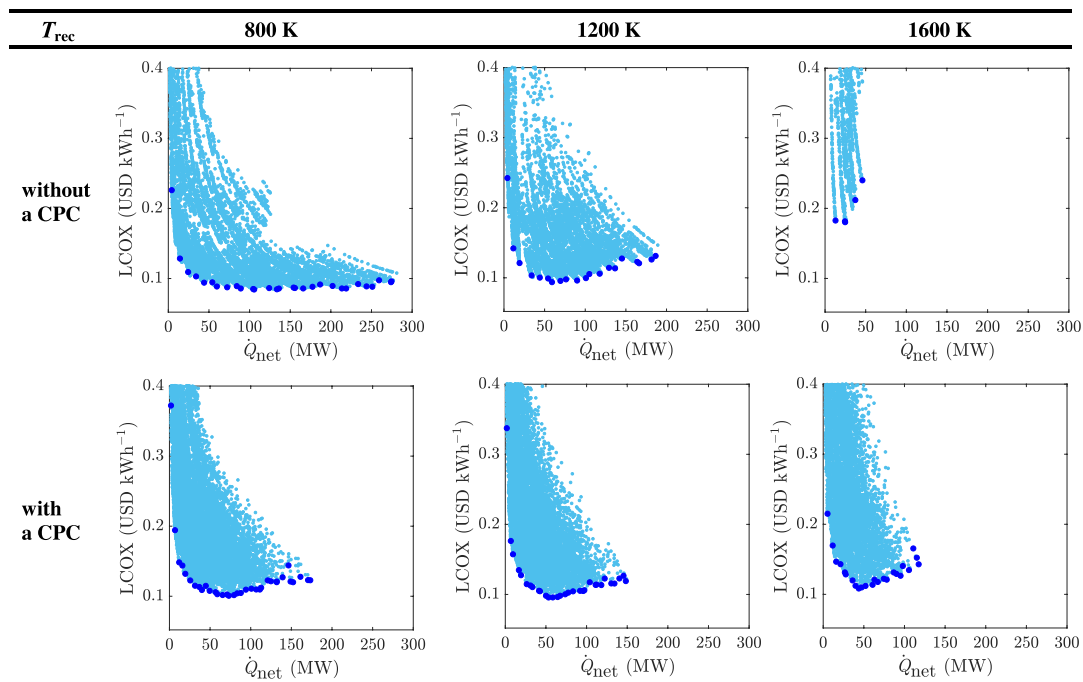


**Fig. 18.** Point clouds of LCOX and net receiver power  $\dot{Q}_{\text{net}}$  (at autumn equinox noon) for 10,080 configurations of non-CPC systems and 42,000 configurations of systems with a CPC and selected values of receiver temperatures  $T_{\text{rec}}$  of 800, 1200 and 1600 K. The dark blue points trace out the minimum-LCOX systems at selected power scales. The configurations with  $\text{LCOX} > 0.4 \text{ USD kWh}^{-1}$  are not shown.

component cost to the installation cost  $C_{\text{capital}}$  is calculated in Section 4.3 (e.g. tower cost fraction  $\kappa_t = C_t/C_{\text{capital}}$ ). The sensitivity study of each component cost is conducted and presented in Section 4.4.

### 3. Methodology

The Monte-Carlo ray-tracing (MCRT) method is applied in optical simulations (Modest, 2013; Li et al., 2019). In the MCRT model, rays carrying the same amount of radiative power are generated uniformly from assumed planes perpendicular to the normal of heliostats. Thus the computational efficiency is increased by avoiding simulating rays hitting the ground. The sun position relative to an observer on the ground as a function of solar time and site latitude is simulated with the method as described in Duffie and Beckman (1980) and Sproul (2007). Reflections from optical surfaces are modeled by considering slope errors (Bader et al., 2015). Atmospheric attenuation accounts for radiation losses occurring in the atmosphere when rays travel from the heliostat surface to the target aperture. Atmospheric attenuation is calculated as a function of the slant distance rays travel (Leary and Hankins, 1979). The annual heliostat field performance is evaluated using the method by Grigoriev et al. (2016) and by employing bicubic spline interpolation (Press et al., 1996) of results for discrete sun positions. Grigoriev et al. (2016) proved that sufficiently good accuracy is obtained with only 32 sampling points for a year, as shown in Fig. 8.

Simulations are carried out for all possible combinations of investigated parameters, as listed in Table 1. The selected values of the target aperture radius employed in the simulations are re-calculated for each heliostat field, to capture assumed fractions  $f_a$  of the incident Gaussian-distributed radiation reflected from the furthestmost heliostat (Rabl, 1985; Schmitz et al., 2006).

## 4. Results and discussions

### 4.1. Model validation

The in-house MCRT optical model is validated by simulating the PS10 heliostat field with the listed parameters in Table 2 (Wang et al., 2020b). Fig. 9 shows the predicted radiative flux distributions on a target plane using ray-tracing tools, including Tonatiuh, SOLSTICE, Tracer, and the MCRT code of the present study. Excellent agreement has been found. The MCRT code for modeling the 3D CPC was previously validated by computing the transmission-angle curve of a CPC with an acceptance angle of  $16^\circ$  and comparing the results with those from Winston et al. (2005) (Li et al., 2019). The optical model was used in a previous optical study of a novel solar beam-down system proposed by Li et al. (2020).

### 4.2. Parametric studies

In this section, we (i) discuss the instantaneous optical efficiencies of the heliostat field at both heliostat-level and field-level (Part 1) and (ii) explore the effects of design parameters (defined in Section 2.1) on the annual system optical, energetic, and economic performance characterized by the metrics defined in Section 2.3 (Part 2).

#### 4.2.1. Parametric studies: Part 1

A baseline system with a tower height  $h_t$  of 120 m, a heliostat surface area  $A_h$  of  $50 \text{ m}^2$ , a receiver aperture tilt angle  $\alpha_{\text{rec,a}}$  of  $60^\circ$ , and a receiver aperture radius  $r_{\text{rec,a}}$  of 3 m is investigated. We use the heliostat field created by removing the heliostats located outside the ellipse created by intersecting the CPC acceptance cone ( $\theta_{\text{CPC}} = 30^\circ$ ) and the horizontal plane containing heliostat centers. The overall instantaneous optical efficiency of each heliostat,  $\eta_h$ , is shown in Fig. 10. Fig. 11

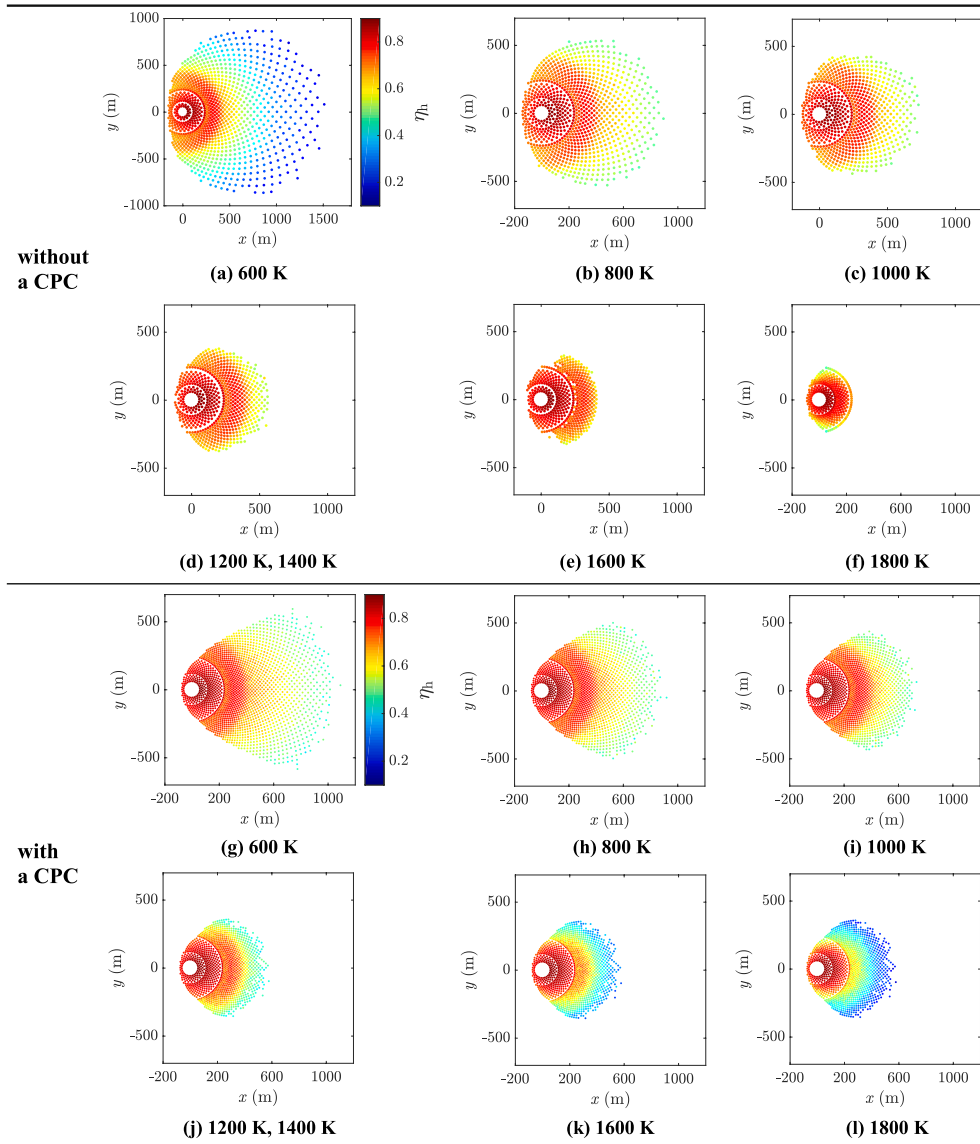


Fig. 19. Heliostat field layouts of cost-optimal systems without and with a CPC for selected receiver temperatures  $T_{rec}$  of 600, 800, 1000, 1200, 1400, 1600, and 1800 K. The colored scale indicates the overall instantaneous (at autumn equinox noon) optical efficiency  $\eta_h$  of each heliostat. Because of the limited simulated parameter space, some optimal configurations are applicable across several temperature values, as indicated in (d) and (j). Note that the x and y scales of Fig. 19a are different from those in Fig. 19b–l.

exhibits the field-average optical efficiencies of all heliostats as functions of solar time and tower height, the two most influential factors.

*Cosine efficiency* of a heliostat is dependent on the relative position of the sun, the heliostat, and the heliostat’s aiming point. The heliostat, whose center point is collinear with the center of the sun and the aiming point, has the maximum cosine efficiency. The cosine efficiency of other heliostats decreases with the increasing distance to the heliostat that has the maximum cosine efficiency (Fig. 10a). *Shading and blocking efficiencies* are mainly affected by the field density (Fig. 10b and c). In general, a higher field density leads to more shading and blocking losses. Shading and blocking losses also increase with a lower sun position (early morning and late afternoon, winter) and a lower tower, respectively. *Spillage loss* is determined by the relative size of the target

aperture and the sun image, the radiative flux distribution at the target aperture, and the angle between the incident beam axis and the normal of the target aperture. The size of the sun image on the target aperture increases with a larger heliostat area  $A_h$ , a larger heliostat surface slope error  $\delta_{h,err}$ , or a larger slant range  $d_{h,slant}$  from the heliostat to the target aperture. Hence, the spillage loss increases with a larger  $h_t$  and a larger distance from the heliostat to the tower (Figs. 10d and 11b). *Atmospheric attenuation loss* is determined by  $d_{h,slant}$ , thus the atmospheric attenuation loss increases with the increase of  $h_t$  and the distance from the heliostat to the tower (Figs. 10e and 11b). In general, the overall optical efficiency of a heliostat decreases with an increasing distance from the heliostat to the tower (Fig. 10f).

According to Fig. 11a, field-average cosine and shading losses

**Table 3**  
System configurations, field layouts, and performance of cost-optimal systems without and with a CPC for selected receiver temperatures.

Cases	Parameters	Symbols	Unit	Value							
				$T_{\text{rec}}$	K	600	800	1000	1200	1400	1600
Without a CPC	Design	$h_t$	m	130	130	130	130	130	130	130	90
		$A_h$	m <sup>2</sup>	250	190	190	160	160	130	100	
		$r_{\text{rec},a}$	m	16.7	9.9	8.1	6.3	6.3	4.7	2.8	
		$\eta_{\text{tr}}$	–	0.2	0.4	0.5	0.6	0.6	0.7	0.7	
		$\alpha_{\text{rec},a}$	°	50	60	60	60	60	60	70	
	Performance	LCOX <sub>min</sub>	USD kWh <sup>-1</sup>	0.098	0.084	0.084	0.093	0.118	0.180	0.366	
		$A_{h,\text{tot}}$	m <sup>2</sup>	355,500	189,620	153,900	117,760	117,760	77,870	35,400	
		CR <sub>rec,a</sub>	–	220	365	454	592	592	733	910	
		$\dot{Q}_{\text{net}}$	MW	186	106	83	60	47	25	8	
		Field layout	–	Fig. 19a	Fig. 19b	Fig. 19c	Fig. 19d	Fig. 19d	Fig. 19e	Fig. 19f	
With a CPC	Design	$h_t$	m	130	130	130	130	130	130	130	
		$A_h$	m <sup>2</sup>	70	70	70	70	70	70	70	
		$r_{\text{rec},a}$	m	6.9	5.6	4.7	3.6	3.6	2.8	2.3	
		$\eta_{\text{tr}}$	–	0.3	0.4	0.5	0.6	0.6	0.6	0.6	
		$\alpha_{\text{CPC}}$	°	30	30	30	50	50	50	50	
	Performance	$\theta_{\text{CPC}}$	°	60	60	60	60	60	60	60	
		LCOX <sub>min</sub>	USD kWh <sup>-1</sup>	0.121	0.100	0.095	0.095	0.100	0.108	0.122	
		$A_{h,\text{tot}}$	m <sup>2</sup>	149,800	134,820	117,530	100,310	100,310	100,310	100,310	
		CR <sub>rec,a</sub>	–	550	765	961	1445	1445	2187	2940	
		$\dot{Q}_{\text{net}}$	MW	82	74	64	54	50	44	38	
Field layout	–	Fig. 19g	Fig. 19h	Fig. 19i	Fig. 19j	Fig. 19j	Fig. 19k	Fig. 19l			

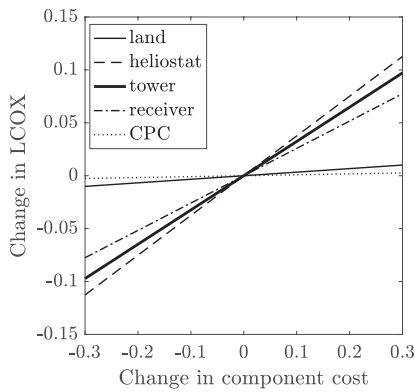


**Fig. 20.** Change of LCOX as a function of change in component costs for the example case of the cost-optimal system with a CPC and a receiver operated at 1200 K.

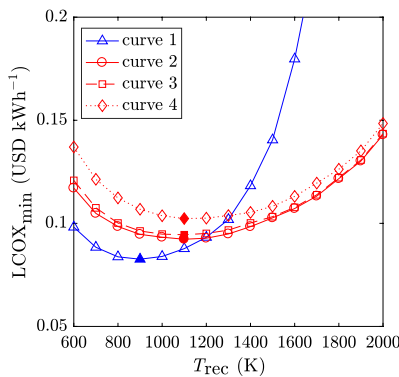


**Fig. 21.** Minimum LCOX of systems without a CPC (curve 1) and systems with a CPC of assumed CPC costs per unit area:  $\beta_{\text{CPC}} = 0$  (curve 2),  $\beta_{\text{CPC}} = 3,000$  USD m<sup>-2</sup> (curve 3), and  $\beta_{\text{CPC}} = 30,000$  USD m<sup>-2</sup> (curve 4).

greatly increase for a lower sun position in the early morning and the late afternoon. The overall field-average optical efficiency,  $\eta_f$ , peaks at solar noon. Based on Fig. 11b,  $\eta_f$  peaks at  $h_t = 180$  m, as a result of the trade-off between the increase in spillage loss and atmospheric attenuation and the decrease in cosine and blocking losses for larger tower heights.

#### 4.2.2. Parametric studies: Part 2

In this section, we investigate the effects of design parameters on the annual system optical, energetic, and economic performance evaluated by the metrics including overall annual field optical efficiency  $\bar{\eta}_f$ , annual CPC transmission efficiency  $\bar{\eta}_{\text{CPC}}$ , annual receiver absorption efficiency  $\bar{\eta}_{\text{rec}}$ , annual solar-to-thermal efficiency  $\bar{\eta}_{s-t}$ , concentration ratio CR<sub>rec,a</sub> at receiver aperture, total number  $A_{h,\text{tot}}$  of heliostats, and LCOX. Baseline systems are defined for systems without and with a CPC and given in the caption of Fig. 12. The receiver temperature is assumed as 1600 K. One parameter is varied at a time while other parameters are taken from the baseline parameter set. The results of MCRT simulations are plotted in Fig. 12. For the parametric studies of systems with a CPC (Fig. 12a and b), the heliostat field boundary is determined without the trimming of low-efficiency heliostats, i.e.,  $\eta_{\text{tr}} = 0$ . For the parametric studies of systems without a CPC (Fig. 12c–g), the heliostat field boundary is fixed as fan-shape with a cone angle of 72° and a radius of 300 m. The effects of each parameter are summarized next.

The CPC acceptance angle  $\theta_{\text{CPC}}$  has multiple effects on the system performance. The actual concentration ratio provided by a 3D CPC, CR<sub>CPC</sub>, is equal to  $\eta_{\text{CPC}}$  multiplied by the theoretical maximum CR boost, i.e.,  $\text{CR}_{\text{CPC}} = \eta_{\text{CPC}}/\sin^2\theta_{\text{CPC}}$ . For a larger  $\theta_{\text{CPC}}$ , the theoretical maximum CR boost decreases, while  $\eta_{\text{CPC}}$  increases due to less backward reflection (Fig. 12a). Moreover, the CPC entry aperture radius  $r_{\text{CPC},\text{in}}$  decreases with a larger  $\theta_{\text{CPC}}$  for a fixed CPC exit aperture radius  $r_{\text{rec},a}$ , resulting in more spillage and lower  $\bar{\eta}_f$ . Additionally, a larger  $\theta_{\text{CPC}}$  leads to an increased size of the heliostat field boundary (the conic section as indicated in Fig. 4b), resulting in a larger field containing more low-efficiency heliostats located further from the tower. All these discussed effects result in optimal  $\theta_{\text{CPC}}$  of around 36° and 52° that offer the maximum  $\bar{\eta}_{s-t}$  of around 0.126 and the minimum LCOX of around 0.39 USD kWh<sup>-1</sup>, respectively. The size of the heliostat field increases as the CPC tilt angle  $\alpha_{\text{CPC}}$  increases, as indicated in Fig. 4c, leading to the increase of  $A_{h,\text{tot}}$ , CR<sub>rec,a</sub>, and  $\bar{\eta}_{\text{rec}}$  (Fig. 12b).

Referring to Fig. 12c,  $\bar{\eta}_f$  and CR<sub>rec,a</sub> peak at tower height  $h_t = 130$  m,



due to the decrease in the cosine and blocking losses and the increase in the atmospheric attenuation and the spillage losses with increasing  $h_t$ , as explained in the discussion of Fig. 11b. Optimal  $h_t$  are identified at approximately 140 m and 90 m for the baseline systems that offer the maximum  $\bar{\eta}_{s-t}$  of around 0.3 and the minimum LCOX of around 0.3 USD kWh<sup>-1</sup>, respectively. As discussed previously in this section, a larger heliostat size  $A_h$  leads to a larger sun image at the target aperture, resulting in more spillage and lower  $\bar{\eta}_f$ . CR<sub>rec,a</sub> and  $\bar{\eta}_{rec}$  are proportional to  $A_{h,tot}$  which is fluctuating with the varying heliostat size (see Fig. 12d). The fluctuation is due to the trimming of heliostats near the field boundary. As shown in Fig. 12e, with a larger receiver aperture radius  $r_{rec,a}$ ,  $\bar{\eta}_f$  increases due to reduced spillage, while  $\bar{\eta}_{rec}$  decreases due to the increase of radiative emission loss. An optimal  $r_{rec,a}$  can be identified at around 1.6 m that offers a maximized value of the product of  $\bar{\eta}_f$  multiplied by  $\bar{\eta}_{rec}$ , namely  $\bar{\eta}_{s-t}$ . An optimal receiver aperture tilt angle  $\alpha_{rec,a}$  can be identified at around 31° that leads to a maximum fraction of the incident radiation captured by the receiver aperture, resulting in the highest  $\bar{\eta}_f$ ,  $\bar{\eta}_{rec}$ ,  $\bar{\eta}_{s-t}$ , and the minimum LCOX (Fig. 12f). This is because the size of the sun image on the target aperture is significantly affected by the cosine of the angle between the incident beam axis and the normal of the target aperture. An optimal field efficiency trimming threshold  $\eta_{tr}$  can be identified at around 0.52 that offers the maximum  $\bar{\eta}_{s-t}$  of around 0.38 (Fig. 12g).  $\bar{\eta}_f$  increases with a larger  $\eta_{tr}$  due to trimming more of the low-efficiency heliostats. However, a larger  $\eta_{tr}$  results in lower CR<sub>rec,a</sub> and radiative power  $Q_{rec,a}$  entering the receiver, thus lower  $\bar{\eta}_{rec}$  and LCOX, respectively.

#### 4.3. Optimization

We optimize optical configurations of CRSs for the receiver temperature  $T_{rec}$  varying from 600 K to 1800 K in 100 K increments. At each  $T_{rec}$ , we optimize the CRS for the maximum annual solar-to-thermal efficiency  $\bar{\eta}_{s-t}$ , the maximum annual solar-to-exergy efficiency  $\bar{\eta}_{s-x}$ , and the minimum LCOX (results are shown in Fig. 13). The parameter space is given in Table 1. The default temperature drop  $\Delta T$  for calculating the receiver absorption efficiency is assumed as zero unless stated otherwise. Fig. 14 depicts the performance of the cost-optimal systems without and with a CPC as functions of  $T_{rec}$ . These figures exhibit the core findings in this study. Under the assumptions made in this study, based on Figs. 13 and 14, we draw the following conclusions.

- (1) For receivers with  $T_{rec} < 1000$  K, systems without and with a CPC show similar optical and energetic performance. For receivers with  $T_{rec} \geq 1000$  K,  $\bar{\eta}_{s-t}$  and  $\bar{\eta}_{s-x}$  are higher for systems with a CPC than those of no-CPC systems, which is consistent with the findings by Segal and Epstein (1999) that the use of a CPC is energetically justified when the receiver temperature is above approximately 1000 K. The maximum  $\bar{\eta}_{s-x}$  of 0.43 and 0.45 are observed at  $T_{rec} = 900$  and 1200 K, respectively, for the system without and with a CPC.
- (2) The minimum LCOX of 0.083 and 0.095 USD kWh<sup>-1</sup> for the system without and with a CPC are observed for  $T_{rec} = 900$  and 1100 K, respectively. The addition of a CPC has a minor impact on the LCOX of systems with  $T_{rec} < 1200$  K. The minimum LCOX for systems without a CPC increases significantly when  $T_{rec}$  exceeds 1200 K, wherein the benefit of better economics resulting from applying a CPC shows up. The application of a CPC mitigates the significant increase of LCOX of systems with elevated  $T_{rec}$ . The magnitude of the improvement in economics by the addition of a CPC increases with an increasing  $T_{rec}$ .
- (3) The overall optimal configuration for minimizing the cost of collected exergy is found to be a non-CPC system operated at 900 K which is the typical CRS currently on the market. The overall optimal configuration for maximizing  $\bar{\eta}_{s-x}$  is found to be a system with a CPC and operated at 1200 K. Moderate high receiver operating temperatures of about 1000–1200 K have been targeted for the

next-generation CSP systems such as particle-based systems and systems with sodium working fluids for enabling the achievement of higher plant thermal efficiency of  $\geq 50\%$  by the use of a supercritical CO<sub>2</sub> Brayton cycle or combined cycles (Mehos et al., 2017).

- (4) For applications at very high receiver temperatures above 1200 K, a CPC is required for better both energetic and economic performance. However, even with a CPC, LCOX<sub>min</sub> increases with the increase of  $T_{rec}$  for  $T_{rec} > 1200$  K. This result suggests that the high-temperature systems may be more suitable for higher-value applications than electricity generation, for example, thermochemical production of solar fuels and chemical processing, whose advantages are not entirely expressed by LCOX.

The stepwise curves observed in Fig. 14 is due to simulated parameter spaces, as in Table 1. Some cost-optimal optical configurations are applicable across several temperature values, as will be shown in Fig. 19.

Figs. 15–19 show the effects of  $T_{rec}$  on selected characteristics of the cost-optimal systems without and with a CPC. Fig. 15 presents the effect of the temperature drop  $\Delta T$  (defined in Section 2.3) varying from 0 to 400 K in 100 K increments on LCOX<sub>min</sub> for each  $T_{rec}$ . It is found that as  $\Delta T$  increases, a higher  $T_{rec}$  is desired for better economics, which is consistent with the previous findings by McGovern and Smith (2012). Fig. 16 shows the fraction  $\kappa$  of each component cost to the total installation cost  $C_{capital}$ , for the cost-optimal systems at selected receiver temperatures. An increase of the tower cost fraction  $\kappa_t$  is observed as  $T_{rec}$  increases, for both systems without and with a CPC. The use of a CPC increases the heliostat cost fraction  $\kappa_h$  for systems operated at elevated  $T_{rec}$ , which is favorable for the economics since a larger heliostat total area yields an increased exergy output. Fig. 17 shows the energy ratios  $\rho$  in the cost-optimal systems. For the system without a CPC (Fig. 17a), the ratio  $\rho_{rec,em}$  of the receiver emission loss increases significantly with an increasing  $T_{rec}$ . The ratio  $\rho_{net}$  of the useful energy output ( $\rho_{net} = \bar{\eta}_{s-t}$ ) decreases and is below 0.4 for  $T_{rec} > 1400$  K. As seen in Fig. 17b, when a CPC is added, the changing gradient of  $\rho_{rec,em}$  and  $\rho_{net}$  with  $T_{rec}$  are much smaller ascribable to the greatly increased CR<sub>rec,a</sub>. Fig. 18 shows the LCOX and the net receiver power  $Q_{net}$  at autumn equinox noon for all modeled optical configurations for selected  $T_{rec} = 800, 1200, \text{ and } 1800$  K. The maximum obtained  $Q_{net}$  is found to be approximately 280 MW and 180 MW, respectively, for systems without and with a CPC. Multiple system configurations of different power output offer proximate LCOX.

Based on Table 3,  $Q_{net}$  from the cost-optimized systems either without or with a CPC is below 100 MW, due to the limited total area of heliostats in a polar field. Although a larger heliostat field can be designed for coupling with an external receiver, a very high heat loss and limited heat transfer area exclude the deployment of such a receiver in high-temperature processing. For low-temperature applications, higher power output can be obtained by the design of optical configuration with a surround field and an external receiver. Hence, other approaches for high-temperature solar processing at higher power levels should be explored.

Fig. 19 shows heliostat field layouts of the cost-optimal systems without and with a CPC, for selected  $T_{rec}$  in the range of 600–1800 K in 200 K increments. The relevant parameters of each cost-optimal system are shown in Table 3. At elevated temperatures, the least-cost systems (whether without or with a CPC) have smaller heliostats, smaller receiver apertures, a higher efficiency trimming threshold, resulting in a smaller field area and smaller net receiver power. The tower heights of cost-optimal systems are essentially the same at 130 m for both cases without and with a CPC.

#### 4.4. Sensitivity study

The sensitivity of LCOX to the variation of selected assumed



component cost parameters is studied by varying the cost of land, heliostat, tower, receiver, and CPC in the range  $\pm 30\%$ . The results shown in Fig. 20 demonstrate that the tower and heliostat costs are the most influential parameters on the LCOX, primarily because of their large shares in the capital investment. Besides, we conducted the optimization with the Blackmon heliostat cost model for the purpose of comparison. It is found that replacing the Kolb model with the Blackmon model has a minor impact on the main conclusions drawn from Fig. 13. The main effect is that the heliostat size of the cost-optimal no-CPC systems, as in Table 3, is changed to  $40 \text{ m}^2$  for all simulated receiver temperatures.

To elucidate the effect of the assumed CPC cost per unit area on the minimum LCOX, we consider three values of the CPC cost per unit area,  $\beta_{\text{CPC}} = 0, 3000, \text{ and } 30,000 \text{ USD m}^{-2}$  (Fig. 21). A higher CPC cost per unit area leads to an increased minimum LCOX and a higher value of the receiver temperature threshold at which the addition of a CPC improves the system LCOX. However, the optimal receiver temperature for a minimum LCOX is constantly at  $1100 \text{ K}$ , independent of the assumed CPC cost per unit area.

## 5. Summary and conclusions

The effects of the receiver temperature and the addition of a compound parabolic concentrator (CPC) on the optical, energetic, and economic characteristics of solar central receiver systems have been investigated. Systems were optimized for the maximum annual solar-to-thermal efficiency, the maximum annual solar-to-exergy efficiency, and the minimum levelized cost of exergy, for receivers operated at temperatures in the range of  $600\text{--}1800 \text{ K}$ . We demonstrated and compared the optical configurations of the cost-optimal central receiver systems operated at each simulated receiver temperature. Parametric studies and optimization were carried out for both systems without and with a CPC, where we identified the temperature thresholds above which the system energetic and economic performance benefit from the addition of a CPC.

Under the assumptions made in this study, it was found that the minimum levelized cost of exergy for systems without and with a CPC is  $0.083$  and  $0.095 \text{ USD kWh}^{-1}$ , respectively, for receivers working at a temperature of  $900$  and  $1100 \text{ K}$ . At higher temperatures, high concentration ratios are required to mitigate the rapid increase of receiver emission losses, for which energetic and economic advantages of adding a CPC show up. The addition of a CPC improves system energetic and economic performance for receiver temperatures above  $900 \text{ K}$  and  $1200 \text{ K}$ , respectively.

## Declaration of Competing Interest

The authors declare that they have no known competing financial interests or personal relationships that could have appeared to influence the work reported in this paper.

## Acknowledgments

The financial support from the Australian Renewable Energy Agency (grant no 2014/RND005) is gratefully acknowledged. This research was undertaken with the assistance of resources and services from the National Computational Infrastructure (NCI), which is supported by the Australian Government. The authors thank Keith Lovegrove, Joe Coventry, and Johannes Pottas for discussing the economics of solar concentrators, and Juan F. Torres, Apurv Kumar, and Ye Wang for their help with supercomputing techniques and resources.

## References

Bader, R., Haussener, S., Lipiński, W., 2015. Optical design of multisource high-flux solar simulators. *J. Sol. Energy Eng.* 137 (2), 021012.

- Bader, R., Lipiński, W., 2017. Solar thermal processing. In: Blanco, M., Ramirez Santigosa, L. (Eds.), *Advances in Concentrating Solar Thermal Research and Technology*. Woodhead Publishing, pp. 403–447.
- Bayon, A., Bader, R., Jafarian, M., Fedunik-Hofman, L., Sun, Y., Hinkley, J., Miller, S., Lipiński, W., 2018. Techno-economic assessment of solid-gas thermochemical energy storage systems for solar thermal power applications. *Energy* 149, 473–484.
- Behar, O., Khellaf, A., Mohammedi, K., 2013. A review of studies on central receiver solar thermal power plants. *Renew. Sust. Energy Rev.* 23, 12–39.
- Blackmon, J.B., 2012. Heliostat size optimization for central receiver solar power plants. In: Lovegrove, K., Stein, W. (Eds.), *Concentrating Solar Power Technology: Principles, Developments and Applications*. Woodhead Publishing, pp. 536–576.
- Blair, N., DiOrio, N., Freeman, J., Gilman, P., Janzou, S., Neises, T., Wagner, M., 2018. System Advisor Model (SAM) General Description (Version 2017.9.5). National Renewable Energy Laboratory (NREL). NREL/TP-6A20-70414. Golden, CO. <https://www.nrel.gov/docs/fy18osti/70414.pdf>.
- Buck, R., 2012. Heliostat field layout using non-restricted optimization. In: *Proceedings of the 2012 SolarPACES Conference*, 11–14 September, Marrakech, Morocco.
- Buie, D., Monger, A., Dey, C., 2003. Sunshape distributions for terrestrial solar simulations. *Sol. Energy* 74 (2), 113–122.
- Carrillo, A.J., González-Aguilar, J., Romero, M., Coronado, J.M., 2019. Solar energy on demand: a review on high temperature thermochemical heat storage systems and materials. *Chem. Rev.* 119, 4777–4816.
- Chaves, J., 2017. *Introduction to Nonimaging Optics*. CRC Press.
- Collado, F.J., Guallar, J., 2012. Campo: generation of regular heliostat fields. *Renew. Energy* 46, 49–59.
- Collado, F.J., Guallar, J., 2013. A review of optimized design layouts for solar power tower plants with campo code. *Renew. Sust. Energy Rev.* 20, 142–154.
- Cooper, T., Dähler, F., Ambrosetti, G., Pedretti, A., Steinfeld, A., 2013a. Performance of compound parabolic concentrators with polygonal apertures. *Sol. Energy* 95, 308–318.
- Cooper, T., Ambrosetti, G., Pedretti, A., Steinfeld, A., 2013b. Theory and design of line-to-point focus solar concentrators with tracking secondary optics. *Appl. Opt.* 52 (35), 8586–8616.
- Coventry, J., Pye, J., 2014. Heliostat cost reduction – where to now? *Energy Procedia* 49, 60–70.
- Dowling, A.W., Zheng, T., Zavala, V.M., 2017. Economic assessment of concentrated solar power technologies: a review. *Renew. Sust. Energy Rev.* 72, 1019–1032.
- Duffie, J.A., Beckman, W.A., 1980. *Solar Engineering of Thermal Processes*. Wiley.
- Dunham, M.T., Kasetty, R., Mathur, A., Lipiński, W., 2013. Optical analysis of a heliostat array with linked tracking. *J. Sol. Energy Eng.* 135 (3).
- Fletcher, E.A., Moen, R.L., 1977. Hydrogen and oxygen from water. *Science* 197 (4308), 1050–1056.
- Grigoriev, V., Corsi, C., Blanco, M., 2016. Fourier sampling of sun path for applications in solar energy. *AIP Conf. Proc.* 1734, 020008.
- Hinkley, J.T., Hayward, J.A., Curtin, B., Wonhas, A., Boyd, R., Grima, C., Tadros, A., Hall, R., Naicker, K., 2013. An analysis of the costs and opportunities for concentrating solar power in Australia. *Renew. Energy* 57, 653–661.
- Hischier, I., Poživil, P., Steinfeld, A., 2012. A modular ceramic cavity-receiver for high-temperature high-concentration solar applications. *J. Sol. Energy Eng.* 134 (1), 011004.
- Ho, C.K., Iverson, B.D., 2014. Review of high-temperature central receiver designs for concentrating solar power. *Renew. Sust. Energy Rev.* 29, 835–846.
- Ineichen, P., 2008. A broadband simplified version of the Solis clear sky model. *Sol. Energy* 82, 758–762.
- Kolb, G.J., Jones, S.A., Donnelly, M.W., Gorman, D., Thomas, R., Davenport, R., Lumia, R., 2007. Heliostat cost reduction study. Sandia Laboratories Report, SAND2007-3293.
- Kolb, G. J., Ho, C. K., Mancini, T. R., and Gary, J. A., 2011. Power tower technology roadmap and cost reduction plan. Sandia Laboratories Report, SAND2011-2419.
- Leary, P.L., Hankins, J.D., 1979. A user's guide for MIRVAL—a computer code for comparing designs of heliostat-receiver optics for central receiver solar power plants. Sandia Laboratories Report SAND77-8280, 14.
- Levêque, G., Bader, R., Lipiński, W., Haussener, S., 2017. High-flux optical systems for solar thermochemistry. *Sol. Energy* 156, 133–148.
- Li, L., Coventry, J., Bader, R., Pye, J., Lipiński, W., 2016. Optics of solar central receiver systems: a review. *Opt. Express* 24 (14), A985–A1007.
- Li, L., Wang, B., Pottas, J., Lipiński, W., 2019. Design of a compound parabolic concentrator for a multi-source high-flux solar simulator. *Sol. Energy* 183, 805–811.
- Li, L., Yang, S., Wang, B., Pye, J., Lipinski, W., 2020. Optical analysis of a solar thermochemical system with a rotating tower reflector and a multi-receiver array. *Opt. Express* 28 (13), 19429–19445.
- Mehos, M., Turchi, C., Vidal, J., Wagner, M., Ma, Z., C. Ho, W. Kolb, C. Andraka, and A. Kruizenga, 2017. Concentrating solar power Gen3 demonstration roadmap. Technical report, NREL/TP-5500-67464.
- McGovern, R.K., Smith, W.J., 2012. Optimal concentration and temperatures of solar thermal power plants. *Energy Convers. Manag.* 60, 226–232.
- Modest, M.F., 2013. *Radiative Heat Transfer*, 3rd edition. Academic Press.
- Mutuberría, A., Pascual, J., Guisado, M.V., Mallor, F., 2015. Comparison of heliostat field layout design methodologies and impact on power plant efficiency. *Energy Procedia* 69, 1360–1370.
- Pfahl, A., 2014. Survey of heliostat concepts for cost reduction. *J. Sol. Energy Eng.* 136 (1), 014501.
- Pfahl, A., Coventry, J., Röger, M., Wolfertstetter, F., Vásquez-Arango, J.F., Gross, F., Arjomandi, M., Schwarzbözl, P., Geiger, M., Liedke, P., 2017. Progress in heliostat development. *Sol. Energy* 152, 3–37.
- Pitz-Paal, R., Botero, N.B., Steinfeld, A., 2011. Heliostat field layout optimization for

- high-temperature solar thermochemical processing. *Sol. Energy* 85, 334–343.
- Press, W. H., Teukolsky, S. A., Vetterling, W. T., Flannery, B. P., and Metcalf, M., 1996. *Numerical Recipes in Fortran 90: The Art of Parallel Scientific Computing, Volume 2 of Fortran Numerical Recipes*, second ed. Cambridge University Press.
- Rabl, A., 1985. *Active Solar Concentrators and Their Applications*. Oxford University Press, New York.
- Romero, M., Steinfeld, A., 2012. Concentrating solar thermal power and thermochemical fuels. *Energy Environ. Sci.* 5, 9234.
- Schmitz, M., Schwarzbözl, P., Buck, R., Pitz-Paal, R., 2006. Assessment of the potential improvement due to multiple apertures in central receiver systems with secondary concentrators. *Sol. Energy* 80 (1), 111–120.
- Segal, A., Epstein, M., 1999. Comparative performances of “tower-top” and “tower-reflector” central solar receivers. *Sol. Energy* 65 (4), 207–226.
- Segal, A., Epstein, M., 2003. Optimized working temperatures of a solar central receiver. *Sol. Energy* 75, 503–510.
- Sproul, A.B., 2007. Derivation of the solar geometric relationships using vector analysis. *Renew. Energy* 32, 1187–1205.
- Wang, B., Li, L., Pottas, J., Bader, R., Kreider, P., Wheeler, V.M., Lipiński, W., 2020a. Thermal model of a solar thermochemical reactor for metal oxide reduction. *J. Sol. Energy Eng.* 142 (5).
- Wang, Y., Potter, D., Asselineau, C.-A., Corsi, C., Wagner, W., Caliot, C., Piaud, B., Blanco, M., Kim, J.-S., Pye, J., 2020b. Verification of optical modelling of sunshape and surface slope error for concentrating solar power systems. *Sol. Energy* 195, 161–474.
- Winston, R., Miñano, J. C., Benítez, P., 2005. *Nonimaging Optics*. Elsevier.
- Yogev, A., Kribus, A., Epstein, M., Kogan, A., 1998. Solar “tower reflector” systems: A new approach for high-temperature solar plants. *Int. J. Hydrog. Energy* 23 (4), 239–245.

---

## Optical analysis of a multi-aperture solar central receiver system for high-temperature concentrating solar applications

---

From the study presented in Chapter 6, it was found that the power output from the optimised polar-field solar CRS is limited to about 50 MW for an example system with a receiver temperature of 1200 K [12]. It is known that the specific cost of a power block decreases with an increasing power level. Hence, this chapter presents an optical study of a multi-aperture solar CRS for increasing the net receiver power [181].

The multi-aperture model system comprises a tower, a multi-aperture receiver, multiple sub-fields, and CPCs. CPCs suitable for high-temperature applications are considered in this study. The heliostat sub-field configuration, the number of apertures, and the optical quality of reflective surfaces are varied in the parametric study. Optical and energetic performance is predicted for systems with receivers operated in a wide temperature range of 600–1800 K. The system performance characterised by the maximum net receiver power and concentration ratio at the receiver aperture, and instantaneous and annual optical, solar-to-thermal and solar-to-exergy efficiencies is examined.



# Optical analysis of a multi-aperture solar central receiver system for high-temperature concentrating solar applications

LIFENG LI,<sup>1</sup> BO WANG,<sup>1</sup> JOHN PYE,<sup>1</sup> ROMAN BADER,<sup>1,2</sup> WUJUN WANG,<sup>3</sup> AND WOJCIECH LIPIŃSKI<sup>1,\*</sup> 

<sup>1</sup>Research School of Electrical, Energy and Materials Engineering, The Australian National University, Canberra, ACT 2600, Australia

<sup>2</sup>Current affiliation: Weisskopf Partner GmbH, Switzerland

<sup>3</sup>Department of Energy Technology, KTH Royal Institute of Technology, 100 44 Stockholm, Sweden

\*wojciech.lipinski@anu.edu.au

**Abstract:** A multi-aperture solar central receiver system is optically analyzed for increasing the net power to the receiver in a wide temperature range of 600–1800 K. A model system comprises a tower, a multi-aperture receiver with compound parabolic concentrators, and heliostat sub-fields. Optical modeling is performed using in-house developed Monte-Carlo ray-tracing programs. The heliostat sub-field geometrical configuration, the number of receiver apertures and optical properties of reflective surfaces are varied in the parametric study. Increasing the number of apertures from one to four increases the maximum net receiver power from 116 MW to 332 MW. The use of more than four apertures results in only limited further gain of the net receiver power but significantly decreases the overall optical efficiency and the solar-to-thermal efficiency. The optimal temperature for the maximized annual solar-to-exergy efficiency is found in the range of 1100–1200 K. This optimal temperature decreases slightly with an increasing number of apertures.

© 2020 Optical Society of America under the terms of the [OSA Open Access Publishing Agreement](#)

## 1. Introduction

High temperatures (>1000 K) have been pursued for both solar thermochemical and concentrating solar power (CSP) applications. In solar thermochemical applications, high temperatures are required by the reduction and oxidation reaction steps of metal oxides to realize solar energy storage or fuel production [1–4]. In CSP applications, high temperatures increase solar energy conversion efficiency because of higher power cycle efficiency [5]. High-temperature receivers bring in high receiver emission losses, necessitating high solar concentration ratios at the receiver aperture (>1000 suns) [6,7]. High concentration ratios could be achieved by the implementation of cavity receivers with relatively small apertures, point-focusing primary optical concentrators such as solar dishes and heliostat fields of central receiver systems (CRSs), and secondary optical concentrators [8–11]. The most widely discussed secondary optical concentrator is the compound parabolic concentrator (CPC) which further increases the solar concentration ratio ideally by a factor of  $1/\sin\theta_{\text{CPC}}$  or  $1/\sin^2\theta_{\text{CPC}}$  for a two-dimensional (2D) or three-dimensional (3D) CPC, respectively, where  $\theta_{\text{CPC}}$  is the acceptance angle of the CPC [3,12–17].

Higher plant power is favorable for the techno-economic performance of solar-driven power systems [18,19]. Our previous work on solar polar-field CRSs revealed that the power output from the cost-optimized high-temperature CRSs was small primarily due to the high spillage losses arising from the great distances from the far-away heliostats to the receiver [17]. For high-temperature applications, the configuration of CRSs with a surround field and an external receiver is not applicable for increasing the power output due to the high radiative emission losses [6]. Higher power output from high-temperature CRSs can be in principle obtained by

(i) a multi-tower CRS created by duplicating a single-tower system that encompasses a tower, a single-aperture receiver, a CPC, and a polar field [20] or (ii) a multi-aperture CRS created by coupling multiple polar fields to a multi-aperture receiver on a single tower. Method (i) offers better optical performance since heliostats are located at optimal positions to towers. However, it requires an increased number of the expensive components—towers, bringing in high capital costs. For method (ii), the investment for the tower can be used by more than one polar fields, thus capital costs are significantly reduced. The study on multi-aperture CRSs is rare in the literature and still far from thorough. The concept of multi-aperture receivers was applied in the 50 MW Khi Solar One plant constructed in South Africa where no CPC is used [21]. Example studies on multi-aperture CRSs with CPCs include that Schmitz et al. compared the performance of systems in three different configurations: a polar field coupled to a single-aperture receiver, a surround field coupled to an external receiver, and six polar fields coupled to a six-aperture receiver [22]. The system with a multi-aperture receiver and three sub-fields was included in an optimization study of a heliostat field layout by Pitz-Paal et al. for high-temperature solar thermochemical processing [23].

This study presents an optical analysis of a multi-aperture, high-temperature solar CRS with CPCs for increasing net receiver power. Optical modeling is performed using in-house Monte-Carlo ray-tracing (MCRT) programs written in Fortran. We explore the effects of heliostat sub-field geometrical configuration, number of apertures and optical properties of reflective surfaces on system optical and energetic performance. Optical systems are studied for applications in a wide temperature range of 600–1800 K in 100 K increments. Optimization for the maximized annual solar-to-thermal efficiency is conducted at each investigated temperature and selected numbers of apertures of 1, 2, 4, 6, and 8.

## 2. Model system

Figure 1(a) shows an example four-aperture CRS and includes the investigated parameters of the number of apertures,  $N_a$ , and the angle between adjacent heliostat sub-fields,  $\beta$ . Figure 1(b) depicts one section of a multi-aperture CRS and includes the investigated geometrical parameters of tower height,  $h_t$ , CPC acceptance angle,  $\theta_{CPC}$ , and CPC entry aperture radius,  $r_{CPC}$ . Each aperture is coupled to a heliostat sub-field and a non-truncated three-dimensional (3D) CPC. We assume that the CPCs are of the same geometry and orientation characterized by a tilt angle,  $\alpha_{CPC}$ , indicating that the shape of heliostat sub-fields before the trimming of low-efficiency heliostats are the same. CPC geometry is determined by the acceptance angle,  $\theta_{CPC}$ , and the entry aperture radius,  $r_{CPC}$ . Table 1 includes details of the modeled CRSs and model assumptions. The shading effects by the tower, receiver and CPCs depend on their specific designs, i.e. size and shape, identification of which is beyond the scope of the present study.

The following two steps are taken for determining the boundary of the heliostat field: (i) We remove the heliostats whose centers are located outside the conic sections created by the intersection of CPC acceptance cones and a horizontal plane containing all heliostat centers [17,22]. The rays reflected by these heliostats are rejected by CPCs due to the CPC backward reflection [12]; (ii) We remove the heliostats with the instantaneous (at autumn equinox noon) overall optical efficiency (defined in Section 3.) lower than a defined threshold  $\eta_{tr}$ . The size of the target aperture, i.e. CPC entry aperture, is calculated for each trimmed sub-field to capture a defined ratio  $f_a$  of the reflected Gaussian-distributed radiation from the furthest heliostat to the tower. This method is adapted from [22] and was also used in our previous studies [17,27].

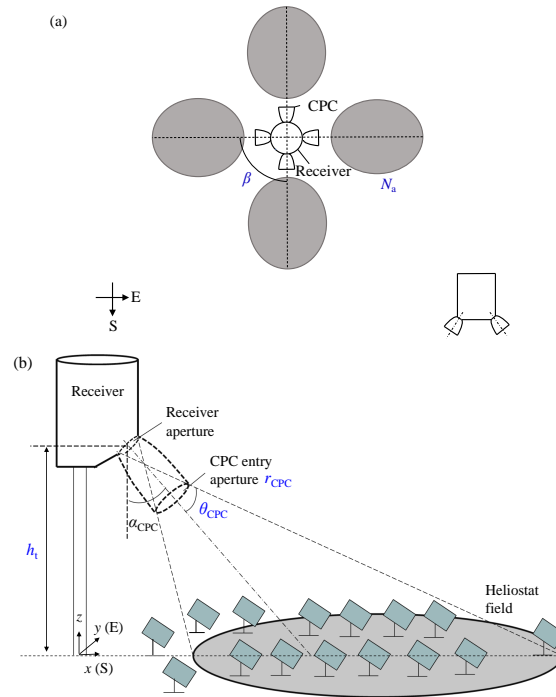


**Fig. 1.** Schematics of multi-aperture solar central receiver systems (CRS): (a) an example CRS comprising a four-aperture receiver, four CPCs and four heliostat sub-fields, and (b) one section of a multi-aperture CRS, adapted from [17]. The investigated geometrical parameters are shown in blue, including number of apertures,  $N_a$ , angle between adjacent heliostat sub-fields,  $\beta$ , tower height,  $h_t$ , CPC acceptance angle,  $\theta_{CPC}$ , and CPC entry aperture radius,  $r_{CPC}$ .

**Table 1. Assumptions made for the simulations.**

Parameters	Value
Plant location	Alice Springs, Australia
Sun shape model	Buie, circumsolar ratio (CSR) = 0.02 [24]
Tracking	azimuth–elevation, no tracking error
Optical surface reflectance	specular, wavelength- and direction-independent
Slope error model of optical surfaces	Rayleigh distribution [25]
Heliostat geometry	square, paraboloidal, single-facet
Heliostat field layout pattern	Campo [26]
Distance from the first heliostat row to tower	80 m
Maximum distance from heliostat to tower	1500 m
Maximum number of heliostat field zones	3
Distance between centers of two adjacent heliostats	1.1×heliostat diagonal length
Shading effects of the tower, receiver and CPCs	neglected

### 3. Analysis

Optical simulations are performed using in-house developed MCRT programs [28]. The MCRT technique provides the most robust, accurate and comprehensive results for predicting the system optical and energetic performance [28]. The real-time clear sky irradiance is modeled using the method described in [29]. Annual performance of the heliostat field is evaluated using the method developed by Grigoriev et al. (2015) and by employing bicubic spline interpolation of results for discrete sun positions [30,31]. The MCRT program for modeling the CPC is verified by computing the transmission-angle curve of a CPC with an acceptance angle of  $16^\circ$ , and comparing the results with those taken from [12]. The verification results were presented in [15]. The MCRT program for simulating CRSs was previously verified by comparing its predictions with those obtained using other ray-tracing tools [17,32].

The geometry and dimension of the intersected conic sections are determined by tower height,  $h_t$ , CPC acceptance angle,  $\theta_{CPC}$  and CPC tilt angle,  $\alpha_{CPC}$ , which was discussed in our previous study [17]. Figure 2 shows the conic sections for example CRSs with multi-aperture receivers of selected numbers of apertures,  $N_a = 1, 2, 4, 6, 8$ . Conic sections of elliptic and hyperbolic shapes are exhibited in Fig. 2(a–e) and (f–j), respectively. Overlap occurs between adjacent conic sections. For heliostats in the overlapped region, their aiming points are selected as the center of the target aperture facing towards the heliostat, to reduce the size of sun images on the target aperture and thus reduce spillage loss. Hence, heliostats in the overlapped regions are evenly distributed into the two adjacent sub-fields by the dashed lines as in Fig. 2. Figure 2 demonstrates that the total intersecting land area of conic sections increases with an increasing  $N_a$  and a larger  $\theta_{CPC}$ , indicating potentially higher power output. However, the concentration ratio boost of the 3D CPC, equal to  $1/\sin^2\theta_{CPC}$ , decreases with the increase of  $\theta_{CPC}$ . As will be illustrated in Eq. (5), the receiver absorption efficiency is reduced as a result of lower concentration ratios at the receiver aperture. The tradeoffs between the increase in net receiver power and the decrease in field optical and receiver absorption efficiencies are addressed in this study.

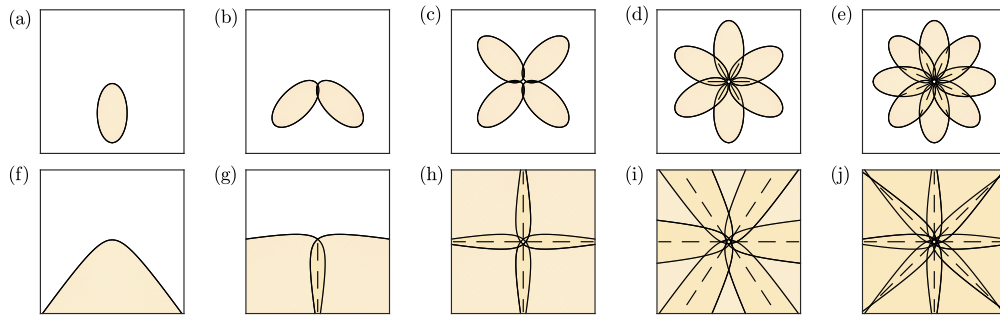


**Fig. 2.** Conic sections created by intersecting CPC acceptance cones with a horizontal plane containing all heliostat centers for an example CRS with a tower height  $h_t$  of 150 m, a CPC tilt angle  $\alpha_{CPC}$  of  $45^\circ$  and a CPC acceptance angles  $\theta_{CPC}$  of  $35^\circ$  and  $55^\circ$  for (a–e) and (f–j), respectively. Elliptic and hyperbolic conic sections are identified for cases (a–e) and (f–j), respectively. Figure (a, f), (b, g), (c, h), (d, i), and (e, j), respectively, show the layouts of CRSs with numbers of apertures,  $N_a = 1, 2, 4, 6, \text{ and } 8$ .

System performance is characterized by (i) instantaneous overall optical efficiency of a single heliostat or a heliostat field,  $\eta_{h,opt}$  and  $\eta_{tot,opt}$ , respectively, and annual overall optical efficiency of a heliostat field,  $\bar{\eta}_{tot,opt}$ , (ii) net receiver power,  $\dot{Q}_{tot,net}$ , i.e. the total radiative power absorbed in the receiver at autumn equinox noon, (iii) average optical concentration ratio at the receiver aperture



at autumn equinox noon,  $C_{\text{rec}}$ , (iv) instantaneous and annual receiver absorption efficiency,  $\eta_{\text{rec}}$  and  $\bar{\eta}_{\text{rec}}$ , respectively, (v) instantaneous and annual solar-to-thermal efficiency,  $\eta_{\text{s-t}}$  and  $\bar{\eta}_{\text{s-t}}$ , respectively, and (vi) annual solar-to-exergy efficiency,  $\bar{\eta}_{\text{s-x}}$ .

**Overall optical efficiency.** Instantaneous overall optical efficiency of a single heliostat and a heliostat field account for cosine, shading, surface absorption, blocking, atmospheric attenuation, and spillage losses [14]. For a heliostat field consisting of a number of sub-fields,  $\eta_{\text{tot,opt}}$  is defined as the total radiative power intercepted by all receiver apertures to the maximum total radiative power  $\dot{Q}_{\text{f,max}}$  collected when sun rays incident normally on an area equal to the total area of installed heliostats,  $A_{\text{h,tot}} = n_{\text{h}}A_{\text{h}}$  ( $n_{\text{h}}$  is the total number of installed heliostats and  $A_{\text{h}}$  is the mirror area of a heliostat) [14,33].

$$\eta_{\text{h,opt}} = \eta_{\text{h,cos}}\eta_{\text{h,shade}}\eta_{\text{h,abs}}\eta_{\text{h,block}}\eta_{\text{h,aa}}\eta_{\text{h,int}} \quad (1)$$

$$\eta_{\text{tot,opt}} \equiv \frac{\dot{Q}_{\text{tot,rec}}}{\dot{Q}_{\text{f,max}}} = \frac{\sum_{i=1}^{N_{\text{a}}} \dot{Q}_{i,\text{rec}}}{Gn_{\text{h}}A_{\text{h}}} = \eta_{\text{cos}}\eta_{\text{shade}}\eta_{\text{abs}}\eta_{\text{block}}\eta_{\text{aa}}\eta_{\text{int}} \quad (2)$$

where  $\dot{Q}_{\text{tot,rec}}$  and  $\dot{Q}_{i,\text{rec}}$  represent the total radiative power intercepted by all apertures and the  $i_{\text{th}}$  aperture, respectively, and  $G$  is the instantaneous clear-sky solar irradiance [17,29].

Annual overall optical efficiency of the field,  $\bar{\eta}_{\text{tot,opt}}$ , is defined as the ratio of the total radiative energy intercepted by all apertures to the maximum radiative energy incident on all heliostats in a year [33].

$$\bar{\eta}_{\text{tot,opt}} = \frac{\sum_{i=1}^{N_{\text{a}}} \int_{\text{year}} \dot{Q}_{i,\text{rec}} dt}{n_{\text{h}}A_{\text{h}} \int_{\text{year}} G dt} \quad (3)$$

**Receiver absorption efficiency.** Net receiver power,  $\dot{Q}_{\text{tot,net}}$ , is equal to the sum of the radiative power absorbed through each aperture,  $\dot{Q}_{i,\text{net}}$ .  $\dot{Q}_{i,\text{net}}$  is equal to the radiative power intercepted by an individual aperture,  $\dot{Q}_{i,\text{rec}}$ , multiplied by the instantaneous receiver absorption efficiency,  $\eta_{i,\text{rec}}$ .

$$\eta_{\text{tot,rec}} \equiv \frac{\sum_{i=1}^{N_{\text{a}}} \dot{Q}_{i,\text{net}}}{\sum_{i=1}^{N_{\text{a}}} \dot{Q}_{i,\text{rec}}} = \frac{\sum_{i=1}^{N_{\text{a}}} \dot{Q}_{i,\text{rec}} \eta_{i,\text{rec}}}{\sum_{i=1}^{N_{\text{a}}} \dot{Q}_{i,\text{rec}}} \quad (4)$$

We assume that the receiver is an iso-thermal, perfectly-insulated blackbody without reflective, conductive and convective heat losses [1,23,34]. The instantaneous absorption efficiency,  $\eta_{i,\text{rec}}$ , at each aperture of the simplified multi-aperture receiver at  $T_{\text{rec}}$  is calculated as

$$\eta_{i,\text{rec}} = 1 - \frac{\sigma T_{\text{rec}}^4}{G_0 C_{i,\text{rec}}} \quad (5)$$

where  $\sigma$  is the Stefan–Boltzmann constant,  $\sigma = 5.67 \times 10^{-8} \text{ W m}^{-2} \text{ K}^{-4}$ , and  $G_0$  is a reference solar irradiance taken as  $1000 \text{ W m}^{-2}$  for the definition of the average optical concentration ratio at the receiver aperture,  $C_{i,\text{rec}}$ .

The annual absorption efficiency of the multi-aperture receiver,  $\bar{\eta}_{\text{tot,rec}}$ , is calculated as:

$$\bar{\eta}_{\text{tot,rec}} = \frac{\sum_{i=1}^{N_{\text{a}}} \int_{\text{year}} \dot{Q}_{i,\text{net}} dt}{\sum_{i=1}^{N_{\text{a}}} \int_{\text{year}} \dot{Q}_{i,\text{rec}} dt} \quad (6)$$

**Solar-to-thermal efficiency.** Instantaneous solar-to-thermal efficiency,  $\eta_{\text{s-t}}$ , is defined as the ratio of the total radiative power absorbed by the multi-aperture receiver,  $\dot{Q}_{\text{tot,net}}$ , to  $\dot{Q}_{\text{f,max}}$ .

$$\eta_{\text{s-t}} = \frac{\dot{Q}_{\text{tot,net}}}{\dot{Q}_{\text{f,max}}} = \frac{\sum_{i=1}^{N_{\text{a}}} \dot{Q}_{i,\text{net}}}{Gn_{\text{h}}A_{\text{h}}} \quad (7)$$



Annual solar-to-thermal efficiency,  $\bar{\eta}_{s-t}$ , is defined as the ratio of the total radiative energy absorbed in the receiver to  $\dot{Q}_{f,max}$  integrated for a year,

$$\bar{\eta}_{s-t} = \bar{\eta}_{tot,opt} \bar{\eta}_{tot,rec} = \frac{\sum_{i=1}^{N_a} \int_{year} \dot{Q}_{i,net} dt}{n_h A_h \int_{year} G dt} \quad (8)$$

The solar-to-thermal efficiency measures the performance of the overall optical system including the heliostat field consisting of multiple sub-fields, the CPCs and the multi-aperture receiver.

**Solar-to-exergy efficiency.** Annual solar-to-exergy efficiency,  $\bar{\eta}_{s-x}$ , is defined as the ratio of the system annual exergy output to  $\dot{Q}_{f,max}$  integrated for a year.  $\bar{\eta}_{s-x}$  is equal to the annual solar-to-thermal efficiency multiplied by the Carnot efficiency.

$$\bar{\eta}_{s-x} = \bar{\eta}_{s-t} \eta_{Carnot} = \bar{\eta}_{s-t} \left( 1 - \frac{T_0}{T_{rec}} \right) \quad (9)$$

where  $T_0$  is the temperature of the cold reservoir of a power cycle and is taken as the ambient temperature of 293 K. The solar-to-exergy efficiency measures the upper limit of the solar-to-electric efficiency for a solar power plant, as well as the maximum solar-to-fuel efficiency for an ideal cyclic process for a solar thermochemical plant [1,17]. High-temperature receivers increase the thermal-to-electric or thermal-to-fuel conversion efficiency, thus leading to a higher solar-to-exergy efficiency.

In a practical plant, thermal expansion and degradation may occur to CPCs since the CPCs are exposed to high-flux irradiation and contaminants from the receiver cavity and the surroundings. High-flux irradiation to the CPCs results from the concentrated solar radiation by optical concentrators and the lost radiation through the high-temperature receiver apertures, namely the receiver radiative emission and reflective losses. The total optical error and reflectance of the heliostat surface are impacted by factors such as structural shape, mirror curvature, tracking error, as well as wind and contamination during operation. Hence, in this study we include the discussion of the effects of the slope error and reflectance of optical surfaces of heliostats and CPCs.

#### 4. Results

Based on the described optical model and assumptions, the results of optical analysis on the multi-aperture CRS are calculated. In Subsections 4.1, 4.2 and 4.3, we present the investigation on the effects of the heliostat sub-field geometrical configuration, the number of apertures, and the optical properties of reflective surfaces, respectively, on system optical and energetic performance. Subsection 4.2 also includes the optimization results of CRSs at each studied receiver temperature and selected numbers of apertures of 1, 2, 4, 6, and 8. Table 2 lists the baseline parameter set.

##### 4.1. Heliostat sub-field geometrical configuration

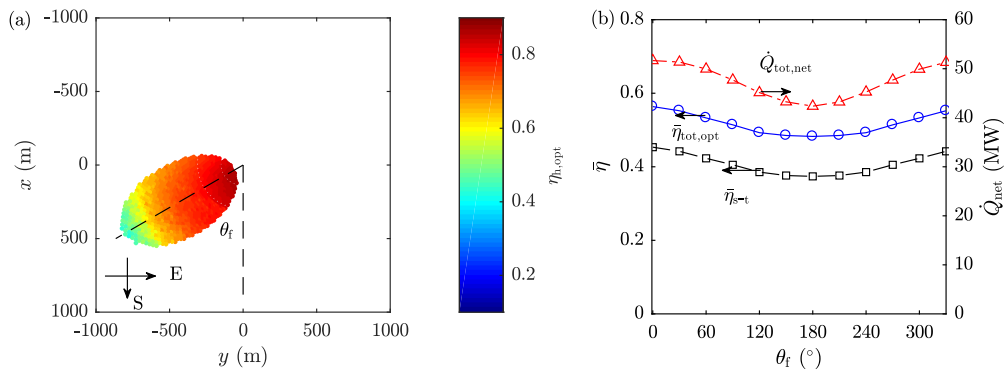
We use the angle between the axis of a polar field and the south direction,  $\theta_f$  (positive: clockwise), to define the relative position of a polar field to the tower (see Fig. 3(a)). We quantitatively evaluate the performance of CRSs with a single-aperture receiver coupled to one polar field, i.e.  $N_a = 1$ , positioned at different directions around the tower. No trimming of low-efficiency heliostats, i.e.  $\eta_{tr} = 0$ , is applied for the parametric study conducted in this section. In Fig. 3(b), we exhibit the annual overall optical efficiency,  $\bar{\eta}_{tot,opt}$ , annual solar-to-thermal efficiency,  $\bar{\eta}_{s-t}$  and net receiver power,  $\dot{Q}_{tot,net}$  for CRSs with selected  $\theta_f$  varying from  $0^\circ$  to  $330^\circ$  in  $30^\circ$  increments. According to Fig. 3, the system performance decreases as the field moves away from the south direction to the tower ( $\theta_f = 0^\circ$ ). East–west symmetry can be seen in Fig. 3(b). The field with the

Table 2. Baseline parameter set of a solar central receiver system

Parameters	Value
Number of apertures, $N_a$	6
Tower height, $h_t$	250 m
Heliostat surface area, $A_h$	100 m <sup>2</sup>
CPC acceptance angle, $\theta_{CPC}$	30°
CPC entry aperture radius, $r_{CPC}$	5 m
CPC axis tilt angle, $\alpha_{CPC}$	45°
Reflectance of heliostat and CPC surfaces, $\rho_h$ and $\rho_{CPC}$	0.9 and 0.95
Slope error of heliostat and CPC surfaces, $\sigma_h$ and $\sigma_{CPC}$	1.5 and 0.5 mrad
Optical efficiency trimming threshold, $\eta_{tr}$	0.6

worst performance is found at  $\theta_f = 180^\circ$  and yields 9.3 MW (1.8%) lower  $\dot{Q}_{net}$ , 8.1% lower  $\bar{\eta}_{opt}$ , and 7.9% lower  $\bar{\eta}_{s-t}$  than the optimal field with  $\theta_f = 0^\circ$ .

Cosine effect is the main reason for causing the performance difference between CRSs of different  $\theta_f$  [35]. Cosine efficiency is determined by the relative position of the sun, the heliostat and the target aperture. Figure 4 exhibits the cosine efficiency map for three example sun positions at 6 am, 9 am and 12 pm on an autumn equinox day. For each sun position, significantly higher cosine efficiencies are observed for positions at the opposite side of the tower as the sun. The cosine efficiency for heliostats at the west/east to the tower is only higher when the sun is in the east/west direction at relatively lower solar irradiance. Hence, the CRS with heliostats arranged to the south of the tower offers the highest cosine efficiency, followed by the east/west and the north. For this reason, the heliostat field is typically arranged to the south or north of the tower for polar-field CRSs constructed in the southern or northern hemisphere, respectively.



**Fig. 3.** Optical and energetic performance of polar-field central receiver systems (CRSs) characterized by (a) instantaneous (at autumn equinox noon) overall optical efficiency of each heliostat,  $\eta_{h,opt}$ , in an example CRS of  $\theta_f = 60^\circ$  and (b) annual overall optical efficiency,  $\bar{\eta}_{tot,opt}$ , annual solar-to-thermal efficiency,  $\bar{\eta}_{s-t}$ , and net receiver power,  $\dot{Q}_{net}$ , for CRSs of selected  $\theta_f$  varying from  $0^\circ$  to  $330^\circ$  in  $30^\circ$  increments and an assumed receiver temperature of 1600 K.

For CRSs with the same number of apertures,  $N_a$ , different angles between two adjacent sub-fields,  $\beta$ , can be applied, resulting in different heliostat sub-field geometrical configurations.

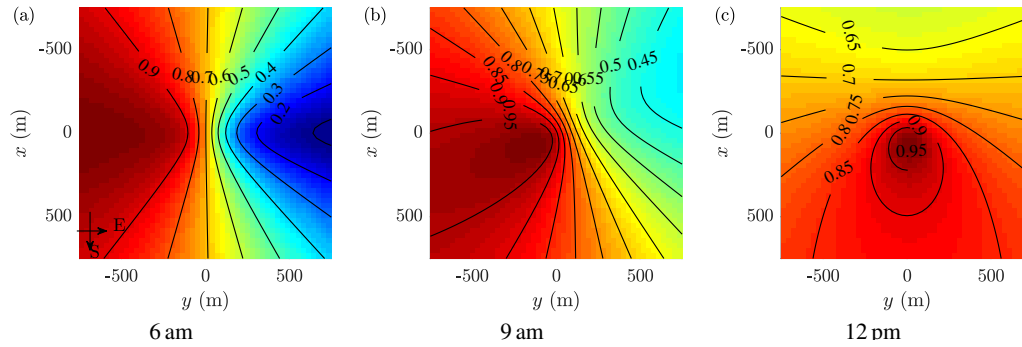


**Fig. 4.** Cosine efficiency maps for three example solar hours of the autumn equinox day: (a) 6 am, (b) 9 am and (c) 12 pm. The tower is located at the origin point.

Figure 5 shows heliostat field layouts of CRSs with selected  $N_a$  of 4, 6, 8, and  $\beta$  of  $20^\circ$ ,  $30^\circ$ ,  $45^\circ$ ,  $60^\circ$ ,  $90^\circ$ . The maximum possible  $\beta$  for CRSs with  $N_a$  of 4, 6, 8 are  $90^\circ$ ,  $60^\circ$ , and  $45^\circ$ , respectively, where the sub-fields are evenly distributed in the field around the tower. The performance, characterized by the instantaneous overall optical efficiency  $\eta_{\text{tot,opt}}$ , instantaneous solar-to-thermal efficiency  $\eta_{\text{s-t}}$ , and  $\dot{Q}_{\text{tot,net}}$ , of each CRS in Fig. 5 is exhibited in Fig. 6. Results of Figs. 5 and 6 are obtained for CRSs with a same assumed receiver aperture radius of 2.5 m.

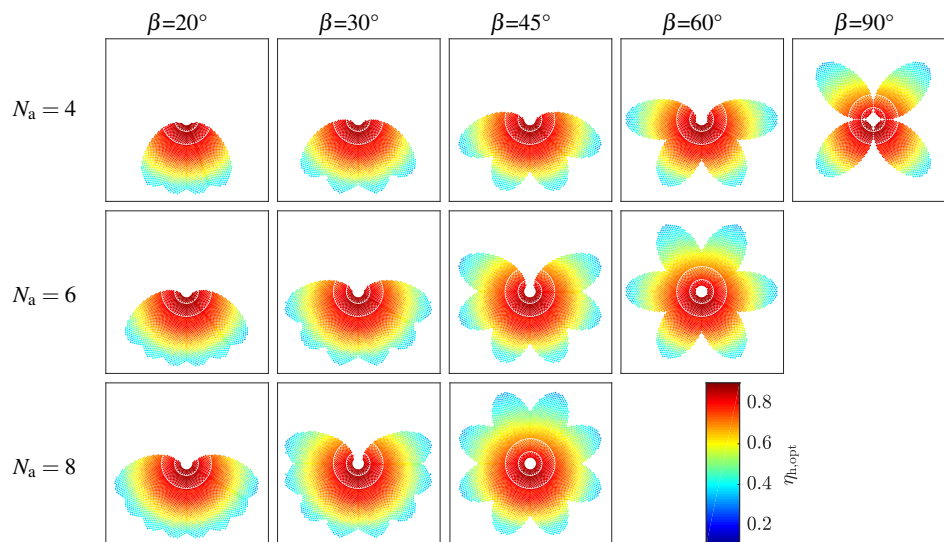


**Fig. 5.** Configurations of heliostat sub-fields for central receiver systems with selected numbers of apertures,  $N_a = 4, 6, 8$ , and angles between sub-fields,  $\beta = 20^\circ, 30^\circ, 45^\circ, 60^\circ, 90^\circ$ . The color scale indicates the instantaneous (at autumn equinox noon) overall optical efficiency of each heliostat,  $\eta_{h,\text{opt}}$ . Other parameters are taken as the parameter set in Table 2.

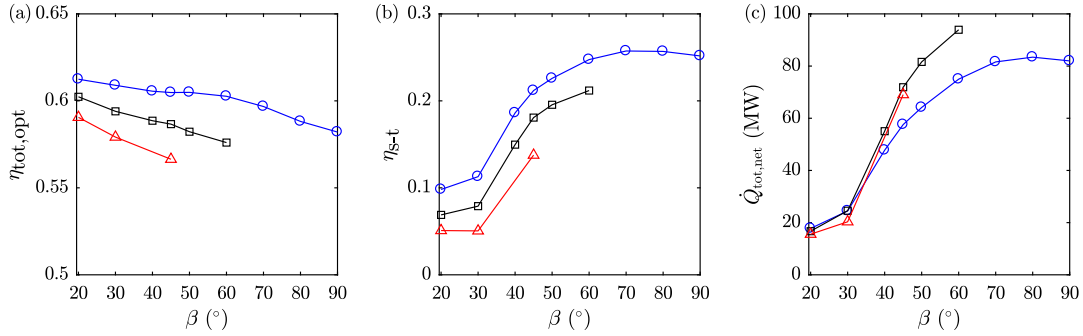


**Fig. 6.** Optical and energetic performance of the systems shown in Fig. 5, characterized by (a) instantaneous overall optical efficiency,  $\eta_{\text{tot,opt}}$ , (b) instantaneous solar-to-thermal efficiency,  $\eta_{\text{s-t}}$ , and (c) net receiver power,  $\dot{Q}_{\text{tot,net}}$ , for selected numbers of apertures,  $N_a$  of 4, 6 and 8, and sub-field angles  $\beta$  in the range of 20–90°. The receiver temperature is assumed as 1200 K.

According to Fig. 5, when the sub-field angle  $\beta$  is increased, the overlapping area decreases while more low-efficiency heliostats located away from the south are included. As a result, as revealed in Fig. 6,  $\eta_{\text{tot,opt}}$  decreases and  $\dot{Q}_{\text{tot,net}}$  increases for a larger  $\beta$ . CRSs with a larger  $\beta$  offer higher  $\eta_{\text{s-t}}$ , which is attributed to the increased concentration ratio at the receiver aperture due to an increasing total number of heliostats. In addition, the decrease in  $\eta_{\text{tot,opt}}$  and  $\eta_{\text{s-t}}$  and the increase in  $\dot{Q}_{\text{tot,net}}$  are observed for increasing  $N_a$  from four to six. However, the further increase of  $N_a$  from six to eight results in reduced  $\dot{Q}_{\text{tot,net}}$  (see Fig. 6(c)), which reveals that the increased receiver emission loss caused by a larger total area of apertures outweighs the gain of intercepted radiation by employing more heliostats. For parametric optimization in Section 4.2, we select sub-field layouts with the maximum possible  $\beta$  for each  $N_a$  to achieve the maximized net receiver power and a larger space between sub-fields for the potential use of CPCs of larger acceptance angles. These results demonstrate the tradeoff between efficiencies and net receiver power for the selection of  $N_a$  and  $\beta$ .

For the maximum  $\beta$ , two geometrical configurations of heliostat sub-fields are possible. For example, Fig. 7 displays the two configurations of heliostat sub-fields in four-aperture, six-aperture and eight-aperture CRSs. By simulating the instantaneous performance, it is found that these two configurations offer similar performance. For example, for the baseline six-aperture systems with layouts 1 (Fig. 7(c)) and 2 (Fig. 7(d)), the instantaneous overall optical and solar-to-thermal efficiencies and net receiver power are 0.516 and 0.515, 0.283 and 0.279, and 125.5 MW and 122.3 MW, respectively, for an assumed receiver temperature of 1200 K.

#### 4.2. Number of apertures

Based on the optical analysis performed with the baseline parameters, we conduct preliminary parametric optimization of CRSs with parameters listed in Table 3. Other parameters not included in Table 3 are taken from the baseline parameter set as in Table 2. Annual simulations are performed for all CRS configurations. For the optical simulations in this section, the maximum possible sub-field angle  $\beta$  of 90°, 60° and 45° are employed for  $N_a$  of 4, 6 and 8, respectively. For  $N_a = 1$ , the field is placed to the south of the tower. For  $N_a = 2$ ,  $\beta$  is selected as 90° and the two sub-fields are positioned to the south of the tower, as can be seen in Fig. 2.

The parameters of the optimized CRSs of  $N_a = 4, 6, 8$  for the maximized  $\eta_{\text{s-t}}$  are found to be:  $h_t = 250$  m,  $\theta_{\text{CPC}} = 30^\circ$ ,  $\eta_{\text{tr}} = 0.6$ , and  $f_a = 0.9$ . Figure 8 shows the geometrical configurations

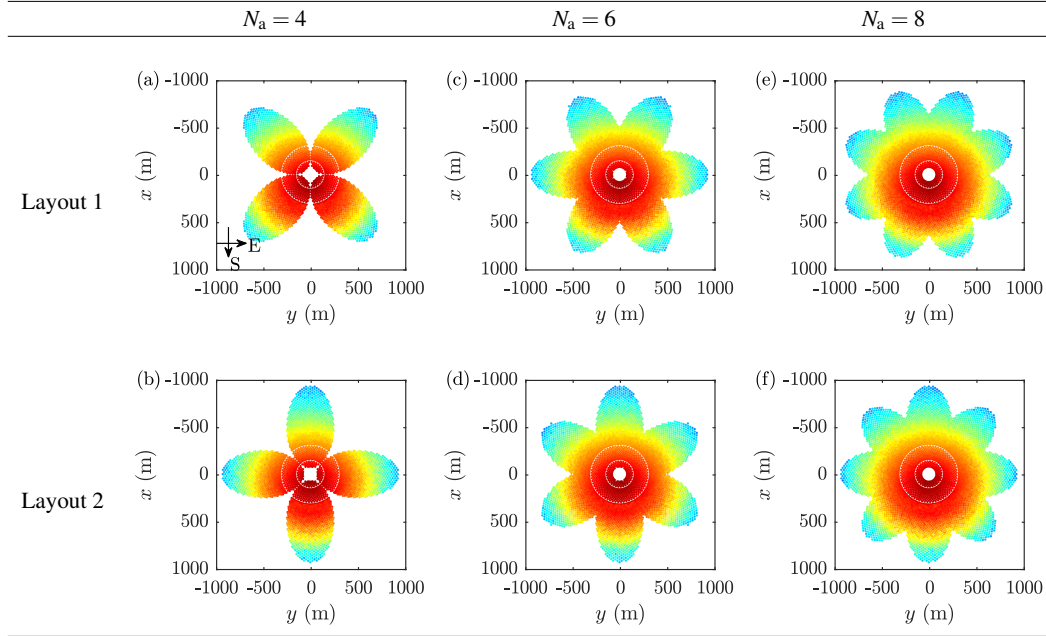


**Fig. 7.** Two configurations of heliostat sub-fields for systems with selected numbers of apertures,  $N_a = 4, 6, 8$ : Layout 1 and 2. The color scale indicates the instantaneous (at autumn equinox noon) overall optical efficiency of each heliostat,  $\eta_{h,opt}$ , using the same legend as that of Fig. 5.

of heliostat sub-fields of these optimized CRSs. Figure 9 shows the Pareto front of  $\bar{\eta}_{s-t}$  and  $\dot{Q}_{tot,net}$  calculated for all simulated CRSs with selected  $N_a$  of 1, 2, 4, 6, 8 and  $T_{rec}$  of 800 K, 1200 K and 1600 K. To determine the Pareto front,  $\dot{Q}_{tot,net}$  is uniformly discretized and the Pareto front is selected as the cases leading to the maximum  $\bar{\eta}_{s-t}$  among all cases within each discretized interval of  $\dot{Q}_{tot,net}$ . Figure 10 shows the maximum annual solar-to-thermal efficiency,  $\bar{\eta}_{s-t,max}$ , and the maximum annual solar-to-exergy efficiency,  $\bar{\eta}_{s-x,max}$ , for CRSs with selected  $N_a = 1, 2, 4, 6, 8$  and  $T_{rec}$  varying from 600 K to 1800 K in 100 K increments. Based on Figs. 8, 9 and 10, it is found that:

- The maximum achievable  $\dot{Q}_{tot,net}$  increases dramatically for  $N_a$  increased from 1 to 4. However, no significant improvement of  $\dot{Q}_{tot,net}$  is found by further increasing  $N_a$  over 4.
- The maximum  $\bar{\eta}_{s-t}$  decreases with an increasing  $N_a$ , due to higher inherent optical losses resulting from using more CPCs and higher receiver emission losses due to a larger total area of apertures.
- According to Fig. 9(c), for CRSs with  $T_{rec} = 1600$  K and  $N_a = 4, 6, 8$ , the maximum  $\bar{\eta}_{s-t}$  of approximately 0.44, 0.438, 0.42, respectively, are obtained where  $\dot{Q}_{net}$  is approximately 150 MW.
- According to Fig. 9, CRSs with  $N_a = 4$  and 6 offer close performance, while CRSs with  $N_a = 8$  yield lower  $\bar{\eta}_{s-t}$ . The difference of  $\bar{\eta}_{s-t}$  between CRSs with  $N_a = 6$  and 8 increases for a higher  $T_{rec}$ .

- $\bar{\eta}_{s-t}$  and  $\dot{Q}_{tot,net}$  decrease as  $T_{rec}$  increases as a result of higher receiver emission losses. The benefits of high-temperature receivers are manifested in higher annual solar-to-exergy efficiency,  $\bar{\eta}_{s-x}$  (see Fig. 10(b)), the maximum values of which peak at  $T_{rec}$  of about 1100–1200 K depending on the implemented  $N_a$ .
- According to Fig. 10(b), the optimum temperatures for the maximized  $\bar{\eta}_{s-x}$  differ for selected  $N_a$  and slightly decrease with an increasing  $N_a$ .

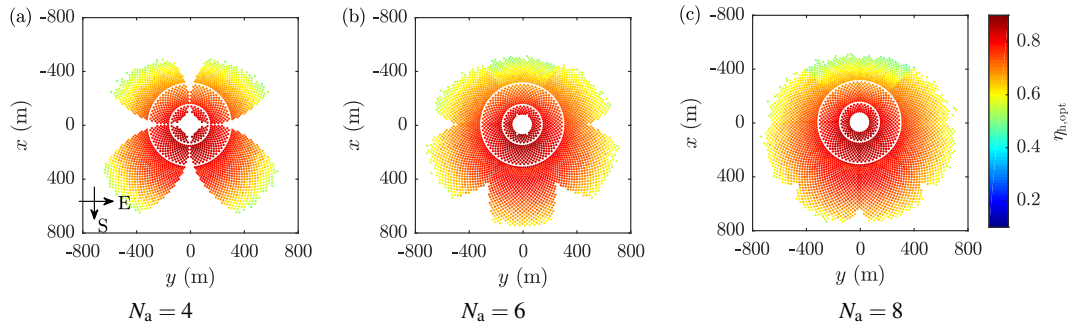


**Fig. 8.** Heliostat field layouts of the optimized solar central receiver systems with selected numbers of apertures  $N_a$  of (a) 4, (b) 6, and (c) 8. The color scale indicates the instantaneous (at autumn equinox noon) overall optical efficiency of each heliostat,  $\eta_{h,opt}$ .

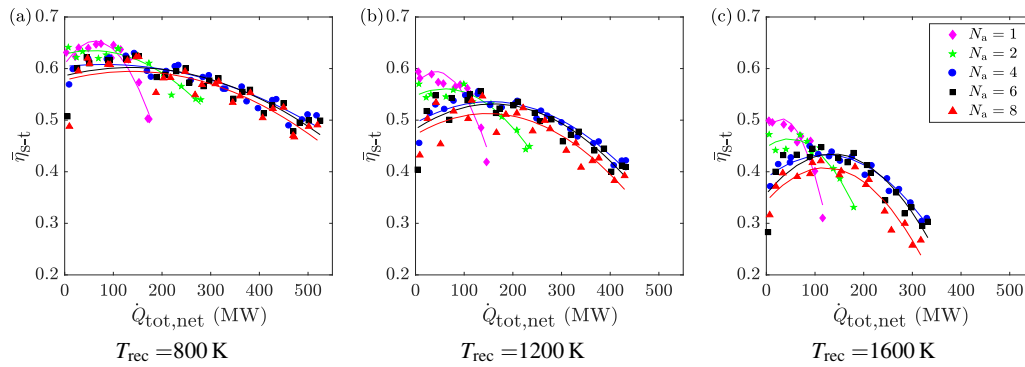


**Fig. 9.** The Pareto front of annual solar-to-thermal efficiency  $\bar{\eta}_{s-t}$  and net receiver power  $\dot{Q}_{tot,net}$  for all simulated systems with selected numbers of apertures,  $N_a$  of 1, 2, 4, 6, 8, and selected receiver temperatures  $T_{rec}$  of (a) 800 K, (b) 1200 K and (c) 1600 K.

#### 4.3. Optical properties of reflective surfaces

We investigate changes in system performance resulting from varying optical properties including the reflectance and the slope error of heliostat and CPC surfaces. Figure 11 shows  $\bar{\eta}_{s-t}$  and  $\dot{Q}_{tot,net}$  as functions of the reflectance and slope error of heliostat and CPC surfaces, varying from 0.7 to 0.95 in 0.05 increments and 0.5 mrad to 5.5 mrad in 1 mrad increments, respectively. The baseline parameter set in Table 2 is taken for the calculations in this section.

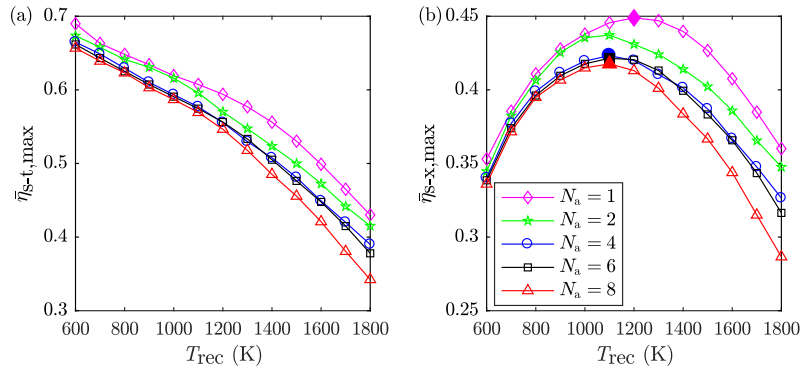


**Fig. 10.** The maximum (a) annual solar-to-thermal efficiency,  $\bar{\eta}_{s-t,max}$ , and (b) annual solar-to-exergy efficiency,  $\bar{\eta}_{s-x,max}$ , of systems with selected numbers of apertures,  $N_a$  of 1, 2, 4, 6, 8, and receiver temperatures  $T_{rec}$  varying from 600 K to 1800 K in 100 K increments.

**Table 3.** Parameters simulated in the optimization

Parameters	Values
Number of apertures, $N_a$	1, 2, 4, 6, 8
Tower height, $h_t$	90, 130, 170, 210, 250 m
CPC acceptance angle, $\theta_{CPC}$	30°, 40°, 50°, 60°, 70°
Optical efficiency trimming threshold, $\eta_{tr}$	0.2, 0.3, 0.4, 0.5, 0.6, 0.7
Parameters determining CPC entry aperture radius, $f_a$	0.7, 0.8, 0.9, 0.95, 0.99

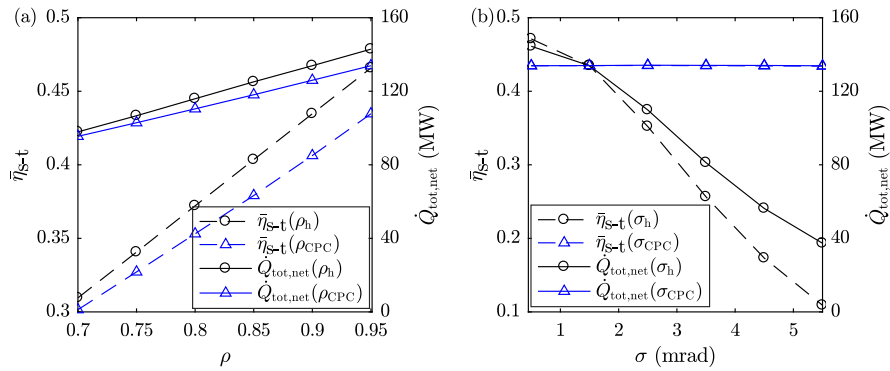


**Fig. 11.** Effects of heliostat and CPC surface (a) reflectance,  $\rho_h$  and  $\rho_{CPC}$ , and (b) slope error,  $\sigma_h$  and  $\sigma_{CPC}$ , on annual solar-to-thermal efficiency,  $\bar{\eta}_{s-t}$ , and net receiver power,  $\dot{Q}_{tot,net}$ , for the baseline system with parameters as in Table 2.



Based on Fig. 11(a), with the increase of heliostat surface reflectance from 0.7 to 0.95,  $\bar{\eta}_{s-t}$  and  $\dot{Q}_{\text{tot,net}}$  increase from 0.31 to 0.435 (31.8%) and 97.9 MW to 133.9 MW (36.8%), respectively. The system energetic performance is slightly more sensitive to the reflectance of the heliostat surface,  $\rho_h$ , than the reflectance of the CPC surface,  $\rho_{\text{CPC}}$ . According to Fig. 11(b), the increase of heliostat surface slope error  $\sigma_h$  from 0.5 mrad to 5.5 mrad leads to a significant drop of  $\dot{Q}_{\text{tot,net}}$  and  $\bar{\eta}_{s-t}$  from 144.5 MW to 37.3 MW (74.2%) and 0.47 to 0.11 (76.6%), respectively. It is worthwhile to note that the CPC surface slope error  $\sigma_{\text{CPC}}$  is found to have a minor effect on the system performance. This is due to a significantly larger optical length from heliostats to the CPC exit aperture than the optical length from the CPC reflective surface to the CPC exit aperture. Considering the short optical length from the CPC reflective surface to the CPC exit aperture, the reflected rays are primarily intercepted by the receiver despite a larger slope error. Based on these results, the reflectance of the CPC optical surface is more important than the slope error and should be paid more attention to in the manufacturing process.

## 5. Summary and conclusions

Optics of a solar central receiver system with a multi-aperture receiver coupled to multiple heliostat sub-fields and compound parabolic concentrators has been studied. Optical simulations were performed using in-house Monte-Carlo ray-tracing programs. We explored the effects of the heliostat sub-field geometrical configuration, the number of apertures and the optical properties of reflective surfaces on the optical and energetic performance of systems with the receiver temperature in the range of 600–1800 K. The system characteristics including the maximum net receiver power, instantaneous and annual overall optical, solar-to-thermal and solar-to-exergy efficiencies were analyzed.

Under the assumptions made in this study, it is found that despite reduced optical and solar-to-thermal efficiencies, the maximum net receiver power is significantly increased via the design of the multi-aperture receiver and multiple heliostat sub-fields. Cosine effect is the main reason for the decreased optical efficiency. We compared two types of sub-field geometrical configurations for systems with the same number of apertures and found that they offer close system performance. From parametric optimization, we demonstrated that the net receiver power is significantly boosted by increasing the number of apertures from one to four, while further increasing the number of apertures over four leads to only limited gain of net receiver power but greatly reduced efficiencies. Optimal receiver temperature for the maximized annual solar-to-exergy efficiency is found in the range of 1100–1200 K and this optimal temperature decreases with an increasing number of apertures. Comparison study on the optical properties of the heliostat and CPC surfaces revealed that the CPC slope error has a minor effect on the system performance. The present optical study enlightens the design of the entire multi-aperture solar central receiver systems in the future.

## Funding

Australian Renewable Energy Agency (2014/RND005).

## Acknowledgments

The financial support from the Australian Renewable Energy Agency (grant no 2014/RND005) is gratefully acknowledged. This research was undertaken with the assistance of resources and services from the National Computational Infrastructure (NCI), which is supported by the Australian Government.

## Disclosures

The authors declare no conflicts of interest.



## References

1. M. Romero and A. Steinfeld, "Concentrating solar thermal power and thermochemical fuels," *Energy Environ. Sci.* **5**(11), 9234–9245 (2012).
2. R. Bader and W. Lipiński, "Solar thermal processing," in *Advances in Concentrating Solar Thermal Research and Technology*, M. Blanco and L. Santigosa, eds. (Woodhead Publishing, 2017), Woodhead Publishing Series in Energy, pp. 403–459.
3. G. Levêque, R. Bader, W. Lipiński, and S. Haussener, "High-flux optical systems for solar thermochemistry," *Sol. Energy* **156**, 133–148 (2017).
4. A. Carrillo, J. González-Aguilar, M. Romero, and J. Coronado, "Solar energy on demand: A review on high temperature thermochemical heat storage systems and materials," *Chem. Rev.* **119**(7), 4777–4816 (2019).
5. M. Mehos, C. Turchi, J. Vidal, M. Wagner, Z. Ma, C. Ho, W. Kolb, C. Andracka, and A. Kruizenga, "Concentrating solar power Gen3 demonstration roadmap," Tech. Rep. NREL/TP-5500-67464, National Renewable Energy Laboratories, Golden, CO (2017).
6. C. Ho and B. Iverson, "Review of high-temperature central receiver designs for concentrating solar power," *Renewable Sustainable Energy Rev.* **29**, 835–846 (2014).
7. M. Sedghi, R. Padilla, R. Taylor, M. Lake, I. Izadgoshab, and A. Rose, "High-temperature, point-focus, pressurised gas-phase solar receivers: A comprehensive review," *Energy Convers. Manage.* **185**, 678–717 (2019).
8. J. Gordon and H. Ries, "Tailored edge-ray concentrators as ideal second stages for Fresnel reflectors," *Appl. Opt.* **32**(13), 2243–2251 (1993).
9. A. Kribus, M. Huleihil, A. Timinger, and R. Ben-Mair, "Performance of a rectangular secondary concentrator with an asymmetric heliostat field," *Sol. Energy* **69**(2), 139–151 (2000).
10. M. Schmitz, T. Cooper, G. Ambrosetti, and A. Steinfeld, "Two-stage solar concentrators based on parabolic troughs: asymmetric versus symmetric designs," *Appl. Opt.* **54**(33), 9709–9721 (2015).
11. F. Dähler, M. Wild, R. Schäppi, P. Haueter, T. Cooper, P. Good, C. Larrea, M. Schmitz, P. Furler, and A. Steinfeld, "Optical design and experimental characterization of a solar concentrating dish system for fuel production via thermochemical redox cycles," *Sol. Energy* **170**, 568–575 (2018).
12. R. Winston, J. Miñano, and P. Benítez, *Nonimaging Optics* (Elsevier, 2005).
13. W. Chueh, C. Falter, M. Abbott, D. Scipio, P. Furler, S. Haile, and A. Steinfeld, "High-flux solar-driven thermochemical dissociation of CO<sub>2</sub> and H<sub>2</sub>O using nonstoichiometric ceria," *Science* **330**(6012), 1797–1801 (2010).
14. L. Li, J. Coventry, R. Bader, J. Pye, and W. Lipiński, "Optics of solar central receiver systems: A review," *Opt. Express* **24**(14), A985–A1007 (2016).
15. L. Li, B. Wang, J. Pottas, and W. Lipiński, "Design of a compound parabolic concentrator for a multi-source high-flux solar simulator," *Sol. Energy* **183**, 805–811 (2019).
16. B. Wang, L. Li, J. Pottas, R. Bader, P. Kreider, V. Wheeler, and W. Lipiński, "Thermal model of a solar thermochemical reactor for metal oxide reduction," *J. Sol. Energy Eng.* **142**(5), 051002 (2020).
17. L. Li, B. Wang, J. Pye, and W. Lipiński, "Temperature-based optical design, optimization and economics of solar polar-field central receiver systems with an optional compound parabolic concentrator," *Sol. Energy* **206**, 1018–1032 (2020).
18. Gas Turbine World, *Gas Turbine World 2019 GTW Handbook* (2019).
19. R. Bader, K. Urkalan, J. Jordan, and K. Lovegrove, "Techno-economic analysis of a solar driven combined power cycle power system with thermochemical energy storage," Tech. Rep. ITP/A0164, ITP Thermal Pty Limited, Canberra, Australia (2019).
20. P. Schramek and D. Mills, "Multi-tower solar array," *Sol. Energy* **75**(3), 249–260 (2003).
21. J. Mucci, "Khi Solar One project review and economic analysis," Master's thesis, Universidad de Oviedo (2015).
22. M. Schmitz, P. Schwarzbözl, R. Buck, and R. Pitz-Paal, "Assessment of the potential improvement due to multiple apertures in central receiver systems with secondary concentrators," *Sol. Energy* **80**(1), 111–120 (2006).
23. R. Pitz-Paal, N. Botero, and A. Steinfeld, "Heliostat field layout optimization for high-temperature solar thermochemical processing," *Sol. Energy* **85**(2), 334–343 (2011).
24. D. Buie, A. Monger, and C. Dey, "Sunshape distributions for terrestrial solar simulations," *Sol. Energy* **74**(2), 113–122 (2003).
25. R. Bader, S. Haussener, and W. Lipiński, "Optical design of multisource high-flux solar simulators," *J. Sol. Energy Eng.* **137**(2), 021012 (2015).
26. F. Collado and J. Guallar, "Campo: Generation of regular heliostat fields," *Renewable Energy* **46**, 49–59 (2012).
27. L. Li, S. Yang, B. Wang, J. Pye, and W. Lipiński, "Optical analysis of a solar thermochemical system with a rotating tower reflector and a multi-receiver array," *Opt. Express* **28**(13), 19429–19445 (2020).
28. M. Modest, *Radiative Heat Transfer* (Academic, 2013), 3rd ed.
29. P. Ineichen, "A broadband simplified version of the Solis clear sky model," *Sol. Energy* **82**(8), 758–762 (2008).
30. V. Grigoriev, C. Corsi, and M. Blanco, "Fourier sampling of sun path for applications in solar energy," in *AIP Conference Proceedings*, vol. 1734 (2016), p. 020008.
31. W. Press, S. Teukolsky, W. Vetterling, B. Flannery, and M. Metcalf, *Numerical Recipes in Fortran 90: The Art of Parallel Scientific Computing, Volume 2 of Fortran Numerical Recipes* (Cambridge University, 1996).
32. L. Li, B. Wang, R. Bader, J. Zapata, and W. Lipiński, "Reflective optics for redirecting convergent radiative beams in concentrating solar applications," *Sol. Energy* **191**, 707–718 (2019).

33. M. Dunham, R. Kasetty, A. Mathur, and W. Lipiński, “Optical analysis of a heliostat array with linked tracking,” *J. Sol. Energy Eng.* **135**(3), 034501 (2013).
34. E. Fletcher and R. Moen, “Hydrogen and oxygen from water,” *Science* **197**(4308), 1050–1056 (1977).
35. J. Duffie and W. Beckman, *Solar Engineering of Thermal Processes* (John Wiley & Sons, 2013), 4th ed.

---

## Optical analysis of a solar thermochemical system with a rotating tower reflector and a receiver–reactor array

---

This chapter presents an optical study of a proposed novel solar beam-down system with a rotating tower reflector and a receiver–reactor array. The proposed system is used for solar thermochemical processes based on the reduction–oxidation cycles of metal oxides for fuel production or energy storage. The reduction step requires concentrated solar energy as the source of high-temperature process heat, while the oxidation step occurs at a relatively lower temperature. The variation of temperatures can be realised in a variety of ways. In this study, we propose a novel idea of rotating the tower reflector in a solar beam-down optical system to alternate the concentrated solar irradiation into an array of solar receiver–reactors for realising the multi-step solar thermochemical redox cycles [170]. Despite the practical difficulty of rotating a large reflector at the top of a tower, the proposed idea has the benefits that (i) the high-temperature receiver–reactors together with their accessories can be placed at ground level, offering reduced operation difficulty and costs, and (ii) it provides the feasibility of designing receiver–reactors with facing-up apertures, which can benefit thermal or fluid flow requirements of specific reactor designs.

The tower reflector axis is required to be tilted for accommodating the receiver–reactor array, resulting in a reduced optical efficiency. Optical simulations are performed for two selected types of optical systems: a simplified 2D system and a realistic 3D beam-down system. Analytical ray tracing is conducted for the 2D system to study the effects of system design parameters on optical characteristics including the required size of the TR, the size of the resulting sun image on the target aperture, the rim angle and the axis tilt angle of the reflected beam from the tower reflector. MCRT simulations are performed for the 3D beam-down system to evaluate the effects of system optical and geometrical parameters on optical and radiative characteristics.

A companion study of thermodynamic analysis of the receiver–reactor array is reported in [182]. The thermodynamic study demonstrates the increase in thermal-to-chemical efficiency by the recuperation process designed for the receiver–reactor array.

## Optical analysis of a solar thermochemical system with a rotating tower reflector and a receiver–reactor array

LIFENG LI,<sup>1</sup> SONG YANG,<sup>1,2</sup> BO WANG,<sup>1</sup> JOHN PYE,<sup>1</sup> AND  
WOJCIECH LIPINSKI<sup>1,\*</sup> 

<sup>1</sup>Research School of Electrical, Energy and Materials Engineering, The Australian National University, Canberra, ACT 2601, Australia

<sup>2</sup>Key Laboratory of Solar Energy Science and Technology in Jiangsu Province, School of Energy and Environment, Southeast University, No. 2 Si Pai Lou, Nanjing 210096, China

\*wojciech.lipinski@anu.edu.au

**Abstract:** We propose a concept of a rotating tower reflector (TR) in a beam-down optical system to alternate concentrated solar irradiation of an array of solar receiver–reactors, realizing multi-step solar thermochemical redox cycles. Optical and radiative characteristics of the proposed system are explored analytically and numerically by Monte-Carlo ray-tracing simulations. We study the effects of the system geometrical and optical parameters on the optical and radiative performance. TR axis is required to be tilted for accommodating the receiver–reactor array, resulting in reduced optical efficiency. We demonstrate that the annual optical efficiency of a baseline system with the receiver–reactor located south of the tower decreases from 46% to 37% for the axis tilt angle of TR increasing from 2° to 20°. The optical analysis conducted in this study provides a general formulation to enable predictions of required gain of thermal-to-chemical efficiency of the receiver–reactor array for obtaining improved overall solar-to-chemical efficiency of the solar thermochemical plant.

© 2020 Optical Society of America under the terms of the [OSA Open Access Publishing Agreement](#)

### 1. Introduction

Multi-step solar thermochemical metal-oxide redox cycles are a viable route to fast and efficient chemical fuel production or thermal energy storage [1–5]. Two-step cycles consist of: (1) a high-temperature solar endothermic reduction step and (2) a non-solar low-temperature exothermic oxidation step. The reduction step is driven by concentrated solar irradiation, which is supplied over a discrete time interval shorter than the cycle duration for temperature-swing redox cycles [6–9]. The operation of the cycle can be realized in a variety of ways, including (i) operating the two steps sequentially in a single cavity receiver–reactor with varied conditions [6,10]; (ii) operating the two steps in two separate receiver–reactors with the metal oxide cycled between the reduction and oxidation reactors [11]; (iii) operating the two steps in two separate reactors exchanging heat alternately within a single receiver [12]; (iv) placing the metal oxide in a rotating reactor component that passes through zones of different conditions [8]; and (v) alternating the solar input into two or more receiver–reactors by moving the focal point of the concentrating system, either directly [13–15] or by means of a secondary concentrator [16]. Dähler et al. summarized six design concepts based on method (v) for alternating the focal point in a solar dish system and experimentally investigated a design with a rotating flat secondary reflector [16]. With method (v), cycle steps can proceed simultaneously in different reactors under continuous irradiation of the receiver–reactor array. Heat recovery can be implemented in the receiver–reactor array, which is reported to result in dramatically improved thermal-to-chemical efficiency of receiver–reactors from 3.5% to 20% [7,17].

To explore the feasibility of method (v) in a large-scale concentrating solar system, we propose a novel concept of a rotating tower reflector (TR) in a beam-down optical system to alternate the concentrated solar irradiation of an array of receiver-reactors. The typical beam-down optical system comprises three main components: a heliostat field, a TR placed on top of a tower, and a receiver at the ground level. The receiver is typically coupled with a secondary optical concentrator such as a compound parabolic concentrator (CPC) [18]. The beam-down optical concept offers advantages for high-temperature solar thermochemical applications. The redirected convergent beam at the ground level enables simpler and cheaper installation and operation of the high-temperature receiver and auxiliary equipment. Besides, the beam-down optical concept enables novel designs of the solar receiver such as fluidized particle bed inside the receiver [6,19–29]. However, the use of the TR results in additional optical losses and magnification of the sun image, necessitating the application of a CPC to reduce the spillage loss and to attain a high concentration ratio (CR) [30,31]. The addition of a CPC also brings additional optical losses due to CPC backward reflection and surface absorption. Practical challenges for realizing the proposed system include manufacturing and maintenance of the complex optical components, such as a large hyperboloidal TR and three-dimensional CPCs. The rotation of the large TR also introduces engineering difficulties. Despite the challenges, the potential of achieving high system-level solar-to-chemical conversion efficiency and the convenience of operating high-temperature receiver-reactors at the ground level make the proposed idea worthwhile to be explored.

The optics of the beam-down system have been extensively studied [30,32–39]. The beam-down optical system has been successfully constructed and tested including demonstration-level systems [27,40,41] and a 50 MW<sub>e</sub> commercial system [42]. Despite a large number of previously studied solar beam-down systems, there are gaps in reports of useful optical characteristics such as the size of sun image on the target, required size of the TR, rim and tilt angles of the reflected beam from the TR, and the annual optical performance of overall systems. The majority of investigated systems include a TR with a vertical axis. For the novel system proposed in this study, the axis of its TR is tilted and the receiver-reactors are dislocated from an optimal position of a single-receiver system to accommodate the receiver-reactor array. Pertinent studies of beam-down systems with dislocated receivers are absent in the literature.

In this study, we investigate the optical and radiative performance of the proposed novel solar thermochemical beam-down system with a rotating TR and a receiver-reactor array. A simplified two-dimensional (2D) system and a more realistic three-dimensional (3D) system are investigated. Firstly, analytical ray tracing is conducted in the 2D system to explore parametrically the geometrical and optical characteristics, including the required size of the TR, size of the sun image on the CPC entry aperture, and rim and axis tilt angles of the incident beam on the CPC entry aperture, as a function of system geometrical parameters. Secondly, in-house developed Monte-Carlo ray-tracing (MCRT) simulations are used to study a 3D system. In the 3D system, we parametrically study the effects of system geometrical parameters on instantaneous (at autumn equinox noon) optical and radiative characteristics including optical efficiency of the heliostat field, the TR and the CPC, radiative power and concentrator ratio at the apertures of the receiver-reactor. Based on the parametric studies, we calculate and analyze the annual optical efficiency of the beam-down optical systems with the receiver-reactors positioned at different positions around the tower.

## 2. 3D beam-down optical system model

### 2.1. Model system

Figure 1 depicts the model of the 3D beam-down optical system comprising a heliostat field, a tower, a rotating hyperboloidal TR, and an example CPC array. Receiver-reactors are not shown in Fig. 1. A single CPC is shown in Fig. 1(b). As shown in Fig. 1(b), the global coordinate

system is constructed with the origin at the center of the tower base, and the positive  $x$ - and  $y$ -axes pointing along the South and East directions, respectively. The local coordinate system of the hyperboloidal surface is constructed with its origin placed half-way between the primary and secondary foci, and the  $z_1$ -axis is selected as the real axis of the hyperboloidal TR.

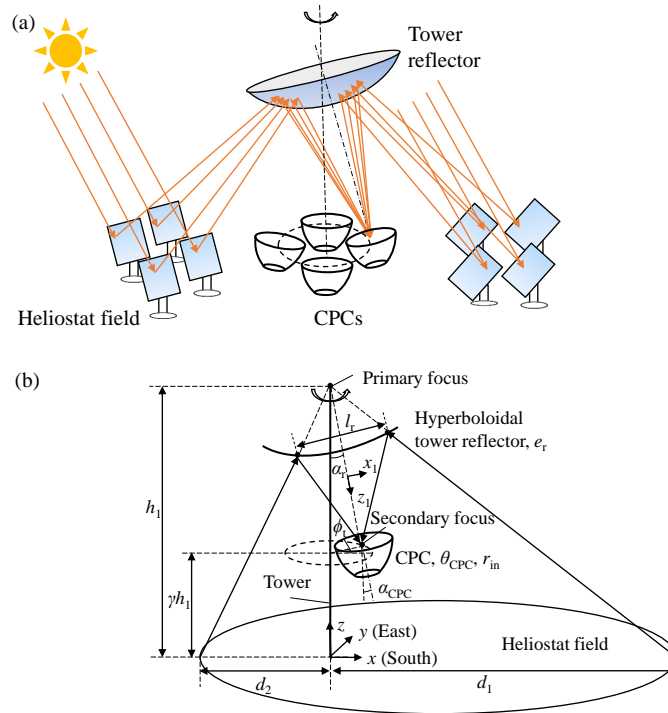


**Fig. 1.** Schematics of a 3D solar beam-down optical system. System components featuring a heliostat field, a tower, a hyperboloidal tower reflector, and an example array of 4 CPCs are depicted in (a). Coordinate systems and geometrical parameters are shown in (b). Receiver-reactors are not shown.

One of the hyperboloid foci is chosen as the primary focus, i.e. the focus of the primary optical concentrators—heliostats, that is located at a height  $h_1$  above the ground level (Fig. 1(b)). The CPC is positioned with its entrance at the secondary focus, i.e. the other focus of the hyperboloidal TR, which is located at a height  $h_2$  above the ground level and with an azimuthal angle  $\phi_t$  relative to the positive  $x$ -axis. A height ratio  $\gamma$  between the secondary and primary foci is used, i.e.  $\gamma = h_2/h_1$ . The hyperboloid axis forms a tilt angle  $\alpha_r$  with the tower. The geometry of an un-truncated 3D CPC is determined by acceptance angle  $\theta_{CPC}$  and entry aperture radius  $r_{in}$ . CPC is oriented with an axis tilt angle  $\alpha_{CPC}$  with respect to the  $z$ -axis. The heliostat field is asymmetric about the  $y$ -axis (East–West direction) (shown in Fig. 1(b)). The maximum length of the heliostat field is given by distances  $d_1$  and  $d_2$  between the tower and the furthest heliostats along the South and North directions, respectively. Hence, geometrical parameters investigated in this study are grouped into (i) CPC parameters: the CPC acceptance angle  $\theta_{CPC}$ , the CPC entry aperture radius  $r_{in}$ , the CPC axis tilt angle  $\alpha_{CPC}$ , and (ii) parameters excluding those of a CPC: the hyperboloidal TR eccentricity  $e_r$ , the TR axis tilt angle  $\alpha_r$ , the azimuthal angle  $\phi_t$ , the

primary focus height  $h_1$ , the focal point height ratio  $\gamma$ , the distance  $d_1$  between the tower and the furthestmost heliostat along the south direction.

The surface equation of a hyperboloid of revolution expressed in the local coordinate system is [43]

$$\frac{x_1^2}{a_r^2} + \frac{y_1^2}{a_r^2} - \frac{z_1^2}{b_r^2} = -1 \quad (1)$$

where  $2a_r$  and  $2b_r$  are the major and minor axis lengths, respectively, which are related to the eccentricity  $e_r$  and linear eccentricity  $c_r$ .

$$c_r = \frac{h_1(1-\gamma)}{2 \cos \alpha_r}, \quad a_r = \frac{c_r}{e_r}, \quad b_r = \sqrt{a_r^2 - c_r^2} \quad (2)$$

For  $e_r \rightarrow \infty$ , a hyperboloidal surface becomes a plane. For the same heliostat field and positions of primary and secondary foci, the required size of a hyperboloidal TR to capture all reflected radiation from the heliostat field is smaller than a flat TR, resulting in reduced shading loss.

Figure 2 depicts an example array with 8 receiver-reactors in total. The receiver-reactor irradiated by the concentrated solar energy has an opened aperture and realizes a reduction reaction. All other receiver-reactors have closed apertures. The receiver-reactor on the opposite side to the reduction reactor realizes an oxidation reaction. Heat is exchanged between reactors other than the reduction and oxidation ones to pre-heat or pre-cool the active redox materials prior to their reduction and oxidation, respectively, allowing for significant gains in thermal-to-chemical efficiency [7–9,17].

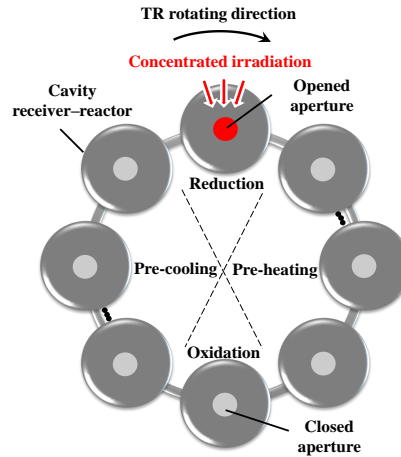
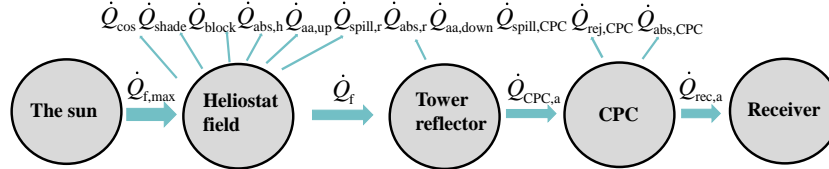


Fig. 2. Schematic of an example array of 8 receiver-reactors.

## 2.2. Performance metrics

Figure 3 shows the power flow in a beam-down optical system. Compared with a solar ‘tower-receiver’ system, where the receiver is placed on the top of the tower [30], additional optical losses occur in the beam-down system including the spillage  $\dot{Q}_{\text{spill},r}$  and absorption losses  $\dot{Q}_{\text{abs},r}$  by the TR, the shading loss  $\dot{Q}_{\text{shade},r}$  of heliostats by the TR, the blocking loss  $\dot{Q}_{\text{block},rec}$  of heliostats by the CPC/receiver, and atmospheric attenuation loss  $\dot{Q}_{\text{aa},down}$  when rays travel from the TR to

the CPC entry aperture. The simulated shading losses  $\dot{Q}_{\text{shade}}$  include  $\dot{Q}_{\text{shade},r}$  and the shading loss  $\dot{Q}_{\text{shade},h}$  between heliostats. The simulated blocking losses  $\dot{Q}_{\text{block}}$  include  $\dot{Q}_{\text{block},rec}$  and the blocking loss  $\dot{Q}_{\text{block},h}$  between heliostats.



**Fig. 3.** Power flow in a beam-down optical system.

The instantaneous optical performance of the beam-down optical system is evaluated with the overall optical efficiency of individual heliostats and heliostat field,  $\eta_{h,opt}$  and  $\eta_{f,opt}$ , respectively, CPC transmission efficiency,  $\eta_{CPC}$ , interception efficiency of TR and CPC,  $\eta_{int,r}$  and  $\eta_{int,CPC}$ , respectively, the radiative power  $\dot{Q}_{rec,a}$  and concentration ratio  $CR_{rec,a}$  at the receiver–reactor aperture, and the instantaneous optical efficiency  $\eta_{sys,opt}$  of the overall optical system.  $\eta_{sys,opt}$  is defined as the ratio of the radiative power  $\dot{Q}_{rec,a}$  intercepted by the receiver–reactor aperture divided by  $\dot{Q}_{f,max}$ , which in turn is the maximum total radiative power collected when solar rays are incident normally on an area equal to the total installed heliostat area  $A_{total,h}$ . The instantaneous optical performance is obtained for autumn equinox noon, i.e. March 21<sup>st</sup> in the southern hemisphere. The overall optical efficiencies of an individual heliostat and a heliostat field,  $\eta_{h,opt}$  and  $\eta_{f,opt}$ , respectively, account for the cosine effect, shading, blocking, surface absorption, atmospheric attenuation, and spillage at the TR.

$$\eta_{f,opt} \equiv \frac{\dot{Q}_f}{\dot{Q}_{f,max}} = \eta_{cos} \eta_{shade} \eta_{block} \eta_{abs,h} \eta_{aa,up} \eta_{int,r} \quad (3a)$$

$$\eta_{int,r} = 1 - \frac{\dot{Q}_{spill,r}}{\dot{Q}_f + \dot{Q}_{spill,r}} \quad (3b)$$

$$\dot{Q}_{f,max} = A_{total,h} \dot{q}_{sol} \quad (3c)$$

$$\eta_{int,CPC} = 1 - \frac{\dot{Q}_{spill,CPC}}{\dot{Q}_{CPC,a} + \dot{Q}_{spill,CPC}} \quad (4a)$$

$$\eta_{CPC} = \frac{\dot{Q}_{rec,a}}{\dot{Q}_{CPC,a}} = 1 - \frac{\dot{Q}_{abs,CPC} + \dot{Q}_{rej,CPC}}{\dot{Q}_{CPC,a}} \quad (4b)$$

$$\eta_{sys,opt} = \frac{\dot{Q}_{rec,a}}{\dot{Q}_{f,max}} \quad (5)$$

where  $\dot{q}_{sol}$  is the real-time direct normal irradiance measured in  $\text{kW m}^{-2}$  [44]. The annual system optical efficiency is defined as the ratio of the annually collected radiative energy at the receiver–reactor aperture and the annual incident radiative energy onto  $A_{total,h}$ .

$$\bar{\eta}_{sys,opt} = \frac{Q_{rec,a}}{Q_{f,max}} = \frac{\sum_{day=1}^{365} \int_{sunrise}^{sunset} \dot{Q}_{rec,a} dt}{\sum_{day=1}^{365} \int_{sunrise}^{sunset} \dot{Q}_{f,max} dt} \quad (6)$$

Note that the model optical systems investigated in this study use one receiver–reactor only of a variable position relative to the tower. The evaluation of the optical performance of the



system with multiple receiver–reactors is not included in this study since it requires detailed information on the geometry, thermal design, and operation of the receiver–reactor array, such as the receiver–reactor dimension as a function of incident radiative power, the clearance between receiver–reactors, the duration time of each receiver–reactor being irradiated, and the rotating speed of the TR.

### 2.3. MCRT model assumptions

Optical modeling of the 3D beam-down optical system is implemented using an in-house developed MCRT program. The optical models for simulating the CPC and the heliostat field as used in the present study were previously developed and verified in [31] and [45], respectively. The modeled plant location is Alice Springs, Australia ( $-23.7^{\circ}\text{N}$ ,  $133.9^{\circ}\text{E}$ ). The sun position relative to an observer on the ground is calculated as a function of solar time and site latitude using the method described in [46] and [47]. Buie sun shape model with an assumed radial displacement of  $\sigma_{\text{sun}} = 4.65$  mrad and a circumsolar ratio of 0.02 is used [48]. A single-facet, point-focusing, and square heliostat is taken, with a surface area of  $16 \text{ m}^2$ . The heliostat, TR and CPC surfaces are assumed to have specular, wavelength- and direction-independent reflectance equal to 0.93, 0.95 and 0.95, respectively. We use the Campo field layout pattern [49]. Reflections from optical surfaces are modeled by considering optical errors [50]. Gaussian surface normal error distributions with assumed standard deviations of 1.5, 1.4 and 0.5 mrad are applied for the heliostat, TR and CPC surfaces, respectively. The assumptions of the reflectance and slope errors of studied optical surfaces are based on the commercial beam-down plant in [42]. Atmospheric attenuation accounts for radiative losses incurred in the atmosphere. The atmospheric attenuation is calculated as a function of the slant distance that rays travel as discussed in [51]. The annual heliostat field performance is evaluated using the method given in [52] and by employing bi-cubic spline interpolation of results for discrete sun positions [53].

The 3D optical model is employed to explore the effects (*i*) of the system geometrical parameters excluding CPC parameters (defined in Subsection 2.1) and the TR size, on system optical and radiative characteristics (see Subsection 4.2.1); (*ii*) of CPC parameters (defined in Subsection 2.1) on instantaneous (at autumn equinox noon) system optical efficiency and concentration ratio at the receiver–reactor aperture (see Subsection 4.2.2), and (*iii*) to predict annual system optical efficiency for the receiver–reactor placed at selected positions around the tower (see Subsection 4.3). The selection of the geometry and orientation of the CPC used in (*iii*) is guided by the results of the analysis in (*ii*).

## 3. Simplified 2D optical system model

To establish the initial size of the TR and the geometry and orientation of the CPC for the 3D MCRT simulations, we employ a simplified 2D model and perform analytical ray tracing to predict geometrical and optical characteristics including the TR size  $l_r$  for capturing all reflected rays from heliostat field, the radius  $r_m$  of the sun image at the CPC entry aperture, and the rim and axis tilt angles of the incident beam on the CPC entry aperture,  $\Phi_m$  and  $\alpha_m$ , respectively. These predictions are based on the edge-ray principle [18], hence, only edge rays are simulated. Figure 4 depicts the simplified 2D model with the investigated geometrical parameters and predicted geometrical and optical characteristics.

The rationale for predicting the parameters  $l_r$ ,  $r_m$ ,  $\Phi_m$ , and  $\alpha_m$  is given next. The distance  $l_{r,\text{min}}$  between the two intersection points  $P_1$  and  $P_2$  of the TR with the two edge rays incident on the TR (Fig. 4) is calculated to characterize the required size of the TR. A larger TR leads to higher TR interception efficiency at the expense of an increased shading loss. The size of CPC entry aperture in the 3D MCRT simulation is matched with the size of the sun image on the CPC entry aperture. With the 2D model, we examine the sun image magnification due to the finite size of the sun and the reflection by optical surfaces, the so-called coma aberration

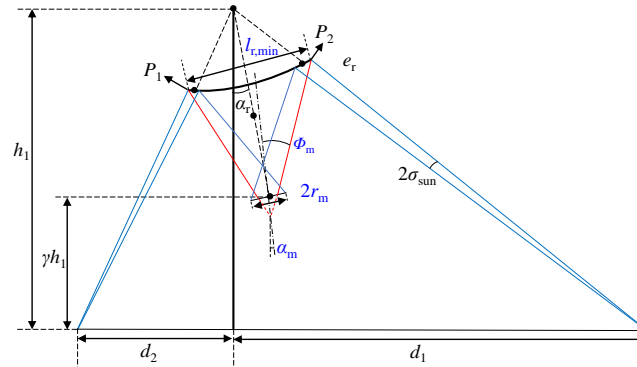


**Fig. 4.** Model of the simplified 2D beam-down optical system. Parameters in black and blue are the investigated geometrical parameters and predicted geometrical and optical characteristics, respectively. Red lines represent the edges of the incident beam at the CPC entry aperture.

[54]. The pillbox-distributed sun shape model is used for the 2D estimation of the sun image radius  $r_m$  [55]. Sun rays can be assumed to originate from a sun disk subtending a cone half angle  $\sigma_{\text{sun}}$  of 4.65 mrad. When sun rays are reflected by perfect, specular primary and secondary optical concentrators, their distribution on a focal plane forms a sun image of radius  $r_m$ . The determination of CPC acceptance and axis tilt angles,  $\theta_{\text{CPC}}$  and  $\alpha_{\text{CPC}}$ , respectively, in the 3D MCRT simulation, is guided by the values of  $\Phi_m$  and  $\alpha_m$  obtained with the 2D model.

Using the simplified 2D system, we explore the effects of (i) the system geometrical parameters excluding CPC parameters (defined in Subsection 2.1) on the above-discussed parameters  $l_{r,\text{min}}$ ,  $r_m$ ,  $\Phi_m$ , and  $\alpha_m$ ; and (ii) the optical imperfections of the heliostat and the TR surface, introduced by modifying the ideal surface normal vector by modelling its polar angle using the pillbox distribution with half-angles of  $\sigma_h$  and  $\sigma_r$ , respectively (see Subsection 4.1).

#### 4. Results and discussion

Firstly, we present the results of the parametric studies with the 2D (Subsection 4.1) and 3D (Subsection 4.2) optical system models. In Subsection 4.3, we discuss the effects of the rotation of the TR and the dislocation of the receiver-reactor on the annual optical performance. The baseline parameter set listed in Table 1 is selected according to preliminary parametric studies and based on the parameters of the existing commercial solar beam-down system presented in [42]. One parameter is varied at a time while other parameters are taken from the baseline set.

##### 4.1. Parametric studies using simplified 2D optical system model

Figure 5 shows the analytical ray-tracing results of the effects of the geometrical parameters excluding those of a CPC (defined in Subsection 2.1) on the required size  $l_{r,\text{min}}$  of the TR and the radius  $r_m$  of the sun image. Schematics showing ray paths for three example values of each parameter are included in the plots to visualize the effects of each parameter. According to Fig. 5(a,d),  $l_{r,\text{min}}$  and  $r_m$  have reverse trends for an increasing TR eccentricity  $e_r$  or focal point height ratio  $\gamma$ . An increase in  $e_r$  leads to a significant decrease in  $r_m$ , especially for  $e_r < 2$ , and a significant increase in  $l_{r,\text{min}}$ . Placing the receiver-reactor closer to the ground level greatly increases  $l_{r,\text{min}}$ . Figure 5(b, c, e) show that a smaller TR axis tilt angle  $\alpha_r$ , a smaller primary

Table 1. Baseline simulation parameters

Model system	Parameters	Value	Unit
2D, 3D	Hyperboloidal TR eccentricity $e_r$	1.95	–
	TR axis tilt angle $\alpha_r$	10	°
	Primary focus height $h_1$	50	m
	Focal point height ratio $\gamma$	0.4	–
	Distances from furthestmost heliostats to tower, $d_1, d_2$	242, 164	m
3D	TR size $l_r$	40	m
	CPC acceptance angle $\theta_{CPC}$	30	°
	CPC entry aperture radius $r_m$	2.8	m
	CPC axis tilt angle $\alpha_{CPC}$	10	°

focus height  $h_1$ , or a smaller distance  $d_1$  of the furthestmost heliostat to the tower result in smaller both  $l_{r,\min}$  and  $r_m$ .

Figure 6 exhibits the magnitude of the increase of  $l_{r,\min}$  and  $r_m$  with the increase of the optical imperfections of the heliostat and TR surfaces, characterized by  $\sigma_h$  and  $\sigma_r$ , respectively. It is found that the increase of  $\sigma_h$  from 0 to around 10 mrad leads to  $l_{r,\min}$  and  $r_m$  increased by about 1.5% and 178%, respectively.  $\sigma_h$  has a significant influence on  $r_m$  but minor impact on  $l_{r,\min}$ . For  $\sigma_r$  increasing from 0 to around 10 mrad,  $r_m$  increases by approximately 27.5%. Compared with  $\sigma_r$ ,  $\sigma_h$  has a greater impact on  $r_m$  due to an optical path from the heliostat surface to the CPC entry aperture longer than that from the TR to the CPC entry aperture.

Figure 7 shows the rim and axis tilt angles of the incident beam on the CPC entry aperture,  $\Phi_m$  and  $\alpha_m$ , respectively, as functions of the system geometrical parameters excluding those of the CPC. As indicated in Fig. 7(a),  $\Phi_m$  is mainly affected by  $e_r$ , followed by  $h_1$ . A smaller  $e_r$  or a larger  $h_1$  lead to a smaller  $\Phi_m$ , allowing the selection of a CPC with a smaller  $\theta_{CPC}$  for achieving a larger theoretical CR boost from the 3D CPC, equal to  $1/\sin^2\theta_{CPC}$ . This is consistent with the findings of the study presented in Ref [56]. Figure 7(b) shows that  $\alpha_m$  is significantly affected by  $\alpha_r$ , followed by  $h_1$  and  $e_r$ .

#### 4.2. Parametric studies using 3D optical system model

In the 3D system model, we select a heliostat field with its boundary determined by removing the heliostats with overall instantaneous optical efficiency  $\eta_{h,opt}$  lower than a selected trimming threshold of 0.6 (see Fig. 8). The distances from the furthestmost heliostats to the tower along the South and North directions of 242 m and 164 m, respectively, are set as the baseline values of  $d_1$  and  $d_2$  for the 2D analysis (Table 1). Table 1 also includes the baseline parameters of the 3D system for parametric studies presented in this subsection.

Figure 9 and Table 2 show the instantaneous optical and radiative performance of the baseline system with one receiver–reactor located south of the tower, i.e.  $\phi_t = 0^\circ$ , and with a TR axis tilt angle  $\alpha_r = 10^\circ$ . The instantaneous optical efficiency of the overall system is around 51% and radiative power of around 15.9 MW is provided to the receiver–reactor. The main optical losses are ascribed to the cosine effect, the spillage at the CPC entry aperture, and the absorption and rejection by the CPC. The system optical efficiency of 51% is lower than the values of approx. 60–70% for a typical beam-down system as discussed in [30] while a high concentration ratio of 2588 is achieved for the present system.

The following sections explore the effects of geometrical parameters excluding those of a CPC (Part 1) and CPC parameters (Part 2) on system optical and radiative performance metrics defined in Section 2.

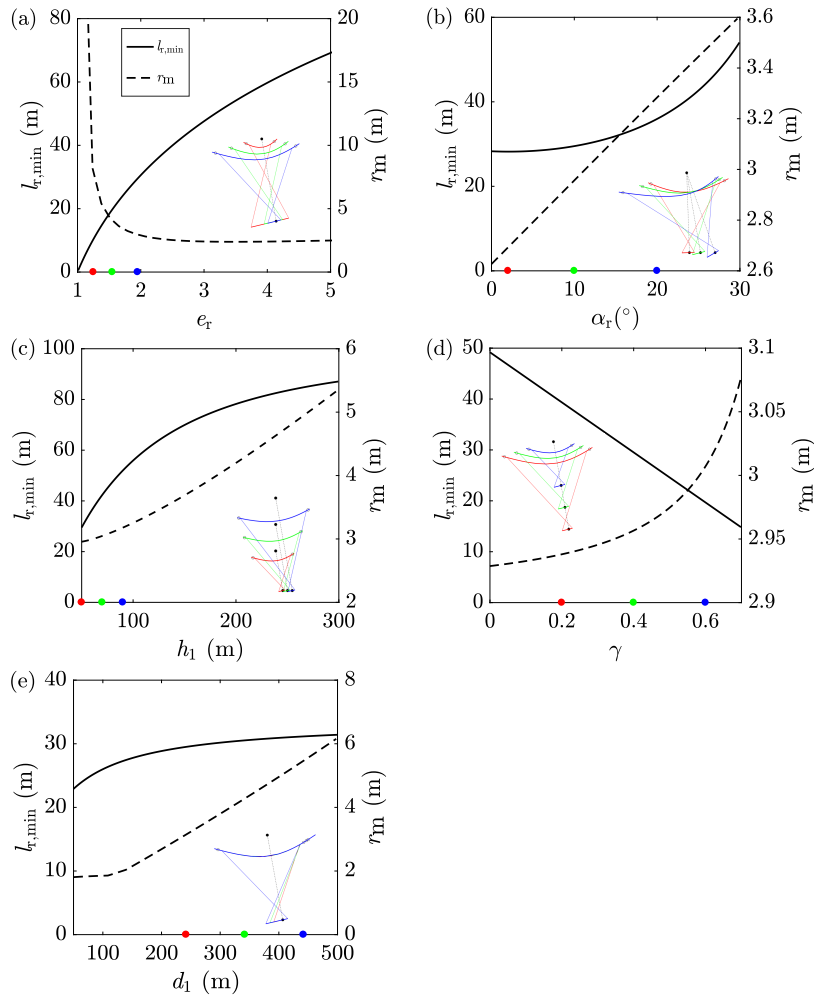


**Fig. 5.** Optical characteristics including required tower reflector (TR) size  $l_{r,min}$  and radius  $r_m$  of sun image on CPC entry aperture, as a function of (a) hyperboloidal TR eccentricity  $e_r$ , (b) TR axis tilt angle  $\alpha_r$ , (c) primary focus height  $h_1$ , (d) focal point height ratio  $\gamma$ , and (e) distance  $d_1$  from the furthestmost heliostat to tower.

**Table 2. Instantaneous optical performance of the baseline case**

Performance metrics	Value	Unit
Total number of heliostats	2258	–
CR at receiver–reactor aperture, $CR_{rec,a}$	2588	–
Radiative power entering receiver–reactor, $\dot{Q}_{rec,a}$	15.9	MW
System optical efficiency $\eta_{sys,opt}$	51%	–

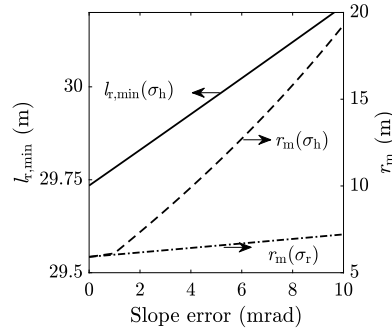


**Fig. 6.** Effects of slope errors of the heliostat and tower reflector (TR) surfaces,  $\sigma_h$  and  $\sigma_r$ , respectively, on required TR size  $l_{r,\min}$  and radius  $r_m$  of sun image on CPC entry aperture.

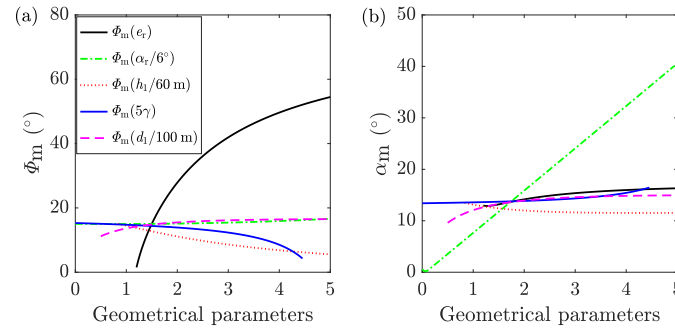


**Fig. 7.** Optical characteristics of the incident beam on the CPC entry aperture including (a) rim angle  $\Phi_m$  and (b) axis tilt angle  $\alpha_m$ , as a function of hyperboloidal tower reflector eccentricity  $e_r$ , TR axis tilt angle  $\alpha_r$ , primary focus height  $h_1$ , focal point height ratio  $\gamma$ , and distance  $d_1$  from the furthest heliostat to tower.

#### 4.2.1. Parametric study: Part 1

To accommodate the receiver–reactor array in the proposed system, the receiver–reactors are moved away from the locations corresponding to the maximum optical performance. For that purpose, we investigate the effects of geometrical parameters excluding those of a CPC in a 3D system with an example dislocated receiver–reactor for which the position is given by  $\alpha_r = 10^\circ$  and  $\phi_t = 0^\circ$ , on the instantaneous system optical and radiative performance characterized by the metrics defined in Subsection 2.2.

Figure 10 shows the results of the parametric studies performed using MCRT simulations. As shown in Fig. 10(a), the TR interception efficiency  $\eta_{\text{int},r}$  decreases with increasing hyperboloidal TR eccentricity  $e_r$  due to the increase of required TR size  $l_{r,\min}$  referring to Fig. 5(a). The CPC interception efficiency  $\eta_{\text{int},\text{CPC}}$  increases with an increasing  $e_r$  due to the decrease of  $r_m$  as indicated in Fig. 5(a). CPC transmission efficiency  $\eta_{\text{CPC}}$  decreases with the increase of  $e_r$  due to the increase of  $\Phi_m$  as seen in Fig. 7(a). Hence, an optimal  $e_r$  can be identified that offers the maximum system optical efficiency  $\eta_{\text{sys,opt}}$ , radiative power and CR at the receiver–reactor aperture. Figure 10(b) shows that the system optical performance is decreased for a larger

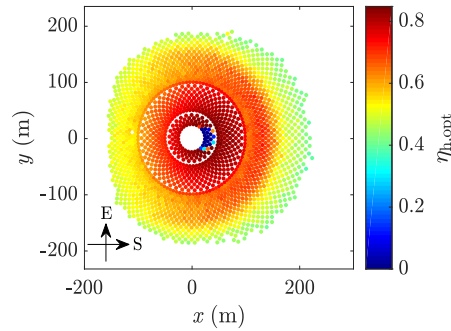


**Fig. 8.** The heliostat field for the baseline MCRT simulation. The color scale indicates the overall instantaneous (at autumn equinox noon) optical efficiency of each heliostat,  $\eta_{h,opt}$ . The tower is at the origin point. The heliostats near the origin point have low overall optical efficiency due to the shading by the tower reflector.

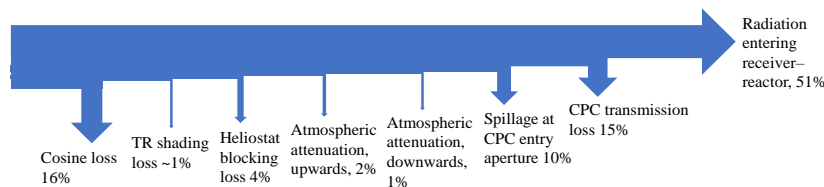


**Fig. 9.** Sankey diagram of instantaneous (at autumn equinox noon) optical losses for the baseline system with the parameter set of Table 1.

tilt angle  $\alpha_r$  of the TR axis, due to the increasing mismatch of the selected  $\alpha_{CPC}$  ( $= \alpha_r$  in the simulations) and  $\alpha_m$  (increasing with  $\alpha_r$  as seen in Fig. 7(b)).

Referring to Fig. 5(c),  $l_{r,min}$  and  $r_m$  increase with the increasing primary focus height  $h_1$ , resulting in decreasing interception efficiency of the TR and CPC,  $\eta_{int,TR}$  and  $\eta_{int,CPC}$ , respectively (Fig. 10(d)). As seen in Fig. 7(a), a higher primary focus results in the beam hitting the CPC entry aperture at a smaller rim angle  $\Phi_m$ , allowing for higher CPC transmission efficiency  $\eta_{CPC}$ .  $\eta_{CPC}$  diminishes as  $h_1$  increases further, because of the increasing misalignment of the axes of the CPC and the incident beam,  $\alpha_{CPC}$  and  $\alpha_m$ , respectively. The optimum  $h_1$  can be identified that offers the maximum radiative power and/or CR. The difference between  $\alpha_{CPC}$  ( $= \alpha_r$  in the simulations) and  $\alpha_m$  (shown in Fig. 7(b)) increases with the increasing focal point height ratio  $\gamma$ , which in turn results in decreasing  $\eta_{CPC}$  (Fig. 10(d)). The increase of  $\eta_{int,TR}$  with the increase of  $\gamma$  is due to the decrease of  $l_{r,min}$  as indicated in Fig. 5(d).

A larger TR leads to reduced TR spillage loss but more shading loss to the heliostat field by the TR. As the TR size increases, more rays reflected from the heliostat field are redirected by the TR, particularly the rays reflected from the heliostats further away from the tower. As a result,  $r_m$  and  $\Phi_m$  increase with a larger TR, which in turn decreases the CPC transmission and interception efficiencies, respectively (see Fig. 10(e)).

#### 4.2.2. Parametric study: Part 2

Parameters determining the geometry and orientation of the CPC coupled with the receiver-reactor are the entry aperture radius  $r_{in}$ , the acceptance angle  $\theta_{CPC}$ , and the axis tilt angle  $\alpha_{CPC}$ . CPC

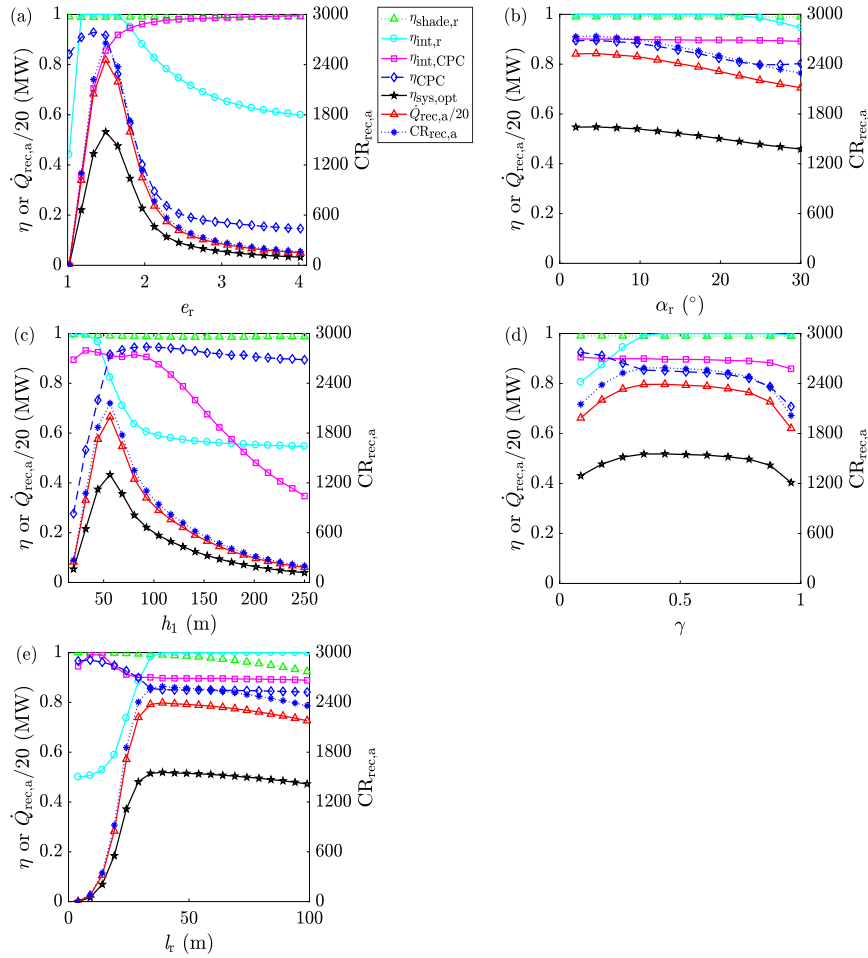


**Fig. 10.** Instantaneous optical efficiencies, radiative power and concentration ratio at receiver-reactor aperture, as a function of (a) hyperboloidal tower reflector (TR) eccentricity  $e_r$ , (b) TR axis tilt angle  $\alpha_r$ , (c) primary focus height  $h_1$ , (d) focal point height ratio  $\gamma$ , and (e) TR size  $l_T$ .

transmission and interception efficiencies,  $\eta_{\text{CPC}}$  and  $\eta_{\text{int,CPC}}$ , respectively, are affected by the difference between  $\alpha_{\text{CPC}}$  and  $\alpha_{\text{m}}$  and the ray distribution of the incident beam.  $\eta_{\text{CPC}}$  and  $\eta_{\text{int,CPC}}$  are also influenced by the difference between  $\alpha_{\text{CPC}}$  and  $\alpha_{\text{m}}$  and the difference between  $r_{\text{in}}$  and  $r_{\text{m}}$ , respectively. Parametric studies on CPC parameters on the instantaneous system optical efficiency  $\eta_{\text{sys,opt}}$  and  $\text{CR}_{\text{rec,a}}$  are carried out for each selected receiver–reactor position and presented in this subsection. Figure 11 shows  $\eta_{\text{sys,opt}}$  and  $\text{CR}_{\text{rec,a}}$  as a function of  $\theta_{\text{CPC}}$  (varying from  $10^\circ$  to  $50^\circ$  in  $5^\circ$  increments),  $r_{\text{in}}$  (varying from 1 m to 10 m in 1 m increments), and  $\alpha_{\text{CPC}}$  (varying from  $2^\circ$  to  $44^\circ$  in approximately  $3.8^\circ$  increments), for the defined receiver–reactor positions with two TR axis tilt angles  $\alpha_{\text{r}}$  of  $5^\circ$  and  $25^\circ$  and four azimuthal angles  $\phi_{\text{t}}$  of  $0^\circ$ ,  $90^\circ$ , and  $180^\circ$ . Optical performance for  $\phi_{\text{t}} = 270^\circ$  and  $\phi_{\text{t}} = 90^\circ$  are the same due to the symmetry of the system geometry, for which the results for  $\phi_{\text{t}} = 270^\circ$  are omitted from Figs. 11 and 12.

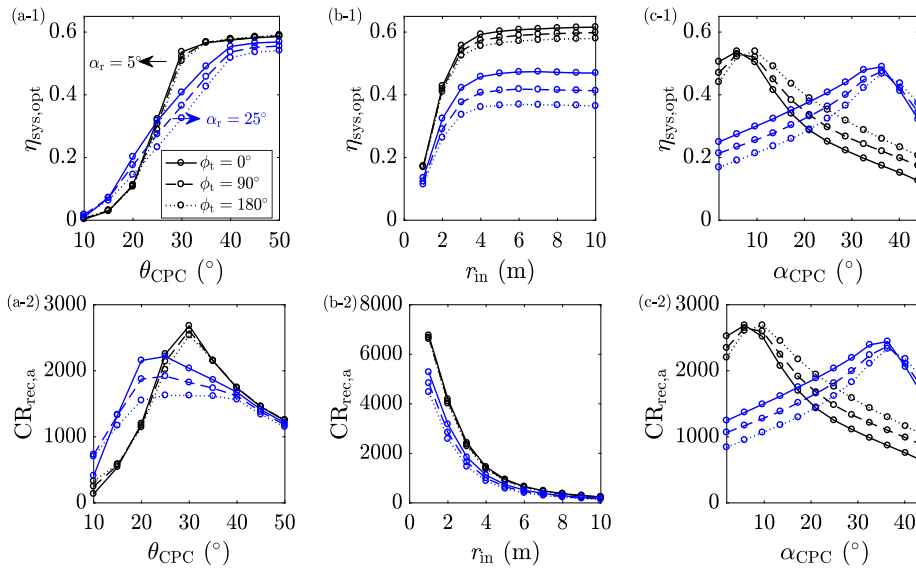


**Fig. 11.** Effects of (a) acceptance angle  $\theta_{\text{CPC}}$ , (b) entry aperture radius  $r_{\text{in}}$ , and (c) axis tilt angle  $\alpha_{\text{CPC}}$  of a CPC on (1) the instantaneous (at autumn equinox noon) system optical efficiency  $\eta_{\text{sys,opt}}$  and (2) concentration ratio  $\text{CR}_{\text{rec,a}}$  at the receiver–reactor aperture, for systems with the receiver–reactor placed at selected positions (characterized by tower reflector axis tilt angle  $\alpha_{\text{r}}$  and azimuthal angle  $\phi_{\text{t}}$ ).

According to Fig. 11, larger  $\theta_{\text{CPC}}$  and  $r_{\text{in}}$  result in higher  $\eta_{\text{sys,opt}}$  due to higher  $\eta_{\text{CPC}}$  and  $\eta_{\text{int,CPC}}$ , respectively (Fig. 11(a-1), (b-1)), but decreased  $\text{CR}_{\text{rec,a}}$  due to reduced maximum theoretical concentration ratio boost from the CPC of  $1/\sin^2\theta_{\text{CPC}}$  and lower mean radiative flux at the CPC entry aperture, respectively (Fig. 11(a-2), (b-2)). For the same  $\alpha_{\text{r}}$ , the highest and lowest  $\eta_{\text{sys,opt}}$  and/or  $\text{CR}_{\text{rec}}$  are found at  $\phi_{\text{t}} = 0^\circ$  and  $180^\circ$ , respectively. For a smaller  $\alpha_{\text{r}}$ , the systems with different  $\phi_{\text{t}}$  have close optical performance. Increasing differences between the optical performance of the systems with  $\phi_{\text{t}} = 0^\circ$  and  $\phi_{\text{t}} = 180^\circ$  are observed for the cases of larger  $\alpha_{\text{r}}$ . It is also found that the optimum  $\theta_{\text{CPC}}$  for maximizing  $\text{CR}_{\text{rec,a}}$  are different for  $\alpha_{\text{r}} = 5^\circ$  and  $\alpha_{\text{r}} = 25^\circ$ , indicating that different acceptance angles of CPCs may be required for the receiver–reactor positions with different TR axis tilt angle  $\alpha_{\text{r}}$ . Based on Fig. 11(c-1) and (c-2), the optimum  $\alpha_{\text{CPC}}$  leading to maximum  $\eta_{\text{sys,opt}}$  and  $\text{CR}_{\text{rec}}$  are equal and close to the selected  $\alpha_{\text{r}}$ . Thus,  $\alpha_{\text{CPC}}$  can be



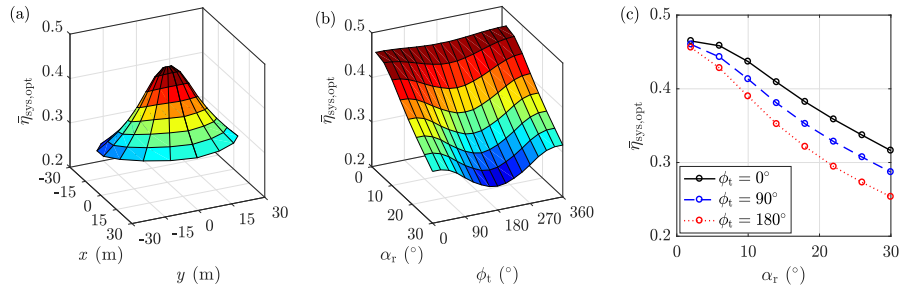


**Fig. 12.** Annual system optical efficiency  $\bar{\eta}_{\text{sys,opt}}$  of a beam-down optical system with one receiver–reactor placed at different relative positions to the tower. Receiver–reactor positions are expressed by (a) global coordinates  $x$  and  $y$ ; and (b,c) tilt angle  $\alpha_r$  of tower reflector axis and azimuthal angle  $\phi_t$  of secondary focus.

determined by optimizing the optical performance, while  $\theta_{\text{CPC}}$  and  $r_{\text{in}}$  should be selected as a trade-off between maximizing  $\eta_{\text{sys,tot}}$  and maximizing  $\text{CR}_{\text{rec,a}}$ .

#### 4.3. Annual simulations of 3D optical systems with selected receiver–reactor positions

Here, we present the annual simulation results for systems with selected receiver–reactor positions, i.e. the TR axis tilt angle  $\alpha_r$  varying from  $2^\circ$  to  $40^\circ$  in  $1.6^\circ$  increments and the azimuthal angle  $\phi_t$  varying from  $0^\circ$  to  $360^\circ$  in  $15^\circ$  increments. The results of the parametric studies presented in Subsection 4.2.2 indicate that the optimal CPC geometry for the maximized system optical performance may be different for each receiver–reactor position. However, it is pragmatic to manufacture CPCs with the same geometry, although with possible differences in their orientations as evident from results presented in Subsections 4.1 and 4.2. Based on the results shown in Fig. 11, we select example values of CPC parameters, i.e.  $\theta_{\text{CPC}}$  of  $30^\circ$ ,  $r_{\text{in}}$  of 2.8 m, and  $\alpha_{\text{CPC}}$  equal to the relevant  $\alpha_r$  for each receiver–reactor position.

Annual system optical efficiency  $\bar{\eta}_{\text{sys,opt}}$  for each system with the selected receiver–reactor position and the designed CPC is calculated and plotted in Fig. 12. Figure 12(a) and (b,c) show the results for the receiver–reactor positions expressed by the global coordinates  $x$  and  $y$ , and  $\alpha_r$  and  $\phi_t$ , respectively. A maximum  $\bar{\eta}_{\text{sys,opt}}$  of 46% is found at  $\alpha_r = 2^\circ$  (the smallest simulated  $\alpha_r$ ) and  $\phi_t = 0^\circ$ .  $\bar{\eta}_{\text{sys,opt}}$  decreases with an increasing  $\alpha_r$ . For a smaller  $\alpha_r$ ,  $\bar{\eta}_{\text{sys,opt}}$  varies little for different  $\phi_t$ . The difference between  $\bar{\eta}_{\text{sys,opt}}$  of the cases with different  $\phi_t$  increases with increasing  $\alpha_r$ . The system with  $\phi_t = 0^\circ$  performs best, followed by  $\phi_t = 90^\circ$  and  $\phi_t = 180^\circ$ . The same  $\bar{\eta}_{\text{sys,opt}}$  is observed for the receiver–reactor positions symmetric about the  $x$ -axis (the North–South direction).

The optical performance of the system with a receiver–reactor array is maximized for  $\alpha_r$  and  $\phi_t$  equal to  $2^\circ$  and  $0^\circ$ , respectively. The average optical efficiency of the system with the receiver–reactor array is affected by factors such as the selected total number of receivers, the finite receiver size, and the inter-receiver clearance required to accommodate potential auxiliary equipment in the receiver–reactor array.

## 5. Summary and conclusions

A novel beam-down optical system with a rotating tower reflector and an array of receiver–reactors has been proposed to realize multi-step solar thermochemical redox cycles for solar fuel production or thermal energy storage applications. Analytical and Monte-Carlo ray-tracing simulations

were performed for a simplified two-dimensional model system and a realistic three-dimensional beam-down optical model system, respectively. Instantaneous and annual optical characteristics were predicted for the proposed system.

The optimal geometrical parameters that offer the maximum system optical efficiency and radiative input to a receiver–reactor were identified. The heliostat surface slope error was found to have a greater influence on the sun image size than the slope error of the tower reflector surface. The baseline system was found to provide a flux concentration ratio of 2588 with an instantaneous system optical efficiency and radiative power to the receiver–reactor of 51% and 16 MW, respectively. We demonstrated that the annual system optical efficiency of the baseline system with a receiver–reactor placed to the south of the tower decreases from 46% to 37% for the axis tilt angle of the tower reflector increasing from 2° to 20°. Locating the receiver–reactor array south of and as close as possible to the tower offers the most promising optical configuration.

### Funding

Australian Renewable Energy Agency (2014/RND005); China Scholarship Council ([2017]3109).

### Acknowledgments

This research was undertaken with the assistance of resources and services from the National Computational Infrastructure (NCI), which is supported by the Australian Government.

### Disclosures

The authors declare no conflict of interest.

### References

1. M. Sturzenegger and P. Nüesch, "Efficiency analysis for a manganese-oxide-based thermochemical cycle," *Energy* **24**(11), 959–970 (1999).
2. M. Romero and A. Steinfeld, "Concentrating solar thermal power and thermochemical fuels," *Energy Environ. Sci.* **5**(11), 9234–9245 (2012).
3. R. Bader and W. Lipiński, "Solar thermal processing," in *Advances in Concentrating Solar Thermal Research and Technology* (Elsevier, 2017), 403–459.
4. G. Levêque, R. Bader, W. Lipiński, and S. Haussener, "High-flux optical systems for solar thermochemistry," *J. Sol. Energy Eng.* **156**, 133–148 (2017).
5. A. J. Carrillo, J. González-Aguilar, M. Romero, and J. M. Coronado, "Solar energy on demand: A review on high temperature thermochemical heat storage systems and materials," *Chem. Rev.* **119**(7), 4777–4816 (2019).
6. W. C. Chueh, C. Falter, M. Abbott, D. Scipio, P. Furler, S. M. Haile, and A. Steinfeld, "High-flux solar-driven thermochemical dissociation of CO<sub>2</sub> and H<sub>2</sub>O using nonstoichiometric ceria," *Science* **330**(6012), 1797–1801 (2010).
7. J. Lapp, J. H. Davidson, and W. Lipiński, "Efficiency of two-step solar thermochemical non-stoichiometric redox cycles with heat recovery," *Energy* **37**(1), 591–600 (2012).
8. J. Lapp, J. H. Davidson, and W. Lipiński, "Heat transfer analysis of a solid-solid heat recuperation system for solar-driven nonstoichiometric redox cycles," *J. Sol. Energy Eng.* **135**(3), 031004 (2013).
9. J. Lapp and W. Lipiński, "Transient three-dimensional heat transfer model of a solar thermochemical reactor for H<sub>2</sub>O and CO<sub>2</sub> splitting via nonstoichiometric ceria redox cycling," *J. Sol. Energy Eng.* **136** (2014).
10. D. Marxer, P. Furler, M. Takacs, and A. Steinfeld, "Solar thermochemical splitting of CO<sub>2</sub> into separate streams of CO and O<sub>2</sub> with high selectivity, stability, conversion, and efficiency," *Energy Environ. Sci.* **10**(5), 1142–1149 (2017).
11. B. Wang, L. Li, R. Bader, J. Pottas, V. Wheeler, P. Kreider, and W. Lipiński, "Thermal model of a solar thermochemical reactor for metal oxide reduction," *J. Sol. Energy Eng.* **142**(5), 051002 (2020).
12. A. Steinfeld, P. Furler, A. Haselbacher, and L. Geissbühler, "A thermochemical reactor system for a temperature swing cyclic process with integrated heat recovery and a method for operating the same," U.S. Patent Application No. 16/342 (2019).
13. M. Roeb, J.-P. Säck, P. Rietbrock, C. Prah, H. Schreiber, M. Neises, L. de Oliveira, D. Graf, M. Ebert, and W. Reinalter, "Test operation of a 100 kW pilot plant for solar hydrogen production from water on a solar tower," *Sol. Energy* **85**(4), 634–644 (2011).
14. E. Koepf, S. Zoller, S. Luque, M. Thelen, S. Brendelberger, J. González-Aguilar, M. Romero, and A. Steinfeld, "Liquid fuels from concentrated sunlight: An overview on development and integration of a 50 kW solar thermochemical reactor and high concentration solar field for the SUN-to-LIQUID project," in *AIP Conference Proceedings*, (AIP Publishing LLC, 2019), 180012.

15. C. Sattler, M. Roeb, C. Agrafiotis, and D. Thomey, "Solar hydrogen production via sulphur based thermochemical water-splitting," *Sol. Energy* **156**, 30–47 (2017).
16. F. Dähler, M. Wild, R. Schäppi, P. Haueter, T. Cooper, P. Good, C. Larrea, M. Schmitz, P. Furler, and A. Steinfeld, "Optical design and experimental characterization of a solar concentrating dish system for fuel production via thermochemical redox cycles," *Sol. Energy* **170**, 568–575 (2018).
17. C. Yuan, C. Jarrett, W. Chueh, Y. Kawajiri, and A. Henry, "A new solar fuels reactor concept based on a liquid metal heat transfer fluid: Reactor design and efficiency estimation," *Sol. Energy* **122**, 547–561 (2015).
18. R. Winston, J. C. Miñano, and P. G. Benitez, *Nonimaging Optics* (Elsevier, 2005).
19. H. Hasuike, Y. Yoshizawa, A. Suzuki, and Y. Tamaura, "Study on design of molten salt solar receivers for beam-down solar concentrator," *Sol. Energy* **80**(10), 1255–1262 (2006).
20. M. Epstein, G. Olalde, S. Santén, A. Steinfeld, and C. Wieckert, "Towards the industrial solar carbothermal production of zinc," *J. Sol. Energy Eng.* **130**(1), 014505 (2008).
21. E. Koepf, S. G. Advani, A. Steinfeld, and A. K. Prasad, "A novel beam-down, gravity-fed, solar thermochemical receiver/reactor for direct solid particle decomposition: Design, modeling, and experimentation," *Int. J. Hydrogen Energy* **37**(22), 16871–16887 (2012).
22. A. Lenert and E. N. Wang, "Optimization of nanofluid volumetric receivers for solar thermal energy conversion," *Sol. Energy* **86**(1), 253–265 (2012).
23. M. Mokhtar, S. A. Meyers, P. R. Armstrong, and M. Chiesa, "Performance of a 100 kW<sub>th</sub> concentrated solar beam-down optical experiment," *J. Sol. Energy Eng.* **136**(4), 041007 (2014).
24. G. Xiao, K. Guo, Z. Luo, M. Ni, Y. Zhang, and C. Wang, "Simulation and experimental study on a spiral solid particle solar receiver," *Appl. Energy* **113**, 178–188 (2014).
25. X. Li, Y. Dai, and R. Wang, "Performance investigation on solar thermal conversion of a conical cavity receiver employing a beam-down solar tower concentrator," *Sol. Energy* **114**, 134–151 (2015).
26. M. Martins, U. Villalobos, T. Delclos, P. Armstrong, P. G. Bergan, and N. Calvet, "New concentrating solar power facility for testing high temperature concrete thermal energy storage," *Energy Procedia* **75**, 2144–2149 (2015).
27. T. Kodama, N. Gokon, H. S. Cho, K. Matsubara, T. Etori, A. Takeuchi, S.-N. Yokota, and S. Ito, "Particles fluidized bed receiver/reactor with a beam-down solar concentrating optics: 30-kW<sub>th</sub> performance test using a big sun-simulator," in *AIP Conference Proceedings*, (AIP Publishing, 2016), 120004.
28. S. Bellan, K. Matsubara, C. H. Cheok, N. Gokon, and T. Kodama, "CFD-DEM investigation of particles circulation pattern of two-tower fluidized bed reactor for beam-down solar concentrating system," *Powder Technol.* **319**, 228–237 (2017).
29. G. Manikandan, S. Iniyar, and R. Goic, "Enhancing the optical and thermal efficiency of a parabolic trough collector – A review," *Appl. Energy* **235**, 1524–1540 (2019).
30. A. Segal and M. Epstein, "Comparative performances of 'tower-top' and 'tower-reflector' central solar receivers," *Sol. Energy* **65**(4), 207–226 (1999).
31. L. Li, B. Wang, J. Pottas, and W. Lipiński, "Design of a compound parabolic concentrator for a multi-source high-flux solar simulator," *Sol. Energy* **183**, 805–811 (2019).
32. C. E. Mauk, H. W. Prengle Jr, and E. C.-H. Sun, "Optical and thermal analysis of a Cassegrainian solar concentrator," *Sol. Energy* **23**(2), 157–167 (1979).
33. A. Yogeve, A. Kribus, M. Epstein, and A. Kogan, "Solar 'tower reflector' systems: a new approach for high-temperature solar plants," *Int. J. Hydrogen Energy* **23**(4), 239–245 (1998).
34. A. Segal and M. Epstein, "The optics of the solar tower reflector," *Sol. Energy* **69**, 229–241 (2001).
35. A. Segal and M. Epstein, "Practical considerations in designing large scale 'beam down' optical systems," *J. Sol. Energy Eng.* **130**(1), 011009 (2008).
36. X. Wei, Z. Lu, W. Yu, and W. Xu, "Ray tracing and simulation for the beam-down solar concentrator," *Renewable Energy* **50**, 161–167 (2013).
37. L. Vant-Hull, "Issues with beam-down concepts," *Energy Procedia* **49**, 257–264 (2014).
38. E. Leonardi, "Detailed analysis of the solar power collected in a beam-down central receiver system," *Sol. Energy* **86**(2), 734–745 (2012).
39. L. Li, J. Coventry, R. Bader, J. Pye, and W. Lipiński, "Optics of solar central receiver systems: a review," *Opt. Express* **24**(14), A985–A1007 (2016).
40. B. Grange, V. Kumar, A. Gil, P. R. Armstrong, D. S. Codd, A. Slocum, and N. Calvet, "Preliminary optical, thermal and structural design of a 100 kW<sub>th</sub> CSPonD beam-down on-sun demonstration plant," *Energy Procedia* **75**, 2163–2168 (2015).
41. Magaldi, retrieved 26 October, 2019, <https://www.magaldi.com/en/products-solutions/csp-concentrating-solar-power>.
42. HELIOSCSP, retrieved 26 October, 2019, <http://helioscsp.com/three-solar-modules-of-worlds-first-commercial-beam-down-tower-concentrated-solar-power-project-to-be-connected-to-grid/>.
43. I. N. Bronshteyn and K. A. Semendyayev, *Handbook of Mathematics* (Springer Science & Business Media, 2013).
44. M. F. Modest, *Radiative Heat Transfer* (Academic, 2013).
45. L. Li, B. Wang, J. Pye, and W. Lipiński, "Temperature-based optical design, optimization and economics of solar polar-field central receiver systems with an optional compound parabolic concentrator," *Sol. Energy*, doi:10.1016/j.solener.2020.05.088 (2020).
46. J. A. Duffie and W. A. Beckman, *Solar Engineering of Thermal Processes* (John Wiley & Sons, 2013).

47. A. B. Sproul, "Derivation of the solar geometric relationships using vector analysis," *Renewable Energy* **32**(7), 1187–1205 (2007).
48. D. Buie, A. Monger, and C. Dey, "Sunshape distributions for terrestrial solar simulations," *Sol. Energy* **74**(2), 113–122 (2003).
49. F. J. Collado and J. Guallar, "Campo: Generation of regular heliostat fields," *Renewable Energy* **46**, 49–59 (2012).
50. R. Bader, S. Haussener, and W. Lipiński, "Optical design of multisource high-flux solar simulators," *J. Sol. Energy Eng.* **137**(2), 021012 (2015).
51. P. Leary and J. Hankins, "User's guide for MIRVAL: a computer code for comparing designs of heliostat-receiver optics for central receiver solar power plants," (Sandia National Laboratories, Livermore, CA (USA), 1979).
52. V. Grigoriev, C. Corsi, and M. Blanco, "Fourier sampling of sun path for applications in solar energy," in *AIP Conference Proceedings*, (AIP Publishing, 2016), 020008.
53. W. H. Press, S. A. Teukolsky, W. T. Vetterling, and B. P. Flannery, *Numerical Recipes in Fortran 90* (Cambridge University, 1996), Vol. 2.
54. W. J. Smith, *Modern Optical Engineering*, 4th ed. (McGraw-Hill, 2008).
55. Y. Wang, D. Potter, C.-A. Asselineau, C. Corsi, M. Wagner, C. Caliot, B. Piaud, M. Blanco, J.-S. Kim, and J. Pye, "Verification of optical modelling of sunshape and surface slope error for concentrating solar power systems," *Sol. Energy* **195**, 461–474 (2020).
56. L. Li, B. Wang, R. Bader, J. Zapata, and W. Lipiński, "Reflective optics for redirecting convergent radiative beams in concentrating solar applications," *Sol. Energy* **191**, 707–718 (2019).

---

## Summary and outlook

---

### 9.1 Summary

In this work, optical studies have been conducted for a high-flux solar simulator (HFSS) based experimental system and commercial-scale solar central receiver systems (CRSs). Optical studies of a compound parabolic concentrator (CPC) and reflective optics were performed to aid in solving the limitations and problems of the HFSS-based experimental system (see Chapters 3 and 4). Commercial-scale solar CRSs were investigated for a wide range of receiver temperatures in two different power levels (see Chapters 6 and 7). A proposed novel solar beam-down system was studied (see Chapter 8). The review of the background information of radiative transfer, CPCs, HFSSs, solar CRSs, and methodology was presented in Chapter 2. Optical modelling was performed using in-house developed two-dimensional (2D) analytical ray-tracing and three-dimensional (3D) Monte-Carlo ray-tracing (MCRT) programs.

The application of primary optics realises an efficient utilisation of the diluted solar radiation. The application of secondary optics further increases solar concentration ratios, thus allows for high-temperature applications. The combined design of primary and secondary optics enables a variety of optical configurations of concentrating solar systems for realising specific design objectives.

#### 9.1.1 HFSS-based experimental systems

The application of multi-source HFSSs was found to be accompanied by limitations of high peak fluxes, high flux non-uniformity, and fixed-axis output beams. A 3D CPC and four types of reflective optics: flat, ellipsoidal, hyperboloidal, and paraboloidal reflectors were designed and investigated for solving these limitations.

Chapter 3 reported the development of a 3D-printed CPC for use in a high-temperature solar reduction reactor operating up to 1300 K. It was the first study in which the 3D CPC was manufactured with the 3D printing technique and without any simplification in its geometry. The CPC geometrical parameters including acceptance angle and entry aperture radius were determined through an optical design guided by optical MCRT simulations. Thermal management strategy of the CPC was developed using simple analytical relations based on the Gnielinski correlation and

the Darcy–Weisbach equation for heat transfer of turbulent flow and pressure drop of cooling water, respectively. The optical simulations demonstrated that the proposed CPC design can significantly reduce flux non-uniformity and radiative peak flux on target surfaces as compared to the case without any CPC applied. The CPC increases the concentration ratio by a factor of 4.1 at an optical efficiency of 85.4%, and reduces the spillage loss from 78.9% to 34.5%. Moreover, the CPC increases the degree of flexibility for utilisation of different combinations of lamps of a multi-source HFSS.

Optical characteristics of beam-redirecting optical systems involving flat, ellipsoidal, hyperboloidal, and paraboloidal reflectors have been investigated for solar systems with point-focusing beams as presented in Chapter 4. The investigated four types of beam-redirecting reflectors redirect the horizontal-axis beam from a solar simulator onto non-horizontal axis targets. A flat reflector retains the characteristics of rim angle and ray distribution of the input beam and enables the highest system optical efficiency at the expense of the smallest clearance between the source, the reflector, and the reflected image. System component distance would increase for input beams with smaller rim angles. Curved reflectors render a larger degree of freedom to design the characteristics of the output beam. Thus, curved reflectors are suitable for applications that require large clearance between system components and/or high peak flux on cavity surface, but at the expense of lower system optical efficiency. Besides the design of secondary optics, this study also uncovered potential improvements in future simulator design: (i) for constructed solar simulators with rim angles less than  $45^\circ$ , a flat reflector is the best and simplest solution for realising the beam redirection, (ii) choose smaller rim angles below  $45^\circ$  when designing solar simulators, which enables the use of a flat reflector for redirecting beams and better flux uniformity when using curved reflectors, and (iii) if an increase of higher radiative power and fluxes output from HFSSs is desired, the added HFSS lamps should be placed along the HFSS axis to avoid the increase of HFSS rim angle. However, this will lead to a larger focal distance, i.e. distance between the HFSS radiation modules and the focal point, and thereby a larger space for the HFSS test facility.

Despite the presented limitations of a HFSS, it is still one of the most powerful facilities for laboratory-scale testing of materials and device prototypes under highly concentrated irradiation. The performance of a HFSS can be significantly improved by the design of secondary optics, although it is accompanied by additional inherent optical losses and costs of secondary optics.

### 9.1.2 Solar central receiver systems

A review study presented in Chapter 5 provided an overview of the state of the art in the optics of solar CRSs, and demonstrated the limitations that exist in the analysis of large-scale multi-stage concentrator technologies for high-temperature applications. Typical system configurations were discussed along with the main components—heliostats, heliostat fields, secondary optical concentrators, and receivers. A review of research studies of optical design, optimisation, and characterisation of heliostats and heliostat fields was conducted. A large variety of optical analysis tools were

developed and applied for the design and optimisation of demonstration and commercial facilities. A relatively small number of published studies report experimental results of on-sun optical characterisation of CRSs. Modelling the optical performance of CRSs is an efficient and accurate approach for the design and optimisation without incurring substantial costs associated with the construction of early-stage prototype systems. The large number of available tools allows optical engineers to reduce the development time. However, the specific configurations of individual designs typically necessitate the extension or development of new, advanced tools that allow for increased simulation accuracy and flexibility, in particular for problems coupling optics, thermophysics, and thermochemistry in plant sub-systems. Optical design and optimisation of CRSs is the key to reduce their capital cost.

Following the review study, Chapter 6 presented an in-depth, comprehensive study of a large-scale, polar-field CRS for high-temperature applications comparing systems with an optional a CPC. The effects of the receiver temperature and the addition of a CPC on the energetic and economic characteristics of solar CRSs were investigated. Systems were optimised for maximum annual solar-to-thermal efficiency, maximum annual solar-to-exergy efficiency, and minimum levelised cost of exergy, for receivers operated at temperatures in the range of 600–1800 K. We demonstrated and compared the optical configurations of the cost-optimal CRSs operated at each simulated receiver temperature. Parametric studies and optimisation were carried out for both systems without and with a CPC, where we identified the temperature thresholds above which the system energetic and economic performance benefit from the addition of a CPC. It was found that the minimum levelised cost of exergy for systems without and with a CPC is 0.083 and 0.095 USD kWh<sup>-1</sup>, respectively, for receivers working at a temperature of 900 and 1100 K. The addition of a CPC improves system energetic and economic performance for receiver temperatures above 900 K and 1200 K, respectively. At higher temperatures above 1200 K, high concentration ratios are required to mitigate the rapid increase of receiver emission losses, for which energetic and economic advantages of adding a CPC show up. This study demonstrated the significance of applying CPCs in systems at elevated temperatures.

We further conducted an optical study of CRSs with a multi-aperture receiver and multiple sub-fields for increasing the power output, as presented in Chapter 7. This study focused on the systems with CPCs due to the aim of high-temperature applications. Effects of the heliostat sub-field configuration, the number of apertures, and the optical properties of reflective surfaces on the optical and energetic performance of systems with the receiver temperature in the range of 600–1800 K were explored. The characteristics of maximum net receiver power, instantaneous and annual overall optical efficiency, solar-to-thermal efficiency, and solar-to-exergy efficiency were predicted. We demonstrated that the net receiver power is significantly boosted by increasing the number of aperture from one to four, while further increasing the number of apertures over four leads to limited gain of power but greatly reduced efficiencies. The CPC slope error was found to have minor effects on the system performance due to a relatively short optical length from CPC reflective surface to receiver aperture. This optical study provided inputs for the determination of a

multi-aperture solar CRS which will be a result of the combined considerations of the system efficiencies, the power output, the economics of optical system, as well as the economics of power block influenced by the net receiver power.

Lastly, optical analysis was performed to investigate a novel solar beam-down optical system with a rotating tower reflector and an array of receiver–reactors, as presented in Chapter 8. This study proposed a new optical method to realise the alternation of solar irradiation into a number of solar receiver–reactors as required by the thermochemical redox cycles. Optical analysis was conducted to explore the effects of the tilt of the tower reflector on the system optical performance. The optimal geometrical parameters that offer the maximum system optical efficiency and radiative input to a receiver–reactor were identified. The heliostat surface slope error was found to have a greater influence on the sun image size than the slope error of the tower reflector surface. The baseline system was found to provide a solar concentration ratio of 2588 suns with an instantaneous system optical efficiency and radiative power to the receiver–reactor of 51% and 16 MW, respectively. We demonstrated that the annual system optical efficiency of the baseline system with a receiver–reactor placed to the south of the tower decreases from 46% to 37% for the axis tilt angle of the tower reflector increasing from  $2^\circ$  to  $20^\circ$ . Locating the receiver–reactor array south of and as close as possible to the tower offers the most promising optical configuration. The benefit of the design was demonstrated in the increase of thermal-to-chemical conversion efficiency of 42% under the assumption of perfect gas-phase heat recovery and a concentration ratio of 5000 suns, as shown in a companion thermodynamic analysis of the receiver–reactor array with heat recuperation [182].

Despite the decreasing cost of electricity produced by the photovoltaic technologies, concentrating solar thermal technologies own the unique advantages of inherent thermal energy storage and suitability for thermochemical processing. Concentrating solar thermochemical technologies can be employed for a wide range of applications such as energy storage, solar fuel production, fossil fuel upgrade,  $\text{CO}_2$  capture, and chemical commodities production.

## 9.2 Outlook

For the HFSS-based experimental system, another interesting topic to be explored in the future is to make the non-uniformly distributed, convergent output beams from the HFSSs approximate the solar radiation arriving at the earth's surface, i.e. both uniformly-distributed and Ccollimated. This will greatly expand the application range of HFSSs in solar-related researches. Moreover, the optics investigated in this work are all reflective optics. The HFSSs experimental system can be further advanced by the design of refractive lenses, Fresnel mirrors, and totally internally reflecting lenses.

For the large-scale solar CRS, we performed extensive simulations for the optimisation using parametric optimisation. Optimisation algorithms can be employed for reducing the computational time and improving the precision of results. Other



types of secondary optics in addition to CPCs can be evaluated for their use in high-temperature CRSs.

For the multi-aperture CRS, the difference between radiative power captured by each receiver–reactor aperture and its change as time are to be addressed in the future. A comparison of the system with and without CPCs as well as the economic analysis, are worthwhile to be investigated. Another approach for increasing the net receiver power is by the design of a multi-tower system via duplicating the single-tower, polar-field system. The multi-tower system potentially leads to higher system optical performance but higher capital costs due to the use of more towers. Energetic and economic analyses can be performed in the future to compare these two approaches of increasing the net receiver power: multi-aperture and multi-tower designs.

The novel beam-down system described in this thesis can be further investigated by *(i)* coupling the optical, heat and mass transfer analyses, *(ii)* examining the concentrated flux on the tower reflector surface, and *(iii)* addressing practical challenges of mechanical and structural issues of rotating the large tower reflector. A further investigation can be performed to compare different concepts of realising the alternation of incident radiation into receiver–reactors in addition to the proposed concept of rotating tower reflector, such as varying aiming points of heliostats.

---

## Bibliography

---

1. R. Corkish, W. Lipiński, and R. J. Patterson. Introduction to solar energy. In G. M. Crawley, editor, *Solar Energy*, volume 2 of *World Scientific Series in Current Energy Issues*, pages 1–29. World Scientific, Singapore, 2016. ISBN 978-981-4689-49-6 (print) and 978-981-4689-51-9 (electronic). (cited on page 1)
2. D. Y. Goswami, F. Kreith, and J. F. Kreider. *Principles of solar engineering*. CRC Press, 2000. (cited on page 1)
3. K. Lovegrove and W. Stein. *Concentrating Solar Power Technology: Principles, Developments and Applications*. Elsevier, 2021. (cited on pages 1, 4, and 71)
4. M. Romero and A. Steinfeld. Concentrating solar thermal power and thermochemical fuels. *Energy and Environmental Science*, 5(11):9234–9245, 2012. (cited on pages 1 and 6)
5. D. Yadav and R. Banerjee. A review of solar thermochemical processes. *Renewable and Sustainable Energy Reviews*, 54:497–532, 2016. (cited on page 6)
6. R. Bader and W. Lipiński. *Advances in Concentrating Solar Thermal Research and Technology*, chapter Solar Thermal Processing, pages 403–447. Woodhead Publishing, 2017. (cited on page 1)
7. A. Steinfeld and R. Palumbo. Solar thermochemical process technology. *Encyclopedia of Physical Science and Technology*, 15(1):237–56, 2001.
8. G. Levêque, R. Bader, W. Lipiński, and S. Haussener. High-flux optical systems for solar thermochemistry. *Solar Energy*, 156:133–148, 2017. (cited on pages 2, 3, and 6)
9. A. J. Carrillo, J. González-Aguilar, M. Romero, and J. M. Coronado. Solar energy on demand: A review on high temperature thermochemical heat storage systems and materials. *Chemical Reviews*, 119(7):4777–4816, 2019. (cited on page 1)
10. A. Bayon, R. Bader, M. Jafarian, L. Fedunik-Hofman, Y. Sun, J. Hinkley, S. Miller, and W. Lipiński. Techno-economic assessment of solid–gas thermochemical energy storage systems for solar thermal power applications. *Energy*, 149:473–484, 2018. (cited on pages 1 and 6)
11. L. Li, J. Coventry, R. Bader, J. Pye, and W. Lipiński. Optics of solar central receiver systems: A review. *Optics Express*, 24(14):A985–A1007, 2016. (cited on pages 1, 2, 4, 5, 9, 12, 14, 17, and 18)

12. L. Li, B. Wang, J. Pye, and W. Lipiński. Temperature-based optical design, optimization and economics of solar polar-field central receiver systems with an optional compound parabolic concentrator. *Solar Energy*, 206:9107–9122, 2020. (cited on pages 1, 23, 71, and 87)
13. F. Dähler. *High-Flux Solar Optics for Thermochemical Fuel Production: Development, Characterization and Field Layouts*. PhD thesis, ETH Zurich, 2018. (cited on page 2)
14. M. F. Modest. *Radiative Heat Transfer*. Academic Press, 2013. (cited on pages 2, 7, 9, 10, and 19)
15. C. N. Vittitoe and F. Biggs. Six-Gaussian representation of the angular-brightness distribution for solar radiation. *Solar Energy*, 27(6):469–490, 1981. (cited on pages 2 and 10)
16. A. Rabl and P. Bendt. Effect of circumsolar radiation on performance of focusing collectors. *Journal of Solar Energy Engineering*, 104(3):237–250, 1982. (cited on page 10)
17. D. Buie, A. Monger, and C. Dey. Sunshape distributions for terrestrial solar simulations. *Solar Energy*, 74(2):113–122, 2003. (cited on pages 2 and 10)
18. J. Coventry and C. Andraka. Dish systems for CSP. *Solar Energy*, 152:140–170, 2017. (cited on page 2)
19. W. Lipiński, E. Abbasi-Shavazi, J. Chen, J. Coventry, M. Hangi, S. Iyer, A. Kumar, L. Li, S. Li, J. Pye, J. F. Torres, B. Wang, Y. Wang, and V. M. Wheeler. Progress in heat transfer research for high-temperature solar thermal applications. *Applied Thermal Engineering*, 184:116137, 2021. (cited on pages 3 and 14)
20. F. Wang, Z. Cheng, J. Tan, Y. Yuan, Y. Shuai, and L. Liu. Progress in concentrated solar power technology with parabolic trough collector system: A comprehensive review. *Renewable and Sustainable Energy Reviews*, 79:1314–1328, 2017. (cited on page 4)
21. E. Bellos. Progress in the design and the applications of linear Fresnel reflectors—A critical review. *Thermal Science and Engineering Progress*, 10:112–137, 2019. (cited on page 4)
22. J. A. Duffie and W. A. Beckman. *Solar Engineering of Thermal Processes*. John Wiley & Sons, 2013. (cited on pages 4 and 20)
23. C.-A. Asselineau, J. Coventry, and J. Pye. Exergy analysis of the focal-plane flux distribution of solar-thermal concentrators. *Applied Energy*, 222:1023–1032, 2018. (cited on page 4)

24. Y. Wang, D. Potter, C.-A. Asselineau, C. Corsi, M. Wagner, C. Caliot, B. Piaud, M. Blanco, J.-S. Kim, and J. Pye. Verification of optical modelling of sunshape and surface slope error for concentrating solar power systems. *Solar Energy*, 195: 461–474, 2020. (cited on pages 4 and 23)
25. L. Li, B. Wang, R. Bader, J. Zapata, and W. Lipiński. Reflective optics for redirecting convergent radiative beams in concentrating solar applications. *Solar Energy*, 191:707–718, 2019. (cited on pages 4 and 33)
26. J. M. Gordon and D. Feuermann. Optical performance at the thermodynamic limit with tailored imaging designs. *Applied Optics*, 44(12):2327–2331, 2005. (cited on page 4)
27. J. M. Gordon. Aplanatic optics for solar concentration. *Optics Express*, 18(101): A41–A52, 2010.
28. H. Mashaal, D. Feuermann, and J. M. Gordon. Expansive scope of aplanatic concentrators and collimators. *Applied Optics*, 58:F14–F20, 2019. (cited on page 4)
29. A. Steinfeld. Cone compared to CPC as secondary concentrator in tandem with a paraboloidal dish primary. *Journal of Solar Energy Engineering*, 114(3):201–202, 1992. (cited on page 5)
30. J. O’Gallagher and R. Winston. Test of a “trumpet” secondary concentrator with a paraboloidal dish primary. *Solar Energy*, 36(1):37–44, 1986. (cited on pages 5 and 6)
31. S. Wang, C.-A. Asselineau, Y. Wang, J. Pye, and J. Coventry. Performance enhancement of cavity receivers with spillage skirts and secondary reflectors in concentrated solar dish and tower systems. *Solar Energy*, 208:708–727, 2020. (cited on page 5)
32. J. Gordon and H. Ries. Tailored edge-ray concentrators as ideal second stages for Fresnel reflectors. *Applied Optics*, 32(13):2243–2251, 1993. (cited on page 5)
33. R. Winston, J. C. Miñano, and P. G. Benitez. *Nonimaging Optics*. Elsevier, 2005. (cited on pages 5, 12, and 22)
34. M. Schmitz, T. Cooper, G. Ambrosetti, and A. Steinfeld. Two-stage solar concentrators based on parabolic troughs: asymmetric versus symmetric designs. *Applied Optics*, 54(33):9709–9721, 2015. (cited on page 5)
35. A. Kribus, M. Huleihil, A. Timinger, and R. Ben-Mair. Performance of a rectangular secondary concentrator with an asymmetric heliostat field. *Solar Energy*, 69(2):139–151, 2000. (cited on pages 5 and 11)
36. J. Chaves. *Introduction to Nonimaging Optics*. CRC Press, 2017. (cited on page 5)

37. A. Kribus, V. Krupkin, A. Yogev, and W. Spirkl. Performance limits of heliostat fields. *Journal of Solar Energy Engineering*, 120(4):240–246, 1998. (cited on page 5)
38. M. Gajic, D. Rodriguez-Sanchez, and G. Rosengarten. Beam splitting with a luminescent solar concentrator in a hybrid photovoltaic/thermal collector. In *ISES Solar World Congress 2017*, 2017. (cited on page 5)
39. W. C. Chueh, C. Falter, M. Abbott, D. Scipio, P. Furler, S. M. Haile, and A. Steinfeld. High-flux solar-driven thermochemical dissociation of CO<sub>2</sub> and H<sub>2</sub>O using nonstoichiometric ceria. *Science*, 330(6012):1797–1801, 2010. (cited on pages 5 and 17)
40. A. Meier, E. Bonaldi, G. M. Cella, W. Lipiński, and D. Wullemmin. Solar chemical reactor technology for industrial production of lime. *Solar Energy*, 80(10):1355–1362, 2006.
41. P. Furler, J. R. Scheffe, and A. Steinfeld. Syngas production by simultaneous splitting of h<sub>2</sub>o and co<sub>2</sub> via ceria redox reactions in a high-temperature solar reactor. *Energy & Environmental Science*, 5(3):6098–6103, 2012. (cited on page 5)
42. A. Lewandowski, C. Bingham, J. O’Gallagher, R. Winston, and D. Sagie. Performance characterization of the SERI high-flux solar furnace. *Solar Energy Materials*, 24(4):550–563, 1991. (cited on page 6)
43. A. Neumann and U. Groer. Experimenting with concentrated sunlight using the DLR solar furnace. *Solar Energy*, 58(4-6):181–190, 1996.
44. G. Flamant, A. Ferriere, D. Laplaze, and C. Monty. Solar processing of materials: opportunities and new frontiers. *Solar Energy*, 66(2):117–132, 1999.
45. P. Haueter, T. Seitz, and A. Steinfeld. A new high-flux solar furnace for high-temperature thermochemical research. *Journal of Solar Energy Engineering*, 121(1):77–80, 1999.
46. J. Fernández-Reche, I. Cañadas, M. Sánchez, J. Ballestrín, L. Yebra, R. Monterreal, J. Rodríguez, G. García, M. Alonso, and F. Chenlo. PSA Solar furnace: A facility for testing PV cells under concentrated solar radiation. *Solar Energy Materials and Solar Cells*, 90(15):2480–2488, 2006.
47. D. Riveros-Rosas, J. Herrera-Vázquez, C. Pérez-Rábago, C. Arancibia-Bulnes, S. Vázquez-Montiel, M. Sánchez-González, F. Granados-Agustín, O. Jaramillo, and C. Estrada. Optical design of a high radiative flux solar furnace for Mexico. *Solar Energy*, 84(5):792–800, 2010.
48. J. C. G. Pereira, K. Rahmani, and L. G. Rosa. Computer modelling of the optical behavior of homogenizers in high-flux solar furnaces. *Energies*, 14(7):1828, 2021. (cited on page 6)

49. A. Munoz Torralbo, C. Hernandez Gonzalvez, C. Ortiz Roses, J. Avellaner Lacal, and F. Sanchez. A Spanish 'power tower' solar system Project CESA-1. *Journal of Solar Energy and Engineering*, 106:78–82, 1984. (cited on page 6)
50. K. Hennecke, P. Schwarzbözl, G. Koll, M. Beuter, B. Hoffschmidt, J. Götsche, and T. Hartz. The solar power tower Jülich–solar thermal power plant for test and demonstration of air receiver technology. In *Proceedings of ISES World Congress 2007 (Vol. I–Vol. V)*, pages 1749–1753. Springer, 2008.
51. P. Schramek, D. R. Mills, W. Stein, and P. Le Lièvre. Design of the heliostat field of the CSIRO solar tower. *Journal of Solar Energy Engineering*, 131(2):024505, 2009.
52. E. Xu, Q. Yu, Z. Wang, and C. Yang. Modeling and simulation of 1 MW DAHAN solar thermal power tower plant. *Renewable Energy*, 36(2):848–857, 2011.
53. A. Salomé, F. Chhel, G. Flamant, A. Ferrière, and F. Thiery. Control of the flux distribution on a solar tower receiver using an optimized aiming point strategy: Application to THEMIS solar tower. *Solar Energy*, 94:352–366, 2013.
54. T. Kodama, N. Gokon, K. Matsubara, K. Yoshida, S. Koikari, Y. Nagase, and K. Nakamura. Flux measurement of a new beam-down solar concentrating system in Miyazaki for demonstration of thermochemical water splitting reactors. *Energy Procedia*, 49:1990–1998, 2014.
55. B. Grange, V. Kumar, A. Gil, P. R. Armstrong, D. S. Codd, A. Slocum, and N. Calvet. Preliminary optical, thermal and structural design of a 100 kW<sub>th</sub> CSPonD beam-down on-sun demonstration plant. *Energy Procedia*, 75:2163–2168, 2015. (cited on page 16)
56. Magaldi, 2019. URL <https://www.magaldi.com/en/products-solutions/csp-concentrating-solar-power>. (cited on pages 6 and 16)
57. K. Lovegrove, G. Burgess, and J. Pye. A new 500 m<sup>2</sup> paraboloidal dish solar concentrator. *Solar Energy*, 85(4):620–626, 2011. (cited on page 6)
58. P. Kuhn and A. Hunt. A new solar simulator to study high temperature solid-state reactions with highly concentrated radiation. *Solar Energy Materials*, 24(1-4):742–750, 1991. (cited on page 6)
59. D. Hirsch, T. Osinga, J. Kinamore, and A. Steinfeld. A new 75 kW high-flux solar simulator for high-temperature thermal and thermochemical research. *Journal of Solar Energy Engineering*, 125(1):117–120, 2003.
60. J. Petrasch, P. Coray, A. Meier, M. Brack, P. Häberling, D. Wüllemmin, and A. Steinfeld. A novel 50kW 11,000 suns high-flux solar simulator based on an array of xenon arc lamps. *Journal of Solar Energy Engineering*, 129(4):405–411, 2007.

61. D. S. Codd, A. Carlson, J. Rees, and A. H. Slocum. A low cost high flux solar simulator. *Solar Energy*, 84(12):2202–2212, 2010.
62. K. R. Krueger, J. H. Davidson, and W. Lipiński. Design of a new 45 kW<sub>e</sub> high-flux solar simulator for high-temperature solar thermal and thermochemical research. *Journal of Solar Energy Engineering*, 133(1):011013, 2011.
63. K. R. Krueger, W. Lipiński, and J. H. Davidson. Operational performance of the university of Minnesota 45 kW<sub>e</sub> high-flux solar simulator. In *Proceedings of the ASME 2012 6th International Conference on Energy Sustainability*, pages 1093–1099, 2013.
64. J. Sarwar, G. Georgakis, R. LaChance, and N. Ozalp. Description and characterization of an adjustable flux solar simulator for solar thermal, thermochemical and photovoltaic applications. *Solar Energy*, 100:179–194, 2014.
65. G. Xiao, K. Guo, Z. Luo, M. Ni, Y. Zhang, and C. Wang. Simulation and experimental study on a spiral solid particle solar receiver. *Applied Energy*, 113:178–188, 2014. (cited on page 17)
66. R. Bader, S. Haussener, and W. Lipiński. Optical design of multi-source high-flux solar simulators. *Journal of Solar Energy Engineering*, 137(2):021012, 2015. (cited on pages 6, 13, and 21)
67. X. Dong, Z. Sun, G. J. Nathan, P. J. Ashman, and D. Gu. Time-resolved spectra of solar simulators employing metal halide and xenon arc lamps. *Solar Energy*, 115:613–620, 2015.
68. B. M. Ekman, G. Brooks, and M. A. Rhamdhani. Development of high flux solar simulators for solar thermal research. *Solar Energy Materials and Solar Cells*, 141:436–446, 2015.
69. R. Gill, E. Bush, P. Haueter, and P. Loutzenhiser. Characterization of a 6 kW high-flux solar simulator with an array of xenon arc lamps capable of concentrations of nearly 5000 suns. *Review of Scientific Instruments*, 86(12):125107, 2015.
70. G. Levêque, R. Bader, W. Lipiński, and S. Haussener. Experimental and numerical characterization of a new 45 kW<sub>e</sub> multi-source high-flux solar simulator. *Optics Express*, 24(22):A1360–A1373, 2016. (cited on page 6)
71. K. Wiegardt, K.-H. Funken, G. Dibowski, B. Hoffschmidt, D. Laaber, P. Hilger, and K.-P. Eßer. SynLight—the world’s largest artificial sun. In *Proceedings of AIP Conference*, volume 1734, page 030038. AIP Publishing, 2016.
72. J. Xu, C. Tang, Y. Cheng, Z. Li, H. Cao, X. Yu, Y. Li, and Y. Wang. Design, construction, and characterization of an adjustable 70 kW high-flux solar simulator. *Journal of Solar Energy Engineering*, 138(4):041010, 2016.

73. A. Boubault, J. Yellowhair, and C. K. Ho. Design and characterization of a 7.2 kW solar simulator. *Journal of Solar Energy Engineering*, 139(3):031012, 2017.
74. W. Wang, L. Aichmayer, J. Garrido, and B. Laumert. Development of a Fresnel lens based high-flux solar simulator. *Solar Energy*, 144:436–444, 2017.
75. S. Dai, Z. Chang, T. Ma, L. Wang, and X. Li. Experimental study on flux mapping for a novel 84 kW<sub>e</sub> high flux solar simulator. *Applied Thermal Engineering*, 162:114319, 2019.
76. J. Jin, Y. Hao, and H. Jin. A universal solar simulator for focused and collimated beams. *Applied Energy*, 235:1266–1276, 2019. (cited on page 6)
77. J. Song, J. Wang, Y. Niu, W. Wang, K. Tong, H. Yu, and Y. Yang. Flexible high flux solar simulator based on optical fiber bundles. *Solar Energy*, 193:576–583, 2019. (cited on page 6)
78. X. Li, J. Chen, W. Lipiński, Y. Dai, and C.-H. Wang. A 28 kW<sub>e</sub> multi-source high-flux solar simulator: Design, characterization, and modeling. *Solar Energy*, 211:569–583, 2020.
79. J. Li and M. Lin. Unified design guidelines for high flux solar simulator with controllable flux vector. *Applied Energy*, 281:116083, 2021. (cited on page 6)
80. J. J. Pottas, M. Habib, and W. Lipiński. Photogrammetric measurement and alignment of radiation modules in a high-flux solar simulator. In *Light, Energy and the Environment 2018*. Optical Society of America, 2018. paper OW3D.4. (cited on page 6)
81. M. Habib. Control system design for a solar receiver-reactor. Master's thesis, The Australian National University, 2019. (cited on page 6)
82. D. N. Harries, M. Paskevicius, D. A. Sheppard, T. E. C. Price, and C. E. Buckley. Concentrating solar thermal heat storage using metal hydrides. *Proceedings of the IEEE*, 100(2):539–549, 2011. (cited on page 6)
83. L. Reich, L. Yue, R. Bader, W. Lipinski, et al. Towards solar thermochemical carbon dioxide capture via calcium oxide looping: A review. *Aerosol and Air Quality Research*, 14(2):500–514, 2014. (cited on page 6)
84. J. Botas, J. Marugán, R. Molina, and C. Herradón. Kinetic modelling of the first step of Mn<sub>2</sub>O<sub>3</sub>/MnO thermochemical cycle for solar hydrogen production. *International Journal of Hydrogen Energy*, 37(24):18661–18671, 2012. (cited on pages 6 and 22)
85. M. Hamidi, A. Bayon, V. M. Wheeler, P. Kreider, M. A. Wallace, T. Tsuzuki, K. Catchpole, and A. W. Weimer. Reduction kinetics for large spherical 2: 1 iron–manganese oxide redox materials for thermochemical energy storage. *Chemical Engineering Science*, 201:74–81, 2019. (cited on pages 6 and 7)



86. M. Hamidi, V. M. Wheeler, X. Gao, J. Pye, K. Catchpole, and A. W. Weimer. Reduction of iron–manganese oxide particles in a lab-scale packed-bed reactor for thermochemical energy storage. *Chemical Engineering Science*, 221:115700, 2020. (cited on pages 6 and 7)
87. Project plan: High temperature solar thermal energy storage via manganese-oxide based redox. Technical report, The Australian National University, Canberra, Australia, 2014. (cited on page 7)
88. B. Wang, L. Li, R. Bader, J. Pottas, V. Wheeler, P. Kreider, and W. Lipiński. Thermal model of a solar thermochemical reactor for metal oxide reduction. *Journal of Solar Energy Engineering*, 142(5):051002, 2020. (cited on pages 7 and 25)
89. B. Wang, L. Li, F. Schäfer, J. Pottas, A. Kumar, V. Wheeler, and W. Lipiński. Thermal reduction of iron–manganese oxide particles in a high-temperature packed-bed solar thermochemical reactor. *Chemical Engineering Journal*, 410(C):128255, 2021. (cited on pages 7 and 25)
90. M. Sturzenegger and P. Nüesch. Efficiency analysis for a manganese-oxide-based thermochemical cycle. *Energy*, 24(11):959–970, 1999. (cited on page 6)
91. T. Block and M. Schmücker. Metal oxides for thermochemical energy storage: A comparison of several metal oxide systems. *Solar Energy*, 126:195–207, 2016. (cited on page 6)
92. J. R. Howell. The Monte Carlo method in radiative heat transfer. *Journal of Heat Transfer*, 120(3):547–560, 1998. (cited on pages 7 and 19)
93. C. Gueymard, D. Myers, and K. Emery. Proposed reference irradiance spectra for solar energy systems testing. *Solar Energy*, 73(6):443–467, 2002. (cited on page 10)
94. C. A. Gueymard. The sun’s total and spectral irradiance for solar energy applications and solar radiation models. *Solar Energy*, 76(4):423–453, 2004. (cited on page 10)
95. F. E. Nicodemus. Directional reflectance and emissivity of an opaque surface. *Applied Optics*, 4(7):767–775, 1965. (cited on page 10)
96. K. E. Torrance and E. M. Sparrow. Theory for off-specular reflection from roughened surfaces. *Journal of the Optical Society of America*, 57(9):1105–1114, 1967. (cited on page 10)
97. R. M. Goody and Y. L. Yung. *Atmospheric Radiation: Theoretical Basis*. Oxford University Press, 1995. (cited on page 11)
98. V. Rozanov, T. Dinter, A. Rozanov, A. Wolanin, A. Bracher, and J. Burrows. Radiative transfer modeling through terrestrial atmosphere and ocean accounting for inelastic processes: Software package SCIATRAN. *Journal of Quantitative Spectroscopy and Radiative Transfer*, 194:65–85, 2017. (cited on page 11)

99. H. Hinterberger and R. Winston. Efficient light coupler for threshold čerenkov counters. *Review of Scientific Instruments*, 37(8):1094–1095, 1966. (cited on page 11)
100. P. Gleckman, J. O’Gallagher, and R. Winston. Concentration of sunlight to solar-surface levels using non-imaging optics. *Nature*, 339(6221):198, 1989. (cited on page 11)
101. A. Yogev, A. Kribus, M. Epstein, and A. Kogan. Solar “tower reflector” systems: A new approach for high-temperature solar plants. *International Journal of Hydrogen Energy*, 23(4):239–245, 1998. (cited on pages 14 and 16)
102. A. Segal and M. Epstein. Comparative performances of ‘tower-top’ and ‘tower-reflector’ central solar receivers. *Solar Energy*, 65(4):207–226, 1999. (cited on page 16)
103. A. Segal and M. Epstein. The optics of the solar tower reflector. *Solar Energy*, 69:229–241, 2001. (cited on pages 14 and 16)
104. T. Cooper, F. Dähler, G. Ambrosetti, A. Pedretti, and A. Steinfeld. Performance of compound parabolic concentrators with polygonal apertures. *Solar Energy*, 95:308–318, 2013. (cited on pages 11 and 12)
105. S. Madala and R. F. Boehm. A review of nonimaging solar concentrators for stationary and passive tracking applications. *Renewable and Sustainable Energy Reviews*, 71:309–322, 2017.
106. M. Tian, Y. Su, H. Zheng, G. Pei, G. Li, and S. Riffat. A review on the recent research progress in the compound parabolic concentrator (CPC) for solar energy applications. *Renewable and Sustainable Energy Reviews*, 82:1272–1296, 2018.
107. D. Patel, P. Brahmhatt, and H. Panchal. A review on compound parabolic solar concentrator for sustainable development. *International Journal of Ambient Energy*, 39(5):533–546, 2018. (cited on page 11)
108. W. Lipiński and A. Steinfeld. Annular compound parabolic concentrator. *Journal of solar energy engineering*, 128(1):121–124, 2006. (cited on page 11)
109. L. Li, B. Wang, J. Pottas, and W. Lipiński. Design of a compound parabolic concentrator for a multi-source high-flux solar simulator. *Solar Energy*, 183:805–811, 2019. (cited on pages 12, 16, 23, and 25)
110. A. Timinger, W. Spirkl, A. Kribus, and H. Ries. Optimized secondary concentrators for a partitioned central receiver system. *Solar Energy*, 69(2):153–162, 2000. (cited on page 12)
111. D. Xu and M. Qu. Compound parabolic concentrators in solar thermal applications: a review. In *Proceedings of the ASME 2013 7th International Conference on Energy Sustainability*, Minneapolis, Minesota, USA, July 2013.

112. S. H. Abu-Bakar, F. Muhammad-Sukki, D. Freier, R. Ramirez-Iniguez, T. K. Mallick, A. B. Munir, S. H. M. Yasin, A. A. Mas'ud, and N. M. Yunus. Performance analysis of a novel rotationally asymmetrical compound parabolic concentrator. *Applied Energy*, 154:221–231, 2015. (cited on page 12)
113. R. Bader, G. Levêque, S. Haussener, and W. Lipiński. High-flux solar simulator technology. In *Optics for Solar Energy*, pages SoM3C–3. Optical Society of America, 2016. (cited on page 13)
114. A. Gallo, A. Marzo, E. Fuentealba, and E. Alonso. High flux solar simulators for concentrated solar thermal research: A review. *Renewable and Sustainable Energy Reviews*, 77:1385–1402, 2017. (cited on page 13)
115. V. M. Wheeler, R. Bader, P. B. Kreider, M. Hangi, S. Haussener, and W. Lipiński. Modelling of solar thermochemical reaction systems. *Solar Energy*, 156:149–168, 2017. (cited on page 14)
116. C. E. Mauk, H. W. Prengle Jr, and E. C.-H. Sun. Optical and thermal analysis of a Cassegrainian solar concentrator. *Solar Energy*, 23(2):157–167, 1979. (cited on pages 14 and 16)
117. A. Segal and M. Epstein. Practical considerations in designing large scale “beam down” optical systems. *Journal of solar energy engineering*, 130(1):011009, 2008.
118. E. Leonardi. Detailed analysis of the solar power collected in a beam-down central receiver system. *Solar Energy*, 86(2):734–745, 2012.
119. X. Wei, Z. Lu, W. Yu, and W. Xu. Ray tracing and simulation for the beam-down solar concentrator. *Renewable Energy*, 50:161–167, 2013. (cited on pages 14 and 16)
120. T. Tan and Y. Chen. Review of study on solid particle solar receivers. *Renewable and Sustainable Energy Reviews*, 14(1):265–276, 2010. (cited on page 14)
121. A. L. Ávila Marín. Volumetric receivers in solar thermal power plants with central receiver system technology: A review. *Solar Energy*, 85(5):891–910, 2011. (cited on page 14)
122. C. K. Ho and B. D. Iverson. Review of high-temperature central receiver designs for concentrating solar power. *Renewable and Sustainable Energy Reviews*, 29:835–846, 2014. (cited on page 14)
123. J. Coventry, C. Andraka, J. Pye, M. Blanco, and J. Fisher. A review of sodium receiver technologies for central receiver solar power plants. *Solar Energy*, 122: 749–762, 2015. (cited on page 14)
124. C. K. Ho. A review of high-temperature particle receivers for concentrating solar power. *Applied Thermal Engineering*, 109:958–969, 2016. (cited on page 14)

125. M. Romero, R. Buck, and J. E. Pacheco. An update on solar central receiver systems, projects, and technologies. *Journal of Solar Energy Engineering*, 124(2): 98–108, 2002. (cited on page 14)
126. P. Garcia, A. Ferriere, and J.-J. Beziau. Codes for solar flux calculation dedicated to central receiver system applications: A comparative review. *Solar Energy*, 82 (3):189–197, 2008. (cited on pages 14 and 19)
127. O. Behar, A. Khellaf, and K. Mohammadi. A review of studies on central receiver solar thermal power plants. *Renewable and Sustainable Energy Reviews*, 23:12–39, 2013. (cited on page 14)
128. V. S. Reddy, S. Kaushik, K. Ranjan, and S. Tyagi. State-of-the-art of solar thermal power plants—A review. *Renewable and Sustainable Energy Reviews*, 27:258–273, 2013. (cited on page 14)
129. T. M. Pavlović, I. S. Radonjić, D. D. Milosavljević, and L. S. Pantić. A review of concentrating solar power plants in the world and their potential use in Serbia. *Renewable and Sustainable Energy Reviews*, 16(6):3891–3902, 2012. (cited on page 14)
130. H. Zhang, J. Baeyens, J. Degève, and G. Cacères. Concentrated solar power plants: Review and design methodology. *Renewable and Sustainable Energy Reviews*, 22:466–481, 2013. (cited on page 14)
131. L. Li, S. Yang, B. Wang, J. Pye, and W. Lipiński. Optical analysis of a solar thermochemical system with a rotating tower reflector and a receiver–reactor array. *Optics Express*, 28(13):19429–19445, 2020. (cited on page 15)
132. J. Coventry and J. Pye. Heliostat cost reduction—where to now? *Energy Procedia*, 49:60–70, 2014. (cited on pages 15 and 71)
133. A. Pfahl. Survey of heliostat concepts for cost reduction. *Journal of Solar Energy Engineering*, 136(1):014501, 2014. (cited on page 15)
134. A. W. Dowling, T. Zheng, and V. M. Zavala. Economic assessment of concentrated solar power technologies: A review. *Renewable and Sustainable Energy Reviews*, 72:1019–1032, 2017. (cited on pages 15 and 71)
135. F. Lipps and L. Vant-Hull. A cellwise method for the optimization of large central receiver systems. *Solar Energy*, 20(6):505–516, 1978. (cited on page 16)
136. C. J. Noone, M. Torrilhon, and A. Mitsos. Heliostat field optimization: A new computationally efficient model and biomimetic layout. *Solar Energy*, 86(2):792–803, 2012. (cited on pages 16 and 71)
137. F. J. Collado and J. Guallar. Campo: Generation of regular heliostat fields. *Renewable Energy*, 46:49–59, 2012. (cited on page 16)

138. F. Siala and M. Elayeb. Mathematical formulation of a graphical method for a no-blocking heliostat field layout. *Renewable Energy*, 23(1):77–92, 2001. (cited on page 16)
139. T. A. Dellin and M. J. Fish. User’s manual for DELSOL: a computer code for calculating the optical performance, field layout, and optimal system design for solar central receiver plants. Technical report, Sandia National Laboratories, Livermore, CA (USA), 1979. (cited on page 16)
140. X. Wei, Z. Lu, Z. Wang, W. Yu, H. Zhang, and Z. Yao. A new method for the design of the heliostat field layout for solar tower power plant. *Renewable Energy*, 35(9):1970–1975, 2010. (cited on page 16)
141. J. Barberena, A. M. Larrayoz, M. Sánchez, and A. Bernardos. State-of-the-art of heliostat field layout algorithms and their comparison. *Energy Procedia*, 93: 31–38, 2016. (cited on page 16)
142. A. Mutuberría, J. Pascual, M. Guisado, and F. Mallor. Comparison of heliostat field layout design methodologies and impact on power plant efficiency. *Energy Procedia*, 69:1360–1370, 2015. (cited on page 16)
143. R. N. Wilson. *Reflecting Telescope Optics II: Manufacture, Testing, Alignment, Modern Techniques*. Springer Science & Business Media, 2013. (cited on page 16)
144. L. Vant-Hull. Issues with beam-down concepts. *Energy Procedia*, 49:257–264, 2014. (cited on page 16)
145. T. Kodama, N. Gokon, H. S. Cho, K. Matsubara, T. Etori, A. Takeuchi, S.-n. Yokota, and S. Ito. Particles fluidized bed receiver/reactor with a beam-down solar concentrating optics: 30-kW<sub>th</sub> performance test using a big sun-simulator. *AIP Conference Proceedings*, 1734(1):120004, 2016. (cited on pages 16 and 17)
146. Helioscsp, 2019. <http://helioscsp.com/three-solar-modules-of-worlds-first-commercial-beam-down-tower-concentrated-solar-power-project-to-be-connected-to-grid/>. (cited on page 16)
147. H. Hasuike, Y. Yoshizawa, A. Suzuki, and Y. Tamaura. Study on design of molten salt solar receivers for beam-down solar concentrator. *Solar Energy*, 80(10):1255–1262, 2006. (cited on page 17)
148. M. Epstein, G. Olalde, S. Santén, A. Steinfeld, and C. Wieckert. Towards the industrial solar carbothermal production of zinc. *Journal of Solar Energy Engineering*, 130(1):014505, 2008.
149. E. Koepf, S. G. Advani, A. Steinfeld, and A. K. Prasad. A novel beam-down, gravity-fed, solar thermochemical receiver/reactor for direct solid particle decomposition: Design, modeling, and experimentation. *International Journal of Hydrogen Energy*, 37(22):16871–16887, 2012.

150. A. Lenert and E. N. Wang. Optimization of nanofluid volumetric receivers for solar thermal energy conversion. *Solar Energy*, 86(1):253–265, 2012.
151. M. Mokhtar, S. A. Meyers, P. R. Armstrong, and M. Chiesa. Performance of a 100 kW<sub>th</sub> concentrated solar beam-down optical experiment. *Journal of Solar Energy Engineering*, 136(4):041007, 2014.
152. X. Li, Y. Dai, and R. Wang. Performance investigation on solar thermal conversion of a conical cavity receiver employing a beam-down solar tower concentrator. *Solar Energy*, 114:134–151, 2015.
153. M. Martins, U. Villalobos, T. Delclos, P. Armstrong, P. G. Bergan, and N. Calvet. New concentrating solar power facility for testing high temperature concrete thermal energy storage. *Energy Procedia*, 75:2144–2149, 2015.
154. S. Bellan, K. Matsubara, C. H. Cheok, N. Gokon, and T. Kodama. CFD-DEM investigation of particles circulation pattern of two-tower fluidized bed reactor for beam-down solar concentrating system. *Powder Technology*, 319:228–237, 2017. (cited on page 17)
155. P. K. Falcone. A handbook for solar central receiver design. Technical report, Sandia National Laboratories, Livermore, CA (USA), 1986. (cited on page 17)
156. C. K. Ho. Software and codes for analysis of concentrating solar power technologies. Technical report, Sandia National Laboratories, Livermore, CA (USA), 2008. (cited on page 19)
157. S.-J. Bode and P. Gauché. Review of optical software for use in concentrating solar power systems. In *Proceedings of South African Solar Energy Conference*, 2012. (cited on page 19)
158. M. Metcalf, J. Reid, and M. Cohen. *Modern Fortran Explained: Incorporating Fortran 2018*. Oxford University Press, 2018. (cited on page 19)
159. C.-A. Asselineau, J. Zapata, and J. Pye. Integration of Monte-Carlo ray tracing with a stochastic optimisation method: application to the design of solar receiver geometry. *Optics Express*, 23(11):A437–A443, 2015. (cited on page 19)
160. A. B. Sproul. Derivation of the solar geometric relationships using vector analysis. *Renewable Energy*, 32(7):1187–1205, 2007. (cited on pages 20 and 22)
161. P. Ineichen. A broadband simplified version of the Solis clear sky model. *Solar Energy*, 82(8):758–762, 2008. (cited on page 20)
162. P. Leary and J. Hankins. User’s guide for MIRVAL: a computer code for comparing designs of heliostat-receiver optics for central receiver solar power plants. Technical report, Sandia National Laboratories, Livermore, CA (USA), 1979. (cited on page 21)

163. K. R. Krueger. *Design and characterization of a concentrating solar simulator*. PhD thesis, University of Minnesota, 2012. (cited on page 21)
164. V. Grigoriev, C. Corsi, and M. Blanco. Fourier sampling of sun path for applications in solar energy. In *AIP Conference Proceedings*, volume 1734, page 020008. AIP Publishing, 2016. (cited on page 22)
165. W. H. Press, S. A. Teukolsky, W. T. Vetterling, and B. P. Flannery. *Numerical Recipes in Fortran 77 and Fortran 90: Source Code for Recipes and Example Programs*. Cambridge University Press, Cambridge, UK, 1997. (cited on page 22)
166. C. Caliot, H. Benoit, E. Guillot, J.-L. Sans, A. Ferriere, G. Flamant, C. Coustet, and B. Piaud. Validation of a Monte Carlo integral formulation applied to solar facility simulations and use of sensitivities. *Journal of Solar Energy Engineering*, 137(2):021019, 2015. (cited on pages 22 and 23)
167. Y. Meller. Tracer—a pythonic ray-tracing package with solar energy focus, Last retrieved on 4 November 2019. URL <https://github.com/yosefm/tracer>. (cited on page 23)
168. M. J. Blanco, J. M. Amieva, and A. Mancillas. The Tonatiuh Software Development Project: An open source approach to the simulation of solar concentrating systems. In *ASME 2005 International Mechanical Engineering Congress and Exposition*, pages 157–164, 2005. (cited on page 23)
169. D. Feuermann and J. M. Gordon. Solar fiber-optic mini-dishes: a new approach to the efficient collection of sunlight. *Solar Energy*, 65(3):159–170, 1999. (cited on page 33)
170. F. Dähler, M. Wild, R. Schächli, P. Haueter, T. Cooper, P. Good, C. Larrea, M. Schmitz, P. Furler, and A. Steinfeld. Optical design and experimental characterization of a solar concentrating dish system for fuel production via thermochemical redox cycles. *Solar Energy*, 170:568–575, 2018. (cited on pages 33 and 103)
171. Y. Zhang, G. Xiao, Z. Luo, M. Ni, T. Yang, and W. Xu. Comparison of different types of secondary mirrors for solar application. *Optik*, 125(3):1106–1112, 2014. (cited on page 33)
172. J. Wang, S. Yang, C. Jiang, Q. Yan, and P. D. Lund. A novel 2-stage dish concentrator with improved optical performance for concentrating solar power plants. *Renewable Energy*, 108:92–97, 2017.
173. S. Yang, J. Wang, P. D. Lund, C. Jiang, and D. Liu. Assessing the impact of optical errors in a novel 2-stage dish concentrator using Monte-Carlo ray-tracing simulation. *Renewable Energy*, 123:603–615, 2018. (cited on page 33)
174. R. Buck. Heliostat field layout using non-restricted optimization. In *SolarPACES Conference*, 2012. (cited on page 71)

175. J. T. Hinkley, J. A. Hayward, B. Curtin, A. Wonhas, R. Boyd, C. Grima, A. Tadros, R. Hall, and K. Naicker. An analysis of the costs and opportunities for concentrating solar power in Australia. *Renewable Energy*, 57:653–661, 2013. (cited on page 71)
176. G. J. Kolb, C. K. Ho, T. R. Mancini, and J. A. Gary. Power tower technology roadmap and cost reduction plan. Technical Report SAND2011-2419, Sandia National Laboratories, Albuquerque, NM, 2011. (cited on page 71)
177. G. J. Kolb, S. A. Jones, M. W. Donnelly, D. Gorman, R. Thomas, R. Davenport, and R. Lumia. Heliostat cost reduction study. Technical Report SAND2007-3293, Sandia National Laboratories, Albuquerque, NM, 2007. (cited on page 71)
178. E. Leonardi, L. Pisani, I. Les, A. M. Larrayoz, S. Rohani, and P. Schöttl. Techno-economic heliostat field optimization: Comparative analysis of different layouts. *Solar Energy*, 180:601–607, 2019. (cited on page 71)
179. R. Pitz-Paal, N. B. Botero, and A. Steinfeld. Heliostat field layout optimization for high-temperature solar thermochemical processing. *Solar Energy*, 85(2):334–343, 2011. (cited on page 71)
180. M. Schmitz, P. Schwarzbözl, R. Buck, and R. Pitz-Paal. Assessment of the potential improvement due to multiple apertures in central receiver systems with secondary concentrators. *Solar Energy*, 80(1):111–120, 2006. (cited on page 71)
181. L. Li, B. Wang, J. Pye, R. Bader, W. Wang, and W. Lipiński. Optical analysis of a multi-aperture solar central receiver system for high-temperature concentrating solar applications. *Optics Express*, 28(25):37654–37668, 2020. (cited on page 87)
182. S. Yang, L. Li, S. Li, B. Wang, P. Lund, J. Wang, and W. Lipiński. Thermodynamic analysis of a novel solar beam-down system with a rotating tower reflector and a receiver–reactor array. *Frontiers in Energy Research*, 2021. under review. (cited on pages 103 and 124)